Interpolative-Based Maximum-Entropy Moment Closures for Predicting Real-Gas Radiative Heat Transfer

by

Joachim André Raymond Sarr

A thesis submitted in conformity with the requirements
for the degree of Doctor of Philosophy
Graduate Department of Aerospace Engineering
University of Toronto

Abstract

Interpolative-Based Maximum-Entropy Moment Closures for Predicting Real-Gas Radiative Heat Transfer

Joachim André Raymond Sarr
Doctor of Philosophy
Graduate Department of Aerospace Engineering
University of Toronto
2023

New, efficient, realizable and hyperbolic interpolative-based first- and second-order maximum entropy, M_1 and M_2, respectively, moment closures for providing approximate numerical solutions to the equation of radiative transfer in both gray (for M_2) and non-gray (for M_1 and M_2) participating media are proposed and thoroughly described. These newly-developed interpolative closure techniques, in addition to retaining many of the desirable mathematical and numerical properties of the original maximum entropy closures, allow to accurately reproduce maximum entropy solutions at a fraction of the computational costs associated with the expensive direct numerical solution of the entropy optimization problem. Furthermore, a new procedure for the particular implementation of the proposed interpolative non-gray M_1 and M_2 closures in the context of a statistical narrow-band correlated-k (SNBCK) model, is also presented. The latter is used for the treatment of the strong spectral dependence exhibited by the absorption coefficient of radiatively participating real gases. New boundary conditions, based on the method of characteristics, are also proposed for use with the hyperbolic systems of moment equations arising from the M_1 and M_2 closures. The predictive capabilities of the M_1 and M_2 closures are then assessed by comparing their solutions to those of the more commonly adopted first-order, P_1, and third-order, P_3, spherical harmonic moment closures, as well as the popular discrete ordinates method (DOM). The latter is used as a bench-

mark for the comparisons whenever exact analytical solutions of the radiative transfer equation (RTE) are not available. A first set of assessments is performed by considering tests problems involving both gray and non-gray radiative heat transfer within one- and two-dimensional enclosures, with prescribed thermochemical quantities. Reactive flows simulations of sooting laminar co-flow diffusion flames are then considered at various pressures. The numerical results for most of the test cases studied in the context of non-reactive flows show that the M_1 maximum-entropy moment closure, in addition to providing extra computational robustness relative to the P_1 and P_3 moment closures, provides solutions of at least comparable accuracy to those of the P_3 closure while incurring only a rather modest or minor increase in computational costs relative to the P_1 spherical harmonic moment closure. In situations where streams of photons emanating from different directions cross each other, the M_2 closure represents a better alternative to the M_1 closure which cannot properly capture such phenomena and instead may yield unphysical solutions, though the computational costs associated with former are observed to be much more involved than those associated with the latter. For the high-pressure reactive flow simulations performed as part of this thesis, the predictive capabilities of the M_1 and M_2 closures were observed to be superior to those of the P_1 closure for all the pressures studied. On the other hand, the P_3 closure was observed to be of comparable accuracy to the M_2 closure at low pressures. However, at higher pressures, both the M_1 and M_2 closures displayed a trend of increasingly improved accuracy compared to the P_3 closure.

Acknowledgements

I owe my deepest gratitude to my thesis supervisor Professor Clinton P. T. Groth for giving me the opportunity to further my education, as a graduate student in the computational fluid dynamics (CFD) and propulsion laboratory, at the University of Toronto Institute for Aerospace Studies (UTIAS). This thesis would not have been possible without his encouragement, guidance, and support from both academic and personal standpoints.

I would like to thank my thesis committee members Professor Ömer Gülder and Dr. Fengshan Liu from the National Research Council Canada (NRC), for their helpful questions, comments, and suggestions during each of my annual research review, as well as Professor Teddy Pichard from "École Polytechnique de Paris" for the collaborative research over the last few years. My research has benefited immensely from their inputs.

I would also like to thank all my friends and family for their support and encouragement. I am particularly indebted to my mother Marianne Sarr who has always been an unwavering supporter of everything I have pursued, as well as my late father Simon Sarr, whom I know would have been extremely proud of my accomplishments thus far.

My fellow students at the university have also added greatly to my experience as a graduate student at UTIAS. I would like to particularly thank Dr. Jacques Xing.

This research was funded by grants and contracts from the Green Aviation Research and Development Network (GARDN), Southern Ontario Smart Computing for Innovation Platform (SOSCIP), as well as Pratt & Whitney Canada, in addition to scholarships from the Natural Sciences and Engineering Research Council (NSERC) of Canada and the Ontario Graduate Scholarship (OGS).

Computational resources for performing all of the calculations reported herein were provided by the SciNet High Performance Computing Consortium at the University of Toronto and Compute/Calcul Canada through funding from the Canada Foundation for Innovation (CFI) and the Province of Ontario, Canada.

Joachim André Raymond Sarr
University of Toronto Institute for Aerospace Studies
2023

Contents

List of Figures

"What one fool can understand, another can."

Richard P. Feynmann, *QED The Strange Theory of Light and Matter*

Chapter 1

Introduction

1.1 Overview

The recent advances in computer science and engineering have paved the way for the more widespread use of numerical modelling for studying the behaviour of physical systems in a wide variety of applications. Despite still relying on empirical data in many cases, whether it be for validation purposes or due to the lack of mathematical models for the purpose of numerical simulations, numerical modelling is also very attractive as it provides greater flexibility for evaluating the sensitivity of a given physical system to any of the parameters that influence its behaviour.

The combustion of hydrocarbons is still today the main source of energy production worldwide [2], despite its negative environmental impact. This, combined with the observed depletion of hydrocarbons resources, and the lack of sufficient alternative resources, has rendered the development of efficient and environmentally friendly combustion devices even more important, whether it be for transportation systems or for industrial energy production. Combustion is however a complex process which involves a wide variety of phenomena including but not limited to fluid dynamics, chemical kinetics, heat transfer. Among such phenomena, a primary focus over the past few decades has been on gaining an improved understanding of the complex physical and chemical processes governing the formation and evolution of soot [3–22].

In hydrocarbon combustion, concentrated regions of participating gases, such as carbon

dioxide (CO_2), water vapour (H_2O) and carbon monoxide (CO), as well as clouds of small particles such as soot, reach high temperatures. This in turn results in significant heat losses to the surroundings, mainly via radiation, with soot accounting for a substantial portion of such radiative heat losses. Since the net production rates of both soot and gaseous species involved in combustion processes are strongly dependent on temperature, it therefore follows that accurate predictions of species concentration and soot formation rely heavily on detailed treatment of thermal radiation [2].

The equation governing the transport of radiative energy within a radiatively participating medium, which is commonly referred to as the radiative transfer equation (RTE) [23], is a complex linear integro-differential equation with high dimensionality, since the distribution of radiation is a function of seven independent variables. The high dimensionality makes it impossible to derive general exact analytical solutions for the RTE in the general case, and approximate solutions of the latter equation are generally obtained by numerical means.

In addition to its spatial and temporal dependencies, the radiative intensity distribution is also a function of frequency or wavenumber and direction of propagation of radiation. The spatial and temporal variations are commonly treated using traditional finite-volume schemes for the solution of discrete governing equations over finite control volumes [24–30]. A wide range of spectral radiation models have been developed for the treatment of the spectral dependence of the distribution of radiative intensity, including the state-of-the-art statistical narrow-band correlated-k (SNBCK) and the full spectrum correlated-k (FSCK) techniques [31–34]. It should be emphasized that, as a result of the high dimensionality of the RTE, the assumption of gray radiatively participating media is also sometimes employed in order to cope with the spectral dependence of the radiative intensity distribution. While simplifying the solution of the RTE, such an assumption, which consists of neglecting the spectral dependence of the absorption coefficient, is however strongly violated in the context of real-gas radiation where such dependence is rather strong and must be properly accounted for accurate predictions of radiation solutions. The treatment of the directional dependence of the radiative intensity distribution, for accurate and efficient predictions of radiative quantities, is still an active research subject.

Stochastic models such as the Monte Carlo method [35] have been reported to yield realistic solutions of the RTE. The zonal method [36] has also been used widely for engineering

radiative heat transfer calculations in multi-dimensional enclosures. Its implementation is however limited to non-scattering media as it cannot be readily adapted for a scattering medium. Both of those methods are also somewhat limited in the sense that they are not compatible with the usual numerical methods used for solving the appropriate variants of the partial differential equations (PDEs) governing the flow and temperature fields arising from the Navier-Stokes equations for a reactive mixture.

The discrete ordinates method (DOM) [37,38] and the finite-volume method (FVM) [39] are some of the most widely used techniques for providing approximate solutions for the RTE. The DOM is based on a direct discretization of the angular dependence of the radiative intensity distribution, and is generally used in conjunction with space marching iterative techniques [37] in order to provide numerical solutions of the RTE for any given problem. While extremely efficient for problems involving relatively simple geometry and simplified physics (e.g., non-scattering media), the space marching techniques can become inefficient for problems with complex three-dimensional geometries and realistic physics [29], as is the case in many practical applications.

The potential computational limitations of the DOM have motivated the investigation of alternative approximate radiation solution techniques, such as the method of moments as originally proposed by Grad [40] in the case of gas-kinetic theory. As the name suggests, the method of moments solves directly for just a finite set of angular integrals of the intensity distribution, instead of solving directly for the angular distribution, and this can afford a reduction in computational costs compared to those associated with solving directly the high-dimensional RTE. The resulting system of equations for the finite set of moments can not be readily solved however, as there are more unknowns than equations. Additional relations, or closure relations, between the highest-order moments (unknown) and the known finite set of lower-order moments are required for closure. The closure relations are generally obtained by making an assumption about the approximate form for the underlying radiative intensity distribution in terms of the lower-order moments, among the infinite family of possible angular distributions reproducing a given finite set of angular moments.

The most common approach for providing closure to the finite-sized systems of angular moment equations arising from the RTE is the spherical harmonic P_N approximation [41, 42], where N refers to the order of the approximation, or the order of the highest

moments in the closed system of moment equations. In the P_N moment closures, the radiative intensity distribution is approximated by a truncated series expansion in terms of a basis of orthogonal spherical harmonic functions. Analytical expressions for the closing relations can be obtained, for any order N, by appropriately integrating the approximate form of the distribution with respect to its angular variables. Nevertheless, one of the main limitations of the P_N moment closures is their inability to properly capture highly anisotropic regimes. In fact, in such regimes, the distribution of radiation is uniquely determined by a Dirac-delta, which is almost impossible to reproduce with a polynomial expansion of the radiative intensity distribution, as in the linear P_N closures.

The lowest-order spherical harmonic approximation, namely the first-order, P_1, closure has been extensively used to provide approximate solutions to the radiative heat transfer equation [43–46], due to its simplicity and relatively low computational costs. However, because the closing relations for the P_1 approximation are similar to those of an isotropic distribution with the same energy density, the latter closure cannot properly describe highly anisotropic distributions of radiation. In fact, the resulting approximate form of the radiative intensity distribution is indeed a first-order polynomial expansion of the true distribution around directional equilibrium. Beyond the P_1 closure, even-order P_N approximations are known to be less accurate than their odd-lower-order counterparts [47] and thus only odd-order spherical harmonic closures are generally considered. While the P_3 approximation can capture more anisotropy in the distribution than its first-order counterpart, this comes at the expense of significant increases in computational costs [47]. Beyond the P_3 closure, it was observed that the efficiency of the P_N approximations degraded rapidly while improvements in terms of accuracy were rather minor [48]. Another important drawback of the P_N closures is that the approximate forms of the distribution of radiative intensity are not strictly positive and the closures are not valid for the full range of physically realizable moments at any order.

As alternatives to spherical harmonic expansions of the radiative intensity distribution, there has recently been particular interest in maximum-entropy-based, M_N, closures to the system of moment equations arising from application of the method of moments to the RTE [49]. Approaches based on the principle of maximization of entropy are particularly attractive for several reasons, among which is the fact that, for a given finite set of moments, they provide the most likely form of the radiative intensity distribution among all the possible forms that reproduce the given set of moments [50], which is a highly

desirable feature for an accurate closure. In fact, unlike their spherical harmonic counterparts, which are based on a mathematical representation of the angular distribution on the surface of the unit sphere, entropy-based moment closures use a physically consistent principle to derive the form of the underlying distribution, for a given finite set of moments. The hierarchy of M_N models also possesses many desirable mathematical and numerical properties, including hyperbolicity and moment realizability. The latter property implies that the entropy-maximizing distribution for a given finite set of moments is strictly non-negative. Furthermore, even the lower-order approximations, including the first-order M_1 maximum entropy moment closure, can accurately capture a wide range of optical conditions, in both equilibrium and non-equilibrium regimes.

The M_1 moment closure for gray gas, with an entropy of radiation obeying Bose-Einstein statistics, is the only member of the hierarchy of maximum entropy moment closures for which there exists a closed form analytical expression for the closing relations. As such, it has been studied by a number of researchers [51, 52]. Its predictive capabilities were observed to be superior to those of the P_1 closure for a relatively wide range of optical conditions. However, one important limitation of the M_1 closure is its inability to properly capture situations where streams of photons travelling in different directions cross one another. In these cases, the M_1 closure generally produces nonphysical solutions in the radiative energy density [51, 53].

Due to the observed limitations of the M_1 closure for particular radiative transfer problems, there has also been interest in the higher-order members of the maximum entropy moment closure hierarchy, beginning with the second-order maximum entropy, M_2, closure. Unfortunately, the application of the higher-order M_N closures is made difficult due to the lack of closed-form analytical expressions for the closing fluxes, even for problems involving gray gases. Repeated numerical solution of the optimization problem for entropy maximization is therefore generally required, which can make the application of the higher-order M_N closures computationally prohibitive. In spite of these difficulties, in a previous study, Hauck [54, 55] explored the predictive capabilities of the higher-order maximum entropy moment closures (i.e., M_2, M_3, M_4 and M_5) for various test problems involving gray-gas radiative heat transfer in one-dimensional slab geometries. In this previous study, the solutions of the aforementioned M_N closures were obtained by solving the optimization problem for entropy maximization via a numerical approach. Furthermore, Hauck compared the predictions of the aforementioned M_N closures to those of the M_1

closure, as well as those obtained using the P_1 and P_3 spherical harmonic approximations and clearly demonstrated that the higher-order M_N closures provided significantly improved predictions of radiative quantities, relative to the M_1 closure. Similar results have been obtained by Monreal and Frank [56], who proposed an analytical approximation for the M_2 closing relations in the one-dimensional case.

Motivated by a desire for moment closures, for practical radiative transport applications, which have the desirable properties of the high-order M_N closures without the prohibitive computational costs associated with the repeated numerical solution of the optimization problem for entropy maximization, Pichard *et al.* [53] recently proposed interpolative-based approximations of the closing relations for both the gray M_1 and the gray M_2 moment closures, in multiple space dimensions, with an entropy of radiation obeying Boltzmann statistics. Similar interpolative-based variants of maximum entropy closures have been considered previously by McDonald and Groth [57] and McDonald and Torrilhon [58] in the case of gas-kinetic theory. The interpolative procedure adopted by Pichard *et al.* [53] for the M_1 closure is based on a convex combination between the known analytical expressions of the Eddington factor, on the upper and lower boundaries of the space of realizable angular moments up to second-order. The convex interpolant is then determined such that numerical values of the Eddington factor as well as its first derivatives, both on the boundaries of the realizable space up to first-order and in the isotropic limit, are exactly reproduced. In addition, the interpolant was also chosen such that the error between the proposed approximation and pre-computed solutions of the optimization problem for entropy maximization, for sets of angular moments uniformly spanning the full realizable space up to first-order, was minimized.

For the M_2 closure, a first set of interpolations was performed in the 1D case, based on convex combinations of the known exact form of the closure relations on the upper and lower boundaries of the realizability domain for angular moments up to third-order. However, since, to date, closed-form analytical expressions for the closing relations on the boundaries of the multi-dimensional realizable space for the third-order moments do not exist, the extension of the interpolation to multi-dimensional physical space was then carried out in the realizable domain for moments up to first-order, the latter being a subset of the full realizable space for the M_2 closure, which involves angular moments up to second-order. It should also be pointed out that a variant of the M_2 closure in multiple space dimensions, the extended quadrature method of moments (EQMOM)-based second-

order moment closure, using a β probability density function, has also been recently developed by Li *et al.* [59]. One of the main advantages of this so-called B_2 model of Li *et al.* [59], compared to the M_2 closure, is the existence of closed-form analytical expressions for the closure relations. Moreover, the B_2 model provides a smooth interpolation between the isotropic and the free-streaming limits. However, this EQMOM-based closure does not really attempt to mimic closely the properties of the M_2 maximum entropy closure and the B_2 model in multiple space dimensions is neither globally realizable nor globally hyperbolic. In fact, Li *et al.* [59] have shown that the quadrature-based approximation to the M_2 closure is only realizable and hyperbolic in a portion of the realizable space defined by the moments up to second order. With the recent significant advances in the field of machine learning, there also has been growing interest in the development of deep learning-based approaches for approximating maximum-entropy-based closures [60, 61]. While certainly promising, issues with ensuring hyperbolicity and avoiding high computational and/or storage costs may be problematic for the latter. Additionally, moment closures based on φ-divergence [62] have also been very recently considered as alternatives to the M_N closures as they result in tractable closure approximations, even for higher-order members of the hierarchy. Despite being able to represent beam-like distributions with reasonable accuracy particularly for large moment sets, the φ-divergence-based closures are not able to capture accurately highly anisotropic and/or bi-modal distributions associated with beam crossings for small moment sets, unlike the M_N closures. Like the P_N approximations on which they are based, the approximate distributions of radiative intensity associated with the φ-divergence closures are also not guaranteed to be strictly positive.

As a result of the lack of closed form analytical expressions for the M_N closures in the general case, there has been a rather limited number of studies involving maximum-entropy-closure-based treatment of radiative transport in the context of real-gas simulations. In the context of reactive flows simulations, the only studies involving maximum-entropy-based moment closures, to our knowledge, were due to Ripoll [63] and Ripoll and Pitsch [64] and were only concerned with the M_1 closure for gray radiation, due to the availability of closed form analytical expressions for the closing fluxes. In particular, the latter authors proposed a RANS-based formulation of the gray M_1 closure. The latter model does not however take into account the spectral variations of the closing fluxes arising from the strong spectral dependence of the absorption coefficient of participating real

gases. For more realistic treatments of radiation in real gases using maximum-entropy closures, the spectral variations of the radiative intensity distribution must be fully accounted for through the use of non-gray maximum entropy moment closures. To date, the only study that have dealt with the issue of assessing moment closures based on the maximum entropy principle in non-gray participating media, in particular the non-gray M_1 closure, is due to Turpault [65, 66]. The latter formulated a multi-group variant of the non-gray M_1 closure, whereby the spectrally dependent form of the entropy maximizing distribution was approximated by averages over groups of frequencies, spanning the spectrum of interest for the computations. For any given set of band-averaged angular moments up to first order, the Eddington factor, which is the only unknown parameter in the closing relations, was then obtained by numerically solving the underlying dual optimization problem for entropy maximization for the corresponding frequency group.

Finally, when solving the resulting system of hyperbolic equations that arise from application of the method of moments, appropriate boundary conditions are generally required for the boundary and initial value problems of interest. In the context of the truncated moment problem, proper prescription of boundary conditions is still an active topic of research [51, 67–69]. From the kinetic point of view, even though the partial moments boundary data prescription would the most logical approach for providing boundary conditions to the infinite system of moment equations that would uniquely characterize a unique distribution, for a finite set of moments, such an approach could result in neglecting crucial angular information that can only be provided by higher-order moments. The type of boundary data prescription used to solve the truncated system of moment equations, for a given test problem, can significantly affect the accuracy of the obtained results and must therefore be chosen carefully. In light of this, several types of boundary conditions for the spherical harmonic moment closures [69] have been considered and assessed, including but not limited to the partial moments, Marshak, and partial numerical flux boundary data prescriptions. It is worth mentioning that such investigation was facilitated by the existence of closed-form analytical expressions for such boundary conditions as far as the hierarchy of spherical harmonic, P_N, moment closures. For the maximum entropy moment closures, on the other hand, there exist no closed-form expressions for the boundary conditions, except for the Bose-Einstein-based gray M_1 closure in one dimension. Assessment of the impact of different types of boundary conditions prescriptions on the accuracy of the M_1 closure, with an entropy of radiation

obeying Boltzmann statistics, in one-dimensional test problems, has been carried out by Brunner and Holloway [51]. Their study clearly demonstrated the importance of the choice of appropriate boundary conditions for accurate predictions of radiative quantities. However, to date there has been no complete and systematic study regarding the assessment of boundary conditions for maximum entropy moment closures in multiple space dimensions.

1.2 Motivation

The literature review of radiation transport modelling and the method of moments presented in the previous section clearly illustrates the potential benefits of entropy-based moment closure techniques, despite the challenges associated with such approaches, including the lack of closed-form analytical expressions for the closing relations, unlike their spherical harmonic counterparts. The interpolative-based approximations of the closing relations for both the gray first- and second-order, respectively M_1 and M_2, maximum-entropy moment closures proposed by Pichard *et al.* [53] in the case of Boltzmann-based entropy of radiation have strongly motivated the use of maximum-entropy-based interpolation procedures in lieu of direct numerical solutions of the maximum entropy optimization problem. Such procedures have the potential to accurately mimic numerical maximum entropy solutions at a fraction of the computational costs associated with the expensive numerical solution of the optimization problem for entropy maximization. However, the interpolative-based gray second-order, M_2, maximum entropy closure proposed by Pichard *et al.* [53] was observed to suffer from several limitations. More specifically, by the way of its construction, the interpolation procedure proposed by Pichard *et al.* [53], for the gray M_2 closure, only mimics accurately the corresponding maximum entropy solutions for one dimensional problems, but not in fully multiple space dimensions. Moreover, the fact that the construction in multiple dimensions is based on the realizability domain for moments up to first order does not take into account the possible regimes that can only be described by higher-order moments describing the realizable space for the M_2 closure. In order to take full advantage of the desirable properties of the original gray M_2 closure, a new interpolation procedure, which accurately reproduces the numerical solutions of the optimization problem for entropy maximization, for sets of moments spanning the full realizable space for angular moments up to second order,

in multiple space dimensions, must be developed. In addition to accuracy with respect to the maximum entropy solutions, it would also be highly desirable for the interpolation procedure to efficiently mimic solutions of the maximum entropy optimization problem at a fraction of the computational costs associated with the direct numerical solution of the latter.

In the context of non-gray radiation, even though the previous study carried out by Turpault [65, 66] has demonstrated the promising predictive capabilities of the non-gray M_1 closure, the repeated numerical solution of the maximum entropy problem carried out in this analysis is rather impractical, especially for engineering applications of interest, where radiation must be coupled with other underlying phenomena. Moreover, the multi-group approach, which consists of approximating spectral radiative quantities over a given group of frequencies by an average over that set, may lead to substantial over- or under-estimations of the spectrally integrated radiative quantities, due to the strong spectral dependence of the absorption coefficient of real gases [70]. Such strong variations of the absorption coefficient with respect to frequency has led to the development of efficient, state-of-the-art spectral techniques for efficient integration of radiative quantities over the full spectrum of frequencies, in particular the SNBCK model [31, 71] and the FSCK [34] method. Both techniques are based on re-ordering of the strongly varying spectral absorption coefficient into a monotonic function of a cumulative distribution function, the main difference between the two approaches being the way in which re-ordering is applied throughout the spectrum. They can yield comparable accuracy with respect to the straightforward and very expensive line-by-line (LBL) calculations [23], but with substantial improvements in computational efficiency relative to the latter. In light of these developments, it would be crucial to develop efficient interpolative-based maximum-entropy moment closures that accurately mimic numerical solutions of the maximum entropy optimization problem and also couple naturally with the SNBCK or other related models, so as to take full advantage of the computational benefits provided by the latter spectral techniques, for radiation calculations in real gases.

In addition to the choice of a suitable closure technique for the truncated moment equations, proper and accurate enforcement of boundary conditions to the resulting closed systems of moment equations is also important in order to obtain realistic numerical solutions. In the context of M_1 and M_2 entropy-based closures which are of interest in the present study, there exist no closed-form expressions for the Roe matrices in multiple

space dimensions, to date. Such matrices would be helpful if the method of characteristics [51, 72] is to be used for the prescription of boundary conditions to the resulting moment equations in multi-dimensional physical space. Furthermore, in the general case, there exist no closed-form analytical expressions for the partial angular moments of the entropy maximizing distributions, unlike their spherical harmonic counterparts. As such, the repeated numerical solution of the entropy optimization problem would be required in the context of the Marshak, partial moments, and partial numerical flux boundary conditions for the M_N-closure-based systems of moment equations. In order to cope with the substantial computational expenses associated with such a numerical approach, interpolative procedures must also be developed for accurately and efficiently computing the partial angular moments arising from the entropy maximizing distributions associated with the M_1 and M_2 closures.

1.3 Research Goals of Thesis

Based on the status of the field and findings of the literature review given above, the objective of this thesis is to develop new efficient interpolative-based non-gray maximum entropy moment closures for the more realistic predictions of radiative heat transfer in reactive flows simulations, in particular laminar co-flow diffusion at elevated pressures with soot formation for a range of optical depths. The proposed interpolative-based M_N closures result in significant computational savings compared to an approach that makes use of the direct numerical solution of the entropy optimization problem, while mimicking very closely the solution quality and desirable properties of the original maximum entropy closures. The objectives of the thesis can be summarized as follows:

- development of new, efficient, realizable and hyperbolic interpolative-based second-order, M_2, maximum-entropy moment closure, obeying Bose-Einstein statistics, for predicting radiation transport in gray participating media;

- development of new, efficient, realizable and hyperbolic interpolative-based first- and second-order, M_1 and M_2, respectively, maximum-entropy moment closures, with an entropy of radiation based on Bose-Einstein statistics, for predicting radiation transport in non-gray participating media;

- development and assessment of boundary conditions for the maximum-entropy-based M_1 and M_2 closures;
- incorporation of non-gray spectral models, in particular the 9-band SNBCK [31,71] technique;
- validation of the implementation of resulting maximum-entropy moment closures in radiation transport problems involving both gray and non-gray, non-reactive, participating media; and
- application and evaluation of resulting non-gray maximum-entropy closures to the prediction of radiation transport in sooting laminar flames at elevated pressures.

The complexity reduction and computational efficiencies offered by the M_1 and M_2 maximum-entropy closures will be evaluated by comparison to both the DOM and the P_N moment closures. For the non-reactive flows test cases, both gray and non-gray radiative transfer between parallel plates, as well as within rectangular enclosures, will be considered. For the laminar flame cases, non-premixed methane-air co-flow flames of the type previously considered by [17, 20, 22, 73–75] will be of interest.

The original contributions resulting from the thesis research are as follows:

- new formulation of gray M_2 closure for Bose-Einstein entropy of radiation;
- new formulation of boundary conditions for both the gray M_1 and M_2 closures;
- new formulation of non-gray M_1 and M_2 closures for Bose-Einstein radiative entropy with realistic absorption models;
- new formulation of boundary conditions for the non-gray M_1 and M_2 closures;
- evaluation of predictive performance of the new gray M_2 maximum-entropy moment closure for gray radiative transport in non-reactive flows; and
- evaluation of predictive performance of the new non-gray maximum-entropy moment closures for non-gray radiative transport in non-reactive flows as well as in sooting laminar diffusion flames.

1.4 Outline of Thesis

The organization of the remainder of this doctoral thesis is as follows. In Chapter 2, a review of the mathematical modelling of reacting gases and of the background theory for radiation transport in both gray and non-gray participating media is provided, along with a description of the more common approaches for solving the radiative transfer equation, in particular the discrete ordinates method. Moment closures based on the spherical harmonic expansion of the underlying angular distribution of the radiative intensity are also discussed, in particular the first- and third-order, P_1 and P_3, respectively, spherical harmonic moment closures. Next, in Chapter 3, moment closure techniques based on the principle of maximization of entropy are presented. A detailed description of the theoretical details pertaining to our proposed interpolation procedures for efficiently computing the closing moment fluxes for the non-gray first-order maximum entropy, M_1, closure, as well as those of the gray and non-gray second-order maximum entropy, M_2, moment closures, in three-dimensional physical space, is carried out. Chapter 4 then provides a description of the state-of-the-art SNBCK spectral radiation model used for the efficient integration of the radiative quantities of interest over the full spectrum of frequencies, in addition to its coupling with our newly-developed interpolative-based non-gray M_1 and M_2 maximum entropy moment closures. This is followed by a description of the efficient Godunov-type finite-volume scheme used for providing numerical solutions for the resulting hyperbolic closed systems of moment equations, in Chapter 5. The remaining chapters are then concerned with the investigation of the predictive capabilities of our interpolative-based maximum entropy moment closures. In particular, Chapters 6 and 7 respectively illustrate numerical results for gray and non-gray participating media with prescribed thermochemical quantities. Numerical results for laminar non-premixed flames at elevated pressures with soot formation are presented in Chapter 8. Finally, a summary of the findings and contributions of the present study is given in Chapter 9 along with suggestions for future research, thereby concluding the thesis.

Chapter 2

Radiation Transport Theory

As gaseous molecules undergo translational, rotational and vibrational motions, or changes in their electronic states, their molecular energy level either increases or decreases via the absorption or emission of electromagnetic waves or photons. This process is referred to as radiation transfer and the energy carried by the photons, as well as the frequency at which they are either emitted or absorbed, is strongly dependent on the temperature of the material under consideration. The absorption and emission of photons occur over a range of wavenumbers. In the context of heat transfer analysis, thermal radiation is of interest and generally occurs at wavelengths ranging from 10^{-7} µm (ultraviolet) to 10^{-3} µm (infrared) [23].

The background gaseous medium can be categorized as either participating or transparent, depending on the nature of its interactions with the radiative field. A medium is said to be participating if it interacts with travelling photons. On the other hand, transparent media do not interact with the photons. As mentioned in the introduction, gases such as H_2O, CO_2 and CO, as well as solid soot particles, fall in the category of radiatively participating species and are some of the main contributors to the typically substantial radiative heat losses from the relatively hot regions to the colder surroundings in hydrocarbon combustion. It therefore follows that proper treatment of thermal radiation is a key component, in numerical simulations of hydrocarbon combustion, for the accurate predictions of the structure of the flame, as well as of the strongly temperature-dependent net production rates of both soot and intermediate species [2, 76].

Numerical predictions of radiative heat losses can be rather complicated as they require

solving a complex integro-differential equation with high dimensionality and strongly varying properties, for which there exists no general exact analytical solution. A wide variety of techniques have been developed for the treatment of the independent variables involved in the equation of radiative transfer and will be discussed to some extent in the present thesis. It is however worth mentioning that the main focus of the present study is on the treatment of the directional dependence of the distribution of the radiative intensity. In particular, the more popular direction-discretization techniques such as the DOM [37,38] and the more common spherical harmonic, P_N, moment closures [41] will be considered herein. Maximum-entropy-based, M_N, moment closure techniques [49] have been gaining attention in the radiative transfer modelling community, and their application and assessment for gray and non-gray radiatively participating media, whether be it for reactive or non-reactive flows, is the primary focus of the thesis. As will be discussed in Chapter 4, the strong spectral variations exhibited by the absorption coefficient of real-gas mixtures is treated herein by means of the SNBCK [31, 71] model whereas the Rayleigh scattering approximation is used for the modelling of the absorption properties of soot particles. Finally, the spatial and temporal dependencies of the radiative intensity distribution of the RTE as represented by the moment equations are treated herein using the now standard and traditional Godunov-type finite-volume scheme for solving discrete governing equations, which is described in Chapter 5.

This chapter provides a brief overview of the governing equations for gaseous combusting flows followed by a description of radiation transport theory, as well as a literature review on the different approaches that have been used to solve the equations of radiative transfer, in particular techniques for the treatment of both the directional and spectral independent variables of the RTE. The direction-discretization-based DOM is then described. Finally, the theory of moments for the RTE is presented, along with the theoretical details pertaining to the spherical harmonic, P_N, moment closures. Entropy-based approaches for providing closure to the finite system of moment equations resulting from the RTE are discussed in the next chapter.

2.1 Governing Equations for Laminar Reactive Flows

Gas-phase multi-component combusting flows can generally be described by a set of equations consisting of the conservation of total mass, individual species mass, mixture momentum, and mixture energy [17, 77]. In addition to those conservation equations, modelling soot formation and destruction in gaseous combustion also requires tracking an additional solid phase and capturing the interactions that occur between the two phases.

The approach used in this thesis for the modelling of the formation and destruction of soot is similar to the one adopted in the computational framework developed by Charest *et al.* [17] for the numerical simulations of sooting laminar reactive flows. In this framework, soot formation and destruction is modelled using the two-equation-based simplified soot kinetics described by Liu *et al.* [78]. This model is based on the reduced soot mechanisms of Leung *et al.* [79] and Fairweather *et al.* [80] which describe the evolution of soot through basic steps for nucleation, surface growth, coagulation, and oxidation. Acetylene is assumed to be the only precursor responsible for the presence of soot. Multi-species diffusion is modelled using the first-order Hirschfelder and Curtiss approximation [81] while soot is assumed to diffuse primarily by thermophoresis using a model based on the limit of free-molecular flow [82]. In addition to contributions from thermophoresis, a small Fickian diffusive flux is included in the soot particle transport equations. The latter procedure, which is similar to that adopted by Kennedy *et al.* [83], is required to enhance numerical stability even though the transport of soot via Brownian motion is generally negligible.

The partial differential equations governing the conservation of global mass, momentum, energy, individual species mass, soot mass, and particle number, under the assumption of a Newtonian flow, can be summarized as follows [17]:

$$\frac{\partial \rho}{\partial t} + \nabla \cdot (\rho \vec{v}) = 0, \tag{2.1}$$

$$\frac{\partial}{\partial t}(\rho \vec{v}) + \nabla \cdot (\rho \vec{v}\vec{v} + p\vec{\mathbf{I}}) = \nabla \cdot \vec{\boldsymbol{\tau}} + \rho \vec{g}, \tag{2.2}$$

$$\frac{\partial}{\partial t}(\rho e) + \nabla \cdot \left[\rho \vec{v}\left(e + \frac{p}{\rho}\right)\right] = \nabla \cdot (\vec{v} \cdot \vec{\boldsymbol{\tau}}) - \nabla \cdot \vec{q} + \rho \vec{g} \cdot \vec{v}, \tag{2.3}$$

$$\frac{\partial}{\partial t}(\rho Y_k) + \nabla \cdot \left[\rho Y_k (\vec{v} + \vec{V}_k)\right] = \dot{\omega}_k, \quad k = 1, 2, \ldots, N, \tag{2.4}$$

$$\frac{\partial}{\partial t}(\rho Y_{\mathrm{s}}) + \nabla \cdot \left[\rho Y_{\mathrm{s}}(\vec{v} + \vec{V}_{\mathrm{y}})\right] = S_{\mathrm{y}}, \tag{2.5}$$

$$\frac{\partial}{\partial t}(\rho N_{\mathrm{s}}) + \nabla \cdot \left[\rho N_{\mathrm{s}}(\vec{v} + \vec{V}_{\mathrm{n}})\right] = S_{\mathrm{n}}, \tag{2.6}$$

where t is the time, ρ is the mixture density, p is the total mixture pressure, $\vec{v}$ is the mixture velocity vector, e is the total mixture energy, Y_k is the mass fraction of species k, Y_{s} is the mass fraction of soot, N_{s} is the soot number density (number of particles per unit mass of mixture), $\vec{V}_{\mathrm{k}}$ is the diffusion velocity of gas species k, $\vec{V}_{\mathrm{y}}$ is the diffusion velocity related to soot mass, $\vec{V}_{\mathrm{n}}$ is the diffusion velocity related to soot number, $\dot{\omega}_k$ is the time rate of change of the k^{th} species mass, S_{y} is the time rate of change of the soot mass, S_{n} is the time rate of change of the soot number, $\vec{\boldsymbol{\tau}}$ is the fluid stress tensor, $\vec{g}$ is the acceleration vector due to gravity, N is the number of gaseous species in the mixture, and $\vec{q}$ is the heat flux vector. The latter contains contributions from conduction, diffusion, and radiation, and is given by

$$\vec{q} = -\kappa \nabla T + \rho \sum_{k=1}^{N+1} h_k Y_k \vec{V}_k + \vec{q}_{\mathrm{rad}}, \tag{2.7}$$

where κ is the mixture thermal conductivity, h_k is the individual species enthalpy, and $\vec{q}_{\mathrm{rad}}$ is the radiative heat flux, the determination of which, along with its divergence, is of particular interest in this study. In Eq. (2.7), and throughout this work, the $(N+1)^{\mathrm{th}}$ species refers to the solid soot particles, the enthalpy of which is approximated using the properties of graphite. The time rate of change of gaseous species includes contributions from both gas-phase chemistry and soot surface reactions.

2.2 Radiative Transfer Equation

The interaction between the radiative field and a radiatively participating background medium can be summarized by three different processes: namely absorption, emission and scattering, as illustrated in Fig. 2.1. In particular, at any given location in physical space, $\vec{x}$, at time, t, and for the wavenumber, η, a stream of photons travelling in the direction of propagation, $\vec{s}$, may be attenuated via absorption by the molecules making up the participating medium, with an absorption coefficient, $\kappa_\eta = \kappa_\eta(\vec{x}, t)$, thereby resulting in increased molecular energy levels. The passing beam of photons travelling along the direction, $\vec{s}$, may also be augmented via emission of radiant energy from the participating

gaseous molecules and soot particles, which in turn translates into lower molecular energy levels and soot temperatures. Scattering involves the deviation of radiative particles into a direction that is different from its original direction of travel. It is characterized by a scattering coefficient, $\sigma_{s\eta} = \sigma_{s\eta}(\vec{x}, t)$, and can be categorized as either in-scattering or out-scattering. The former refers to the deviation of streams of photons travelling in another direction, $\vec{s}\,'$, into the direction of interest, $\vec{s}$. On the other hand, the latter can be thought of as the loss of radiant energy along the direction, $\vec{s}$, via scattering into another direction $\vec{s}\,'$.

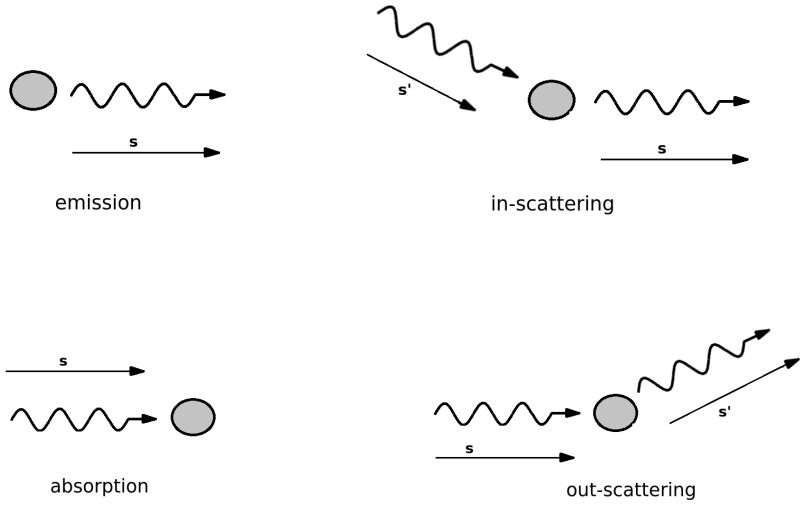

Figure 2.1: Processes resulting from the interactions between the incident radiation (arrows) and a radiatively participating matter (circles).

For a Cartesian coordinate system, the unit vector defining the direction of travel of radiant energy, $\vec{s}$, also called the direction cosine vector, can be expressed in terms of the associated polar and azimuthal angles, θ and ψ, respectively, as follows

$$\vec{s} = \Omega_1 \vec{i} + \Omega_2 \vec{j} + \Omega_3 \vec{k}, \tag{2.8}$$

where $\Omega_1 = \sin\theta\cos\psi$, $\Omega_2 = \sin\theta\sin\psi$, and $\Omega_3 = \cos\theta$ are the corresponding direction cosines and $\vec{i}$, $\vec{j}$, and $\vec{k}$ are unit normal vectors in the positive directions of the x, y, and z Cartesian axes, respectively.

The radiative transfer equation can be obtained by applying an energy balance to a monochromatic beam of photons confined to a infinitesimal solid angle element and

passing through an infinitesimal volume of participating media along the direction of propagation, $\vec{s}$, yielding [84]

$$\frac{1}{c}\frac{\partial I_\eta}{\partial t} + \vec{s}.\vec{\nabla} I_\eta = \kappa_\eta I_{b\eta} - (\kappa_\eta + \sigma_{s\eta}) I_\eta + \frac{\sigma_{s\eta}}{4\pi}\int_{4\pi} I_\eta(\vec{s}\,')\Phi_\eta(\vec{s}\,', \vec{s})\mathrm{d}\Omega', \tag{2.9}$$

where c is the speed of light in a vacuum, $I_\eta = I_\eta(\vec{x}, \vec{s}, t)$ is the spectral radiative intensity distribution, $I_{b\eta} = I_{b\eta}(T)$ (where $T = T(\vec{x}, t)$ is the temperature field) is the spectral Planck function or black-body intensity, Ω denotes solid angle, and $\Phi_\eta(\vec{s}\,', \vec{s})$ is the scattering phase function. The latter describes the probability that a ray travelling in direction, $\vec{s}\,'$, will be scattered into direction, $\vec{s}$, and is also a function of location in physical space and time. The subscript, η, indicates a spectrally varying quantity.

Taking the integral of I_η over the full range of solid angles, Ω, after pre-multiplying it by the vector of propagation, $\vec{s}$, yields the net flow of radiant energy due to radiation in all directions per unit area, time and wavenumber interval. The latter quantity can be interpreted as the spectral radiative flux vector and reads as follows

$$\vec{q_\eta} = \int_0^{4\pi} \vec{s} I_\eta \mathrm{d}\Omega. \tag{2.10}$$

The divergence of the spectral heat flux vector can be obtained by integrating the RTE over all solid angles and neglecting the temporal derivatives, yielding

$$\nabla \cdot \vec{q_\eta} = \kappa_\eta \left(4\pi I_{b\eta} - \int_0^{4\pi} I_\eta \mathrm{d}\Omega\right) = \kappa_\eta \left(4\pi I_{b\eta} - G_\eta\right), \tag{2.11}$$

where G_η is the spectral incident radiation and is given by

$$G_\eta = \int_0^{4\pi} I_\eta \mathrm{d}\Omega. \tag{2.12}$$

For gas mixtures with spectrally varying radiative properties, Eq. (2.11) must be integrated over the full spectrum of wavenumbers or frequencies to yield the divergence of the total radiative heat flux vector, $\nabla \cdot \vec{q}_{\mathrm{rad}}$, which is the radiative quantity of interest in the energy equation, Eq. (2.3), an can be formulated as follows

$$\nabla \cdot \vec{q} = \int_0^{\infty} \nabla \cdot \vec{q_\eta} d\eta = \int_0^{\infty} \kappa_\eta \left(4\pi I_{b\eta} - G_\eta\right) d\eta. \tag{2.13}$$

For non-polarized light, the RTE, as given in Eq. (2.9), is a complex linear integro-differential equation with high dimensionality (7 independent variables) as it involves

dependencies on the spatial variables characterized by the location vector, $\vec{x}$, a three-component vector in three-dimensional physical space, the temporal variable, t, the spectral variable, η, and the direction variables parameterized by the polar and azimuthal angles, θ and ψ, respectively. One must typically rely on numerical solution methods involving approximate treatments of the independent variables since there exists no general exact analytical solution to the RTE. As mentioned earlier, the now standard family of upwind Godunov-type finite-volume techniques for hyperbolic governing equations [24] are the most commonly used numerical techniques for the treatment of both the temporal and spatial dependencies.

As noted in the introduction to this thesis, several approaches have been developed for the treatment of the angular (directional) dependence of the radiative intensity distribution [2]. Monte Carlo methods are known to be the most accurate and computationally expensive [35]. Hotel's zonal method [36, 85] has been used widely for engineering radiative heat transfer calculations in multi-dimensional enclosures. It consists of dividing the solid angle domain into a finite set of zones and performing energy balances of the radiative exchange between the zones. Its implementation is however limited to non-scattering media as is cannot be readily adapted for a scattering medium. The discrete ordinates method (DOM) [37,38] has also been used extensively to solve the RTE, due to its good balance between accuracy and computational efforts, especially in the absence of scattering. The finite-volume method (FVM) [39, 86] for radiation is a variation of the DOM, whereby the RTE is solved over finite-sized control angles rather than along discrete directions as in the DOM. The discrete transfer method (DTM) of Lockwood and Shah [87] has also been used extensively in the radiative transfer modelling community. The method of moments, originally proposed by Grad [40] in the field of gas-kinetic theory, has also gained popularity in the radiation modelling community. It consists of solving directly for a finite set of angular moments of the distribution of the radiative intensity and is particularly attractive due to its potential to capture a relatively wide range of optical conditions with a relatively low number of unknowns, relative to the DOM. The more commonly used technique for tackling the underlying closure problem for a finite set of moment is the so-called spherical harmonic approximation [41, 42] whereby the distribution of radiant energy is approximated by a truncated series expansion in terms of orthogonal spherical harmonic functions of the directional variables. Entropy-based approaches [49] for providing closure to the unclosed finite system of moment equations

arising from the method of moments have more recently been considered. Instead of a mathematical representation of the radiative intensity distribution as advocated in the spherical harmonic, P_N, moment closures, entropy-based, M_N, closures make use of the physically consistent principle of maximization/minimization of entropy to construct the distribution.

Another challenge associated with the solution of the RTE is the treatment of the spectral dependence of the optical properties of the background medium. A common assumption that is made to cope with such a dependence and also reduce the dimensionality of the RTE as well as the complexity associated with the numerical solution of the latter is that of a gray medium. A medium is said to be gray if its radiative properties can be assumed to be independent of wavenumber, i.e., $\kappa_\eta = \kappa$ and $\sigma_{s\eta} = \sigma_s$. Under such an assumption, the RTE of Eq. (2.9) can be directly integrated over the full spectrum of frequencies, thereby yielding the following form for the RTE [84]

$$\frac{1}{c}\frac{\partial I}{\partial t} + \vec{s}.\vec{\nabla} I = \kappa I_b - (\kappa + \sigma_s) I + \frac{\sigma_s}{4\pi}\int_{4\pi} I(\vec{s}\,')\Phi(\vec{s}\,', \vec{s})\mathrm{d}\Omega', \tag{2.14}$$

where $I = \int_0^\infty I_\eta d\eta$ is the total, spectrally integrated radiative intensity distribution.

Compared to the RTE of Eq. (2.9), the form given in Eq. (2.14) only involves 6 independent variables, since the spectral variable, η, has been integrated out in the latter. The assumption of gray radiation, while convenient when solely focusing on the treatment of the directional dependence of the radiative intensity distribution, is however violated in real-gas radiation which typically involves strong and chaotic variations of the spectral absorption coefficient with respect to wavenumber, η. Such strong variations must be properly accounted for in order to more accurately predict total spectrally-integrated radiative quantities and consequently yield more realistic predictions of radiative heat losses in real-gas simulations, such as in hydrocarbon combustion.

In the context of real-gas radiation simulations, a variety of spectral radiation models have been proposed for the numerical integration of spectral radiative quantities over the full spectrum of frequencies [23]. LBL calculations are the most detailed and computationally expensive approaches. In LBL computations, the RTE is solved for each of the hundred thousands lines making up the absorption spectrum of the gas mixture under consideration followed by integration of the results over the spectrum. In narrow-band models, the spectrum is subdivided into small spectral intervals, and radiative quantities, averaged over each band, are calculated from the absorption spectrum (correlated-k

(CK) model), or from the statistical properties of the lines (SNBCK model). Global models attempt to calculate the total radiative quantities directly, using spectrally integrated radiative properties. An example of global model is the weighted-sum-of-gray-gases (WSGG) model [88]. More recently, a more advanced global spectral technique, the so-called FSCK method [34] has been developed and has been shown to be superior to the WSGG model, to which it reduces in its crudest implementation.

The SNBCK model is an attractive method allowing to compute low-resolution spectral intensity with levels of accuracy similar to those of the line-by-line calculations and significantly reduced computational efforts compared to the latter approach. It employs the same reordering concepts as the CK model [89]. However, instead of computing the cumulative distribution function from large line-by-line spectroscopic databases as is done in the CK model [71, 90], the SNBCK model avoids such expensive calculations by building the cumulative distribution function analytically from statistical narrow-band (SNB) parameters [89].

It is worth mentioning that scattering is usually neglected in numerical simulations of many reactive flows as it is assumed to be insignificant relative to absorption [2]. Furthermore, in sooting flames, soot radiation must also be included for it is often stronger than the radiation arising from the combustion gases. In general, soot particles are assumed to be very small, and their radiative properties are determined by means of Rayleigh's theory for small particles [84].

2.3 Discrete Ordinates Method (DOM)

In the DOM, angular quadrature is used to transform the equation of radiative transfer into a set of PDEs with only spectral, spatial and temporal dependencies. The angular discretization technique makes use of the assumption that the radiation is transported only along a finite set of discrete directions, instead of the effectively infinite number of directions allowed in Eq. (2.14) by a continuous representation of the solid angle. In other words, the solid angle is divided into a finite number, M, of discrete directions (or ordinates), $\vec{s}_m$, $m = 0, 1, \ldots, M$. In this way, the RTE is transformed into a system of

M coupled equations given by

$$\frac{1}{c}\frac{\partial I_{\eta,m}}{\partial t} + \vec{s}_m.\vec{\nabla} I_{\eta,m} = \kappa_\eta I_{b\eta} - (\kappa_\eta + \sigma_{s\eta}) I_{\eta,m} + \frac{\sigma_{s\eta}}{4\pi}\sum_{n=1}^{M} w_n I_{\eta,n}\Phi_\eta(\vec{s}_n, \vec{s}_m), \qquad (2.15)$$

where the subscript m denotes the index of the discrete ordinate direction, I_m is the intensity in the m^{th} direction and w_m is the quadrature weight associated with the direction, $\vec{s}_m$. Several angular quadrature rules have been developed for the DOM, including the S_N schemes of Lathrop and Carlson [91] and the T_N schemes of Thurgood *et al.* [92]. The T_4 quadrature scheme is used in this thesis for all of the reported DOM simulation results.

The DOM has been used extensively to provide approximate solutions to the RTE due its good balance between accuracy and computational efficiency. In fact, to date, along with the DTM method, it has been one of the most widely used approaches for the treatment of radiative transfer in reactive flows simulations involving hydrocarbon combustion with soot formation [9, 11, 76, 78, 93–106]. However, this direct discretization technique is associated with two major limitations [107]: false scattering and ray effects. The former is due to the spatial discretization of the RTE whereas the latter is related to the discretization of the angular distribution of the radiative intensity. Several approaches have been proposed in order to cope with such issues [92, 108–112]. Additionally, as mentioned in the introduction, the space marching techniques commonly used to solve the resulting discretized equations of the DOM can be extremely efficient for problems involving relatively simple geometries and physics; however, the space marching techniques may exhibit poor convergence for applications involving complex three-dimensional geometries and complex physics [29] (e.g., highly scattering media, turbulent reactive flows, etc.).

2.4 Moment Closure Techniques

An alternative approach to the DOM for the treatment of the angular dependence of the radiative intensity distribution involves solving directly for the angular integrals or

macroscopic moments, $I_\eta^{(n)}$, of the distribution, which can be written as follows

$$\begin{aligned} I_\eta^{(n)}(\vec{x},t) = \langle \vec{s}^{\,n} I_\eta(\vec{x},\vec{s},t)\rangle &= \int_{4\pi} \vec{s}^{\,n} I_\eta(\vec{x},\vec{s},t)\,\mathrm{d}\Omega \\ &= \int_0^{2\pi}\int_0^{\pi} \vec{s}^{\,n} I_\eta(\vec{x},\vec{s},t)\sin\theta \mathrm{d}\theta\mathrm{d}\psi, \end{aligned} \tag{2.16}$$

where $\vec{s}^{\,n} = \vec{s}\otimes \overset{n}{\ldots} \otimes\vec{s}$, for $n = 0, 1, \ldots \infty$, are the weights associated with the angular moments and whose independent entries form a monomial basis in terms of the angular variables. One particular feature of the method of moments is that the quantities of interest can be computed directly from the solution of the resulting governing equations, whereas, for the DOM, angular numerical quadrature is used to compute such quantities once values of the intensity distribution in the discrete directions are known.

The first few angular moments, as defined by Eq. (2.16), can be related to well-known physical quantities. More specifically, the zeroth-order moment, $I_\eta^{(0)}$, which is a scalar, is related to the radiative energy density, the first-order moment, $I_\eta^{(1)}$, a three-component vector in three-dimensional physical space, is associated with the radiative flux, and finally, the second-order moment, $I_\eta^{(2)}$, which is a second-order tensor with six independent entries in three dimensions, is associated to the radiative pressure. Beyond second order, the angular moments, which then correspond to symmetric tensors of order at least three, have no well-established physical interpretation. One can also define the normalized angular moments of order n, denoted by $N^{(n)}$, as follows

$$N^{(n)} = \frac{I_\eta^{(n)}}{I_\eta^{(0)}}. \tag{2.17}$$

Taking angular integrals of the RTE, Eq. (2.9), results in a system of moment equations of infinite size characterizing uniquely an arbitrary distribution. Solving such an infinite system of equations is however obviously unfeasible from a practical viewpoint. Instead, a reduced finite set of moments and their transport equations are considered, in practice. In this case however, a solution to the so-called closure problem is then required as the resulting system of transport equations for the finite set of moments generally involves the next higher-order moments. In particular, additional expressions relating the highest-order moments to the tracked or known lower-order moments are required for closure. These so-called closing relations are usually obtained via the reconstruction of an assumed form for the underlying strictly non-negative angular distribution in terms of the known finite set of lower-order moments.

There exists a wide range of possible forms for the approximate distribution of radiative intensity yielding a closed system of moment equations. In fact, there is effectively an infinite set of possible distributions sharing the same finite set of known lower-order moments. However, the choice of the approximate form generally dictates the many important mathematical properties of the resulting closed system of moment equations: namely the realizability of the predicted moments and hyperbolicity of the resulting moment equations. A set of moments is said to be physically realizable if there exists a strictly non-negative-valued distribution of the radiative intensity that will yield the given moments [27]. The set of all realizable moments up to a given order, n, then defines the so-called n-dimensional phase space of physically realizable moments and is denoted here as $\mathcal{R}^{(n)}$. This region is generally described by a set of inequalities on the values of the moments: so-called moment realizability conditions. In this thesis, approximate forms for the angular distribution resulting from the spherical harmonic approximation as well as the principle of maximization of entropy will be considered for providing closure to the finite-sized truncated systems of moment equations and their application to radiative transport in non-gray media will be the primary focus.

Another important consideration for the moment closure techniques outlined above is the selection or choice of the number of moments to be included in the closure of interest, and which are subsequently used to reconstruct the approximate angular intensity distribution. In general, only the zeroth- and first-order moments, namely the radiative energy density, $I_\eta^{(0)}$, and the radiative heat flux, $I_\eta^{(1)}$, respectively, are of primary interest in engineering applications. However, the more angular moments that are used in the closure to reconstruct the approximate distribution, the wider the range of optical conditions that may be captured accurately by the closure.

2.4.1 Spherical Harmonic (P_N) Moment Closures

In the spherical harmonic, P_N, moment closures, the spectral radiative intensity distribution, $I_\eta(\vec{x}, \vec{s}, t)$, is approximated by a truncated series expansion in terms of orthogonal spherical harmonic functions as follows [41, 84]

$$I_\eta(\vec{x}, \vec{s}, t) = \sum_{n=0}^{N} \sum_{m=-n}^{n} I_{\eta,n}^{m}(\vec{x}, t) Y_n^m(\vec{s}), \tag{2.18}$$

where N is the order of the series expansion or of the highest moment in the closed system, $I^m_{\eta,n}(\vec{x},t)$ are location-dependent coefficients of the series expansion which can be directly related to the know finite set of moments, and $Y^m_n(\vec{s})$ is the spherical harmonic function of degree, n, and order, m, having the form

$$Y^m_n(\vec{s}) = \begin{cases} \cos(m\psi)P^m_n(\cos\theta), & \text{for } m \geq 0, \\ \sin(|m|\psi)P^{|m|}_n(\cos\theta), & \text{for } m < 0, \end{cases} \tag{2.19}$$

and where $P^m_n(\cos\theta)$ is the associated Legendre polynomial.

2.4.2 First-Order P_1 Spherical Harmonic Moment Closure

The first-order P_1 spherical harmonic approximation provides closure to the system of transport equations for angular moments up to first order, which only involves transport equations for the zeroth- and first-order moments, $I^{(0)}_\eta$ and $I^{(1)}_\eta$, respectively (i.e., a set of four moments in three space dimensions for the scalar radiative energy density and vector of energy fluxes in each coordinate direction). This is achieved by approximating the distribution using the form given in Eq. (2.18), with $N = 1$, which is then reconstructed in terms of angular moments up to first order. The second-order moment, $I^{(2)}_\eta$, is a dyadic quantity (i.e., a second-order tensor) and is involved in the transport equation for $I^{(1)}_\eta$. This quantity can be directly expressed in terms of the lower-order moments via integration of the reconstructed distribution, yielding

$$I^{(2)}_{ij,\eta} = \frac{\delta_{ij}}{3} I^{(0)}_\eta, \tag{2.20}$$

where δ_{ij} is the Kronecker delta operator. This is the so-called P_1 approximation, which is generally considered to be accurate only for optically thick media as it is associated with nearly-isotropic distributions of the radiative intensity. Due to its simplicity and relatively straightforward implementation, the P_1 closure has been widely used to provide approximate solutions to the RTE in the context of real-gas simulations in combustion systems [43–46].

2.4.3 Third-Order P_3 Spherical Harmonic Moment Closure

Closure to the system of transport equations for angular moments up to third order, $I^{(n)}_\eta$, $n \in \{0,1,2,3\}$, can be obtained via the use of the form for the distribution given in

Eq. (2.18), with $N = 3$, and with known angular moments up to third order. The fourth-order moments, $I_\eta^{(4)}$, involved in the transport equations for the third-order moments can then be expressed directly in terms of the known lower-order moments, thereby yielding the so-called third-order P_3 spherical harmonic moment closure. The resulting closing relations can be summarized as follows

$$\begin{aligned} I_{iiii,\eta}^{(4)} &= -\frac{3}{35} I_\eta^{(0)} + \frac{6}{7} I_{ii,\eta}^{(2)}, \quad & I_{iiij,\eta}^{(4)} &= \frac{3}{7} I_{ij,\eta}^{(2)}, \\ I_{iijj,\eta}^{(4)} &= \frac{4}{35} I_\eta^{(0)} - \frac{1}{7} I_{jj,\eta}^{(2)}, \quad & I_{iijk,\eta}^{(4)} &= \frac{1}{7} I_{jk,\eta}^{(2)}. \end{aligned} \tag{2.21}$$

It has been shown previously that the third-order P_3 spherical harmonic closure yields significantly improved predictions compared the P_1 closure [47]. This accuracy improvement however comes at the expense of a significant increases in computational costs and storage requirements. More specifically, for any given wavenumber, η, in two-dimensional physical space, the P_1 closure requires the solution of 3 transport equations, whereas the P_3 closure involves 10 unknowns, per grid point. For fully three-dimensional problems the P_1 and P_3 closures involve 4 and 20 unknowns, respectively, for any given wavenumber and per grid point. Due to the increased mathematical and numerical complexity of the P_3 closure relative to its lover-order P_1 counterpart, there has been a rather limited number of studies where the P_3 closure was used to provide approximate numerical solutions of the RTE [23]. Moreover, higher-order approximations ($N > 3$) of the hierarchy of spherical harmonic moment closures result in further substantial increases in computational efforts, whereas the accuracy improvements with increasing N are somewhat more modest [113, 114]. For these reasons, it is felt that the P_3 approximation provides a reasonable balance between accuracy and computational costs, relative to its higher- and lower-order counterparts.

Chapter 3

Maximum Entropy Moment Closures

Despite their relative simplicity, the spherical harmonic, P_N, moment closures do not always guarantee the physical requirement of non-negativity of the reconstructed distribution of the radiative intensity. Moreover, Dirac-like distributions, which are encountered in the free-streaming limit of radiation, cannot be properly captured by a polynomial representation of the radiative intensity distribution as is carried out in the P_N moment closures. In light of these, entropy-based models represent rather promising approaches for providing approximate forms of the intensity distribution. For a given realizable finite set of angular moments, they provide the most likely form of the distribution among the infinite family of possible forms for the distribution reproducing such moments [50]. In addition, they always guarantee non-negativity of the reconstructed distribution of the radiative intensity and can also capture both isotropic and anisotropic radiative intensity distributions, the latter regime being characterized by Dirac-delta-like distributions. As a result of the many desirable properties of the hierarchy of the M_N closures described above, application of entropy-based moment closure techniques has gained considerable interest in the radiation modelling community.

In this chapter, a review of the theoretical details pertaining to maximum-entropy-based moment closures is carried out in Section 3.1, as well as a brief discussion of the challenges associated with the use of such approaches, including the lack of closed-form expressions for the closing fluxes or higher-order moments, for any given finite set of moments,

in the general case. Evaluation of the closing fluxes for a given finite set of angular moments typically requires the direct numerical solution of the entropy maximization problem, which, in addition to being prohibitively expensive, can be very challenging, especially as any of the boundaries of the realizable space for the given set of lower-order angular moments is approached. A description of the algorithm used for the numerical solution of the optimization problem for entropy maximization is presented in Section 3.2, along with the strategies adopted as part of this thesis to improve convergence of the algorithm near the boundaries of the realizable space of interest. Efficient interpolative-based approximations of the closing fluxes arising from the first few lower-order members of the hierarchy of M_N closures, in particular the first-order, M_1, and second-order, M_2, closures, are then proposed and thoroughly described. The proposed interpolative-based approximations accurately reproduce the numerical maximum entropy solutions associated with the closing fluxes for any given set of realizable angular moments up to first order for the M_1 closure and up to second order for the M_2 closure, at a fraction of the computational costs associated with the expensive, direct, and multiple (i.e., many times over) numerical solution of the maximum-entropy optimization problem.

A brief review of the M_1 closure for gray-gas radiation is given in Section 3.3.1, the latter being the only member of the hierarchy of M_N closures for which there exists closed-form analytical expressions for the second-order closing fluxes, in the case of an entropy of radiation obeying Bose-Einstein statistics. This is followed by a thorough and comprehensive description, in Section 3.3.2, of the theoretical details pertaining to the newly-proposed interpolative-based procedure for the approximation of the second-order closing fluxes for the first-order, M_1, maximum entropy closure, in the case of non-gray radiation. Section 3.4 then presents a new interpolative procedure for the approximation of the third-order closing fluxes arising from the second-order, M_2, maximum entropy moment closure for gray radiation, as well as its extension to the case of non-gray radiation.

3.1 Maximum-Entropy (M_N) Moment Closures

Among the infinite family of possible distributions that can be used to approximate the underlying distribution of the radiative intensity, the most probable form of the latter is given, according to Jaynes [50], by the distribution that maximizes the radiative

entropy, $H_R(I_\eta)$, subject to the constraints that a finite set of its angular moments, $I_\eta^{(n)}$, $n = 0, 1, \ldots, N$, is known. The problem of finding such a distribution can be formulated in mathematical terms as follows:

$$\begin{aligned} \mathcal{I}_\eta &= \arg\max_{I_\eta} H_R(I_\eta) \\ \text{s.t.} \quad \langle \vec{s}^{\,(n)} I_\eta \rangle &= I_\eta^{(n)}, \quad n = 0, 1, \ldots, N, \end{aligned} \tag{3.1}$$

where N is the order of the highest moments in the closed system of moment equations and

$$H_R(I_\eta) = \langle h_R \rangle = \int_{4\pi} h_R(I_\eta) d\Omega, \tag{3.2}$$

and where h_R denotes the radiative entropy density, which, for combustion applications, corresponds to the entropy of radiation obeying Bose-Einstein statistics [115] and is given by

$$h_R(I_\eta) = \frac{2k\eta^2}{c}[(n+1)\ln(n+1) - n\ln(n)], \quad n = \frac{I_\eta}{2hc\eta^3}. \tag{3.3}$$

In Eq. (3.3), n is the occupation number, and h and k are the Planck and Boltzmann constants, respectively. The Lagrangian of the optimization problem given in Eq. (3.1) is

$$\mathcal{L}(I_\eta, \boldsymbol{\alpha}) = H_R(I_\eta) - \boldsymbol{\alpha}^T(\langle \mathbf{m}(\vec{s}) I_\eta \rangle - \mathbf{E}_\eta), \tag{3.4}$$

where $\mathbf{E}_\eta$ is a vector containing all the independent entries of $I_\eta^{(n)}$, $n = 0, 1, \ldots, N$, $\mathbf{m}(\vec{s})$ is a vector containing all the independent entries of $\vec{s}^{\,(n)}$, $n = 0, 1, \ldots, N$, and $\boldsymbol{\alpha}$ is the vector of Lagrange multipliers associated with the moment constraints.

For a given finite set of angular moments with associated Lagrange multipliers, $\boldsymbol{\alpha}$, the form of the entropy maximizing distribution can be derived via the stationary point of the Lagrangian, Eq. (3.4), i.e., $\partial\mathcal{L}(I_\eta, \boldsymbol{\alpha})/\partial I_\eta = 0$, which yields the following expression [49]

$$\mathcal{I}_\eta(\boldsymbol{\alpha},\, \mathbf{m}) = 2hc\eta^3 \left[\exp\left(\frac{c^2 h\eta}{k}\boldsymbol{\alpha}^T \mathbf{m}(\vec{s}\,)\right) - 1\right]^{-1}. \tag{3.5}$$

In Eq. (3.5), the radiative intensity distribution is expressed in terms of the Lagrange multipliers, $\boldsymbol{\alpha}$, which depend on the angular moments of the distribution, $\mathbf{E}_\eta$. With the exception of the gray M_1 closure [49], there exists no analytical expressions for the Lagrange multipliers in terms of the known lower-order angular moments. The former must therefore be determined numerically in terms of the latter by solving the Lagrangian dual optimization problem

$$\max_{\boldsymbol{\alpha}} \{\mathcal{L}^*(\boldsymbol{\alpha})\}, \tag{3.6}$$

where $\mathcal{L}^*(\boldsymbol{\alpha})$ is the Legendre transform of $\mathcal{L}(I_\eta, \boldsymbol{\alpha})$, Eq. (3.4), and has the form

$$\mathcal{L}^*(\boldsymbol{\alpha}) = \frac{2k\eta^2}{c} \left\langle \log \left[\exp\left(\frac{c^2 h\eta}{k} \boldsymbol{\alpha}^T \mathbf{m}(\vec{s}\,) \right) - 1 \right] \right\rangle - \boldsymbol{\alpha}^T \mathbf{E}_\eta. \tag{3.7}$$

The wavenumber variable within the exponential term of Eq. (3.7) is rather inconvenient, since the Lagrange multipliers must then be solved not only for the given realizable finite set of moments, but also for values of wavenumber spanning the semi-infinite interval $[0,\ +\infty]$. A more convenient form for the optimization problem for entropy maximization, Eqs. (3.6) and (3.7), for the purpose of the proposed interpolation procedures, can however be obtained by the change of variables $\boldsymbol{\beta} = (c^2 h\eta)\boldsymbol{\alpha}/k$, such that

$$\mathcal{L}^*(\boldsymbol{\beta}) = \left\langle \log \left[\exp\left(\boldsymbol{\beta}^T \mathbf{m}(\vec{s}\,) \right) - 1 \right] \right\rangle - \boldsymbol{\beta}^T \mathbf{E}^\star_\eta, \quad \mathcal{L}^*(\boldsymbol{\alpha}) = 2ck\eta^2 \mathcal{L}^*(\boldsymbol{\beta}), \tag{3.8}$$

where

$$\mathbf{E}^\star_\eta = \frac{\pi \mathbf{E}_\eta}{C_1 \eta^3} = \{ I^{(0)\star}_\eta, I^{(1)\star}_\eta, \ldots \}, \quad I^{(n)\star}_\eta = \frac{\pi I^{(n)}_\eta}{C_1 \eta^3}, \tag{3.9}$$

represents the set of angular moments up to order N used for the solution of the dual optimization problem, Eq. (3.8), and $C_1 = 2\pi hc^2$ is the so-called first radiation constant. It is clear from Eq. (3.8) that, for any given wavenumber, η, maximizing $\mathcal{L}^*(\boldsymbol{\beta})$ is equivalent to maximizing $\mathcal{L}^*(\boldsymbol{\alpha})$. Furthermore, the form of the former allows the parameterization of the Lagrange multipliers in terms of the ratio $I^{(0)}_\eta/\eta^3$, instead of $I^{(0)}_\eta$ and η, separately, and this parameterization yields a reduction in the number of independent variables for the proposed interpolation procedures of the non-gray M_1 and M_2 closures, which will be described in the sections to follow.

While the radiative properties of participating real gases, in particular the absorption coefficient, is strongly dependent on the wavenumber, the assumption of gray radiation, which consists of neglecting the spectral dependence of the radiative properties of the participating gases, is sometimes employed when studying radiative transfer problems. The latter assumption indeed yields significant simplifications to radiative transfer problems and, when used in conjunction with the moment closure techniques under consideration in the present study, allows to solely focus on the ability of the closures to accurately treat the directional dependence of the radiative intensity distribution. In the context of entropy-based closures obeying Bose-Einstein statistics, the form of the distribution resulting from the assumption of gray radiation can be obtained via integration of the spectral entropy-maximizing distribution function, Eq. (3.5), over the full spectrum of

frequencies ($\eta \in [0,\, \infty]$), yielding

$$\mathcal{I}(\boldsymbol{\alpha},\, \mathbf{m}) = \frac{\sigma_{stef}}{\pi} \left[\boldsymbol{\alpha}^T \mathbf{m}(\vec{s})\right]^{-4}, \tag{3.10}$$

where σ_{stef} is the Stephan-Boltzmann constant, and reads as follows

$$\sigma_{stef} = \frac{2\pi^5 k^4}{15c^2h^3}. \tag{3.11}$$

In Eq. (3.10), the radiative intensity distribution is again expressed in terms of the Lagrange multipliers, $\boldsymbol{\alpha}$, which have to be determined from the set of nonlinear coupled algebraic equations $\langle \mathbf{m}(\vec{s})I \rangle = \mathbf{E}$, where $\mathbf{E} = \int_0^\infty \mathbf{E}_\eta d\eta$.

With the exception of the gray M_1 model [49], the Lagrange multipliers, in the case of gray radiation, must be determined numerically by solving the Lagrangian dual optimization problem for entropy maximization given by

$$\arg\max_{\boldsymbol{\alpha}} \{\mathcal{L}^*(\boldsymbol{\alpha})\}, \tag{3.12}$$

where $\mathcal{L}^*(\boldsymbol{\alpha})$ is the Legendre transform of $\mathcal{L}(I, \boldsymbol{\alpha})$, and has the form

$$\mathcal{L}^*(\boldsymbol{\alpha}) = -\frac{\sigma_{stef}}{3\pi} \left\langle \left[\boldsymbol{\alpha}^T \mathbf{m}(\vec{s})\right]^{-3} \right\rangle - \boldsymbol{\alpha}^T \mathbf{E}. \tag{3.13}$$

The nonlinear optimization problem for entropy maximization, given in Eqs. (3.12) and (3.13) for gray radiation and Eqs. (3.6) and (3.8) in the case of non-gray radiation, can be solved relatively easily for sets of angular moments characterized by near-uniform angular distributions of the radiative intensity. However, as one of the boundaries of the realizable space for the given finite set of moments is approached, the maximum entropy optimization problem becomes increasingly difficult to solve due to ill-conditioning of the Hessian matrix of the dual objective function. In fact, near the boundaries of the realizable space, the distribution of radiative intensity becomes nearly-singular along a set of directions corresponding to a subset of the full solid angle. The difficulty in solving the maximum-entropy problem near the realizable boundary is further exacerbated by the necessity of using an inexact quadrature and finite-precision arithmetic to approximate the angular integrals of the radiative intensity distribution. The contribution to the quadrature may effectively be zero for most of the quadrature points, which may result in singularity of the computed Hessian. Furthermore, in the context of nearly singular distributions of the radiative intensity, suitable quadrature schemes must be designed so

as to properly capture the essential features of the distribution and consequently yield accurate estimates of its angular moments. One way to achieve the latter is by clustering the integration nodes in the regions where the peaks occur, and such a procedure is adopted in the present study, and is described in the next section. In particular, the domain of integration is divided into smaller sub-intervals, especially in the areas where the peaks occur, and static quadrature rules are then applied within each sub-interval.

3.2 Numerical Solution of the Optimization Problem for Entropy Maximization

The entropy of radiation based on Bose-Einstein statistics given by Eqs. (3.2) and (3.3) is a strictly convex functional, and, as such, any locally optimal set of Lagrange multipliers, $\boldsymbol{\alpha}$, would also be a globally optimal set. The sequential quadratic programming (SQP) algorithm as implemented in the software package NLopt [116–118] an open source library for nonlinear optimization was therefore used herein for the solution of the optimization problem as defined by Eqs. (3.12) and (3.13) for gray radiation and by Eqs. (3.6) and (3.8) in the case of non-gray radiation. In this implementation, an objective function and its gradients, as well as additional constraints, are supplied by the user. The Hessian matrix of second derivatives, which is required for solving the Newton system of equations, is then estimated by means of the Broyden-Fletcher-Goldfarb-Shanno (BFGS) algorithm, which provides substantial computational savings compared to the direct evaluation of the Hessian matrix.

The SQP algorithm provides very good convergence for sets of moments far away from the boundaries of the realizability domain. However, as one of the boundaries is approached, the dual optimization problem becomes increasingly difficult to solve and might even fail to converge due to ill-conditioning of the Hessian matrix. In order to improve the condition number of the Hessian matrix, a preconditioning of the latter, similar to that described by Alldredge *et al* [119] is advocated. The preconditioning is equivalent to an adaptive change of polynomial basis, relative to the original basis, $\mathbf{m}(\vec{s})$, such that the Hessian is the identity matrix in the new basis system. In addition, the regularization scheme introduced by Alldredge *et al.* [120] is employed to make the optimization algorithm more robust, especially for very ill-conditioned problem. Instead of

using a Cholesky factorization of the Hessian for the preconditioning as chosen by Alldredge *et al.* [119], the numerically stable modified Gram-Schmidt algorithm, described by Abramov [121], is adopted. Instead of preconditioning the Hessian matrix at each Newton steps during the optimization, the procedure advocated by Abramov [122], allowing for several Newton steps between successive reorthogonalizations, is adopted. The procedure consists of tracking the condition number of the inverse of the Hessian during the BFGS iterations, and then precondition the Hessian matrix whenever the condition number exceeds a threshold value of 20.

3.3 First-Order Maximum-Entropy M_1 Moment Closure

As an alternative to the first-order spherical harmonic, P_1, moment closure, the system of transport equations for angular moments up to first order can be closed by assuming an entropy maximizing distribution, of the form given in Eq. (3.10) for gray radiation or Eq. (3.5) for non-gray radiation, based on the known angular moments up to first order. The reconstructed approximate form of the distribution can then be integrated using the appropriate angular weights to obtain the closing second-order moments in terms of the lower-order moments, i.e., $I^{(2)} = I^{(2)}(I^{(0)}, I^{(1)})$ in the case of gray radiation and $I_\eta^{(2)\star} = I_\eta^{(2)\star}(I_\eta^{(0)\star}, I_\eta^{(1)\star})$ for non-gray radiation. This procedure results in the so-called first-order maximum-entropy, M_1, moment closure. One peculiarity of angular distributions of radiative energy represented only by their angular moments up to first order, as is the case for the P_1 and M_1 closures, is the fact that such distributions are symmetric with respect to the direction described by the corresponding first-order moment vector, as the latter is the only available information for describing departures from the isotropic limit. Using this property, in conjunction with suitable frame rotations, it is a simple exercise to show that the tensor of second-order normalized moments, $N^{(2)}$, for all first-order moment closures, can be written in the so-called Eddington form given by [123]

$$N^{(2)} = \frac{1-\chi_2}{2}\vec{\vec{I}} + \frac{3\chi_2 - 1}{2}\vec{n}\otimes\vec{n}, \tag{3.14}$$

where $\vec{\vec{I}}$ is the identity dyad, $\vec{n} = N^{(1)}/\|N^{(1)}\|$ is the unit vector in the direction of the vector of first-order normalized moments, $N^{(1)}$, and χ_2 is the so-called Eddington fac-

tor, a scalar quantity which is the only unknown in Eq. (3.14). A closed-form analytical expression of the Eddington factor for the M_1 closure only exists in the case of gray radiation, as will be illustrated in Section 3.3.1. In the more general case of non-gray radiative transfer, one must therefore rely on the numerical solution of the optimization problem for entropy maximization, Eqs. (3.6) and (3.8), to compute the second-order closing fluxes of the M_1 closure. Such an approach however, if adopted repeatedly whenever an update of the radiation solutions is required, can make the application of the closure extremely computationally expensive and consequently undesirable for the applications of interest in the present study (i.e., hydrocarbon combustion).

To circumvent the need for the repetitive use of the costly solution of the optimization problem to determine the Lagrange multipliers defining the maximum entropy distribution, an alternative interpolative-based approach, for accurately approximating pre-computed values of the second-order closing fluxes for the non-gray M_1 closure [124], is proposed herein. This approximation, in addition to attempting to retain many of the desirable properties of the original model (e.g., moment realizability and hyperbolicity of the moment equations), also results in substantially reduced computational costs compared to the repeated solution of the entropy maximization problem. The proposed interpolant is formulated to closely match the form of the M_1 maximum entropy solutions over the full spectrum of frequencies as well as over the entire space of physically realizable moments defined by the angular moments up to first order (i.e., the space defined by the set of necessary and sufficient conditions such that there exists a non-negative distribution reproducing angular moments up to first order). More specifically, a convex combination of the known analytical forms of the Eddington factor in the isotropic and free-streaming limits, in terms of $I_\eta^{(0)\star}$ and $\|N^{(1)}\|$, is adopted as an approximation for the closing fluxes. The interpolant is chosen such that the known analytical expressions of the Eddington factor in the isotropic and anisotropic limits are exactly reproduced. In the interior of the realizable space, the convex interpolant also exactly reproduces pre-computed numerical solutions of the Eddington factor at a finite set of points, chosen such that the overall accuracy of the interpolation, over the full range of realizable angular moments up to first order as well as over the full spectrum of frequencies, is optimized. Furthermore, the nodal distribution chosen for the purpose of the proposed interpolation procedure also allows for derivatives of the Eddington factor in the isotropic and free-streaming limits to be exactly reproduced for a finite set of values of the radiative energy density. The

development and description of the proposed interpolative-based non-gray first-order M_1 closure are given below in Section 3.3.2.

It is worth pointing out that a related interpolative-based approximation of the gray M_1 closure for radiative transport obeying Boltzmann statistics was previously proposed by Pichard *et al.* [53], as already discussed in the introduction of this thesis. The interpolation procedure of Pichard *et al.* consists of approximating the Eddington factor as a convex combination between the upper and lower boundaries of the realizable space for the second-order moments. The convex interpolant is defined as a polynomial expression in terms of the normalized first-order moment, $\|N^{(1)}\|$, which exactly reproduces known exact analytical expressions of the Eddington factor as well as its first derivatives in both the isotropic and free-streaming limits. The remaining free coefficients of the polynomial expression were then determined such that the accuracy of the proposed interpolation procedure, evaluated via the error with respect to solutions of the optimization problem for entropy maximization, computed for a large set of evaluation points uniformly distributed between the isotropic and free-streaming limits, is optimized.

Unlike the interpolation procedure proposed by Pichard *et al.* [53], the proposed approximation of the Eddington factor herein is an interpolant based on the solutions in the isotropic and free-streaming limits. Moreover, instead of expanding the interpolant in terms of a monomial basis, an expansion in terms of orthogonal Chebyshev polynomials is adopted, thereby resulting in a very well conditioned Vandermonde system, with interpolation points corresponding to Chebyshev-Gauss-Lobatto nodes. This choice of interpolation nodes allows accurate reproduction of the derivatives of the Eddington factor in the isotropic and anisotropic limits, and provides a quasi-optimal approximation of the maximum entropy solutions everywhere within the realizable space for angular moments up to first order. In addition to the above, the type of interpolation nodes adopted in the present study minimizes so-called Runge oscillations of the approximated Eddington factor near the free-streaming, which may result in loss of hyperbolicity and realizability near such boundaries. Moreover, while the assumption of gray radiation was invoked in the study by Pichard *et al.* [53], non-gray participating media are of interest in this thesis, which involve the additional dependencies of the Eddington factor on the radiative energy density and wavenumber.

It should be pointed out that, prior to the recent study by Sarr *et al.* [74], there had

been no development of interpolative-based approximations of the M_1 closure in the case of non-gray radiation transport obeying Bose-Einstein statistics, to our knowledge. In fact, the only other previous attempt to solve the system of moment equations arising from the non-gray M_1 closure with Bose-Einstein entropy is by Turpault [65, 66]. In his approach, the latter author transformed the optimization problem for entropy maximization, Eq. (3.1), into several maximum entropy optimization problems, defined over groups of frequencies spanning the whole spectrum of interest for their applications. The second-order closing fluxes, for any realizable, group-averaged, set of moments up to first order, were then obtained via numerical solution of the corresponding optimization problem for entropy maximization. However, as mentioned earlier, the expensive repeated numerical solution of the maximum entropy problem should be avoided for practical applications, where the radiation transport is coupled to the mathematical modelling of other phenomena, making computational efficiency an equally important criterion.

It should also be pointed out that the proposed treatment of the spectral dependence of the Eddington factor, as well as its dependence on the radiative energy density, has been extended and enhanced significantly in this thesis as compared to the approach described by Sarr *et al.* [74] in the recent practical application of the closure to laminar flames. Instead of a simple algebraic mapping of the radiative energy density, as adopted in the laminar-flame study, an exponential mapping is proposed here, as it was observed to better capture the variations of the Eddington factor throughout the full spectrum of frequencies. Moreover, instead of choosing an arbitrary value for the length scale of the mapping, as was proposed in [74], the present study considers a more systematic choice of the length scale, such that the resulting non-gray M_1 closure is realizable and hyperbolic everywhere within the realizable space of interest, and the accuracy of the proposed approximation for the Eddington factor is optimized for the full spectrum of possible frequencies.

3.3.1 First-Order Maximum Entropy M_1 Moment Closure for Gray Gas

Using the Eddington form given in Eq. (3.14), the closing relations for the M_1 closure for gray radiation can be derived and expressed as

$$I^{(2)} = N^{(2)} I^{(0)}, \tag{3.15}$$

where the tensor of second-order normalized moments, $N^{(2)}$, is given in Eq. (3.14) in terms of the Eddington factor, χ_2, which has the explicit analytical form

$$\chi_2 = \frac{3 + 4\|N^{(1)}\|^2}{5 + 2\xi}, \quad \xi = \sqrt{4 - 3\|N^{(1)}\|^2}. \tag{3.16}$$

In spite of the ability to capture a wider range of optical conditions than the P_1 model, the M_1 closure is known to produce nonphysical solutions in the radiative energy density in the context of crossing streams of radiative particles emanating from different directions [51, 53]. In fact, when the zeroth- and first-order angular moments are the only available information for reconstructing the angular distribution of radiative energy, the only possible form for the latter in the case of crossing streams of photons with zero net flux is that of an isotropic distribution, even though the underlying angular distributions are highly non-isotropic. This issue can however be remedied by considering high-order members of the maximum-entropy hierarchy [53–55]. The second-order M_2 closure is also considered as part of this thesis.

3.3.2 Interpolative-Based First-Order Maximum-Entropy M_1 Moment Closure for Non-Gray Gas

As for the case of a gray gas, the second-order closing fluxes arising from the M_1 closure in the context of non-gray radiation can again be written in the following form

$$I_\eta^{(2)\star} = N^{(2)} I_\eta^{(0)\star}, \tag{3.17}$$

where the tensor of second-order normalized moments, $N^{(2)}$, is again given in terms of the Eddington factor, χ_2, in Eq. (3.14). However, unlike the case of the M_1 closure for a gray gas, there exists no closed-form exact analytical expression for the Eddington

factor for a non-gray gas. Values of the latter must therefore be determined numerically by solving the relatively expensive optimization problem for entropy maximization, Eqs. (3.6) and (3.8), for any given realizable set of moments up to first order. For the purpose of radiative transport in real gases, repetition of this prohibitively expensive procedure is avoided here by constructing an interpolative-based approximation of the Eddington factor, the description of which is presented here in this section. Following a brief overview of the realizable space for moments up to first order, an in-depth description of the theoretical details of the interpolative procedure for the non-gray M_1 closure is provided, followed by the assessment of several key mathematical properties. The moment realizability of the resulting approximation of the Eddington factor, for sets of angular moments up to first order spanning the full realizable space, and for values of wavenumbers spanning the full spectrum of frequencies, is considered. Following this, the hyperbolicity of the closed system of partial differential equations for the angular moments, resulting from the interpolative non-gray M_1 closure, is then discussed later in Section 5.1.2 of Chapter 5.

The space of realizable moments up to order one is defined by the set of necessary and sufficient conditions for the existence of a non-negative distribution yielding physically-realistic moments up to first order. This space is denoted here by $\mathcal{R}^{(1)}$ and can be defined as follows

$$\mathcal{R}^{(1)} = \{(I_\eta^{(0)}, I_\eta^{(1)}) \in \mathbb{R} \times \mathbb{R}^3 \quad \text{s.t.} \quad I_\eta^{(0)} \geq 0 \quad \text{and} \quad ||N^{(1)}|| \leq 1\}. \tag{3.18}$$

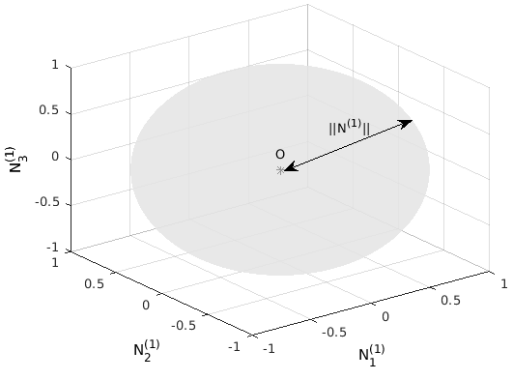

Figure 3.1: Realizable space $\mathcal{R}^{(1)}$ for the first-order moments for any non-negative energy density, $I_\eta^{(0)}$.

Table 3.1: Form of the entropy maximizing distribution on the boundaries of the realizable space for angular moments up to first order.

Regime	**Form of the Distribution**
$\|N^{(1)}\| = 1$	$I_\eta = I_\eta^{(0)}\delta(\vec{s} - N^{(1)})$
$I_\eta^{(0)} \to 0$	$\mathcal{I}_\eta(\boldsymbol{\alpha},\, \mathbf{m}) = 2hc\eta^3 \exp\left(-\frac{c^2h\eta}{k}\boldsymbol{\alpha}^T\mathbf{m}(\vec{s})\right)$
$I_\eta^{(0)} \to +\infty$	$\mathcal{I}_\eta(\boldsymbol{\alpha},\, \mathbf{m}) = \frac{2k\eta^2}{c}\left[\boldsymbol{\alpha}^T\mathbf{m}(\vec{s})\right]^{-1}$
$\widetilde{\mathcal{R}}^{(1)}$	$\mathcal{I}_\eta(\boldsymbol{\alpha},\, \mathbf{m}) = 2hc\eta^3\left[\exp\left(\frac{c^2h\eta}{k}\boldsymbol{\alpha}^T\mathbf{m}(\vec{s})\right) - 1\right]^{-1}$

As can be seen from Eq. (3.18), the realizability domain, $\mathcal{R}^{(1)}$, spans the semi-infinite interval $[0,\, +\infty]$ for any realizable vector of first-order moments, $N^{(1)}$, and the unit ball for any non-negative density, $I_\eta^{(0)}$, as illustrated in Fig. 3.1. It is worth mentioning that the radiation entropy based on Bose-Einstein statistics, given previously in Eq. (3.3), becomes singular on the boundaries of the realizable moment space, denoted here by $\partial\mathcal{R}^{(1)}$, and where the inequalities defining the realizable space, $\mathcal{R}^{(1)}$, become sharp such that

$$\partial\mathcal{R}^{(1)} = \{(I_\eta^{(0)}, I_\eta^{(1)}) \in \mathbb{R}\times\mathbb{R}^3 \quad \text{s.t.} \quad I_\eta^{(0)} \to 0 \quad \text{or} \quad I_\eta^{(0)} \to +\infty \quad \text{or} \quad ||N^{(1)}|| = 1\}. \tag{3.19}$$

In particular, on $\partial\mathcal{R}^{(1)}$, the non-gray entropy maximizing distribution of Eq. (3.5) is either uniquely determined by a Dirac-delta distribution (for $\|N^{(1)}\| = 1$), or takes a particular form, as in the case of the limit where $I_\eta^{(0)} \to 0$ or $I_\eta^{(0)} \to +\infty$, which are referred to as the hyperbolic and the logarithmic limits [125], respectively. The expressions for the entropy maximizing distribution associated with each of the aforementioned limits, are summarized in Table 3.1, where $\widetilde{\mathcal{R}}^{(1)}$ denotes the interior of the realizable space, $\mathcal{R}^{(1)}$.

Based on the above, maximum-entropy solutions for the Eddington factor throughout the full realizable space, $\mathcal{R}^{(1)} = \widetilde{\mathcal{R}}^{(1)}\cup\partial\mathcal{R}^{(1)}$, can then be obtained by solving the optimization problem for entropy maximization using the appropriate form of the distribution for any given set of moments up to first order. For illustration purposes, numerical values of the Eddington factor throughout $\mathcal{R}^{(1)}$, as well as over the full spectrum of frequencies, obtained by solving the dual maximum-entropy problem for 100 values of $\|N^{(1)}\|$ equally distributed within $[0,\, 1]$, with values of $I_\eta^{(0)\star}$ (see Eq. (3.9)) ranging from the hyperbolic to the logarithmic limits for any given frequency, are illustrated in Fig. 3.2. It can be observed that, for any given value of $I_\eta^{(0)\star}$, the Eddington factor displays a smooth,

monotonically increasing solution between the isotropic and free-streaming limits. As such, we then choose to write the latter, i.e., the Eddington factor, $\chi_2 = \chi_2(I_\eta^{(0)\star}, \|N^{(1)}\|)$, as a smooth interpolant between the two aforementioned limits as follows

$$\chi_2 = \frac{1}{3} + \frac{2}{3} f_{\chi_2}, \tag{3.20}$$

where the convex interpolant, $f_{\chi_2} = f_{\chi_2}(I_\eta^{(0)\star}, \|N^{(1)}\|)$, is chosen such that the known exact expressions for χ_2 are exactly reproduced in both the isotropic and anisotropic limits, corresponding to $\|N^{(1)}\| = 0$ and $\|N^{(1)}\| = 1$, respectively. The interpolant, f_{χ_2}, is then taken to have the form

$$f_{\chi_2} = \|N^{(1)}\|^2 \left[1 + \left(1 - \|N^{(1)}\|^2\right) g_{\chi_2}\right]. \tag{3.21}$$

It can be easily shown from Eqs. (3.20) and (3.21) that $\chi_2(I_\eta^{(0)\star}, 0) = 1/3$, and $\chi_2(I_\eta^{(0)\star}, 1) = 1$. It is also worth mentioning that, for reasons of simplicity especially when evaluating derivatives of the Eddington factor, the expression for f_{χ_2} is different from that proposed previously in the application to laminar flames by Sarr *et al.* [74].

The weighting function, $g_{\chi_2} = g_{\chi_2}(I_\eta^{(0)\star}, \|N^{(1)}\|)$, appearing in Eq. (3.21), is chosen to be a polynomial expression, the coefficients of which are chosen such that maximum-entropy solution for the Eddington factor are accurately reproduced for all realizable

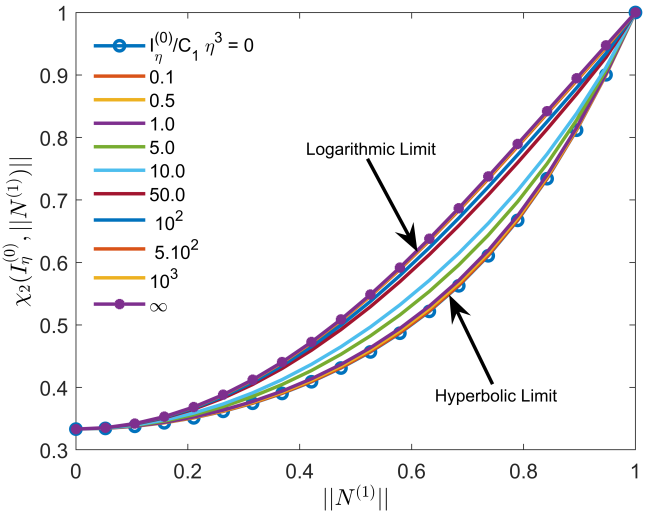

Figure 3.2: Non-gray M_1 Eddington factor, χ_2, solution profiles with respect to $\|N^{(1)}\|$ for different values of the radiative energy density, $I_\eta^{(0)\star}$, ranging from the hyperbolic limit ($I_\eta^{(0)\star} \to 0$) to the logarithmic limit ($I_\eta^{(0)\star} \to +\infty$) for any given frequency.

sets of angular moments up to first order. However, instead of adopting a least-squares curve fitting procedure in terms of monomials [74], a more robust approach is adopted for the interpolation procedure applied to g_{χ_2} herein. In particular, an approach based on truncated series expansion in terms of orthogonal Chebyshev polynomials is advocated, the coefficients of which are determined via the solution of the Vandermonde system of equations associated with suitably chosen interpolation nodes. In this case, g_{χ_2} is expressed as

$$g_{\chi_2} = \sum_{i=0}^{n_i} \sum_{j=0}^{n_j} T_i \left(\mathcal{M}_{I_\eta^{(0)\star}} \right) T_{2j} \left(\| N^{(1)} \| \right) D_{ij}^{\chi_2}, \tag{3.22}$$

with $n_i = n_j = 5$, where T_n is the Chebyshev polynomial of the first kind of degree n, and $\mathcal{M}_{I_\eta^{(0)\star}}$ represents an exponential mapping for the zeroth-order moment, $I_\eta^{(0)\star}$, of the following form

$$\begin{aligned} \mathcal{M}_{I_\eta^{(0)\star}} \quad &: \quad [0,\ +\infty] \rightarrow [-1,\ 1], \\ & \qquad I_\eta^{(0)\star} \rightarrow 1 - 2 \exp\left(- \frac{I_\eta^{(0)\star}}{L_{\chi_2}} \right), \end{aligned} \tag{3.23}$$

and where L_{χ_2} is the length scale of the mapping, $\mathcal{M}_{I_\eta^{(0)\star}}$.

The evaluation of L_{χ_2} is particularly important to the accuracy and robustness of the proposed interpolative closure. Rather than adopting an arbitrary scalar-valued mapping length scale as considered in the previous application to laminar flames [74], a more systematic evaluation of L_{χ_2} is proposed herein, such that the accuracy of the approximation for the Eddington factor compared to the values associated with the numerical maximum-entropy solutions, is optimized systematically, for sets of angular moments up to first order spanning $\widetilde{\mathcal{R}}^{(1)} \cup \partial\mathcal{R}^{(1)}$, and over the full spectrum of frequencies. The choice of the form of the mapping length scale is also dictated by some of the desirable properties of the original non-gray M_1 closure: in particular, realizability of the interpolative Eddington factor as well as hyperbolicity of the resulting closed system of moment equations. An in-depth description of the procedure adopted here for determining the optimal distribution of L_{χ_2} is given later in this section.

In Eq. (3.22), the coefficients, $D_{ij}^{\chi_2}$, $i = 0, 1, \ldots, n_i$, $j = 0, 1, \ldots, n_j$, defining the vector of coefficients, $\mathbf{D}^{\chi_2}$, are determined via the solution of the Vandermonde system arising from the enforcement of Eq. (3.22) at several interpolation nodes spanning $\widetilde{\mathcal{R}}^{(1)} \cup \partial\mathcal{R}^{(1)}$. Here, the interpolation points for $\mathcal{M}_{I_\eta^{(0)\star}}$ and $\| N^{(1)} \|$ were chosen to coincide with extrema

of Chebyshev polynomials of the first kind of order n_i and $2n_j$, respectively, including the endpoints, for given values of n_i and n_j. Such interpolation nodes, also known as Chebyshev-Gauss-Lobatto points, yield a quasi-optimal approximation of the Eddington factor over the full realizable space, $\mathcal{R}^{(1)}$. Moreover, the fact that this choice of interpolation nodes also includes the endpoints allows for the derivatives of the Eddington factor to be accurately reproduced in both the isotropic and anisotropic limits. This feature is quite desirable as it ensures that the proposed interpolative-based approximation of the Eddington factor accurately captures the rates of change of the original maximum entropy solutions in these limits, and, consequently, oscillations of the interpolated solutions as theses limits are approached, which can yield both realizability and hyperbolicity issues, are minimized. Nevertheless, computations of the numerical values of g_{χ_2} from the maximum entropy solutions, using Eqs. (3.20) and (3.21), for the purpose of solving the Vandermonde system for the vector of coefficients, $\mathbf{D}^{\chi_2}$, defined by Eq. (3.22), though straightforward for distributions away from the isotropic and free-streaming limits, result in undetermined expressions in these two limits. The procedure adopted here to compute the corresponding numerical values in such cases makes use of the l'Hopital's rule and is summarized in Appendix A.

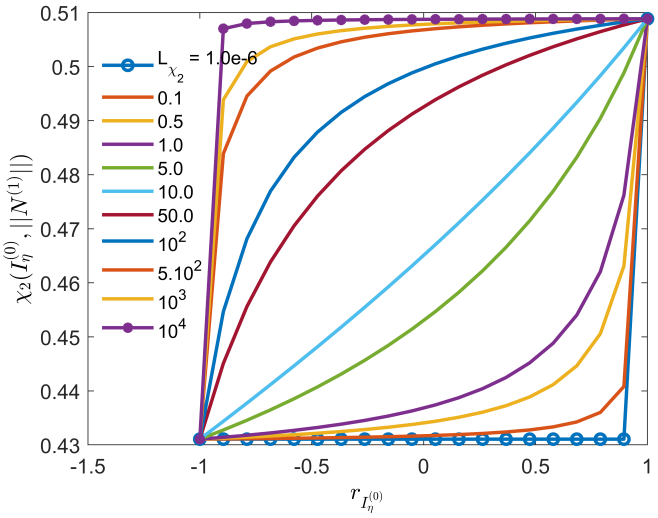

Figure 3.3: Non-gray M_1 Eddington factor, χ_2, solution profiles with respect to the exponential mapping, $\mathcal{M}_{I_\eta^{(0)\star}}$, obtained for $\|N^{(1)}\| = 0.5$, for different values of the length scale L_{χ_2}.

For illustration purposes, pre-computed solutions of the Eddington factor with respect to $\mathcal{M}_{I_\eta^{(0)\star}}$, given in Eq. (3.23), for different values of the length scale, L_{χ_2}, are presented in Fig. 3.3, for $\|N^{(1)}\| = 0.5$. It can be observed that the rate of change of χ_2 with respect to $\mathcal{M}_{I_\eta^{(0)\star}}$ is strongly affected by the values of the length scale. More specifically, for very small or very large values of L_{χ_2}, the Eddington factor changes very rapidly near the logarithmic or the hyperbolic limit, and such strong variations cannot be easily captured by standard polynomial approximations, especially relatively low-degree polynomials. On the other hand, for intermediate values of the length scale, the Eddington factor is observed to be more well behaved (i.e, varies more linearly), with rates of change that can be easily captured using relatively low-order polynomials. This can be explained by the fact that small values of L_{χ_2} cluster the interpolation nodes for the radiative energy density near the hyperbolic limit, whereas, conversely, very large values of L_{χ_2} concentrate the interpolation points closer to the logarithmic limit, leading to under-resolution, and consequently the large rates of change of the Eddington factor as the opposite limit is approached. Similar features are also observed for any given value of the anisotropic factor, $\|N^{(1)}\|$, between the isotropic and the free-streaming limits. These findings suggest that, for any given value of $\|N^{(1)}\|$, an optimal value of the length scale, L_{χ_2}, can be found, which minimizes the error of our interpolative-based approximation of the Eddington factor over the full spectrum of frequencies and energy levels. Based on the above, the length scale, $L_{\chi_2} = L_{\chi_2}\left(\|N^{(1)}\|\right)$, is expressed here in the following form

$$L_{\chi_2} = \exp\left[\sum_{j=0}^{n_j} T_{2j}\left(\|N^{(1)}\|\right) D_j^{L_{\chi_2}}\right], \tag{3.24}$$

where the coefficients, $D_j^{L_{\chi_2}}$, $j = 0, 1, \ldots, n_j$, defining the vector of coefficients, $\mathbf{D}^{L_{\chi_2}}$, are chosen so as to accurately mimic numerical solutions of the entropy optimization problem for the Eddington factor over the full realizable space, $\widetilde{\mathcal{R}}^{(1)} \cup \partial\mathcal{R}^{(1)}$, as well as over the full spectrum of frequencies.

In the present study, the vector of coefficients, $\mathbf{D}^{L_{\chi_2}}$, is determined via the solution of a nonlinear least-squares problem, which consists of minimizing the L^2 error of the interpolative-based approximation of the Eddington factor, and can be summarized by

the following procedure

$$\begin{aligned} &\min_{\mathbf{D}^{L_{\chi 2}}} \{\text{error}_{g_{\chi_2}}\}, \\ \text{error}_{g_{\chi_2}} &= \sum_{i=1}^{N_i}\sum_{j=1}^{N_j}\sum_{k=1}^{N_k} w_i w_j w_k (g^{ijk}_{\chi 2,\text{fit}} - g^{ijk}_{\chi 2,\text{numerical}})^2. \end{aligned} \tag{3.25}$$

In Eq. (3.25), $g^{ijk}_{\chi 2,\text{numerical}}$ represents values of the weighting function, g_{χ_2}, of Eq. (3.22), of the affine interpolant, obtained via numerical solution of the optimization problem for entropy maximization for $N = N_i N_j N_k = 10^6$ evaluation points. These test points consist of $N_i = 100$ values of $\mathcal{M}_{I_\eta^{(0)\star}}$ following a Gauss-Lobatto-Chebyshev distribution in $[-1,\ 1]$, with associated weights, w_i, $N_j = 100$ values of $\|N^{(1)}\|$ associated with non-negative Gauss-Lobatto-Chebyshev points in $[-1,\ 1]$, with weighting w_j, and $N_k = 100$ values of L_{χ_2} based on roots of Laguerre polynomials with weighting w_k. Moreover, $g_{\chi 2,\text{fit}}$ corresponds to values of the weighting function, g_{χ_2}, computed via evaluation of the proposed polynomial approximation, Eq. (3.22), at the test points. At each iteration of the nonlinear least-squares problem defined by Eq. (3.25), the iterate, $\mathbf{D}^{L_{\chi 2}}$, can be used, in conjunction with Eq. (3.24) as well as the inverse of the exponential mapping of Eq. (3.23), to compute values of $I_\eta^{(0)\star}$ associated with the chosen interpolation nodes for $\mathcal{M}_{I_\eta^{(0)\star}}$, and consequently solve the corresponding dual maximum-entropy problem, Eqs. (3.6) and (3.8), at each of the interpolation points. The vector of coefficients, $\mathbf{D}^{\chi 2}$, given in Eq. (3.22), is then obtained via solution of the associated Vandermonde system, and the resulting polynomial expression of Eq. (3.22) is subsequently used to compute approximate values of $g_{\chi 2,\text{fit}}$ at each of the evaluation points.

It is worth pointing out that, while the choice of uniformly distributed points for $\mathcal{M}_{I_\eta^{(0)\star}}$ and $\|N^{(1)}\|$ for the purpose of assessing the error in the least-squares problem of Eq. (3.25) may be more intuitive and straightforward, such an approach was observed to be problematic in our study. In particular, with the current choice choice of Chebyshev-Gauss-Lobatto nodes for the interpolation procedure, the use of uniform distributions for computing the error in Eq. (3.25) resulted in an under-resolution of the latter in areas of the realizable space, $\widetilde{\mathcal{R}}^{(1)} \cup \partial\mathcal{R}^{(1)}$, with larger densities of interpolation points, i.e., in the hyperbolic and logarithmic limits for $\mathcal{M}_{I_\eta^{(0)\star}}$, and in the free-streaming limit for $\|N^{(1)}\|$. Moreover, over-resolution of the error was also observed in regions of $\mathcal{R}^{(1)}$ with relatively small density of interpolation points. To alleviate this issue, Chebyshev-Gauss-Lobatto nodal distribution of points for $\mathcal{M}_{I_\eta^{(0)\star}}$ and $\|N^{(1)}\|$ were also employed for computing the

error given in Eq. (3.25), similar to those used for the interpolation points.

Two equally important properties to consider for the purpose of our interpolation procedure, in addition to accuracy with respect to numerical maximum-entropy solutions, are realizability and hyperbolicity of the interpolative-based non-gray M_1 closure, throughout the full realizable space for angular moments up to first order, in multiple space dimensions, as well as over the full spectrum of frequencies. The necessary and sufficient conditions for realizability of the second-order normalized moments, $N^{(2)}$, for any given realizable set of moments up to first order, $\{I_\eta^{(0)}, I_\eta^{(1)}\}$, are well established and are given by [126]

$$N^{(2)} - N^{(1)}(N^{(1)})^T \geq 0. \tag{3.26}$$

The conditions for moment realizability for moment systems up to second order are also reviewed later in this chapter in Section 3.4.1.

Using the Eddington form of $N^{(2)}$, presented in Eq. (3.14), it can be shown that the realizability conditions above are satisfied if and only if the Eddington factor, χ_2, satisfies the following inequality constraints

$$\|N^{(1)}\|^2 \leq \chi_2 \leq 1. \tag{3.27}$$

In order to ensure realizability of our interpolative-based approximation of the Edding-

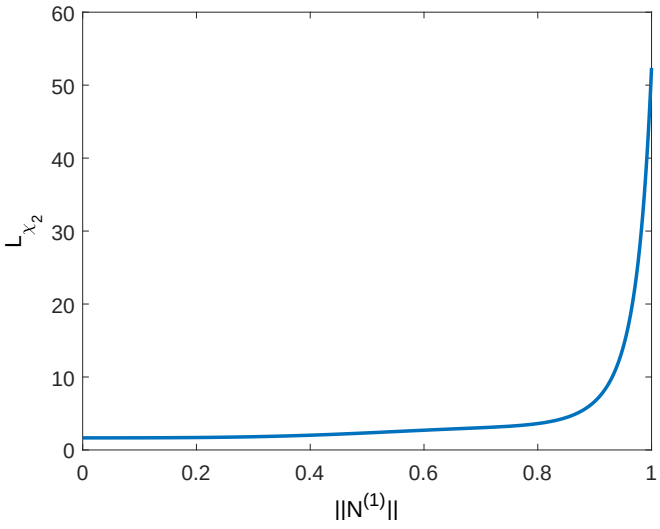

Figure 3.4: Optimal values of the length scale, L_{χ_2}, for the exponential mapping, $\mathcal{M}_{I_\eta^{(0)\star}}$, of the radiative energy density for different levels of anisotropy.

ton factor, at every step of the non-linear least-squares optimization problem defined by Eq. (3.25), the constraint of Eq. (3.27) is enforced, for a large set of sample points, consisting of 10^3 values of $\mathcal{M}_{I_\eta^{(0)\star}}$ following a Gauss-Lobatto-Chebyshev distribution in $[-1,\ 1]$, 10^3 values of $\|N^{(1)}\|$ coinciding with non-negative Gauss-Lobatto-Chebyshev points in $[-1,\ 1]$, and 10^2 values of L_{χ_2} based on roots of Laguerre polynomials. Moreover, hyperbolicity is also enforced at each step of the least-squares optimization problem, Eq. (3.25), by also applying constraints on the eigenvalues of the flux Jacobians of the resulting closed system of equations, as discussed in Section 5.1.2. The additional realizability constraints minimize the risk of the optimization algorithm used to solve the least-squares problem converging to a local minimum outside the realizable space. The latter was sometimes encountered when the additional realizability conditions were not enforced throughout the non-linear least-squares iterations, especially near the free-streaming limit.

Optimal values of the length scale, L_{χ_2}, obtained using the procedure described above, are depicted in Fig. 3.4, for various levels of anisotropy between the isotropic and free-streaming limits. It can be observed that the length scale, L_{χ_2}, as defined by Eq. (3.24), displays little to no variations with respect to the anisotropic factor in the vicinity of the isotropic limit. As the free-streaming limit is approached, on the other hand, monotonically increasing rates of change of the optimal length scale are observed. Compared to the interpolative procedure adopted previously by Sarr *et al.* [74], where the choice of the length scale was arbitrary, the interpolation procedure for the non-gray M_1 closure proposed herein considers a more systematic choice of the distribution of the length of the mapping of the radiative energy density. This in turn yields a more robust and accurate approximation of the Eddington factor, throughout the full realizable space for angular moments up to first order, and over the full spectrum of frequencies. More specifically, a value of $L_{\chi_2} = 1$ was employed by Sarr *et al.* [74], which yielded rather accurate approximations of maximum entropy solutions closer to the hyperbolic limit. However, as the logarithmic limit was approached, the relatively large rates of change of the Eddington factor with respect to the corresponding algebraic mapping resulted in a less accurate interpolative-based procedure, especially near the free-streaming limit, where this issue also translated into loss of realizability.

For the sake of improving the efficiency of the interpolative non-gray M_1 closure, the final polynomial expressions, given in Eqs. (3.22) and (3.24), can be rewritten in terms of monomials with respect to the independent variables. The resulting polynomial ex-

pressions, expressed in monomial bases, can consequently be evaluated very efficiently by means of Horner's method [127, 128] when implemented in a computer code.

The optimal sets of coefficients, $\mathbf{D}^{\chi_2}$, and $\mathbf{D}^{L_{\chi_2}}$, defined by Eqs. (3.22) and (3.24), respectively, resulting from the numerical solution of the non-linear least-squares problem of Eq. (3.25), in conjunction with the constraints of realizability given by Eq. (3.27), yield a closure that is realizable at all the points where the inequality constraints are enforced. This is illustrated in Fig. 3.5 where iso-contours of the parameter, $f_{\text{realiz}} = \big(\chi_2 - \|N^{(1)}\|^2\big)/\big(1 - \|N^{(1)}\|^2\big)$, are shown. As can be expected, the realizability conditions of Eq. (3.27), which require that $0 \leq f_{\text{realiz}} \leq 1$, appear to be satisfied everywhere in $\mathcal{R}^{(1)}$ and over the full spectrum of frequencies. While this is certainly not a proof that the proposed interpolative-based non-gray M_1 closure, Eqs. (3.20)–(3.24), is realizable everywhere within $\widetilde{\mathcal{R}}^{(1)} \cup \partial\mathcal{R}^{(1)}$ and over the full spectrum of frequencies, the local realizability of the proposed closure at all the points examined demonstrates the extent to which the latter closely mimics the exact non-gray M_1 closure, which is known to be everywhere realizable.

Similar to the underlying original maximum-entropy model, the non-gray interpolative-based M_1 model developed in this study, in addition to its desirable mathematical prop-

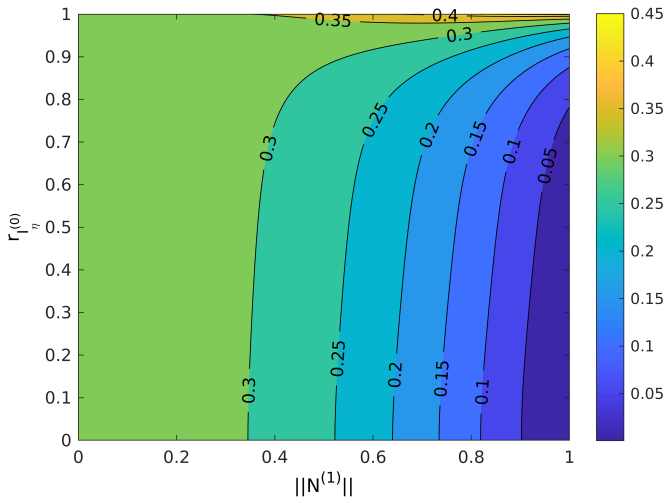

Figure 3.5: Realizability contours for the Eddington factor of the non-gray M_1 closure for sets of moments $\{I_\eta^{(0)}, I_\eta^{(1)}\}$ spanning the whole realizability domain for moments up to first order, $\mathcal{R}^{(1)}$, and wavenumbers, η, spanning the full spectrum of frequencies.

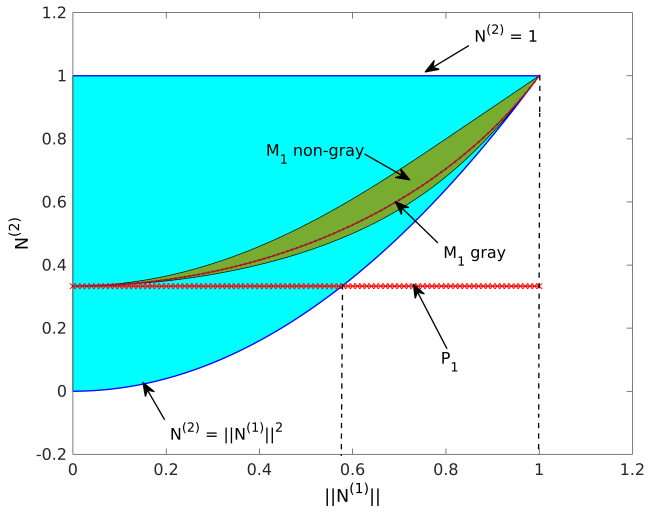

Figure 3.6: Eddington factor corresponding to non-gray first-order maximum entropy (M_1) moment closure for all realizable sets of moments $\{I_\eta^{(0)}, I_\eta^{(1)}\}$, and values of wavenumber, η, spanning the full spectrum of frequencies.

erties, is able to capture radiative transfer regimes lying anywhere between the isotropic limit ($\|N^{(1)}\| = 0$) and anisotropic limit ($\|N^{(1)}\| = 1$). On the other hand, its spherical harmonic counterpart, i.e., the first-order, P_1, closure, can only accurately capture small to moderate departures from equilibrium since the corresponding closure relation is equivalent to that of an isotropic distribution with the same radiative energy density, $I_\eta^{(0)}$. These facts are illustrated in Fig. 3.6, where the realizability domain for the Eddington factor, χ_2, is shown along with the range of values of the latter obtained using the first-order maximum entropy, M_1, and the first-order spherical harmonic, P_1, closures for sets of angular moments up to first order, $\mathbf{E}_\eta = \{I_\eta^{(0)}, I_\eta^{(1)}\}$, spanning $\mathcal{R}^{(1)}$, and wavenumber values spanning the full spectrum of frequencies. It can be observed that the M_1 closure is realizable throughout $\mathcal{R}^{(1)}$ whereas the P_1 approximation is only strictly realizable for $\|N^{(1)}\| \leq \sqrt{3}/3$.

3.4 Second-Order Maximum-Entropy M_2 Moment Closure

The next member of the maximum-entropy hierarchy is the second-order, M_2, closure, which, in a procedure similar to that described for the M_1 closure, provides closing relations to the system of moment equations up to second order via reconstruction of an entropy maximizing distribution in terms of its known angular moments up to order two. The reconstructed distribution again takes the form given in Eq. (3.10) in the case of gray radiative transfer or Eq. (3.5) for non-gray radiation. Computing the resulting third-order angular moments then yields the third-order closing fluxes, arising from the M_2 closure, in terms of the lower-order angular moments, i.e., $I^{(3)} = I^{(3)}(I^{(0)}, I^{(1)}, I^{(2)})$ for gray radiation and $I_\eta^{(3)\star} = I_\eta^{(3)\star}(I_\eta^{(0)\star}, I_\eta^{(1)\star}, I_\eta^{(2)\star})$ in the case of non-gray radiation. Unfortunately, as mentioned earlier, it is not possible to obtain closed-form analytical expressions for the closing moment fluxes for the M_N closures, to the exception of the Bose-Einstein-based M_1 closure for a gray medium. As such, repeated numerical solution of the optimization problem for entropy maximization, given in Eqs. (3.12) and (3.13) for gray radiation and in Eqs. (3.6) and (3.8) for non-gray radiation, would therefore be necessary for computing the third-order closing fluxes arising from the M_2 closure, whenever an update of the radiation solutions is required, making the application of the second-order closure computationally expensive.

To circumvent the need for the costly solutions of the optimization problem to determine the Lagrange multipliers defining the maximum entropy distribution, alternative interpolative-based approaches for accurately approximating pre-computed values of the third-order closing fluxes, for both the gray and non-gray M_2 closures, are proposed herein. These approximations, in addition to attempting to retain key desirable properties of the original closures (e.g., hyperbolicity of the closed systems of moment equations), also result in substantially reduced computational costs compared to the repeated solution of the optimization problem for entropy maximization.

The proposed interpolation procedure for the gray M_2 closure is formulated so as to closely match the form of the gray M_2 maximum entropy solutions, for the third-order closing fluxes, over the entire space of physically realizable moments up to second order (i.e., the space defined by the set of necessary and sufficient conditions such that

there exists a non-negative distribution reproducing moments up to second order). More specifically, a procedure based on affine combinations of the known analytical expressions of the normalized third-order angular moments, $N^{(3)}$, on some of the boundaries of the realizable space for the second-order angular moments, is adopted to provide approximations for the closing fluxes of the gray M_2 closure. The interpolants are chosen such that known analytical expressions of the third-order closing fluxes in the isotropic and the free-streaming limits, as well as on the boundaries of the realizable space for the second-order moments, are exactly reproduced. In the interior of the realizable space for the M_2 closure, the interpolants also exactly reproduce pre-computed numerical maximum entropy solutions at a finite set of points, chosen to coincide with roots or extrema of suitably selected orthogonal polynomials, which are known to provide quasi-optimal approximation to a function.

It is worth mentioning that the theoretical details pertaining to the development of the M_2 closure for gray radiation proposed in this thesis, have also been presented previously by Sarr and Groth [129, 130]. However, the present formulation considers a more suitable choice of orthogonal polynomial basis for the interpolation over the realizable space for the second-order angular moments, in addition to exploiting evenness of the third-order closing fluxes so as to reduce the number of coefficients required for the interpolation. In the case of the M_2 closure for non-gray radiation, which also involves the additional dependencies of the third-order closing fluxes on the radiative energy density and wavenumber relative to its gray counterpart, the proposed interpolation procedure is a direct extension of the framework adopted herein for the interpolative-based approximation of the gray M_2 closure. More specifically, the interpolant is formulated so as to closely match the form of the non-gray M_2 maximum entropy solutions for the third-order closing fluxes over the entire space of physically realizable moments up to second order as well as over the full spectrum of frequencies. The additional dependencies on the radiative energy density and wavenumber are treated in a similar way as was done for the non-gray M_1 closure presented in Section 3.3.2. In particular, an exponential mapping of the radiative energy density, $I_\eta^{(0)\star}$, is employed for the purpose of our polynomial interpolation procedure, and the length scale of the mapping is systematically chosen so as optimize the accuracy with respect to numerical maximum entropy solutions, while resulting in an overall hyperbolic closed system of moment equations up to second order. However, unlike the procedure adopted for the non-gray M_1 closure, realizability of the

closing fluxes of the non-gray M_2 closure is not considered herein for the determination of the distribution of the length scale of the exponential mapping, due to the lack of necessary and sufficient conditions for realizability of angular moments up to third order.

It should also be noted that several authors have recently developed interpolative-based approximations of the M_2 maximum-entropy moment closure for gray radiation in multi-dimensional physical space. Firstly, as noted earlier in the thesis, Pichard *et al.* [53] proposed an extension of the previously-developed approximation to the M_2 closure by Monreal and Frank [56] for one space dimension to multiple dimensions. The multi-dimensional interpolative-based M_2 closure proposed by Pichard *et al.* [53] was formulated for radiative transport obeying Boltzmann statistics. However, by way of its construction, the resulting interpolation procedure only mimics accurately the corresponding maximum entropy solutions in one dimensional physical space, but not in multiple space dimensions. Moreover, the fact that the construction in multiple dimensions is based on the realizability domain for moments up to first order does not take into account some of the possible regimes that can only be described by higher-order moments describing the realizable space of the M_2 closure.

More recently, an extended quadrature method of moments (EQMOM)-based second-order moment closure was developed by Li *et al.* [59], as an approximation to the M_2 maximum-entropy closure. While attractive due to the existence of closed-form analytical expressions for the third-order closing fluxes, this so-called B_2 model of Li *et al.* [59] does not really attempt to mimic closely the properties of the M_2 maximum entropy closure and, in multiple space dimensions, is neither globally realizable nor globally hyperbolic. In fact, Li *et al.* [59] have shown that the quadrature-based approximation to the M_2 closure is not realizable and hyperbolic everywhere within the realizable space defined by moments up to second order. It is worth mentioning that, prior to the present thesis study, there has been no development or investigation of any kind for the second-order maximum entropy, M_2, closure in the case of non-gray radiation.

Unlike the interpolative procedure adopted by Pichard *et al.* [53], the M_2 closure for gray radiation proposed in this thesis aims at fully mimicking the maximum entropy solutions everywhere within the realizable space for angular moments up to second order in multiple space dimensions. In particular, suitable choices for the form of the interpolants for the third-order closing fluxes are made through a careful study and characteriza-

tion of the realizable space for angular moments up to second order in multiple space dimensions. Such a characterization also allows to gain better insight as far as the appropriate choice of orthogonal polynomials bases for the expansion and approximation of the third-order closing fluxes. More specifically, the interpolation procedure proposed herein makes use of the known closed-form analytical expressions for the third-order closing fluxes on the boundaries of the realizable space for angular moments up to second order in multi-dimensional physical space, the derivation of which is presented in the sections to follow. On the other hand, the interpolative approach adopted by Pichard *et al.* [53] for the M_2 closure is based on the form of the third-order closing fluxes on the boundaries of the realizable space for the third-order angular moments, the closed-form expressions of which only exist in one dimensional physical space. Furthermore, while geometrical mappings of the realizable space, in particular triangle to rectangle mapping, were carried out by Pichard *et al.* [53] for the polynomial interpolation over the full realizable space, the proposed interpolative-based M_2 closure for gray radiation directly interpolates maximum-entropy solutions over the realizable space for angular moments up to order 2 via expansion with respect to appropriately selected orthogonal polynomial bases. The construction of the interpolative-based third-order closing fluxes based on the non-gray M_2 closure is directly inspired from the proposed procedure for its gray counterpart, while also taking into account the additional dependencies on the spectral variable and the radiative energy density.

The development and description of the proposed interpolative-based second-order M_2 closures for gray and non-gray radiation are given below in the sections to follow. More specifically, after revisiting the necessary and sufficient conditions for the realizability of angular moments up to second order, an in-depth description of the theoretical details of the interpolative procedures adopted for both the gray and non-gray M_2 closures is carried out. Hyperbolicity of the closed system of partial differential equations for the angular moments, resulting from our proposed interpolative M_2 closures, is discussed later in Section 5.1.3 of Chapter 5.

3.4.1 Necessary and Sufficient Conditions for Realizability of Angular Moments Up to Second Order

As a first step in the development of the M_2 closures, the necessary and sufficient conditions for realizability of angular moments up to second order are presented and given. A proof of sufficiency is also provided. These conditions and the proof were previously established for both one- and multi-dimensional radiative heat transfer problems by Kershaw [126]. They were also key elements in the construction of the previous second-order closures of Pichard *et al.* [53] and Li *et al.* [59]; however, as they are crucial to the development of the proposed interpolative-based approximations of the M_2 closure for both gray and non-gray radiation, they are re-summarized here. In particular, a geometrical interpretation of Kershaw's proof of sufficiency [126] is proposed here, which subsequently provides the inspiration for the construction of the interpolative M_2 closures. For the sake of notational simplicity, the wavenumber subscript is dropped, though the derivations to follow for moment realizability also apply to spectrally-dependent angular distributions of the radiative intensity.

Realizability of the predicted angular moments of a given closure deals with the issue of whether or not a physically realistic (i.e., strictly positive valued or non-negative) angular distribution of the radiation intensity can be associated with the given set of moments. If such an angular distribution can be identified, then the moment set is deemed to be realizable. The conditions for moment realizability give rise to a set of constraints or realizability conditions on the predicted moments which can be used to define the extent of possible closure solutions in moment space. The approach essentially consists of multiplying a presumed non-negative distribution by a non-negative polynomial test function defined in terms of the angular variables, from which necessary conditions for realizability of the moments can be derived. For angular moments up to second order, necessary realizability conditions can be obtained by constructing the polynomial, $\mathcal{P}(\vec{s}) = \mathbf{a}^{\mathrm{T}}\mathbf{S}$, where $\mathbf{S} = [1, \vec{s}^{\mathrm{T}}]^{\mathrm{T}}$ is the set of angular weights up to first order and $\mathbf{a}^{\mathrm{T}}$ are the coefficients of the polynomial. It then follows that for any globally positive-valued angular distribution, I, one must have [131]

$$\left\langle ||\mathcal{P}(\vec{s})||^2 I \right\rangle = \mathbf{a}^{\mathrm{T}} \left\langle \mathbf{S}\mathbf{S}^{\mathrm{T}} I \right\rangle \mathbf{a} \geq 0\,, \tag{3.28}$$

which, for an arbitrary polynomial, requires that the real symmetric matrix, $\mathbf{M}$, given

by

$$\mathbf{M} = \left\langle \mathbf{S}\mathbf{S}^{\mathrm{T}} I \right\rangle , \tag{3.29}$$

must be positive definite. For situations in which this matrix is negative definite, it follows that the moment set is not consistent with any possible positive-valued distribution, I, and, hence, the moments are not physically realizable.

It is worth mentioning that the realizability constraints above yield necessary realizability conditions on the second-order angular moments. The necessary conditions on the zeroth-order angular moment can be easily derived from the fact that the underlying radiative intensity distribution must be strictly non-negative. On the other hand, for the first-order angular moments, conditions for realizability can be obtained by considering the polynomial $\mathcal{P}(\vec{s}) = 1 - \vec{s} \cdot \vec{u}$, where $\vec{u}$ is an arbitrary unit vector. It is clear that $\mathcal{P}(\vec{s})$ is non-negative and consequently $\langle ||\mathcal{P}(\vec{s})||I \rangle = I^{(0)} - I^{(1)} \cdot \vec{u} \geq 0$. Taking $\vec{u} = N^{(1)}$ then yields the conditions on the first-order angular moments. For angular moments up to second order associated with an every-where non-negative angular distribution of the radiative intensity, the necessary realizability conditions, defining the realizable space, $\mathcal{R}^{(2)}$, can then be summarized as follows [126]:

$$\begin{aligned} \mathcal{R}^{(2)} = \{ (I^{(0)}, I^{(1)}, I^{(2)}) \in \mathbb{R} \times \mathbb{R}^3 \times \mathbb{R}^{3\times 3}, \quad \text{s.t.} \quad I^{(0)} \geq 0, \quad \|N^{(1)}\| \leq 1, \\ N^{(2)} - N^{(1)}(N^{(1)})^T \geq 0, \quad tr(N^{(2)}) = 1 \quad \text{and} \quad N^{(2)}_{ij} = N^{(2)}_{ji} \} . \end{aligned} \tag{3.30}$$

The proof of the existence of a non-negative distribution reproducing moments in $\mathcal{R}^{(2)}$ also provides a proof that the conditions given in Eq. (3.30) are both necessary and sufficient. One of the key steps in the demonstration of this proof is the rotational transformation of $\mathcal{R}^{(2)}$ which places the Cartesian axes in the coordinate frame where the covariance matrix, $\left(N^{(2)} - N^{(1)}(N^{(1)})^T\right)$, is diagonal, i.e., the Cartesian axes aligned with the principal axes of the covariance matrix. Such a transformation can be summarized as follows:

$$\begin{aligned} \mathbb{T} : (I^{(0)}, I^{(1)}, I^{(2)}) \rightarrow (I'^{(0)}, I'^{(1)}, I'^{(2)}) \\ \text{s.t.} \quad (N'^{(2)} - N'^{(1)}(N'^{(1)})^T) \quad \text{is diagonal positive definite,} \end{aligned} \tag{3.31}$$

where $I'^{(i)}$, $i \in \{0, 1, 2\}$, denote the images of the angular moments, $I^{(i)}$, $i \in \{0, 1, 2\}$, under the rotational transformation which aligns the coordinate axes with the principal axes of the covariance matrix. The latter can be expressed in terms of the former via the following relationships

$$I'^{(0)} = I^{(0)}, \quad I'^{(1)}_i = R_{ji} I^{(1)}_j, \quad I'^{(2)}_{ij} = R_{pi} R_{qj} I^{(2)}_{pq}, \tag{3.32}$$

where $\mathbf{R}$ is the rotation matrix such that $\mathbf{R}^T(N^{(2)} - N^{(1)}(N^{(1)})^T)\mathbf{R}$ is diagonal positive definite.

In Eq. (3.31), the quantities, $N'^{(i)}$, $i \in \{1, 2\}$, represent normalized angular moments associated with the transformed full angular moments, $I'^{(i)}$, $i \in \{1, 2\}$. In the new coordinate frame, the transformed second-order moment tensor can be written as follows

$$N'^{(2)} = N'^{(1)}(N'^{(1)})^T + \left(1 - \|N'^{(1)}\|^2\right) \mathrm{diag}(\gamma_1, \gamma_2, \gamma_3), \tag{3.33}$$

where γ_i, $i \in \{1, 2, 3\}$, are the normalized eigenvalues of the covariance matrix, which satisfy the constraints $\gamma_i \geq 0$ and $\sum_{i=1}^{3} \gamma_i = 1$ (please refer to Appendix B.1 for further details), and where the former constraint is a consequence of the positive semi-definiteness of the covariance matrix, whereas the latter equality stems from the trace equality on the covariance matrix. The realizability conditions in the new coordinate frame can then be summarized as follows

$$\begin{aligned} \mathcal{R}_T^{(2)} = \{(I'^{(0)}, I'^{(1)}, I'^{(2)}) \in \mathbb{R} \times \mathbb{R}^3 \times \mathbb{R}^{3\times 3}, \quad \text{s.t.} \quad I'^{(0)} \geq 0, \quad \|N'^{(1)}\| \leq 1, \\ 0 \leq \gamma_i \leq 1, \quad i \in \{1, 2, 3\}, \quad \text{and} \quad \sum_{i=1}^{3} \gamma_i = 1\}. \end{aligned} \tag{3.34}$$

The transformation which aligns the Cartesian axes with the principal axes of the covariance matrix clearly allows for a more straightforward characterization of the realizable space for angular moments up to second order via a reduction in the number of independent variables from 9 to 6, in three-dimensional physical space. In fact, the set of angular moments up to second order is represented by 9 independent variables since the zeroth-order moment, $I^{(0)}$, is a scalar, the first-order moment, $I^{(1)}$, is a 3-component vector, and the second-order moment, $I^{(2)}$, is a symmetric second-order dyad or tensor with 5 unique entries.

A graphical representation of the transformed realizability domain for angular moments up to second order, $\mathcal{R}_T^{(2)}$, is shown in Fig. 3.7, for any given non-negative radiative energy density, $I'^{(0)}$. It can be clearly observed that for any given realizable first-order angular moment vector, the matrix of second-order angular moments is realizable if and only if its normalized eigenvalues lie within the equilateral triangle (P_1, P_2, P_3) in the coordinates frame $(\gamma_1, \gamma_2, \gamma_3)$. At the vertices of the latter triangle, the underlying distributions, I_{P_i}, $i \in \{1, 2, 3\}$, are uniquely determined by a combination of Dirac deltas, as demonstrated

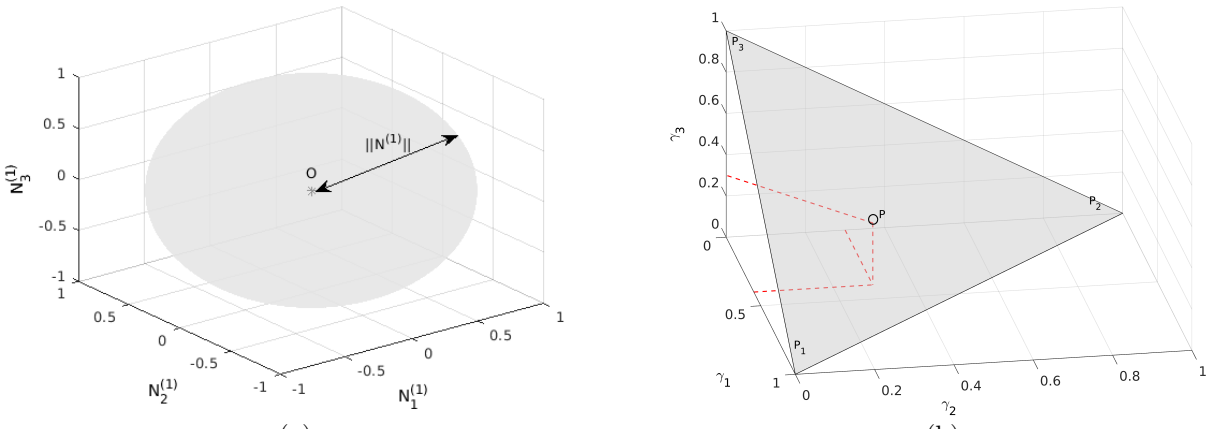

(a) (b)

Figure 3.7: Realizability domain, $\mathcal{R}_T^{(2)}$, for the M_2 closure in the frame where the covariance matrix, $\left(N^{(2)} - N^{(1)}(N^{(1)})^T\right)$, is diagonal positive definite for any given non-negative radiative energy density, $I'^{(0)}$, and (a) a fixed set of normalized eigenvalues $\{\gamma_1, \gamma_2, \gamma_3\}$; and (b) a fixed set of first-order moments $\{N_1'^{(1)}, N_2'^{(1)}, N_3'^{(1)}\}$.

in Appendix B.2, and take the form

$$I_{P_i} = I'^{(0)} \left[\rho_i^+ \delta\left(\Omega_i - x_i^+\right) + \rho_i^- \delta\left(\Omega_i - x_i^-\right)\right] \delta\left(\Omega_j - N_j'^{(1)}\right) \delta\left(\Omega_k - N_k'^{(1)}\right), \tag{3.35}$$

where $(i, j, k) \in (1, 2, 3)$ with $i \neq j \neq k$

$$x_i^{\pm} = \pm\sqrt{1 - \|N'^{(1)}\|^2 + \left(N_i'^{(1)}\right)^2}, \tag{3.36}$$

and

$$\rho_i^{\pm} = \frac{N_i'^{(1)} - x_i^{\mp}}{2x_i^{\pm}}. \tag{3.37}$$

It is a simple exercise to show that distributions of the form given in Eq. (3.35) are non-negative for any given realizable set of angular moments up to first order. The distribution at any point, P, lying inside the triangle defined by points, P_i, $i \in \{1, 2, 3\}$, can then be written as a barycentric interpolant of the distributions at P_i, denoted by I_{P_i}, and expressed as

$$I_P = \sum_{i=1}^{3} \gamma_i I_{P_i}. \tag{3.38}$$

It is clear that the distribution given in Eq. (3.38) is non-negative since it corresponds to a convex combination of non-negative distributions, I_{P_i}, $i \in \{1, 2, 3\}$. In order to complete

the proof of sufficiency, it must be shown that the distribution given by Eq. (3.38) also reproduces moments lying inside the realizable space, $\mathcal{R}_T^{(2)}$ (see Appendix B.3). The distributions I_{P_i}, $i \in \{1,2,3\}$, reproduce moments at the vertices of the triangle (P_1, P_2, P_3), and, as such, any convex combination of these three distributions will therefore reproduce moments lying within the triangle and consequently within $\mathcal{R}_T^{(2)}$. This completes the proof of moment realizability.

It is worth pointing out that the distribution of Eq. (3.38) is similar to the one given by Kershaw [126] in the multi-dimensional case and also reduces to his results in the one-dimensional case, i.e., for $N_2'^{(1)} = 0$ and $N_3'^{(1)} = 0$. More specifically, in the case where $N_{11}'^{(2)} = 1$, i.e., $\gamma_1 = 1$, Eq. (3.38) reduces to

$$I_P = I'^{(0)} \left[\frac{1 + N_1'^{(1)}}{2} \delta(\Omega_1 - 1) + \frac{1 - N_1'^{(1)}}{2} \delta(\Omega_1 + 1) \right] \delta(\Omega_2)\delta(\Omega_3), \tag{3.39}$$

and for $N_{11}'^{(2)} = (N_1'^{(1)})^2$, i.e., $\gamma_1 = 0$, one obtains

$$I_P = I'^{(0)} \left[\rho_i^+ \delta(\Omega_i - x_i) + \rho_i^- \delta(\Omega_i + x_i) \right] \delta(\Omega_j - N_j'^{(1)}) \delta(\Omega_k - N_k'^{(1)}). \tag{3.40}$$

Armed with the necessary and sufficient realizability conditions for moments up to second order, we can now proceed with the development of interpolative-based approximations of the M_2 closure for radiative heat transfer in both gray and non-gray participating media.

3.4.2 Interpolative-Based Second-Order Maximum-Entropy M_2 Moment Closures

The interpolation procedure proposed herein for the approximation of the third-order closing fluxes arising from the gray and non-gray M_2 closures is inspired from the approach used to prove sufficiency of the realizability conditions for moments up to order two. More specifically, the third-order closing fluxes are approximated within $\mathcal{R}_T^{(2)}$ via affine combinations of their known closed-form analytical expressions at the vertices, P_i, $i \in \{1,2,3\}$. These expressions, the derivations of which are presented in Appendix B.2, are summarized in Table 3.2.

The interpolative-based approximations of the third-order closing fluxes for the M_2 closure proposed herein are expressed in the frame where the covariance matrix is diagonal,

Table 3.2: Closed-Form Analytic Expressions of M_2 Closing Relations at the Vertices of the Triangle (P_1, P_2, P_3).

Vertex	$N'^{(3)}_{111}$	$N'^{(3)}_{122}$	$N'^{(3)}_{123}$
P_1	$N'^{(1)}_1\left[(N'^{(1)}_1)^2+\left(1-\|N'^{(1)}\|^2\right)\right]$	$N'^{(1)}_1\left(N'^{(1)}_2\right)^2$	$N'^{(1)}_1 N'^{(1)}_2 N'^{(1)}_3$
P_2	$\left(N'^{(1)}_1\right)^3$	$N'^{(1)}_1\left[(N'^{(1)}_2)^2+\left(1-\|N'^{(1)}\|^2\right)\right]$	$N'^{(1)}_1 N'^{(1)}_2 N'^{(1)}_3$
P_3	$\left(N'^{(1)}_1\right)^3$	$N'^{(1)}_1\left(N'^{(1)}_2\right)^2$	$N'^{(1)}_1 N'^{(1)}_2 N'^{(1)}_3$

the latter being characterized by the realizable space, $\mathcal{R}^{(2)}_T$. Following the interpolation procedure, the third-order closing fluxes in the original coordinate frame, characterized by $\mathcal{R}^{(2)}$, may be obtained via the inverse of the following transformation

$$I'^{(3)}_{ijk} = R_{li}R_{mj}R_{nk}I^{(3)}_{lmn}. \tag{3.41}$$

It is worth pointing out that the third-order normalized moment tensor, $N'^{(3)}$, is also symmetric and therefore has just 10 unique, independent entries, in three-dimensional physical space. Furthermore, knowledge of just 3 of these entries, namely $N'^{(3)}_{111}$, $N'^{(3)}_{122}$ and $N'^{(3)}_{123}$, is sufficient to obtain expressions for the remaining 7 independent entries, $N'^{(3)}_{ijk} = N'^{(3)}_{ijk}(I'^{(0)\star}_\eta, N'^{(1)}_1, N'^{(1)}_2, N'^{(1)}_3, \gamma_1, \gamma_2)$, which, in the context of non-gray radiation, can be related to these 3 entries as follows:

$$\begin{aligned}
N'^{(3)}_{222} &= N'^{(3)}_{111}(I'^{(0)\star}_\eta, N'^{(1)}_2, -N'^{(1)}_1, N'^{(1)}_3, \gamma_2, \gamma_1),\\
N'^{(3)}_{333} &= N'^{(3)}_{111}(I'^{(0)\star}_\eta, N'^{(1)}_3, N'^{(1)}_2, -N'^{(1)}_1, \gamma_3, \gamma_2),\\
N'^{(3)}_{112} &= N'^{(3)}_{122}(I'^{(0)\star}_\eta, N'^{(1)}_2, -N'^{(1)}_1, N'^{(1)}_3, \gamma_2, \gamma_1),\\
N'^{(3)}_{113} &= N'^{(3)}_{122}(I'^{(0)\star}_\eta, N'^{(1)}_3, N'^{(1)}_1, N'^{(1)}_2, \gamma_3, \gamma_1),\\
N'^{(3)}_{133} &= N'^{(3)}_{122}(I'^{(0)\star}_\eta, N'^{(1)}_1, N'^{(1)}_3, -N'^{(1)}_2, \gamma_1, \gamma_3),\\
N'^{(3)}_{223} &= N'^{(3)}_{122}(I'^{(0)\star}_\eta, N'^{(1)}_3, N'^{(1)}_2, -N'^{(1)}_1, \gamma_3, \gamma_2),\\
N'^{(3)}_{233} &= N'^{(3)}_{122}(I'^{(0)\star}_\eta, N'^{(1)}_2, N'^{(1)}_3, N'^{(1)}_1, \gamma_2, \gamma_3).
\end{aligned} \tag{3.42}$$

For gray radiative transfer, the same relationships as those given in Eq. (3.42) hold, except for the fact that the third-order closing fluxes no longer depend on the radiative energy density, $I'^{(0)\star}_\eta$.

It is also worth mentioning that the optimization problem for entropy maximization given by Eqs. (3.6) and (3.8) for non-gray radiation cannot be solved directly on the boundaries of the realizability domain, $\mathcal{R}^{(2)}_T$, denoted here as $\partial\mathcal{R}^{(2)}_T$. On these boundaries, some of

Table 3.3: Form of the entropy maximizing distribution for non-gray radiation on the boundaries of the realizable space for angular moments up to second-order.

Regime	**Form of the Distribution**
$\|N'^{(1)}\| = 1$	$I_\eta = I_\eta^{(0)}\delta(\vec{\Omega} - N^{(1)})$
$\gamma_i = 0$ or $\gamma_i = 1$	see [130]
$I_\eta'^{(0)} \to 0$	$\mathcal{I}_\eta(\boldsymbol{\alpha},\, \mathbf{m}) = 2hc\eta^3 \exp\left(-\frac{c^2 h\eta}{k}\boldsymbol{\alpha}^T\mathbf{m}(\vec{s})\right)$
$I_\eta'^{(0)} \to +\infty$	$\mathcal{I}_\eta(\boldsymbol{\alpha},\, \mathbf{m}) = \frac{2k\eta^2}{c}\left[\boldsymbol{\alpha}^T\mathbf{m}(\vec{s})\right]^{-1}$
$\widetilde{\mathcal{R}}_T^{(2)}$	$\mathcal{I}_\eta(\boldsymbol{\alpha},\, \mathbf{m}) = 2hc\eta^3\left[\exp\left(\frac{c^2 h\eta}{k}\boldsymbol{\alpha}^T\mathbf{m}(\vec{s})\right) - 1\right]^{-1}$

the inequalities defining the realizable space, $\mathcal{R}_T^{(2)}$, become sharp, i.e.,

$$\partial\mathcal{R}_T^{(2)} = \{(I_\eta'^{(0)}, I_\eta'^{(1)}, I_\eta'^{(2)}) \in \mathbb{R}\times\mathbb{R}^3\times\mathbb{R}^{3\times 3} \quad \text{s.t.} \quad I_\eta'^{(0)} \to 0 \quad \text{or} \quad I_\eta'^{(0)} \to +\infty \\ \text{or} \quad ||N'^{(1)}|| = 1, \quad \text{or} \quad \gamma_i = 0 \quad \text{or} \quad \gamma_i = 1, \quad i \in \{1,2,3\}\}. \tag{3.43}$$

In fact, on $\partial\mathcal{R}_T^{(2)}$, the entropy maximizing distribution of Eq. (3.5) becomes singular due to the fact that propagation of radiation is then only allowed along specific directions, instead of spanning the full solid angle. More specifically, the entropy maximizing distribution is either uniquely determined by a single Dirac-delta distribution (for $\|N^{(1)}\| = 1$), a combination of Dirac-delta distributions (for $\gamma_i = 1, \quad i \in \{1,2,3\}$, see [130]), or takes a particular form, as in the case of the limit where $I_\eta'^{(0)} \to 0$ or $I_\eta'^{(0)} \to +\infty$, also known as the hyperbolic and the logarithmic limits [125], respectively. In the case where only one eigenvalue vanishes, i.e., $\gamma_i = 0, \quad i \in \{1,2,3\}$, the distribution still has the form given in Eq. (3.5) for the entropy maximizing distribution, but is only defined over a circle instead of the full solid angle, as it becomes singular with respect to one of the direction cosines of the vector, $\vec{s}$, characterizing the direction of propagation of the radiation. The expressions for the entropy maximizing distribution associated with each of the aforementioned limits, are summarized in Table 3.3, where $\widetilde{\mathcal{R}}_T^{(2)}$ denotes the interior of the realizable space, $\mathcal{R}_T^{(2)}$.

The finding discussed above in the context of non-gray radiation also hold for gray radiative transfer. In particular, the entropy optimization problem for gray radiation given in Eqs. (3.12) and (3.13) cannot be readily solved on the boundaries, $\partial\mathcal{R}_T^{(2)}$, of $\mathcal{R}_T^{(2)}$, to the exception of the hyperbolic and the logarithmic limits. On such boundaries, the entropy

Table 3.4: Form of the entropy maximizing distribution for gray radiation on the boundaries of the realizable space for angular moments up to second-order.

Regime	**Form of the Distribution**
$\|N'^{(1)}\| = 1$	$I = I^{(0)}\delta(\vec{\Omega} - N^{(1)})$
$\gamma_i = 0$ or $\gamma_i = 1$	see [130]
$\widetilde{\mathcal{R}}_T^{(2)}$	$\mathcal{I}(\boldsymbol{\alpha},\, \mathbf{m}) = \frac{\sigma_{stef}}{\pi}\left[\boldsymbol{\alpha}^T\mathbf{m}(\vec{s}\,)\right]^{-4}$

maximizing distribution of Eq. (3.10) no longer spans the full solid angle, but is rather defined on a subset of the latter, since propagation of radiation is then only allowed along specific directions. However, unlike the case of non-gray radiation, the form of the entropy maximizing distribution for gray radiation remains unchanged in either the hyperbolic or the logarithmic limits. Table 3.4 presents a summary of the expressions for the gray entropy maximizing distribution of Eq. (3.10) associated with the various limits.

Based on the above, numerical maximum-entropy solutions for the third-order closing fluxes throughout the full realizable space, $\mathcal{R}_T^{(2)} = \widetilde{\mathcal{R}}_T^{(2)} \cup \partial\mathcal{R}_T^{(2)}$, can then be obtained by solving the optimization problem for entropy maximization using the appropriate form of the distribution for any given set of moments up to second order. The third-order closing fluxes at any point within $\mathcal{R}_T^{(2)}$ are then approximated by writing the entries, $N'^{(3)}_{uvw} = N'^{(3)}_{uvw}(I'^{(0)\star}_\eta, N'^{(1)}_1, N'^{(1)}_2, N'^{(1)}_3, \gamma_1, \gamma_2)$, $\{uvw\} = \{\{1,1,1\},\{1,2,2\},\{1,2,3\}\}$, as affine interpolants between their known closed-form expressions at the vertices of the triangle (P_1, P_2, P_3) (see Table 3.2) as follows:

$$N'^{(3)}_{111} = N'^{(1)}_1\left[\left(N'^{(1)}_1\right)^2 + f_{N'^{(3)}_{111}}\left(1 - \|N'^{(1)}\|^2\right)\right], \tag{3.44}$$

$$N'^{(3)}_{122} = N'^{(1)}_1\left[\left(N'^{(1)}_2\right)^2 + f_{N'^{(3)}_{122}}\left(1 - \|N'^{(1)}\|^2\right)\right], \tag{3.45}$$

and

$$N'^{(3)}_{123} = f_{N'^{(3)}_{123}} N'^{(1)}_1 N'^{(1)}_2 N'^{(1)}_3, \tag{3.46}$$

where $f_{N'^{(3)}_{uvw}} = f_{N'^{(3)}_{uvw}}(I'^{(0)\star}_\eta, N'^{(1)}_1, N'^{(1)}_2, N'^{(1)}_3, \gamma_1, \gamma_2)$, $\{uvw\} = \{\{1,1,1\},\{1,2,2\},\{1,2,3\}\}$, are polynomial expressions defined such that the proposed approximations of the third-order closing fluxes exactly match the known closed-form expressions at the vertices of the triangle, (P_1, P_2, P_3), and takes the forms

$$f_{N'^{(3)}_{111}} = \gamma_1\left[1 + (1-\gamma_1)g_{N'^{(3)}_{111}}\right], \tag{3.47}$$

$$f_{N'^{(3)}_{122}} = \gamma_2 \left[1 + (1-\gamma_2) g_{N'^{(3)}_{122}}\right], \tag{3.48}$$

and

$$f_{N'^{(3)}_{123}} = 1 + \gamma_1\gamma_2\gamma_3 g_{N'^{(3)}_{123}}, \tag{3.49}$$

and where $g_{N'^{(3)}_{uvw}} = g_{N'^{(3)}_{uvw}}(I'^{(0)\star}_{\eta}, N'^{(1)}_1, N'^{(1)}_2, N'^{(1)}_3, \gamma_1, \gamma_2)$,
$\{uvw\} = \{\{1,1,1\},\{1,2,2\},\{1,2,3\}\}$, are polynomial expressions which are chosen such that numerical solutions of the optimization problem for entropy maximization, for the third-order closing fluxes, are accurately reproduced for any given set of angular moments up to second order in $\mathcal{R}^{(2)}_T$. The choices of the forms of the polynomial expressions, $g_{N'^{(3)}_{uvw}}$, for the purpose of our interpolation procedure, are discussed in the sections to follow, for both gray and non-gray radiation, in that order.

It is worthwhile defining the polar and azimuthal angles characterizing the direction of the normalized first-order angular moment vector, $N'^{(1)}$, in a spherical coordinate system, denoted by θ and ϕ respectively, as follows

$$\theta = \arccos\left(\frac{N'^{(1)}_1}{\|N'^{(1)}\|}\right), \quad \phi = \arccos\left(\frac{N'^{(1)}_2}{\sqrt{(N'^{(1)}_2)^2 + (N'^{(1)}_3)^2}}\right). \tag{3.50}$$

For the interpolation of maximum-entropy solutions over the realizable space for the first-order moment vector, which spans the unit ball, spherical coordinates represent a rather natural and more suitable choice over Cartesian coordinates. In fact, performing the interpolation over the unit ball, spanned by the first-order moment vector, with respect to the latter coordinate system would require a mapping of the unit ball into more conventional geometries for Cartesian coordinate frames, in particular cubic shapes.

3.4.3 Polynomial Interpolation Procedure for Gray M_2 Moment Closure

For gray-gas radiation, we aim to write the weighting functions, $g_{N'^{(3)}_{uvw}}$,
$\{uvw\} = \{\{1,1,1\},\{1,2,2\},\{1,2,3\}\}$, as truncated series expansions in terms of orthogonal polynomials as follows

$$g_{N'^{(3)}_{uvw}} = \sum_{j=0}^{n_j}\sum_{k=0}^{n_k}\sum_{l=0}^{k}\sum_{p=0}^{n_p}\sum_{q=0}^{n_p-p} C^{N'^{(3)}_{uvw}}_{jklpq} T_{2j}(\|N'^{(1)}\|) Y^{2l}_{2k}(\theta,\phi) P_{pq}(\gamma_1,\gamma_2), \tag{3.51}$$

where T_n represent Chebyshev polynomials of the first kind of degree n, Y_k^l are spherical harmonic functions of degree k and order l, and P_{pq} correspond to Proriol polynomials of order, $p+q$. The coefficients, $C_{jklpq}^{N'^{(3)}_{uvw}}$, $j = 0, 1, \ldots, n_j$, $k = 0, 1, \ldots, n_k$, $l = 0, 1, \ldots, k$, $p = 0, 1, \ldots, n_p$, $q = 0, 1, \ldots, n_p - p$, appearing in Eq. (3.51), and defining the vector of coefficients, $\mathbf{C}^{N'^{(3)}_{uvw}}$, are determined via the solution of the Vandermonde system arising from the enforcement of the latter equation at several, suitably chosen, interpolation nodes spanning $\mathcal{R}_T^{(2)}$. In the present study, the interpolation points for $\|N'^{(1)}\|$ are chosen to coincide with extrema of Chebyshev polynomials of the first kind of order $2n_j$, including the endpoints. On the other hand, for the eigenvalues of the covariance matrix, a distribution similar to the one proposed by Blyth and Pozrikidis [132] for the interpolation over the standard triangle is employed, which yields

$$\gamma_{1,i} = \frac{1}{3}(1 + 2v_i - v_j - v_k), \quad \gamma_{2,j} = \frac{1}{3}(1 + 2v_j - v_i - v_k), \tag{3.52}$$

where $i = 1, 2, \ldots, n_p + 1$, $j = 1, 2, \ldots, n_p + 2 - i$, and $k = n_p + 3 - i - j$, and where v_m, $m = 1, 2, \ldots, n_p + 1$, are chosen to coincide with extrema of the shifted Chebyshev polynomial of the first kind of order n_p, also including the endpoints. The interpolation nodes for the polar angle θ were chosen such that $\cos\theta$ coincides with roots of the Legendre polynomials of order $(2n_k + 1)$, whereas, for the azimuthal angle, ϕ, a set of $4n_k$ points uniformly distributed on the unit circle were selected as the interpolation points.

The choice of extrema of Chebyshev polynomials of the first kind, including the endpoints, also known as Chebyshev-Gauss-Lobatto points, for the purpose of interpolating over the domain spanned by the norm of the first-order normalized moment vector, $\|N'^{(1)}\|$, as well as over the triangle (P_1, P_2, P_3), allows for the derivatives of the third-order closing fluxes to be accurately reproduced in the isotropic ($\|N^{(1)}\| = 0$) and free-streaming ($\|N^{(1)}\| = 1$) limits, as well as on the boundaries (edges) of the triangle (P_1, P_2, P_3), which correspond to situations where at least one of the eigenvalues of the covariance matrix vanishes. This feature is quite desirable as it ensures that our interpolative-based approximations of the third-order closing fluxes accurately capture the rates of change of the original maximum entropy solutions in such limits, and, consequently, Runge-type oscillations of the interpolated solutions as such limits are approached, which can yield both realizability and hyperbolicity issues, are minimized. However, computations of the numerical values for $g_{N'^{(3)}_{111}}$, $g_{N'^{(3)}_{122}}$, and $g_{N'^{(3)}_{123}}$ from the maximum entropy solutions, using Eqs. (3.44) and (3.47) for $N'^{(3)}_{111}$, Eqs. (3.45) and (3.48) for $N'^{(3)}_{122}$, or Eqs. (3.46) and (3.49) for $N'^{(3)}_{123}$, respectively, for the purpose of solving the Vandermonde system for the vector

of coefficients, $\mathbf{C}^{N'^{(3)}_{111}}$, $\mathbf{C}^{N'^{(3)}_{122}}$, and $\mathbf{C}^{N'^{(3)}_{123}}$, from Eq. (3.51), though straightforward for distributions away from the isotropic and free-streaming limits, as well as distributions away from the edges of the triangle described by the eigenvalues of the covariance matrix, result in undetermined expressions in these limits. In this study, l'Hopital's rule is used to provide computable expressions for $g_{N'^{(3)}_{111}}$, $g_{N'^{(3)}_{122}}$, and $g_{N'^{(3)}_{123}}$ in such limits, the derivation of which is presented in Appendix C of the thesis.

The weighting functions, $g_{N'^{(3)}_{uvw}}$, $\{uvw\} = \{\{1,1,1\},\{1,2,2\},\{1,2,3\}\}$, are chosen such that $n_j = n_p = 4$ and $n_k = 2$, as this choice was observed to yield a good balance between accuracy and efficiency for the proposed polynomial interpolation procedure. To assess the accuracy of the proposed interpolative-based approximations of the third-order closing fluxes, $N'^{(3)}_{111}$, $N'^{(3)}_{122}$, and $N'^{(3)}_{123}$, for the M_2 closure for gray radiation, predicted values of these closing fluxes are compared to numerical solutions of the optimization problem for entropy maximization for sets of angular moments up to second order spanning the full realizable space, $\mathcal{R}^{(2)}_T$. More specifically, a set of 20 values of $\|N'^{(1)}\|$ uniformly distributed in $[0,\ 1]$, 40 values of ϕ equally distributed in $[0,\ 2\pi]$, 20 values of θ evenly distributed in $[0,\ \pi]$, as well as $20(20+1)/2 = 210$ sets of $(\gamma_1, \gamma_2, \gamma_3)$ equally distributed within the triangle $(P_1,\ P_2,\ P_3)$ (see Fig. 3.7) were considered for the assessment of the accuracy of the proposed interpolation procedure for the third-order closing fluxes. The errors in the L^∞-norm sense was 1.811×10^{-2} for $N'^{(3)}_{111}$, 2.6113×10^{-2} for $N'^{(3)}_{122}$, and 7.54×10^{-3} for $N'^{(3)}_{123}$. The interpolated third-order closing fluxes and the errors associated with the corresponding interpolation procedure are illustrated graphically in Figs. 3.8 and 3.9 for moment $N'^{(3)}_{111}$ and Figs. 3.10 and 3.11 for moment $N'^{(3)}_{122}$, respectively. These figures show the aforementioned quantities with respect to both the norm of the first-order normalized moment, $\|N'^{(1)}\|$, and the eigenvalues of the covariance matrix, γ_1 and γ_2.

It should be pointed out that the polynomial interpolation procedure proposed in the present study, for the third-order closing fluxes of the gray M_2 closure, involves several improvements, in terms of both efficiency and accuracy, compared to the approach adopted in the recent paper by Sarr and Groth [130]. First, instead of the rectangle-triangle mapping adopted by Sarr and Groth [130], in conjunction with a product of Chebyshev polynomials, the procedure adopted in this thesis makes use of Proriol polynomials for the interpolation over the triangle, $(P_1,\ P_2,\ P_3)$. Proriol polynomials form a complete set of orthogonal basis polynomials on the standard triangle, and result in a well-conditioned Vandermonde matrix when used in conjunction with the nodal distribu-

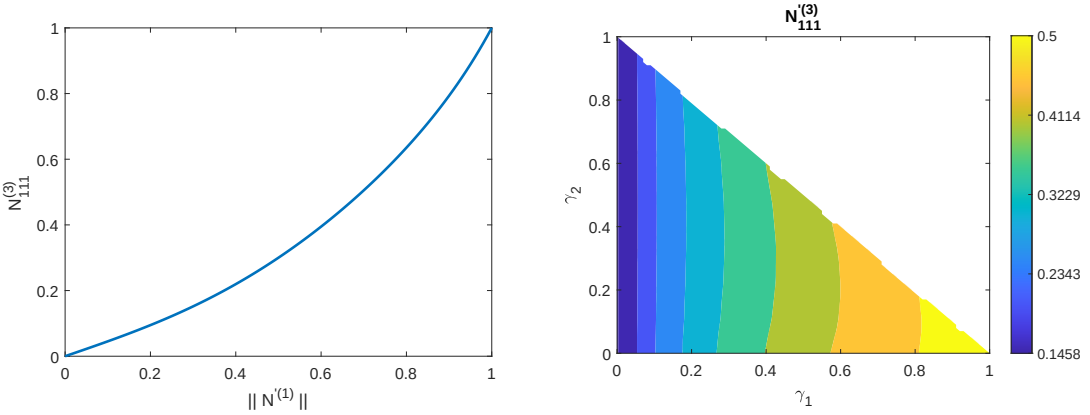

(a) $\gamma_1 = 0.2222$, $\gamma_2 = 0.5556$ (b) $\|N'^{(1)}\| = 0.5263$

Figure 3.8: Interpolated third-order closing flux, $N'^{(3)}_{111}$, with respect to (a) the norm of the first-order normalized moment, $\|N'^{(1)}\|$, and (b) the eigenvalues of the covariance matrix, γ_1 and γ_2.

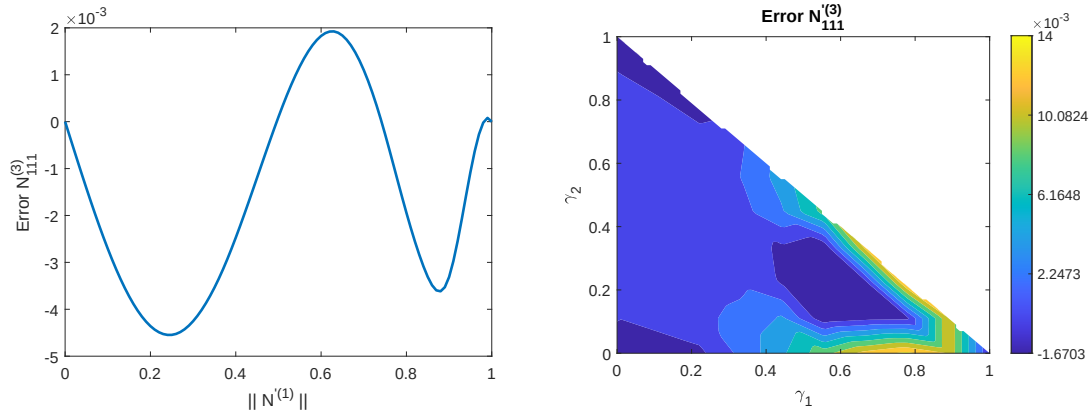

(a) $\gamma_1 = 0.2222$, $\gamma_2 = 0.5556$ (b) $\|N'^{(1)}\| = 0.5263$

Figure 3.9: Interpolation error for the third-order closing flux, $N'^{(3)}_{111}$, with respect to (a) the norm of the first-order normalized moment, $\|N'^{(1)}\|$, and (b) the eigenvalues of the covariance matrix, γ_1 and γ_2.

tion given in Eq. (3.52), for the interpolation over the triangle, (P_1, P_2, P_3). Moreover, the latter nodal distribution, i.e., that of Eq. (3.52), provides a better distribution of interpolation nodes over the triangle, compared to the rectangle-triangle mapping approach employed by Sarr and Groth [130], which unnecessarily and undesirably clusters the interpolation points near one of the vertices or edges of the triangle. As for the

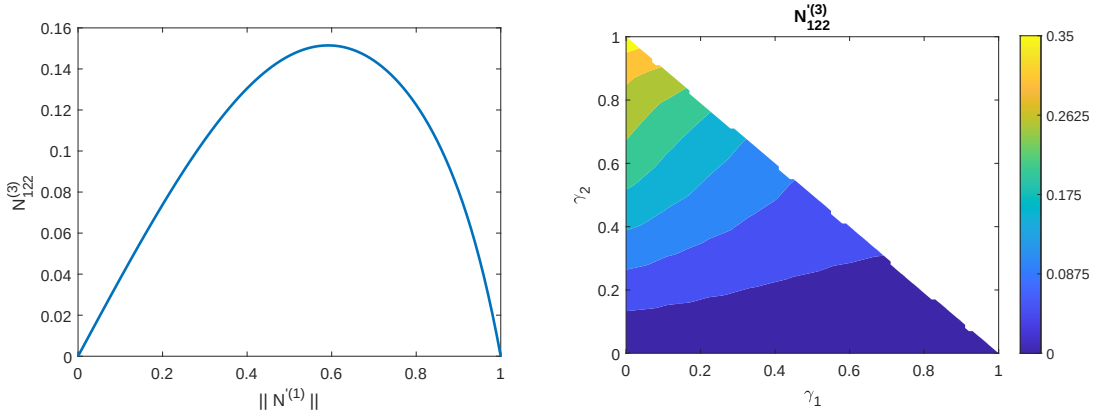

(a) $\gamma_1 = 0.2222$, $\gamma_2 = 0.5556$ (b) $\|N'^{(1)}\| = 0.5263$

Figure 3.10: Interpolated third-order closing flux, $N'^{(3)}_{122}$, with respect to (a) the norm of the first-order normalized moment, $\|N'^{(1)}\|$, and (b) the eigenvalues of the covariance matrix, γ_1 and γ_2.

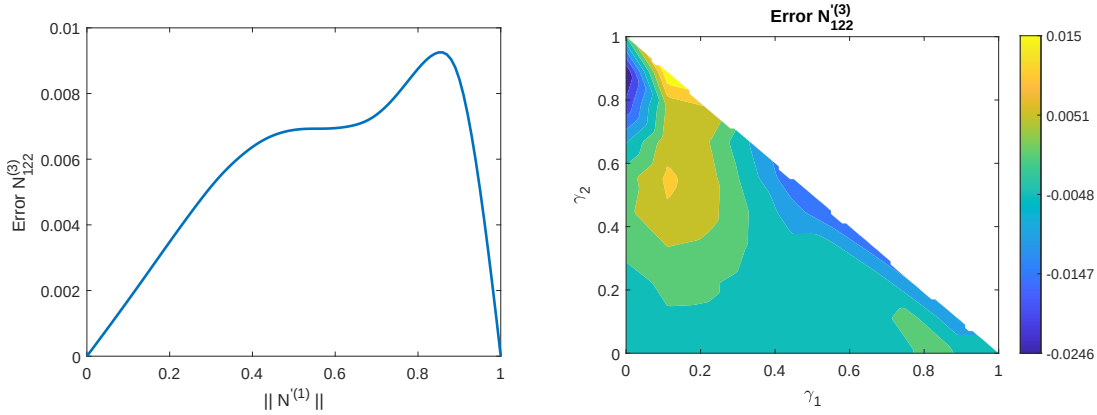

(a) $\gamma_1 = 0.2222$, $\gamma_2 = 0.5556$ (b) $\|N'^{(1)}\| = 0.5263$

Figure 3.11: Interpolation error for the third-order closing flux, $N'^{(3)}_{122}$, with respect to (a) the norm of the first-order normalized moment, $\|N'^{(1)}\|$, and (b) the eigenvalues of the covariance matrix, γ_1 and γ_2.

spherical harmonic expansion in terms of the polar and azimuthal angles describing the direction of the vector of first-order moments, a careful analysis of the evenness of the third-order closing fluxes revealed that only the spherical harmonic functions of even degree or order need to be retained for the interpolations, instead of including all the terms in the expansion, as was done in the previous study [130]. The adoption of these

modifications yields a reduction in the total number of coefficients for the interpolations by at least a factor of a half.

The aforementioned improvements, despite resulting in a more efficient interpolative procedure for the third-order closing fluxes of the M_2 closure, still yield a relatively computationally expensive closure in comparisons to its lower-order counterpart, the gray M_1 closure, described in Section 3.3.1, as well as the P_1 and P_3 spherical harmonic moment closures. In fact, the set of orthogonal polynomial bases, used for the interpolation of maximum entropy solutions, for the third-order closing fluxes, over the full realizable space for moments up to second order, while very convenient for accurately computing the coefficients associated with the proposed polynomial approximations of Eq. (3.51), would involve repeated computations of factorial expressions, among others, if implemented directly as written here when computing the approximations to the entries of $N'^{(3)}$. Further substantial computational savings can be achieved by reformulating the polynomial expressions, $g_{N'^{(3)}_{uvw}}$, for $\{uvw\} = \{\{1,1,1\},\{1,2,2\},\{1,2,3\}\}$, in terms of monomials with respect to the independent variables, and recomputing the coefficients, $\mathbf{C}^{N'^{(3)}_{111}}$, $\mathbf{C}^{N'^{(3)}_{122}}$, and $\mathbf{C}^{N'^{(3)}_{123}}$, in a monomial basis once the interpolation procedure has been carried out. The resulting polynomial expressions, can then be evaluated very efficiently by means of the well known Horner scheme [127, 128].

3.4.4 Polynomial Interpolation Procedure for Non-Gray M_2 Moment Closure

As discussed earlier in Section 3.4, the closing relations for the non-gray M_2 closure involve the additional dependencies on the radiative energy density and wavenumber when compared to the M_2 closure for gray radiation. Inspired by this knowledge, the approximate forms of the weighting functions, $g_{N'^{(3)}_{uvw}}$, for $\{uvw\} = \{\{1,1,1\},\{1,2,2\},\{1,2,3\}\}$ in the context of non-gray radiation are constructed herein via extension of the polynomial interpolant given in Eq. (3.51) for gray radiative transfer, such that the spectral and energy density dependencies are also accounted for. More specifically, the weighting functions, $g_{N'^{(3)}_{uvw}}$, are expressed as truncated series expansions in terms of orthogonal

polynomials as follows

$$g_{N'^{(3)}_{uvw}} = \sum_{i=0}^{n_i}\sum_{j=0}^{n_j}\sum_{k=0}^{n_k}\sum_{l=0}^{k}\sum_{p=0}^{n_p}\sum_{q=0}^{n_p-p} C^{N'^{(3)}_{uvw}}_{ijklpq} T_i\left(\mathcal{M}_{I'^{(0)\star}_{\eta}}\right) T_{2j}(\|N'^{(1)}\|) Y^{2l}_{2k}(\theta,\phi) P_{pq}(\gamma_1,\gamma_2), \tag{3.53}$$

with $n_i = n_j = n_p = 4$ and $n_k = 2$, where again T_n are Chebyshev polynomials of the first kind of degree n, Y^l_k are spherical harmonic functions of degree k and order l, and P_{pq} represent Proriol polynomials of order, $p+q$. Furthermore, $\mathcal{M}_{I'^{(0)\star}_{\eta}}$ represents an exponential mapping of the radiative energy density, similar to the procedure adopted for the interpolative non-gray M_1 closure as given in Eq. (3.23), of the form:

$$\begin{aligned} \mathcal{M}_{I'^{(0)\star}_{\eta}} \quad &: \quad [0,\ +\infty] \rightarrow [-1,\ 1], \\ & \qquad I'^{(0)\star}_{\eta} \rightarrow 1 - 2\exp\left(-\frac{I'^{(0)\star}_{\eta}}{L_{N'^{(3)}}}\right), \end{aligned} \tag{3.54}$$

where $L_{N'^{(3)}}$ is the length scale of the mapping, $\mathcal{M}_{I'^{(0)\star}_{\eta}}$, the distribution of which is chosen such that the accuracy of our interpolative-based approximations of the third-order closing fluxes, with respect to numerical maximum-entropy solutions, is optimized, for sets of angular moments up to second order spanning $\mathcal{R}^{(2)}_T$ and over the full spectrum of frequencies. As for the M_1 closure, the choice of the form of the mapping length scale is also dictated by some of the desirable properties of the original non-gray M_2 closure, in particular hyperbolicity of the resulting closed system of moment equations. An in-depth description of the procedure adopted in the present study for determining the optimal distribution of $L_{N'^{(3)}}$ is presented below.

The coefficients, $C^{N'^{(3)}_{uvw}}_{ijklpq}$, $i = 0, 1, \ldots, n_i$, $j = 0, 1, \ldots, n_j$, $k = 0, 1, \ldots, n_k$, $l = 0, 1, \ldots, k$, $p = 0, 1, \ldots, n_p$, $q = 0, 1, \ldots, n_p - p$, appearing in Eq. (3.53), and making up the vector of coefficients, $\mathbf{C}^{N'^{(3)}_{uvw}}$, are determined via the solution of the Vandermonde system arising from the enforcement of the latter equation at several, suitably chosen, interpolation nodes spanning $\mathcal{R}^{(2)}_T$. For the interpolation of the third-order closing fluxes arising from the non-gray M_2 closure over the unit ball spanned by the first-order moment vector, as well as over the equilateral triangle describing the realizable space for the eigenvalues of the covariance matrix, nodal distributions similar to those adopted for the interpolative-based gray M_2 closure are employed herein. More specifically, the interpolation within the unit ball is carried out by considering extrema of Chebyshev polynomials of the first kind of order $2n_j$ (including the endpoints) for $\|N'^{(1)}\|$, roots of the Legendre polynomials of order $(2n_k + 1)$ for the cosine of the polar angle, i.e., $\cos\theta$, and $4n_k$ points evenly

distributed on the unit circle for the azimuthal angle, ϕ. Moreover, for the interpolation procedure over the standard triangle spanned by the eigenvalues of the covariance matrix, a nodal distribution similar to the one proposed by Blyth and Pozrikidis [132] and given in Eq. (3.52) is adopted. Finally, the interpolation over the full spectrum of frequencies as well as over the realizable energy levels, which was not of concern in the context of the gray M_2 closure, is carried out by choosing $\mathcal{M}_{I_\eta'^{(0)\star}}$ to coincide with extrema of Chebyshev polynomials of the first kind of order n_i, including the endpoints. Similar to the interpolative procedure adopted for its gray counterpart, the choice of Chebyshev-Gauss-Lobatto-based nodal distributions for the interpolation of the non-gray M_2 closing fluxes with respect to the norm of the first-order normalized moment vector, $\|N'^{(1)}\|$, as well as over the triangle (P_1, P_2, P_3), minimizes the risk of oscillations near the realizable boundaries and consequently helps with realizability and hyperbolicity of the resulting interpolative-based closure. The solution of the Vandermonde systems arising from Eq. (3.53), for the determination of the vectors of coefficients, $\mathbf{C}^{N_{111}'^{(3)}}$, $\mathbf{C}^{N_{122}'^{(3)}}$, and $\mathbf{C}^{N_{123}'^{(3)}}$, requires computations of the weighting functions, $g_{N_{111}'^{(3)}}$, $g_{N_{122}'^{(3)}}$, and $g_{N_{123}'^{(3)}}$, at the selected interpolation points, from the solutions of the maximum entropy problem of Eqs. (3.6) and (3.8). Such computations can be carried out in a rather straightforward manner for distributions away from the isotropic and free-streaming limits, as well as distributions away from the edges of the triangle described by the eigenvalues of the covariance matrix. In fact, for distributions away from such limits, $g_{N_{111}'^{(3)}}$, $g_{N_{122}'^{(3)}}$, and $g_{N_{123}'^{(3)}}$ can be directly computed using Eqs. (3.44) and (3.47) for $N_{111}'^{(3)}$, Eqs. (3.45) and (3.48) for $N_{122}'^{(3)}$, or Eqs. (3.46) and (3.49) for $N_{123}'^{(3)}$, respectively. However, for distributions associated with the aforementioned limits, the latter procedure cannot be readily used to compute the weighting functions, $g_{N_{111}'^{(3)}}$, $g_{N_{122}'^{(3)}}$, and $g_{N_{123}'^{(3)}}$, as it would result in undetermined expressions. In this study, l'Hopital's rule is again used to provide computable expressions for $g_{N_{111}'^{(3)}}$, $g_{N_{122}'^{(3)}}$, and $g_{N_{123}'^{(3)}}$ in such limits, similar to the gray M_2 closure, and the corresponding procedure is summarized in Appendix C.

In the present study, the form of the length scale, $L_{N'^{(3)}}$, of the exponential mapping given in Eq. (3.54) is inspired from the expression proposed and given in Eq. (3.24) in the case of the non-gray M_1 closure, and can be seen as an extension of the latter to the case of known angular moments up to second order. More specifically, the length scale,

$L_{N'^{(3)}} = L_{N'^{(3)}}(N_1'^{(1)}, N_2'^{(1)}, N_3'^{(1)}, \gamma_1, \gamma_2)$, is written in the following form

$$L_{N'^{(3)}} = \exp\left[\sum_{j=0}^{n_j}\sum_{k=0}^{n_k}\sum_{l=0}^{k}\sum_{p=0}^{n_p}\sum_{q=0}^{n_p-p} C_{jklpq}^{L_{N'^{(3)}}} T_{2j}(\|N'^{(1)}\|) Y_{2k}^{2l}(\theta,\phi) P_{pq}(\gamma_1,\gamma_2)\right], \tag{3.55}$$

where $C_{jklpq}^{L_{N'^{(3)}}}$, $j = 0, 1, \ldots, n_j$, $k = 0, 1, \ldots, n_k$, $l = 0, 1, \ldots, k$, $p = 0, 1, \ldots, n_p$, $q = 0, 1, \ldots, n_p - p$, are the coefficients of our proposed interpolative-based approximation of the mapping length scale, $L_{N'^{(3)}}$, and make up the vector of coefficients, $\mathbf{C}^{L_{N'^{(3)}}}$. The latter coefficients are chosen such that the proposed interpolative-based approximations of the third-order closing fluxes accurately mimic the corresponding numerical solutions of the entropy optimization problem over the full realizable space for angular moments up to second order, $\mathcal{R}_T^{(2)}$, as well as over the full spectrum of frequencies. In the context of the interpolative non-gray M_1 closure proposed in Section 3.3.2, the determination of the coefficients for the length scale of the exponential mapping was only concerned with the Eddington factor. In fact, since the latter is the only unknown in the second-order closing fluxes of the M_1 closure, it therefore follows that an accurate approximation of the Eddington factor would directly translate into an accurate approximation of the second-order closing fluxes. On the other hand, the interpolation procedure for the non-gray M_2 closure is rendered more complicated, when compared to its lower-order counterpart, due to the fact that the tensor of third-order closing fluxes cannot be parameterized with respect to a single unknown. Instead, 3 entries, i.e., $N_{111}'^{(3)}$, $N_{122}'^{(3)}$, and $N_{123}'^{(3)}$, must be approximated simultaneously, which, in conjunction with considerations of symmetry (see Eq. (3.42)), yield an approximation for all the entries making up the tensor of third-order angular moments. In order to account for each of these 3 entries in the determination of the optimal distribution of the length scale, $L_{N'^{(3)}}$, a multi-objective least-squares optimization problem is advocated, which consists of minimizing a weighted sum of the L^2 errors of the interpolative-based approximations of the third-order closing fluxes, $N_{111}'^{(3)}$, $N_{122}'^{(3)}$, and $N_{123}'^{(3)}$, and can be summarized by the following expressions

$$\begin{gathered}\min_{\mathbf{C}^{L_{N'^{(3)}}}} \{\text{error}_{g_{N'^{(3)}}}\}, \\ \text{error}_{g_{N'^{(3)}}} = w_{N_{111}'^{(3)}}.\text{err}_{g_{N_{111}'^{(3)}}} + w_{N_{122}'^{(3)}}.\text{err}_{g_{N_{122}'^{(3)}}} + w_{N_{123}'^{(3)}}.\text{err}_{g_{N_{123}'^{(3)}}},\end{gathered} \tag{3.56}$$

where the weights, $w_{N_{111}'^{(3)}} = 0.4$, $w_{N_{122}'^{(3)}} = 0.3$, and $w_{N_{123}'^{(3)}} = 0.3$, respectively express the relative importance of each of the third-order closing fluxes, $N_{111}'^{(3)}$, $N_{122}'^{(3)}$, and $N_{123}'^{(3)}$, in the determination of the coefficients of the length scale of the exponential mapping of the

radiative energy density. In Eq. (3.56), $\text{err}_{g_{N'^{(3)}_{uvw}}}$ represents the error of the interpolative-based approximation of the weighting function, $g_{N'^{(3)}_{uvw}}$, of Eq. (3.53) associated with the third-order closing flux, $N'^{(3)}_{uvw}$, with respect to numerical solutions of the maximum entropy problem of Eqs. (3.6) and (3.8), and is evaluated as follows

$$\text{err}_{g_{N'^{(3)}_{uvw}}} = \sum_{i=1}^{N_i}\sum_{j=1}^{N_j}\sum_{k=1}^{2N_k}\sum_{l=1}^{N_k}\sum_{p=1}^{N_p}\sum_{q=1}^{N_p-p}\sum_{r=1}^{N_r} w_i w_j w_k w_l w_{pq} w_r \left(g^{ijklpqr}_{N'^{(3)}_{uvw},\text{fit}} - g^{ijklpqr}_{N'^{(3)}_{uvw},\text{numerical}}\right)^2. \tag{3.57}$$

In Eq. (3.57), $g^{ijklpqr}_{N'^{(3)}_{uvw},\text{numerical}}$ represents values of the weighting function, $g_{N'^{(3)}_{uvw}}$, and are computed from the solutions of the entropy optimization problem of Eqs. (3.6) and (3.8), for a given set of test points spanning the full realizable space for angular moments up to second order, $\mathcal{R}^{(2)}_T$, as well as the full spectrum of frequencies. The weighting functions are computed from the maximum entropy solutions for the third-order closing fluxes using Eqs. (3.44) and (3.47) for $g_{N'^{(3)}_{111}}$, Eqs. (3.45) and (3.48) for $g_{N'^{(3)}_{122}}$, or Eqs. (3.46) and (3.49) for $g_{N'^{(3)}_{123}}$. In situations where undetermined expressions are encountered using the above procedure, as is the case in the isotropic and free-streaming limits, as well as along the edges of the triangle (P_1, P_2, P_3), the procedure described in Appendix C of the thesis may be used to compute the weighting functions, $g_{N'^{(3)}_{111}}$, $g_{N'^{(3)}_{122}}$, and $g_{N'^{(3)}_{123}}$. Furthermore, $g^{ijklpqr}_{N'^{(3)}_{uvw},\text{fit}}$ corresponds to values of the weighting function, $g_{N'^{(3)}_{uvw}}$, computed via evaluation of the proposed polynomial approximation, Eq. (3.53), at the test points.

The error given in Eq. (3.57) is computed using a set of $N = 2N_iN_j(N_k)^2N_{pq}N_r = 6.72\times 10^9$ evaluation points. The latter consist of $N_i = 20$ values of $\mathcal{M}_{I'^{(0)\star}_\eta}$ following a Gauss-Lobatto-Chebyshev distribution in $[-1,\ 1]$, with associated weights, w_i, $i = 1, 2, \ldots, N_i$, $N_j = 20$ values of $\|N'^{(1)}\|$ associated with non-negative Gauss-Lobatto-Chebyshev points in $[-1,\ 1]$, with weighting w_j, $j = 1, 2, \ldots, N_j$, and $N_r = 100$ values of $L_{N'^{(3)}}$ based on roots of Laguerre polynomials with weighting w_r, $r = 1, 2, \ldots, N_r$. Moreover, $N_k = 20$ values of θ and 40 values of ϕ (see Eq. (3.50)) uniformly distributed in $[0,\ \pi]$ and $[0,\ 2\pi]$, respectively, with weights, w_l, $l = 1, 2, \ldots, N_k$, and w_k, $k = 1, 2, \ldots, 2N_k$, were also used in the solution of the least-squares problem, in addition to $N_{pq} = N_p(N_p + 1)/2 = 210$ points (with $N_p = 20$) following the distribution given in Eq. (3.52), with associated weights, w_{pq}, $p = 1, 2, \ldots, N_p$, $q = 1, 2, \ldots, N_p - p$, for the eigenvalues of the covariance matrix.

At each iteration of the nonlinear least-squares problem defined by Eq. (3.56), the iter-

ate, $\mathbf{C}^{L_{N'(3)}}$, can be used, in conjunction with Eq. (3.55) as well as the inverse of the exponential mapping of Eq. (3.54), to compute values of $I_\eta'^{(0)\star}$ associated with the chosen interpolation nodes for $\mathcal{M}_{I_\eta'^{(0)\star}}$, and consequently solve the corresponding dual maximum-entropy problem at each of the interpolation points. The vectors of coefficients, $\mathbf{C}^{N'^{(3)}_{111}}$, $\mathbf{C}^{N'^{(3)}_{122}}$, and $\mathbf{C}^{N'^{(3)}_{123}}$ (see Eq. (3.53)), are then obtained via solution of the associated Vandermonde systems, and the resulting polynomial expressions of Eq. (3.53) are then used to compute the quantities, $g_{N'^{(3)}_{111},\text{fit}}$, $g_{N'^{(3)}_{122},\text{fit}}$, and $g_{N'^{(3)}_{123},\text{fit}}$, at the evaluation points.

Two equally important properties to consider for the purpose of our interpolation procedure, in addition to accuracy with respect to numerical maximum-entropy solutions for the third-order closing fluxes, are realizability and hyperbolicity of the interpolative-based non-gray M_2 closure, throughout the full realizable space for angular moments up to second order, in multiple space dimensions, as well as over the full spectrum of frequencies. Unfortunately, unlike the case for the non-gray M_1 closure, identification and proof of the necessary and sufficient conditions for realizability of angular moments up to third order in multi-dimensional physical space are not available theoretically to date, and, as such, realizability of the third-order closing fluxes is not considered in the proposed interpolation procedure. On the other hand, hyperbolicity of the proposed non-gray M_2 closure is sought by enforcing, at each step of the multi-objective least-squares optimization problem of Eq. (3.56), appropriate constraints on the eigenvalues of the flux Jacobian of the resulting closed system of equations, as discussed in Section 5.1.3 of Chapter 5 to follow.

Following the interpolation procedure outlined above for the third-order closing fluxes of the non-gray M_2 closure, leading to the determination of the coefficients, $\mathbf{C}^{N'^{(3)}_{111}}$, $\mathbf{C}^{N'^{(3)}_{122}}$, $\mathbf{C}^{N'^{(3)}_{123}}$, and $\mathbf{C}^{L_{N'(3)}}$ of Eqs. (3.53) and (3.55), respectively, a procedure similar to the one described in Section 3.4.3 can be adopted in order to improve efficiency. In particular, once the interpolative procedure has been carried out, substantial computational savings can be achieved by reformulating the polynomial expressions for $g_{N'^{(3)}_{111}}$, $g_{N'^{(3)}_{122}}$, and $g_{N'^{(3)}_{123}}$, as well as for $L_{N'(3)}$, in terms of monomials with respect to the independent variables, and recomputing the coefficients in the monomial bases. The resulting polynomial interpolants, can then again be evaluated very efficiently by means of the well known Horner scheme [127, 128].

Chapter 4

Spectral Radiation Models

The RTE, as given in Eq. (2.9) of Chapter 2, represents the transport of radiation for a single wavenumber. Moreover, the numerical approaches described in the previous two chapters have focused on coping with the angular/directional dependence of the radiative intensity distribution, for a given wavenumber. In reactive flows however, the radiative properties of participating real-gas mixtures, in particular the absorption coefficient, vary strongly throughout the spectrum. A comprehensive and realistic radiation model must therefore account for these non-gray effects through the use of real-gas spectral properties and accurate approximations for the optical characteristics of soot. From the computational point of view, incorporation of non-gray effects involves solution of the RTE of Eq. (2.9) for different values of the absorption coefficient over the full spectrum of frequencies followed by integration over the spectrum to obtain the quantities of interest such as the divergence of the total radiant heat flux given in Eq. (2.13).

In the present study, real-gas radiation over the full spectrum of frequencies is accounted for using the SNBCK technique [31, 71] whereas the optical properties of soot are estimated by means of Rayleigh theory for small particles. This chapter provides a description of the background theory for the SNBCK spectral radiation technique along with its incorporation with the DOM, P_1, and P_3 radiation models, as well as with the newly-developed interpolative-based non-gray M_1 and M_2 closures.

4.1 Statistical Narrow-Band Correlated-k Model

In the SNBCK model [31,71], the spectral domain is divided into bands of frequencies of size $\Delta\eta$. The width of the bands is chosen to be sufficiently small such that the Planck function, $I_{b\eta}$, can be assumed to be constant within each band. A cumulative distribution function for the absorption coefficient is then introduced, which allows the reordering of the strongly spectrally varying absorption coefficient into a monotonic function, such that the number of evaluations of the RTE, required for accurate integration over each narrow-band, is substantially reduced in comparison to straightforward LBL methods.

For illustration purposes, the absorption coefficient of CO_2 across a small portion of its 4.3 µm band is shown in Fig. 4.1(a). Over such a narrow spectral interval, the Planck function is essentially constant, while the absorption coefficient varies rather strongly, attaining the same value several times. Since every identical value for absorption coefficient produces identical solutions for the RTE in the case of a constant Planck function, substantial computational savings, compared to LBL calculations, can indeed be achieved by re-ordering the absorption coefficient into a monotonically increasing function. This re-ordering concept was first reported about five decades ago by Arking and Grossman [133] but has received significant attention in the heat transfer community only in the last three decades [90,134,135]. The re-ordering introduces a distribution function, $f(k)$, such that $f(k)dk$ represents the fraction of the spectrum between η and $\eta + \Delta\eta$ where the absorption coefficient lies between k and $k + dk$. The distribution function, $f(k)$, is directly computed from the absorption coefficient spectrum as a weighted sum of the number of points where $\kappa_\eta = k$ [23]. As can be seen in Fig. 4.1(b) however, the distribution function, $f(k)$, is ill-behaved and would still require a large number of quadrature points for the accurate integration of the absorption coefficient over the narrow band. To alleviate this issue, a cumulative distribution function, $g(k)$, is introduced, of the form

$$g(k) = \int_0^k f(k')dk'. \tag{4.1}$$

The cumulative distribution function, $g(k)$, for the absorption coefficient can be interpreted as a dimensionless wavenumber coordinate. It is a monotonically increasing function varying between 0 and 1, and represents the fraction of the spectrum where $\kappa_\eta \leq k$. Figure 4.1(c) illustrates the cumulative distribution function associated with the absorption band of CO_2 shown in Fig.4.1(a). It is evident that $g(k)$ is much better behaved

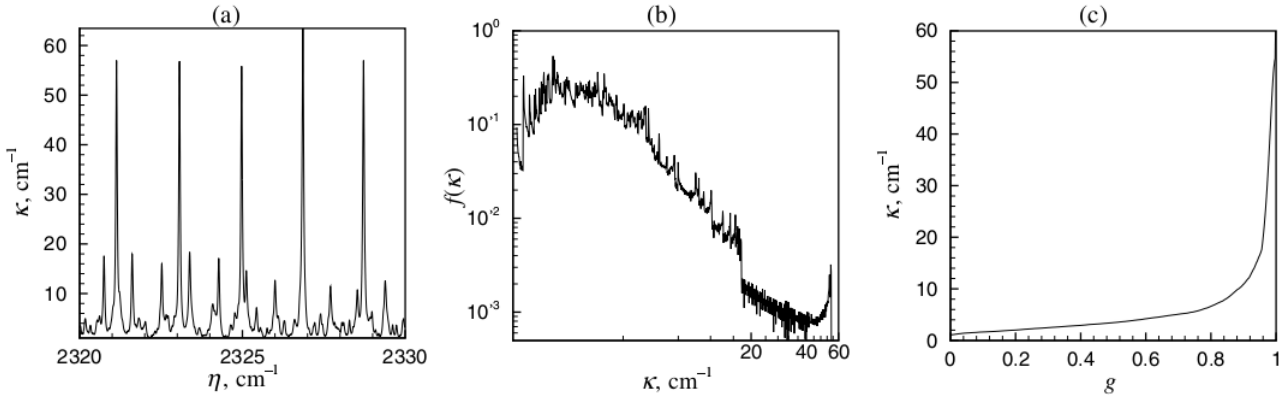

Figure 4.1: (a) Absorption coefficient for the 4.3 µm CO_2 band at $T = 1000K$ and $p = 1$ bar; (b) The PDF of the absorption coefficient for the 4.3 µm CO2 band; (c) The k-distribution of absorption coefficient for the 4.3 µm CO_2 band [1]

than $f(k)$ and should be expected to require substantially fewer quadrature points for the accurate spectral integration over the narrow band.

Using the reordering concepts presented above, the RTE of Eq. (2.9), integrated over each narrow band, under the assumption of a non-scattering medium, yields

$$\int_0^1 \frac{1}{c}\frac{\partial I_g}{\partial t}dg + \int_0^1 \vec{s}.\vec{\nabla} I_g dg = \int_0^1 k(g)(I_{b\eta_c} - I_g)dg, \tag{4.2}$$

where

$$I_g = \frac{\int_{\Delta\eta} I_\eta \delta(k - \kappa_\eta)d\eta}{\int_{\Delta\eta} \delta(k - \kappa_\eta)d\eta}, \tag{4.3}$$

and where $I_{b\eta_c}$ is the Planck function evaluated at the wavenumber corresponding to the band centre, denoted herein by η_c. The integration over each narrow band is performed by means of numerical quadrature, such that the spectrally integrated intensity for each band can be computed as

$$\overline{I_{\Delta\eta}} = \sum_{i=1}^{N_g} w_i I(g_i), \tag{4.4}$$

where N_g is the number of quadrature points, g_i, $i = 0, 1, \ldots, N_g$, correspond to the abscissas of the quadrature scheme and w_i are the associated quadrature weights. Based on the findings of Liu *et al.* [31], a four-point Gauss-Legendre quadrature was observed to provide good balance between accuracy and computational costs and is therefore used in the present study. The divergence of the total radiative heat flux, also referred to as

the radiative source term, is then evaluated as

$$S_R = \nabla \cdot \vec{q}_{\text{rad}} \approx \sum_{j=1}^{N_b} \sum_{i=1}^{N_g} w_i \kappa(g_i) \left[4\pi I_{b\eta_{cj}} - \langle I(g_i) \rangle \right] \Delta\eta_j, \tag{4.5}$$

where N_b is the number of narrow bands, $\Delta\eta_j$ is the width of the j^{th} narrow band, and $\langle I(g_i) \rangle$ represents the angular integral, more specifically the zeroth-order moment defined in Eq. (2.16), of the intensity distribution obtained by solving the RTE at quadrature point g_i.

While the CK method outlined above computes numerically the distribution function, $f(k)$, using line-by-line data for the absorption coefficient from databases like HITRAN [136], the SNBCK method employs a more efficient alternative whereby the distribution function is computed analytically using SNB parameters. More specifically, assuming the participating gas follows the Malkmus model [137], a closed-form analytical expression for the k-distribution function can be obtained by taking the inverse Laplace transformation of the statistical narrow-band transmissivity [71]

$$f(k) = \mathcal{L}^{-1}\{\overline{\tau_{\Delta\eta}}\} = \frac{1}{2} k^{-3/2} (BS)^{1/2} \exp\left[\frac{\pi B}{4} \left(2 - \frac{S}{k} - \frac{k}{S} \right) \right], \tag{4.6}$$

where $\mathcal{L}^{-1}$ is the inverse Laplace transform, $\overline{\Delta\eta}$ is the narrow-band averaged transmissivity, B is the effective line half-width, and S represents the effective line strength. Using the form of the k-distribution function given in Eq. (4.6) and substituting the latter in Eq. (4.1) yields the following form for the cumulative distribution function

$$g(k) = \frac{1}{2} \text{erfc}\left(\frac{a}{\sqrt{k}} - b\sqrt{k} \right) + \frac{1}{2} \text{erfc}\left(\frac{a}{\sqrt{k}} + b\sqrt{k} \right) \exp\left(\pi B \right), \tag{4.7}$$

where $\text{erfc}(x)$ is the complementary error function, $a = \frac{1}{2}\sqrt{\pi BS}$ and $b = \frac{1}{2}\sqrt{\pi B/S}$. The band model parameters, B and S, are generated from the narrow-band dataset of Soufiani and Taine [138]). This dataset accounts for gas-band radiation from water vapour (H_2O), carbon dioxide (CO_2) and carbon monoxide (CO) only, and consists of 367 uniformly-spaced bands between $150\,\text{cm}^{-1}$ to $9300\,\text{cm}^{-1}$ with a bandwidth of $25\,\text{cm}^{-1}$. For any given value, g_i, of the cumulative distribution function at a given quadrature point, a Newton-Raphson procedure is used to invert Eq. (4.7) and compute the corresponding value for the absorption coefficient, $k_i = k(g_i)$. Solutions of the RTE are then obtained at each quadrature point of the SNBCK approach.

The SNBCK is exact for homogeneous media for which it can achieve the same accuracy as line-by-line calculations while significantly reducing the required number of spectral evaluations. For non-homogeneous media on the other hand, some assumptions about the k-distribution functions have to be made since both $f(k)$ and $g(k)$ vary with position, and, as such, there is no way to uniquely invert the cumulative distribution function $g(k)$ to obtain $k(g)$. Two commonly used methods for addressing non-homogeneity are the scaling approximation and the assumption of a correlated k-distribution [139], the latter being the foundation of the SNBCK method. The scaling approximation is based on the assumption that the spectral and spatial dependencies of the absorption coefficient are separable. The correlated-k assumption, on the other hand, operates under the basis that the cumulative distribution function, $g(k)$, at any given location maps to the same value of $g(k)$ at another location, but with a different value of k. The correlated-k assumption has been shown to be very accurate in meteorological applications, characterized by large pressure variations and only moderate temperature changes. However, the assumption of a correlated absorption coefficient breaks down in the presence of strong temperature gradients [140, 141], as encountered in high-temperature combustion applications. The scaling approximation can produce superior results in such cases, owing to the fact that the scaling function can be optimized for the problem at hand.

In order to achieve further computational savings, the three radiating gases are approximated by a single gas with effective narrow-band parameters based on the optically thin limit [33]. In addition, the band lumping procedure described by Liu *et al.* [32] is also adopted, whereby several bands are combined to form wide bands. A total of nine non-uniformly spaced wide bands are employed herein based on the recommendation of Goutiere *et al.* [142].

4.2 Soot Radiation

For the purposes of radiation transport, soot particulates are generally assumed to be small spherical particles and their optical properties are estimated by means of Rayleigh's scattering approximation. The latter is a particular case of Mie scattering theory [143] and is valid for spherical particles that are small in comparison with the wavelength of the incident radiation. In most combustion applications however, soot particles typically

have diameters smaller than 50 nm while being irradiated by light with a wavelength of approximately 3 µm [84]. Scattering from soot is usually neglected due their typically small sizes [2].

Under the assumption of a constant index of refraction over the spectrum of frequencies and based on the above, the spectral absorption coefficient of soot following from the Rayleigh limit of Mie theory can be written as follows

$$\kappa_{\eta,\text{soot}} = C f_v \eta, \tag{4.8}$$

where f_v is the soot volume fraction and C is an empirical constant, which is taken to have the value of 5.5 as suggested by Liu *et al.* [78].

The definition of soot spectral absorption coefficient given above in Eq. (4.8) yields a difference of only about 6% for the mean absorption coefficients in the optically-thin and optically-thick limits. As such, based on the work of Felske and Tien [144], the following average is used as an approximation of the absorption coefficient of soot for all optical regimes:

$$\kappa_{\text{soot}} = 3.72\, C f_v T / C_2 \tag{4.9}$$

where $C_2 = 1.4388\,\text{cm K}$ is the second Planck function constant.

It is worth mentioning that the above derivation is only valid for very small soot particles and results in an underestimation of the extinction coefficient for aggregates or for particles with sizes exceeding the limits of applicability of Rayleigh scattering theory.

4.3 Mixture Spectral Absorption Coefficient

As mentioned above, soot is treated in the present study as a gray absorber while the gas absorption coefficient is allowed to vary over the whole spectrum. The spectral absorption coefficient for the gas-soot mixture is given by

$$\kappa_{\eta,\text{mix}} = \kappa_{\text{soot}} + \kappa_{\eta,\text{g}} \tag{4.10}$$

where $\kappa_{\eta,\text{g}}$ and $\kappa_{\eta,\text{mix}}$ are the spectral absorption coefficients for the gas and mixture, respectively.

4.4 Implementation of M_N Closures with Narrow-Band Correlated-k Model

Using either the DOM or P_N moment closures, an estimate of the radiative energy density, $\langle I(g_i)\rangle$, at each of the quadrature points, g_i, for use in Eq. (4.5), can be easily obtained. However, for the proposed interpolative-based non-gray M_1 and M_2 closures, coupling with the SNBCK presents additional challenges due to the explicit wavenumber dependencies of the resulting closing relations. Nevertheless, closer inspection of the entropy maximizing distribution of Eq. (3.5) reveals that it has the same form as the Planck function given by

$$I_{b\eta}(T) = 2hc\eta^3 \left[\exp\left(\frac{hc\eta}{kT}\right) - 1\right]^{-1}. \tag{4.11}$$

It can be observed that the Planck function and the entropy maximizing distribution, for a given finite set of angular moments, only differ by the expressions in the respective exponential terms. More specifically, for any given wavenumber, the Planck function can be thought of as an isotropic distribution of the radiative intensity, while the entropy maximizing distribution allows departures from the equilibrium or isotropic distribution via the Lagrange multipliers. This suggests that, for the same energy density (zeroth-order moment), the entropy maximizing distribution has similar profiles compared to the blackbody intensity over the full spectrum of frequencies, except that the former is shifted relative to the latter in frequency space. As such, similar to how the Planck function is assumed to be essentially constant within a narrow-band band, it would seem reasonable to make the same assumption for the entropy maximizing distribution and consequently evaluate the spectrally dependent closing relations for the non-gray M_N closures at the wavenumber corresponding to the band centre. Such a procedure is adopted in the present study.

Chapter 5

Finite-Volume Numerical Solution Method

Similar to the P_1 and P_3 moment closures, as well as the M_1 closure for gray radiation, the proposed interpolative-based first-order M_1 (for non-gray radiation) and second-order M_2 (for gray and non-gray radiation) maximum-entropy moment closures are expected to be strictly hyperbolic in the sense of Lax [145], as will be explored later in this chapter. In the original definition, quasi-linear inhomogeneous PDEs are said to be strictly hyperbolic if the eigenvalues associated with the eigensystem of the coefficient matrices and flux Jacobians are all real and distinct. A slightly less restrictive demand for strict hyperbolicity is that the eigenvalues are all real (i.e., repeated eigenvalues are permitted) and that the corresponding right eigenvectors form a complete and linearly independent set such that the coefficient matrices and flux Jacobians are diagonalizable. Levermore [146] has shown that the maximum-entropy closures applied to the Boltzmann equations of gas kinetic theory with the Boltzmann entropy result in moment equations that are symmetric hyperbolic systems and strictly hyperbolic. Dubroca and Feugeas [49] also showed that the systems of angular moment equations arising from the Bose-Einstein maximum-entropy-based closures for radiative transfer are hyperbolic.

The quasi-linear hyperbolic PDEs of the type governing the system of angular moments for the M_1 and M_2 closures are very well suited to solution by the now standard family of upwind finite-volume spatial discretization techniques originally developed by Godunov [24] for hyperbolic systems of conservation laws. In this study, numerical solutions of the

system of moment equations arising from the M_1, M_2, P_1 and P_3 closures, in the cases of either gray or non-gray radiation, are all obtained using a parallel, implicit, upwind Godunov-type finite-volume scheme with block-based anisotropic AMR. The proposed scheme is similar to those previously described by Groth and co-workers [25–30] for systems of partial differential equations, where the moment equations are integrated over quadrilateral cells of a two-dimensional body-fitted, multi-block mesh.

In what follows, the main elements of the proposed upwind finite-volume scheme used to provide numerical solutions to the governing moment equations arising from the various closure techniques are presented. In particular, a brief summary of the weak conservation form of the moment equations is given in Section 5.1, in addition to the description of the eigenstructure and demonstration of hyperbolicity of the closed systems of moment equations arising from the moment closures under consideration in the present study. In the context of the proposed interpolative-based M_1 and M_2 closures, hyperbolicity is explored by numerical means, but not proven. Following the latter, the key elements of the finite-volume spatial discretization scheme as well as the details related to the evaluation of the hyperbolic numerical fluxes are presented in Section 5.2. Boundary conditions prescriptions for the angular moment equations are then discussed in Section 5.3. In Section 5.4, the incorporation of the finite-volume scheme within a parallel block-based anisotropic adaptive mesh refinement (AMR) is discussed. Finally, the solution of the resulting semi-discrete form of the conservation equations via a parallel implicit Newton-Krylov iterative technique is described in Section 5.5.

5.1 Weak Conservation Form of Moment Equations

The finite-volume scheme used for numerically solving the governing moment equations arising from the M_1, M_2, P_1 and P_3 closure techniques, for both gray and non-gray participating media, considers the solution of the weak conservation form of the moment equations on two-dimensional, body-fitted, multi-block, quadrilateral meshes. The weak conservation form of the transport equations, for angular moments up to third order, for a two-dimensional Cartesian coordinate system can be obtained by taking appropriate angular moments of the underlying RTE. In the context of non-gray radiation, the form of the RTE given in Eq. (2.9) is employed, which, in conjunction with the SNBCK treatment

of the spectral absorption coefficient, yields the following weak conservation form

$$\frac{\partial \mathbf{U}}{\partial t} + \frac{\partial \mathbf{F}}{\partial x} + \frac{\partial \mathbf{G}}{\partial y} = \mathbf{S}\,, \tag{5.1}$$

where $\mathbf{U}$ is the vector of conserved moments, $\mathbf{F}$ and $\mathbf{G}$ are the flux vectors in the x- and y-coordinate directions, respectively, and $\mathbf{S}$ represents the source term vector.

For the M_1 and P_1 closures, for which angular moments up to only first order are solved for, $\mathbf{U}$, $\mathbf{F}$ and $\mathbf{G}$ are respectively given by

$$\begin{aligned} \mathbf{U} &= \left[\; I_g^{(0)}, I_{g,1}^{(1)}, I_{g,2}^{(1)} \;\right]^T, \\ \mathbf{F} &= c\left[\; I_{g,1}^{(1)}, I_{g,11}^{(2)}, I_{g,12}^{(2)} \;\right]^T, \\ \mathbf{G} &= c\left[\; I_{g,2}^{(1)}, I_{g,12}^{(2)}, I_{g,22}^{(2)} \;\right]^T. \end{aligned} \tag{5.2}$$

The unknown second-order closing fluxes can be related to the known lower-order moments using the closure relations of Eq. (2.20) for P_1 or Eqs. (3.14), (3.17), and (3.20)–(3.24) for M_1. Furthermore, under the assumption of isotropic scattering, the source term column vector for the system of angular moment equations arising from either the M_1 or the P_1 closures, $\mathbf{S}$, is given by

$$\mathbf{S} = c\begin{bmatrix} k(g)(4\pi I_{b\eta_c} - I_g^{(0)}) \\ -(k(g)+\sigma_s)I_{g,1}^{(1)} \\ -(k(g)+\sigma_s)I_{g,2}^{(1)} \end{bmatrix}. \tag{5.3}$$

In the context of the M_2 closure, which involves the solution of angular moments up to second order, $\mathbf{U}$, $\mathbf{F}$ and $\mathbf{G}$ are respectively given by

$$\begin{aligned} \mathbf{U} &= \left[\; I_g^{(0)}, I_{g,1}^{(1)}, I_{g,2}^{(1)}, I_{g,11}^{(2)}, I_{g,12}^{(2)}, I_{g,22}^{(2)} \;\right]^T, \\ \mathbf{F} &= c\left[\; I_{g,1}^{(1)}, I_{g,11}^{(2)}, I_{g,12}^{(2)}, I_{g,111}^{(3)}, I_{g,112}^{(3)}, I_{g,122}^{(3)} \;\right]^T, \\ \mathbf{G} &= c\left[\; I_{g,2}^{(1)}, I_{g,12}^{(2)}, I_{g,22}^{(2)}, I_{g,211}^{(3)}, I_{g,212}^{(3)}, I_{g,222}^{(3)} \;\right]^T. \end{aligned} \tag{5.4}$$

In the context of the proposed interpolative-based non-gray M_2 closure, the unknown third-order closing fluxes are expressed in terms of the lower-order moments via the expressions given in Eqs. (3.41), (3.42), (3.44)–(3.50), and (3.53)–(3.55). Under the assumption of isotropic scattering, the source term vector associated with the resulting

system of angular moments up to second order takes the form

$$\mathbf{S} = c \begin{bmatrix} k(g)(4\pi I_{b\eta_c} - I_g^{(0)}) \\ -(k(g)+\sigma_s) I_{g,1}^{(1)} \\ -(k(g)+\sigma_s) I_{g,2}^{(1)} \\ \frac{1}{3}(4\pi k(g) I_{b\eta_c} + \sigma_s I_g^{(0)}) - (k(g)+\sigma_s) I_{g,11}^{(2)} \\ -(k(g)+\sigma_s) I_{g,12}^{(2)} \\ \frac{1}{3}(4\pi k(g) I_{b\eta_c} + \sigma_s I_g^{(0)}) - (k(g)+\sigma_s) I_{g,22}^{(2)} \end{bmatrix}. \tag{5.5}$$

Finally, the P_3 closure results in a system of angular moment equations whose unknowns consist of angular moments up to third order, and for which the vectors $\mathbf{U}$, $\mathbf{F}$ and $\mathbf{G}$ are respectively given by

$$\begin{aligned} \mathbf{U} &= \left[\; I_g^{(0)}, I_{g,1}^{(1)}, I_{g,2}^{(1)}, I_{g,11}^{(2)}, I_{g,12}^{(2)}, I_{g,22}^{(2)}, I_{g,111}^{(3)}, I_{g,112}^{(3)}, I_{g,122}^{(3)}, I_{g,222}^{(3)} \; \right]^T, \\ \mathbf{F} &= c \left[\; I_{g,1}^{(1)}, I_{g,11}^{(2)}, I_{g,12}^{(2)}, I_{g,111}^{(3)}, I_{g,112}^{(3)}, I_{g,122}^{(3)}, I_{g,1111}^{(4)}, I_{g,1112}^{(4)}, I_{g,1122}^{(4)}, I_{g,1222}^{(4)} \; \right]^T, \\ \mathbf{G} &= c \left[\; I_{g,2}^{(1)}, I_{g,12}^{(2)}, I_{g,22}^{(2)}, I_{g,211}^{(3)}, I_{g,212}^{(3)}, I_{g,222}^{(3)}, I_{g,2111}^{(4)}, I_{g,2112}^{(4)}, I_{g,2122}^{(4)}, I_{g,2222}^{(4)} \; \right]^T, \end{aligned} \tag{5.6}$$

and the corresponding source term vector, $\mathbf{S}$, based on the assumption of isotropic scattering, takes the form

$$\mathbf{S} = c \begin{bmatrix} k(g)(4\pi I_{b\eta_c} - I_g^{(0)}) \\ -(k(g)+\sigma_s) I_{g,1}^{(1)} \\ -(k(g)+\sigma_s) I_{g,2}^{(1)} \\ \frac{1}{3}(4\pi k(g) I_{b\eta_c} + \sigma_s I_g^{(0)}) - (k(g)+\sigma_s) I_{g,11}^{(2)} \\ -(k(g)+\sigma_s) I_{g,12}^{(2)} \\ \frac{1}{3}(4\pi k(g) I_{b\eta_c} + \sigma_s I_g^{(0)}) - (k(g)+\sigma_s) I_{g,22}^{(2)} \\ -(k(g)+\sigma_s) I_{g,111}^{(3)} \\ -(k(g)+\sigma_s) I_{g,112}^{(3)} \\ -(k(g)+\sigma_s) I_{g,122}^{(3)} \\ -(k(g)+\sigma_s) I_{g,222}^{(3)} \end{bmatrix}. \tag{5.7}$$

The unknown fourth-order closing fluxes are expressed in terms of known lower-order moments via the relationships given in Eq. (2.21), thereby resulting in the P_3 closure.

It is worth mentioning that the subscript, g, indicates a reordered quantity, from frequency space to the domain defined by the cumulative distribution function, g, and the following definition holds

$$I_g^{(n)}(\vec{x}, t) = \langle \vec{s}^{\,n} I_g(\vec{x}, \vec{s}, t) \rangle, \tag{5.8}$$

where the reordered intensity distribution, I_g, is defined in Eq. (4.3). The corresponding normalized angular moments in the reordered space are computed in a similar way as in Eq. (2.17), except that the wavenumber subscript is replaced by a subscript based on the cumulative distribution function, g.

In the context of gray radiation, taking appropriate angular moments of the form of the RTE given in Eq. (2.14) yields a system of moment equations the weak conservation form of which can be written in a similar way as for non-gray participating media. However, in the case of gray radiation, the subscript g appearing in the entries of the vector of conserved moments and of the flux vectors, Eq. (5.2) for M_1 and P_1, Eq. (5.4) for M_2, and Eq. (5.6) for P_3, must be dropped since spectrally integrated quantities must be solved for directly. Moreover, the source term vector, $\mathbf{S}$, for gray participating media with isotropic scattering, is given by

$$\mathbf{S} = c \begin{bmatrix} \kappa(4\pi I_b - I^{(0)}) \\ -(\kappa + \sigma_s) I_1^{(1)} \\ -(\kappa + \sigma_s) I_2^{(1)} \end{bmatrix}, \tag{5.9}$$

for the M_1 and P_1 closures,

$$\mathbf{S} = c \begin{bmatrix} \kappa(4\pi I_b - I^{(0)}) \\ -(\kappa + \sigma_s) I_1^{(1)} \\ -(\kappa + \sigma_s) I_2^{(1)} \\ \frac{1}{3}(4\pi\kappa I_b + \sigma_s I^{(0)}) - (\kappa + \sigma_s) I_{11}^{(2)} \\ -(\kappa + \sigma_s) I_{12}^{(2)} \\ \frac{1}{3}(4\pi\kappa I_b + \sigma_s I^{(0)}) - (\kappa + \sigma_s) I_{22}^{(2)} \end{bmatrix}, \tag{5.10}$$

for the M_2 closure, and

$$\mathbf{S} = c \begin{bmatrix} \kappa(4\pi I_b - I^{(0)}) \\ -(\kappa + \sigma_s) I_1^{(1)} \\ -(\kappa + \sigma_s) I_2^{(1)} \\ \frac{1}{3}(4\pi\kappa I_b + \sigma_s I^{(0)}) - (\kappa + \sigma_s) I_{11}^{(2)} \\ -(\kappa + \sigma_s) I_{12}^{(2)} \\ \frac{1}{3}(4\pi\kappa I_b + \sigma_s I^{(0)}) - (\kappa + \sigma_s) I_{22}^{(2)} \\ -(\kappa + \sigma_s) I_{111}^{(3)} \\ -(\kappa + \sigma_s) I_{112}^{(3)} \\ -(\kappa + \sigma_s) I_{122}^{(3)} \\ -(\kappa + \sigma_s) I_{222}^{(3)} \end{bmatrix}, \tag{5.11}$$

for the P_3 closure.

In Eq. (5.9)–(5.11), $I_b = \int_0^\infty I_{b\eta} \mathrm{d}\eta = 4\sigma_{stef} T^4$ is the spectrally integrated Planck function or blackbody intensity and where σ_{stef} is the Stephan-Boltzmann constant defined in Eq. (3.11). While the closing relations for the P_1 and P_3 spherical harmonic moment closures are similar for both gray and non-gray radiation, to the exception of the spectral dependence which must be dropped for the former, the same principle does not hold for the M_N maximum-entropy moment closures. In particular, the closing relations of Eqs. (3.14), (3.15), and (3.16) must be used in the case of the M_1 closure for gray radiation whereas, for the gray M_2 closure, the relationships of Eqs. (3.41), (3.42), (3.44)–(3.50), and (3.51) are to be employed.

It should be emphasized that when axisymmetric flows are of interest, as is the case in many laminar reactive flows simulations, the governing equations given in Eq. (5.1) must be expressed in a cylindrical coordinates. Compared to the Cartesian coordinate frame however, expressing the governing equations in a curvilinear coordinate basis presents additional challenges due to the fact that there can be non-zero Christoffel symbols [147–150] which in turn may give rise to the so-called axisymmetric source terms. The weak conservation forms of the governing equations arising from the M_1, M_2, P_1, and P_3 closures in cylindrical coordinates (r, θ, z) are given in Appendix F and can be summarized as follows

$$\frac{\partial \mathbf{U}}{\partial t} + \frac{\partial \mathbf{F}}{\partial r} + \frac{\partial \mathbf{G}}{\partial z} = -\frac{\mathbf{S}_A}{r} + \mathbf{S}\,, \tag{5.12}$$

where $\mathbf{U}$ is again the vector of conserved moments, $\mathbf{F}$ and $\mathbf{G}$ are the flux vectors in the r- and z-coordinate directions, respectively, $\mathbf{S}$ again represents the source term vector, and $\mathbf{S}_A$ corresponds to the axisymmetric source term vector.

It is now worthwhile to investigate the hyperbolicity of the closed systems of moment equations arising from the moment closures studied herein. As a first step, the weak conservation form of the governing equations, Eq. (5.1), is re-expressed in the following form

$$\frac{\partial \mathbf{U}}{\partial t} + \mathbf{A}\frac{\partial \mathbf{U}}{\partial x} + \mathbf{B}\frac{\partial \mathbf{U}}{\partial y} = \mathbf{S}, \tag{5.13}$$

where $\mathbf{A} = \partial \mathbf{F}/\partial \mathbf{U}$ and $\mathbf{B} = \partial \mathbf{G}/\partial \mathbf{U}$ are the flux Jacobians in the x- and y- directions, respectively. The hyperbolic nature of the moment equations, in two space dimensions, is investigated by considering the eigenvalues of the flux Jacobians, $\mathbf{A}$ and $\mathbf{B}$. Hyperbolicity is ensured if the eigenvalues of $\mathbf{A}$ and $\mathbf{B}$ are all real. In what follows however, we will

solely focus on the properties of the x-direction flux Jacobian, $\mathbf{A}$, as similar findings are expected for the y-direction flux Jacobian, $\mathbf{B}$, due to the geometric symmetries of the closures. In particular, we aim to find a decomposition of $\mathbf{A}$ of the form

$$\mathbf{A} = \mathbf{R}\mathbf{\Lambda}\mathbf{R}^{-\mathbf{1}}, \tag{5.14}$$

where $\mathbf{R}$ represents the matrix of right eigenvectors, and $\mathbf{\Lambda}$ is the diagonal matrix of eigenvalues of $\mathbf{A}$.

5.1.1 Eigenstructure of the P_1 and P_3 Spherical Harmonic Moment Closures

For the first-order, P_1, spherical harmonic moment closure, the x-direction flux Jacobian takes the form

$$\frac{\partial \mathbf{F}}{\partial \mathbf{U}} = c \begin{bmatrix} 0 & 1 & 0 \\ \frac{1}{3} & 0 & 0 \\ 0 & 0 & 0 \end{bmatrix} \tag{5.15}$$

and the corresponding diagonal matrix of eigenvalues and matrix of right eigenvectors, respectively, are given by

$$\mathbf{\Lambda} = c \begin{bmatrix} 0 & 0 & 0 \\ 0 & -\frac{\sqrt{3}}{3} & 0 \\ 0 & 0 & \frac{\sqrt{3}}{3} \end{bmatrix}, \tag{5.16}$$

and

$$\mathbf{R} = \begin{bmatrix} 0 & 1 & 1 \\ 0 & -\frac{\sqrt{3}}{3} & \frac{\sqrt{3}}{3} \\ 1 & 0 & 0 \end{bmatrix}. \tag{5.17}$$

For the third-order, P_3, spherical harmonic closure technique, the x-direction flux Jaco-

bian is given by

$$\frac{\partial \mathbf{F}}{\partial \mathbf{U}} = c \begin{bmatrix} 0 & 1 & 0 & 0 & 0 & 0 & 0 & 0 & 0 & 0 \\ 0 & 0 & 0 & 1 & 0 & 0 & 0 & 0 & 0 & 0 \\ 0 & 0 & 0 & 0 & 1 & 0 & 0 & 0 & 0 & 0 \\ 0 & 0 & 0 & 0 & 0 & 0 & 1 & 0 & 0 & 0 \\ 0 & 0 & 0 & 0 & 0 & 0 & 0 & 1 & 0 & 0 \\ 0 & 0 & 0 & 0 & 0 & 0 & 0 & 0 & 1 & 0 \\ -\frac{3}{35} & 0 & 0 & \frac{6}{7} & 0 & 0 & 0 & 0 & 0 & 0 \\ 0 & 0 & 0 & 0 & \frac{3}{7} & 0 & 0 & 0 & 0 & 0 \\ -\frac{1}{35} & 0 & 0 & \frac{1}{7} & 0 & \frac{1}{7} & 0 & 0 & 0 & 0 \\ 0 & 0 & 0 & 0 & \frac{3}{7} & 0 & 0 & 0 & 0 & 0 \end{bmatrix}. \tag{5.18}$$

The diagonal matrix of eigenvalues corresponding to the latter Jacobian matrix can be written as follows

$$\mathbf{\Lambda} = c \begin{bmatrix} 0 & 0 & 0 & 0 & 0 & 0 & 0 & 0 & 0 & 0 \\ 0 & 0 & 0 & 0 & 0 & 0 & 0 & 0 & 0 & 0 \\ 0 & 0 & \lambda^{-}_{P_3} & 0 & 0 & 0 & 0 & 0 & 0 & 0 \\ 0 & 0 & 0 & \lambda^{+}_{P_3} & 0 & 0 & 0 & 0 & 0 & 0 \\ 0 & 0 & 0 & 0 & -\lambda^{-}_{P_3} & 0 & 0 & 0 & 0 & 0 \\ 0 & 0 & 0 & 0 & 0 & -\lambda^{+}_{P_3} & 0 & 0 & 0 & 0 \\ 0 & 0 & 0 & 0 & 0 & 0 & -\frac{\sqrt{7}}{7} & 0 & 0 & 0 \\ 0 & 0 & 0 & 0 & 0 & 0 & 0 & \frac{\sqrt{7}}{7} & 0 & 0 \\ 0 & 0 & 0 & 0 & 0 & 0 & 0 & 0 & -\frac{\sqrt{21}}{7} & 0 \\ 0 & 0 & 0 & 0 & 0 & 0 & 0 & 0 & 0 & \frac{\sqrt{21}}{7} \end{bmatrix}, \tag{5.19}$$

where

$$\lambda^{\pm}_{P_3} = \sqrt{\frac{3}{7} \pm \frac{2\sqrt{30}}{35}}. \tag{5.20}$$

Furthermore, the matrix of right eigenvectors associated with the form of the Jacobian

matrix given in Eq. (5.18) may be written in the following form

$$\mathbf{R} = \begin{bmatrix} 0 & 0 & a^+x_R^- & -a^-x_R^+ & -a^+x_R^- & a^-x_R^+ & 0 & 0 & 0 & 0 \\ 0 & 0 & 5-\frac{\sqrt{30}}{2} & 5+\frac{\sqrt{30}}{2} & 5-\frac{\sqrt{30}}{2} & 5+\frac{\sqrt{30}}{2} & 0 & 0 & 0 & 0 \\ 1 & 0 & 0 & 0 & 0 & 0 & 0 & 0 & \frac{7}{3} & \frac{7}{3} \\ 0 & 0 & -b^-x_R^- & b^+x_R^+ & b^-x_R^- & -b^+x_R^+ & 0 & 0 & 0 & 0 \\ 0 & 0 & 0 & 0 & 0 & 0 & 0 & 0 & -\frac{\sqrt{21}}{3} & \frac{\sqrt{21}}{3} \\ 0 & 0 & \frac{\sqrt{35}x_R^-\left(x_R^+\right)^2}{105} & -\frac{\sqrt{35}x_R^+\left(x_R^-\right)^2}{105} & -\frac{\sqrt{35}x_R^-\left(x_R^+\right)^2}{105} & \frac{\sqrt{35}x_R^+\left(x_R^-\right)^2}{105} & -\sqrt{7} & \sqrt{7} & 0 & 0 \\ 0 & 0 & 3-\frac{\sqrt{30}}{2} & 3+\frac{\sqrt{30}}{2} & 3-\frac{\sqrt{30}}{2} & 3+\frac{\sqrt{30}}{2} & 0 & 0 & 0 & 0 \\ 0 & 0 & 0 & 0 & 0 & 0 & 0 & 0 & 1 & 1 \\ 0 & 0 & 1 & 1 & 1 & 1 & 1 & 1 & 0 & 0 \\ 0 & 1 & 0 & 0 & 0 & 0 & 0 & 0 & 1 & 1 \end{bmatrix}, \tag{5.21}$$

where

$$\begin{aligned} a^\pm &= \frac{\sqrt{35}(\sqrt{30} \pm 18)}{42}, \\ b^\pm &= \frac{\sqrt{35}(\sqrt{30} \pm 10)}{70}, \\ x_R^\pm &= \sqrt{15 \pm 2\sqrt{30}}. \end{aligned} \tag{5.22}$$

As can be seen from Eq. (5.16), the system of moment equations arising from the P_1 closure is hyperbolic, since the eigenvalues of the x-direction flux Jacobian are all real, for any given finite set of angular moments up to first order. Similar observations can be made for the P_3 closure by inspection of the diagonal matrix of eigenvalues given in Eq. (5.19), i.e., the system of moment equations arising from the latter closure is hyperbolic for any given set of angular moments up to third order. Furthermore, as both systems give rise to a complete set of linearly independent eigenvectors, the moments equations are also strictly hyperbolic in the sense of Lax.

5.1.2 Eigenstructure and Hyperbolicity of Gray and Interpolative-Based Non-Gray M_1 Moment Closures

For the M_1 closure in the context of non-gray radiation, the flux Jacobian in the x-direction, $\mathbf{A}$, can be written as

$$\frac{\partial \mathbf{F}}{\partial \mathbf{U}} = c \begin{bmatrix} 0 & 1 & 0 \\ \frac{\partial I_{g,11}^{(2)}}{\partial I_g^{(0)}} & \frac{\partial I_{g,11}^{(2)}}{\partial I_{g,1}^{(1)}} & \frac{\partial I_{g,11}^{(2)}}{\partial I_{g,2}^{(1)}} \\ \frac{\partial I_{g,12}^{(2)}}{\partial I_g^{(0)}} & \frac{\partial I_{g,12}^{(2)}}{\partial I_{g,1}^{(1)}} & \frac{\partial I_{g,12}^{(2)}}{\partial I_{g,2}^{(1)}} \end{bmatrix}, \tag{5.23}$$

where

$$\frac{\partial I_{g,ij}^{(2)}}{\partial I_g^{(0)}} = \frac{1-\chi_T}{2}\delta_{ij} + \frac{3\chi_T - 1}{2} n_i n_j, \quad \chi_T = \chi_2 + I_g^{(0)} \frac{\partial \chi_2}{\partial I_g^{(0)}}, \tag{5.24}$$

and where

$$\frac{\partial I_{g,ij}^{(2)}}{\partial I_{g,l}^{(1)}} = \frac{1}{\|N^{(1)}\|} \left[\frac{3\chi_2 - 1}{2} (n_j \delta_{il} + n_i \delta_{jl} - 2 n_i n_j n_k \delta_{lk}) + \frac{3 n_i n_j - \delta_{ij}}{2} N_k^{(1)} \delta_{kl} \frac{\partial \chi_2}{\partial \|N^{(1)}\|} \right]. \tag{5.25}$$

Analytical expressions for the derivatives of the Eddington factor, χ_2, with respect to the lower-order moments, U_q, $q \in \{1,2,3\}$ (see Eq. (5.2)), in $\mathcal{R}^{(1)}$, can be readily derived from the proposed interpolative-based approximation of χ_2 as given in Eqs. (3.20)–(3.24). In the case of gray radiation, the x-direction flux Jacobian for the M_1 closure reads in a similar way as in Eq. (5.23), except that the subscript g must be dropped. Moreover, the derivatives of the second-order closing fluxes with respect to the lower-order moments read in a similar way as in the relationships given in Eqs. (5.24) and (5.25), where the subscript g must again be dropped. Closed-form analytical expressions for the derivatives of the Eddington factor, χ_2, with respect to the lower-order moments can then be easily derived from the relationship given in Eq. (3.16).

The matrix of right eigenvectors associated with the form of the flux Jacobian given in Eq. (5.23) can be written in the following form

$$\mathbf{R} = \begin{bmatrix} 1 & 1 & 1 \\ \frac{\lambda_1^{M_1}}{c} & \frac{\lambda_2^{M_1}}{c} & \frac{\lambda_3^{M_1}}{c} \\ -\frac{cA_{21} + \lambda_1^{M_1}(A_{22} - \lambda_1^{M_1})}{cA_{23}} & -\frac{cA_{21} + \lambda_2^{M_1}(A_{22} - \lambda_2^{M_1})}{cA_{23}} & -\frac{cA_{21} + \lambda_3^{M_1}(A_{22} - \lambda_3^{M_1})}{cA_{23}} \end{bmatrix}, \tag{5.26}$$

where $\lambda_i^{M_1}$, $i \in \{1,2,3\}$, are the eigenvalues associated with the form of the flux Jacobian given in Eq. (5.23), and $A_{ij} = \partial F_i / \partial U_j$ represents the entry of the flux Jacobian

associated with the i^{th} line and j^{th} column. Closed-form analytical expressions for the eigenvalues of the M_1 closure in the context of gray radiation for two-dimensional problems exist, the diagonal matrix of which can be written as follows

$$\mathbf{\Lambda} = c \begin{bmatrix} \frac{N_1^{(1)} - \Upsilon}{\xi} & 0 & 0 \\ 0 & \frac{N_1^{(1)} + \Upsilon}{\xi} & 0 \\ 0 & 0 & \frac{N_1^{(1)}(2-\xi)}{\|N^{(1)}\|^2} \end{bmatrix}, \tag{5.27}$$

where

$$\Upsilon = \frac{\sqrt{2(\xi-1)(\xi+2)\left(2(\xi-1)(\xi+2) + 3\left(N_2^{(1)}\right)^2\right)}}{\sqrt{3}(\xi+2)}, \tag{5.28}$$

and where ξ is a scalar quantity defined in Eq. (3.16).

A close inspection of the last two equations, Eqs. (5.27) and (5.28), shows that the eigenvalues of the flux Jacobian matrix associated with the M_1 closure for gray radiation are all real everywhere within the realizable space for angular moments up to first order, $\mathcal{R}^{(1)}$. Furthermore, a complete set of linearly independent eigenvectors exists. It therefore follows that the resulting system of moment equations is strictly hyperbolic everywhere within $\mathcal{R}^{(1)}$.

In the context of non-gray radiative transfer on the other hand, the eigenvalues of the flux Jacobian matrix for the M_1 closure cannot be expressed in a relatively compact form similar to its counterpart in the case of gray radiation. In the present study, the eigenvalues of the system of moment equations arising from the non-gray M_1 closure, for two-dimensional problems, are obtained via numerical solution of a cubic characteristic polynomial equation associated with the flux Jacobian of Eq. (5.23). The discriminant of the cubic polynomial characteristic equation has the following form

$$\Delta = 18abcd - 4b^3d + b^2c^2 - 4ac^3 - 27a^2d^2, \tag{5.29}$$

where

$$\begin{aligned} a &= -1, \\ b &= A_{22} + A_{33}, \\ c &= A_{12}A_{21} - A_{22}A_{33} + A_{23}A_{32}, \\ d &= -A_{12}A_{21}A_{33} + A_{12}A_{23}A_{31}. \end{aligned} \tag{5.30}$$

A necessary and sufficient condition for the eigenvalues of the associated flux Jacobian to be real is that the discriminant of the characteristic polynomial, given in Eq. (5.29), be non-negative, i.e.,

$$\Delta \geq 0. \tag{5.31}$$

In order to ensure hyperbolicity of the system of equations resulting from the proposed interpolative non-gray M_1 closure, the constraint of Eq. (5.31) is enforced, at every step of the non-linear least-squares optimization problem, Eq. (3.25), for a large set of sample points consisting of 10^3 values of $\mathcal{M}_{I_\eta^{(0)\star}}$ following a Gauss-Lobatto-Chebyshev distribution in $[-1,\ 1]$, 10^3 values of $\|N^{(1)}\|$ associated with non-negative Gauss-Lobatto-Chebyshev points in $[-1,\ 1]$, 10^2 values of ϕ uniformly distributed in $[0,\ 2\pi]$, where ϕ represents the polar angle characterizing the direction of the vector of first-order moments, $N^{(1)}$, and is defined as follows

$$\phi = \arccos\left(\frac{N_1^{(1)}}{\|N^{(1)}\|}\right). \tag{5.32}$$

The numerical solution of the non-linear least-squares problem, Eq. (3.25), in conjunction with constraints of realizability and hyperbolicity discussed above, yields a minimum value of the discriminant, $\Delta \approx -10^{-6}$. Thus, to a numerical accuracy of 10^{-6}, the eigenvalues of the flux Jacobian, $\mathbf{A}$, are all real valued for all of the points considered within the space of realizable moments.

It should be emphasized that the above findings in the case of the non-gray M_1 closure are certainly not a proof that the eigenvalues are everywhere real nor was the issue of strict hyperbolicity tested as part of this thesis research. In particular, it was indeed felt that the distinct nature of the eigenvalues and/or non-degenerate nature of the eigenstructure can be difficult to confirm by numerical means. Nevertheless, the local hyperbolicity of the proposed interpolative-based closure for all points examined within the space of physically realizable moments is very encouraging and provides strong evidence of the extent to which the proposed interpolative-based closure mimics the actual non-gray first-order, M_1, maximum-entropy model, which of course is known to be strictly hyperbolic.

5.1.3 Eigenstructure and Hyperbolicity of Interpolative-Based Gray and Non-Gray M_2 Moment Closures

For the non-gray M_2 closure, the flux Jacobian in the x-direction, $\mathbf{A}$, can be written as

$$\mathbf{A} = c \begin{bmatrix} 0 & 1 & 0 & 0 & 0 & 0 \\ 0 & 0 & 0 & 1 & 0 & 0 \\ 0 & 0 & 0 & 0 & 1 & 0 \\ \frac{\partial I^{(3)}_{g,111}}{\partial I^{(0)}_{g}} & \frac{\partial I^{(3)}_{g,111}}{\partial I^{(1)}_{g,1}} & \frac{\partial I^{(3)}_{g,111}}{\partial I^{(1)}_{g,2}} & \frac{\partial I^{(3)}_{g,111}}{\partial I^{(2)}_{g,11}} & \frac{\partial I^{(3)}_{g,111}}{\partial I^{(2)}_{g,12}} & \frac{\partial I^{(3)}_{g,111}}{\partial I^{(2)}_{g,22}} \\ \frac{\partial I^{(3)}_{g,112}}{\partial I^{(0)}_{g}} & \frac{\partial I^{(3)}_{g,112}}{\partial I^{(1)}_{g,1}} & \frac{\partial I^{(3)}_{g,112}}{\partial I^{(1)}_{g,2}} & \frac{\partial I^{(3)}_{g,112}}{\partial I^{(2)}_{g,11}} & \frac{\partial I^{(3)}_{g,112}}{\partial I^{(2)}_{g,12}} & \frac{\partial I^{(3)}_{g,112}}{\partial I^{(2)}_{g,22}} \\ \frac{\partial I^{(3)}_{g,122}}{\partial I^{(0)}_{g}} & \frac{\partial I^{(3)}_{g,122}}{\partial I^{(1)}_{g,1}} & \frac{\partial I^{(3)}_{g,122}}{\partial I^{(1)}_{g,2}} & \frac{\partial I^{(3)}_{g,122}}{\partial I^{(2)}_{g,11}} & \frac{\partial I^{(3)}_{g,122}}{\partial I^{(2)}_{g,12}} & \frac{\partial I^{(3)}_{g,122}}{\partial I^{(2)}_{g,22}} \end{bmatrix}, \tag{5.33}$$

where the derivatives of the third-order closing fluxes with respect to the lower-order angular moments making up the components of the solution vector, U_q, $q = 1, 2, \ldots, 6$ (see Eq. (5.4)), in $\mathcal{R}^{(2)}$, can be written, using the product rule, in conjunction with the inverse of the relationship of Eq. (3.41), in the form

$$\frac{\partial I^{(3)}_{g,ijk}}{\partial U_q} = I'^{(3)}_{g,lmn} \frac{\partial}{\partial U_q} \left(R_{il} R_{jm} R_{kn} \right) + R_{il} R_{jm} R_{kn} \frac{\partial I'^{(3)}_{g,lmn}}{\partial U_q}. \tag{5.34}$$

Further applying the product rule for the derivatives appearing in the first term on the right hand side of the latter equation allows one to write

$$\frac{\partial}{\partial U_q} \left(R_{il} R_{jm} R_{kn} \right) = R_{jm} R_{kn} \frac{\partial R_{il}}{\partial U_q} + R_{il} R_{kn} \frac{\partial R_{jm}}{\partial U_q} + R_{il} R_{jm} \frac{\partial R_{kn}}{\partial U_q}. \tag{5.35}$$

To further decompose the derivatives involved in the second term on the right hand side of Eq. (5.34), we make use of the chain rule, which, when combined with the application of the product rule on the relationship, $U'_i = T_{ij} U_j$, yields the following expression

$$\frac{\partial I'^{(3)}_{g,lmn}}{\partial U_q} = \frac{\partial I'^{(3)}_{g,lmn}}{\partial U'_p} \left(T_{pq} + U_r \frac{\partial T_{pr}}{\partial U_q} \right), \tag{5.36}$$

where $\mathbf{T}$ represents the rotation matrix which transforms the components of the vector of conserved variables, $\mathbf{U}$, in $\mathcal{R}^{(2)}$, into the elements of the vector of conserved variables, $\mathbf{U}'$, in $\mathcal{R}^{(2)}_T$.

Analytical expressions for the derivatives of the closing fluxes $I'^{(3)}_{g,ijk}$, in $\mathcal{R}^{(2)}_T$, with respect to the lower-order moments, U'_q, in $\mathcal{R}^{(2)}_T$, can be readily derived by using the relationships given in Eqs. (3.41), (3.42), (3.44)–(3.50), and (3.53)–(3.55). Furthermore, the

derivatives appearing in Eq. (5.35) can also be obtained from the analytical form of the rotation matrix, $\mathbf{R}$, with respect to the lower-order moments, U_q, $q = 1, 2, \ldots, 6$, in $\mathcal{R}^{(2)}$. In the case of the M_2 closure for gray radiation, the same expressions as those given in Eqs. (5.33)–(5.36) may be used, with the only exception that the subscript g must be dropped to account for the fact that spectrally integrated quantities are under consideration. Moreover, analytical expressions for the derivatives of the third-order closing fluxes, $I'^{(3)}_{ijk}$, in $\mathcal{R}^{(2)}_T$, with respect to the lower-order moments, U'_q, in $\mathcal{R}^{(2)}_T$, can then be readily derived by making use of the relationships given in Eqs. (3.41), (3.42), (3.44)–(3.50), and (3.51).

Unlike its first-order counterpart, the matrix of eigenvectors associated with the Jacobian of the flux corresponding to the M_2 closure, for either gray or non-gray radiation, cannot be written in a relatively compact form. In the present study, the diagonal matrix of eigenvalues and the matrix of eigenvectors for both the gray and non-gray M_2 closures are computed numerically via an efficient iterative QR decomposition algorithm provided by the LAPACK library [151].

In the present study, hyperbolicity of the proposed interpolative-based M_2 closure for gray radiation was assessed by computing the eigenvalues of the x-direction flux Jacobian, $\mathbf{A}$, of Eq. (5.33), for sets of angular moments up to second order spanning the full realizable space, $\mathcal{R}^{(2)}_T$. More specifically, 50 values of $\|N^{(1)}\|$ equally distributed in [0, 1], 20 values of θ and 40 values of ϕ (see Eq. (3.50)) uniformly distributed in $[0,\ \pi]$ and $[0,\ 2\pi]$, respectively, $20(20+1)/2 = 210$ points following the distribution given in Eq. (3.52) for the eigenvalues of the covariance matrix, γ_i, $i \in \{1, 2, 3\}$, were used for the assessment. The numerical study revealed that the eigenvalues of the flux Jacobian, $\mathbf{A}$, are all real valued for all of the points considered within the space of realizable moments.

In order to ensure hyperbolicity of the system of equations arising from the proposed interpolative non-gray M_2 closure, constraints on the eigenvalues of the flux Jacobian of Eq. (5.33), such that the latter are real valued, are enforced, at every step of the non-linear least-squares optimization problem, Eq. (3.56), for each of the sample points used to assess the error given in the latter equation. The numerical solution of the non-linear least-squares problem, Eq. (3.56), in conjunction with the constraints of hyperbolicity discussed above, yields a distribution of the length scale, $L_{N'^{(3)}}$ (see Eq. (3.55)), of the exponential mapping for which the eigenvalues of the flux Jacobian, $\mathbf{A}$, are all real valued

for all of the test points considered within the space of realizable moments up to second order.

Similar to the findings for the non-gray M_1 closure above, the procedure followed herein for assessing the hyperbolicity of the gray and non-gray M_2 closures does not yield a formal proof that the eigenvalues are everywhere real or that the resulting closed systems of moment equations are strictly hyperbolic. Despite these facts, the local hyperbolicity of the proposed interpolative-based M_2 closures, for all points examined within $\mathcal{R}_T^{(2)}$, illustrate the extent to which they can mimic the actual second-order, M_2, maximum-entropy closures, which of course are provably strictly hyperbolic.

5.2 Finite-Volume Spatial Discretization Method

The basic concept of a finite-volume approach consists of solving the governing partial differential equations on a domain discretized into series of contiguous control volumes or cells making up the computational grid for the geometry of interest. The finite-volume method used in this thesis follows from the integral form of the governing conservation equations. By integrating the differential form of the governing equations given in Eq. (5.1) over a two-dimensional control volume in physical space and subsequently applying the divergence theorem, the following integral form can be obtained

$$\frac{d}{dt}\int_A \mathbf{U}\, dA + \oint_C \vec{\mathbf{F}} \cdot \vec{n}\, dl = \int_A \mathbf{S}\, dA, \tag{5.37}$$

where A is the control volume (actually area in 2D), C is the closed contour containing the control volume, and $\vec{n}$ is the unit outward vector normal to the closed contour. For axisymmetric geometries, the source vector of Eq. (5.37) includes sources associated with both absorption/emission/scattering and axisymmetric geometry as defined in Eq. (5.12). The flux dyad, $\vec{\mathbf{F}} = (\mathbf{F}, \mathbf{G})$, represents the flux of solution quantities through the boundaries of the control volume. These fluxes can be generally categorized as either arising from wave propagation phenomena (hyperbolic fluxes) or from diffusion processes (elliptic fluxes). Governing equations of the type arising from the moment closures considered in the present study are however only concerned with the former, i.e., hyperbolic fluxes.

In the finite-volume method, the integral form of the governing equations is enforced discretely in each of many small contiguous control volumes making up a computational

mesh. Using Eq. (5.37), the net rate of change of any radiative quantity, for example the radiative energy density or the radiative heat flux, within each finite control volume can be expressed as a balance between the net solution fluxes through the surface containing the volume of interest and volumetric sources tending to increase or decrease its value. For details regarding conservation equations and their properties, the reader is referred to the textbooks by Toro [152], Hirsch [153, 154], and Lomax *et al.* [155].

For the purpose of briefly illustrating the main elements of a finite-volume method, one can consider the discretization of the equations for the angular moments over a set of control volumes in a two-dimensional coordinate frame where it is assumed that the control volumes (areas in two space dimensions) do not vary with time. The cell-averaged solution and source vectors, $\overline{\mathbf{U}}$ and $\overline{\mathbf{S}}$, respectively, within each cell or control volume, can then be defined by an integration over the control volume as follows

$$\overline{\mathbf{U}} \equiv \frac{1}{A}\int_A \mathbf{U}\, dA, \tag{5.38}$$

$$\overline{\mathbf{S}} \equiv \frac{1}{A}\int_A \mathbf{S}\, dA, \tag{5.39}$$

where A is the cell area. Substituting these last two expressions into Eq. (5.37) the latter to be rewritten as

$$\frac{d\overline{\mathbf{U}}}{dt} + \frac{1}{A}\oint_C \vec{\mathbf{F}}\cdot\vec{n}\, dl = \overline{\mathbf{S}}(\overline{\mathbf{U}}), \tag{5.40}$$

where dl is an element of the closed contour containing the control volume or cell of interest. Under the assumption that the control volume (i, j) is a polygon defined by N_f straight-line segments or cell faces ($N_f = 4$ for quadrilateral cells) and a standard mid-point quadrature rule is used in the flux integration, Eq. (5.40) can be rewritten in semi-discrete form as follows

$$\frac{\mathrm{d}\overline{\mathbf{U}}_{i,j}}{\mathrm{d}t} = -\frac{1}{A_{i,j}}\sum_{m=1}^{N_f} \vec{\mathbf{F}}_{i,j,m}\cdot\vec{n}_{i,j,m}\,\Delta l_{i,j,m} + \overline{\mathbf{S}}_{i,j}(\overline{\mathbf{U}}), \tag{5.41}$$

or

$$\frac{\mathrm{d}\overline{\mathbf{U}}_{i,j}}{\mathrm{d}t} = -\mathbf{R}_{i,j}(\overline{\mathbf{U}}), \tag{5.42}$$

where $\Delta l_{i,j,m}$ and $\vec{n}_{i,j,m}$ are the length and unit outward normal vector of the m^{th} face of cell (i, j), respectively, and $\mathbf{R}_{i,j}(\overline{\mathbf{U}})$ is the so-called residual operator for computational cell (i, j).

The semi-discrete form of Eq (5.41) is a coupled non-linear system of first-order ordinary differential equations (ODEs), whereby the integration of the solution flux over the

cell surface has been replaced by the mid-point quadrature rule (valid for second-order accuracy). The solution procedure for solving the latter equation involves three steps: **reconstruction**, **flux evaluation** and **evolution**. In the first step, for a given value of $\overline{\mathbf{U}}$ in each computational cell, an approximation of $\mathbf{U}(\vec{x})$ throughout each cell is constructed and used to find $\mathbf{U}$ at the boundaries of the corresponding cell. The accuracy of this so-called solution reconstruction procedure directly affects the spatial order of accuracy of the solution as well as the accuracy of the cell-normal flux evaluation. In this thesis, a piecewise linear limited reconstruction is used, the details of which are presented in Section 5.2.1. Next, the flux, $\vec{\mathbf{F}}(\overline{\mathbf{U}})$ at the cell boundaries is evaluated as a function of the discontinuous states on either side of the interface, where the discontinuities arise due to the piecewise approximations of $\mathbf{U}$ within each control volume. In this thesis, the numerical flux at each cell face is evaluated as the solution of the approximate Riemann problem based on either the Harten-Lax-van-Leer-Einfeldt (HLLE) flux function [156] or Roe flux function [157]. The evaluation of the numerical fluxes is discussed in Section 5.2.1. Finally, steady-state solutions of the semi-discrete form of the governing equations are obtained here using an implicit Newton-Krylov Schwarz (NKS) iterative algorithm with Generalized Minimal Residual (GMRES) technique. Details of the NKS solution procedure adopted in this study can be found in Section 5.5.

The remainder of this chapter outlines aspects of the finite-volume scheme used for providing numerical solutions to the system of moments equations arising from the M_1, M_2, P_1 and P_3 moment closures. For notational simplicity, in the remainder of the thesis, the overline sign "$^-$" is dropped for cell-averaged solution and source vectors.

5.2.1 Hyperbolic Flux Evaluation

The original Godunov method makes use of the solution of locally one-dimensional Riemann problems in order to evaluate the numerical fluxes at the cell boundaries, and is based on a piecewise constant reconstruction of the solution within each cell of the computational domain. The piecewise constant reconstruction reduces the accuracy of the overall scheme to first order. The latter can be further improved to yield high-resolution schemes. In particular, the components of the flux, $\vec{\mathbf{F}}$, appearing in Eq. (5.41) are evaluated herein by means of a second-order Godunov-type upwind finite-volume spatial discretization procedure, based on approximate Riemann solvers and least-squares piecewise

limited linear solution reconstruction. The emergence of high-resolution Godunov-type methods motivated the design of effective limiters for use in higher-order reconstructions [156, 158, 159].

Piecewise Limited Linear Reconstruction

The solution reconstruction procedure adopted in the present study achieves higher-order accuracy (i.e., second-order in smooth regions) compared to the original Godunov method via a limited linear spatial reconstruction of the solution in each computational cell. The values of the left and right solution states at a cell interface are determined by means of a least-squares piecewise limited linear solution reconstruction. More specifically, for a given cell (i, j), at the cell interface $(i + \frac{1}{2}, j)$, the flux is computed as follows

$$\vec{\mathbf{F}}_{i,j,m} \cdot \vec{n}_{i,j,m} = \vec{\mathbf{F}} \left(\mathcal{R} \left(\mathbf{W}_L, \mathbf{W}_R, \vec{n}_{i,j,m} \right) \right) \tag{5.43}$$

where $\vec{n}_{i,j,m}$ corresponds to the outward unit vector normal to the cell interface, $\mathcal{R}$ represents the solution of the Riemann problem, and $\mathbf{W}_L$ and $\mathbf{W}_R$ are the left and right primitive solution vectors from the piecewise limited linear reconstruction procedure at the cell interface $(i + \frac{1}{2}, j)$, and are respectively given by

$$\begin{aligned} \mathbf{W}_L &= \mathbf{W}_{i,j} + \mathbf{\Phi}_{i,j} \vec{\nabla} \mathbf{W}_{i,j} \cdot \Delta \vec{x}_L, \\ \mathbf{W}_R &= \mathbf{W}_{i+1,j} + \mathbf{\Phi}_{i+1,j} \vec{\nabla} \mathbf{W}_{i+1,j} \cdot \Delta \vec{x}_R. \end{aligned} \tag{5.44}$$

In Eq. (5.44), $\mathbf{\Phi}$ is the slope limiter, $\mathbf{W}_{i,j}$ and $\mathbf{W}_{i+1,j}$ are cell-averaged primitive solution vectors in the neighbouring cells, $\Delta \vec{x}_L$ and $\Delta \vec{x}_R$ are the distances between the centroid of the cell and the cell interface for the left and right cells, respectively, and are given by the following relationships

$$\begin{aligned} \Delta \vec{x}_L &= \vec{x} - \vec{x}_{i,j}, \\ \Delta \vec{x}_R &= \vec{x} - \vec{x}_{i+1,j}, \end{aligned} \tag{5.45}$$

and where $\vec{x}$ is the location of the cell interface and $\vec{x}_{i,j}$ and $\vec{x}_{i+1,j}$ represent the position vectors of the centers of the left and right cells, respectively.

The slope limiter, $\mathbf{\Phi}$, is introduced for the purpose of limiting the solution gradient so as to ensure solution monotonicity. In the present study, the slope limiter proposed by Venkatakrishnan [160] was adopted for the solution reconstruction procedure, and is of

the following form

$$\Phi_{i,j,q} = \begin{cases} \phi\left(\frac{W_{\max,q}-W_{i,j,q}}{W_{k,q}-W_{i,j,q}}\right) & \text{if} \quad W_{k,q} - W_{i,j,q} > 0, \\ \phi\left(\frac{W_{\min,q}-W_{i,j,q}}{W_{k,q}-W_{i,j,q}}\right) & \text{if} \quad W_{k,q} - W_{i,j,q} < 0, \\ 1 & \text{otherwise}, \end{cases} \tag{5.46}$$

where $\phi(y)$ is a smooth function given by

$$\phi(y) = \frac{y^2 + 2y}{y^2 + y + 2}, \tag{5.47}$$

and where $\mathbf{W}_k$ is the unlimited reconstructed solution vector at the k^{th} flux quadrature point, and $W_{\max,q} = \max\left(W_{i,j,q}, W_{\text{neighbours},q}\right)$ and $W_{\min,q} = \min\left(W_{i,j,q}, W_{\text{neighbours},q}\right)$, $q = 1, 2, \ldots, N_c$ (where N_c represents the number of conserved variables), are respectively the maximum and minimum cell averaged values of the q^{th} primitive solution between cell (i, j) and its neighbouring cells used in the reconstruction procedure.

Least-Squares Gradient Evaluation

The gradients of the primitive variables, $\vec{\nabla}\mathbf{W}$, are determined by applying a least-squares approach [161], which relies on a stencil formed by the nearest and possibly next to nearest neighbouring cells. For the boundary stencil, a layer of ghost cells containing boundary condition information is used to generalize the procedure without reducing the reconstruction stencil. For a cell-centered discretization in two dimensions, the stencil is formed by joining the nearest eight neighbouring cell centroids. For the q^{th} primitive variable, W_q, the approximate gradients, $\vec{\nabla}W_q$, using the least-squares gradient construction procedure are obtained by minimizing the error defined by

$$\sum_{k=1}^{N} \epsilon_{ik,q}^2 = \sum_{k=1}^{N} (\Delta W_{ik,q} - \vec{\nabla}W_{i,q} \cdot \Delta\vec{x}_{ik})^2, \; q = 1, 2, \ldots, N_c, \tag{5.48}$$

where $\Delta W_{ik,q} = W_{i,q} - W_{k,q}$, $\Delta\vec{x}_{ik} = \vec{x}_i - \vec{x}_k$, and $N = 8$ in two dimensions. The 2×2 system of linear algebraic equations resulting from the minimization problem can be expressed as

$$\begin{bmatrix} \overline{(\Delta x)^2} & \overline{\Delta x \Delta y} \\ \overline{\Delta x \Delta y} & \overline{(\Delta y)^2} \end{bmatrix} \begin{bmatrix} \frac{\partial W_q}{\partial x} \\ \frac{\partial W_q}{\partial y} \end{bmatrix} = \begin{bmatrix} \overline{\Delta W_q \Delta x} \\ \overline{\Delta W_q \Delta y} \end{bmatrix}, \tag{5.49}$$

where

$$\overline{\Delta x^2} = \frac{1}{N} \sum_{k=1}^{N} \Delta x_{ki}^2, \tag{5.50}$$

$$\overline{\Delta x \Delta y} = \frac{1}{N} \sum_{k=1}^{N} \Delta x_{ki} \Delta y_{ki}, \tag{5.51}$$

and

$$\overline{\Delta W_q \Delta x} = \frac{1}{N} \sum_{k=1}^{N} \Delta W_{ki,q} \Delta x_{ki}. \tag{5.52}$$

The other terms in Eq. (5.49) can be formulated similarly. The above expressions only depend on grid geometry and can therefore be precomputed and stored. Solutions of the 2×2 linear system represented by Eq. (5.49) can be readily obtained using Cramer's rule.

Riemann Problem

A Riemann problem is a special form of a one-dimensional initial value problem (IVP) with discontinuous initial data and self-similar solutions. It can be seen to be posed at the interface between adjacent computational cells and is used in Godunov-type finite-volume methods as a mean for evaluating the numerical fluxes at cell boundaries. For a one-dimensional system of conservation laws given by

$$\frac{\partial \mathbf{U}}{\partial t} + \frac{\partial \mathbf{F}}{\partial x} = \frac{\partial \mathbf{U}}{\partial t} + \mathbf{A} \frac{\partial \mathbf{U}}{\partial x} = 0, \tag{5.53}$$

where $\mathbf{A} = \partial \mathbf{F} / \partial \mathbf{U}$ is the Jacobian matrix, the corresponding initial conditions for the Riemann problem can be expressed as follows

$$\mathbf{U}(x, 0) = \begin{cases} \mathbf{U}_L & \text{if } x < 0, \\ \mathbf{U}_R & \text{if } x > 0, \end{cases} \tag{5.54}$$

and where $\mathbf{U}_L$ and $\mathbf{U}_R$ respectively correspond to the left and right initial states on either side of the discontinuity occurring at the cell interface characterized by $x = 0$ (see Fig. 5.1 for illustrations). The discontinuities between the initial states and the subsequent time evolution of the latter are representative of conditions present between neighbouring cells in finite-volume methods. The state variables in the intermediate region, represented by $\mathbf{U}_\star$, are the conservative unknowns in this problem, the solution of which provides a means to compute the flux, $\mathbf{F}_\star$, at the interface ($x = 0$).

An intuitive approach for the solution of the Riemann problem is the use of numerical iterative solution procedures, which tend to be rather computationally involved. In the

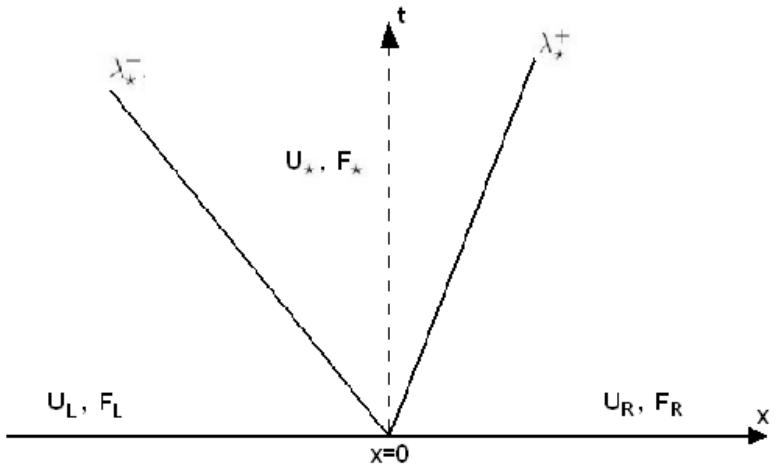

Figure 5.1: Illustration of the one-dimensional Riemann problem.

context of the conservation equations governing a compressible polytropic gas, a very efficient exact solution procedure for the Riemann problem has been proposed by Gottlieb and Groth [162]. For more general systems of conservation laws, such as those arising from the moments closures of interest in the present study, an approximation is often sufficient for use in finite-volume schemes. The approximate methods of Roe [157] and Osher [163] are the most detailed approximations for the wave system associated with the Riemann problem. The former solution procedure is based on a local linearization of the governing equations, whereas the latter replaces shock waves by inverted isentropic waves. In situations where the detailed Riemann solution is complicated, the family of solvers presented by Harten, Lax, and van Leer (HLL) [156], in which a reduced number of waves are considered, may be suitable.

In this thesis, both the Roe and Harten-Lax-van Leer Einfeldt (HLLE) [156, 164] approximate Riemann solvers are used, the theoretical details of which are given in what follows.

Roe Approximate Riemann Solver

Roe's approximate Riemann solver is based on the fact that for a strictly linear system of equations, the Riemann problem can be solved exactly by making use of the eigenstructure of the system. For nonlinear hyperbolic equations, locally linearized characteristic

variables are used to provide approximation to the solution. In order to illustrate Roe's approach, let us consider the nonlinear system of conservation equations in one-space dimension of the form given in Eq. (5.53). In the context of Roe's approach, the latter nonlinear system is solved in an approximate manner via linearization of the Jacobian matrix, $\mathbf{A}$. In particular, an approximation, $\bar{\mathbf{A}}$, to the Jacobian matrix, $\mathbf{A}$, is sought, which generally depends non-linearly on the initial states $\mathbf{U}_L$ and $\mathbf{U}_R$, and results in the following "linearized" system of equations

$$\frac{\partial \mathbf{U}}{\partial t} + \bar{\mathbf{A}} \frac{\partial \mathbf{U}}{\partial x} = 0. \tag{5.55}$$

The so-called Roe matrix, $\bar{\mathbf{A}}$, must satisfy several conditions so as to accurately mimic the behaviour of the original Jacobian. These conditions, making up Roe's so-called property U [157] can be summarized as follows:

1. An exact solution exists for an isolated discontinuity between $\mathbf{U}_L$ and $\mathbf{U}_R$, such that

$$\Delta \mathbf{F} = \bar{\mathbf{A}} \left(\mathbf{U}_L, \mathbf{U}_R \right) \Delta \mathbf{U}, \tag{5.56}$$

   where

$$\Delta \mathbf{U} = \mathbf{U}_R - \mathbf{U}_L, \quad \Delta \mathbf{F} = \mathbf{F}_R - \mathbf{F}_L. \tag{5.57}$$

2. In the limit that $\mathbf{U}_L = \mathbf{U}_R = \mathbf{U}$, $\bar{\mathbf{A}} \left(\mathbf{U}_L, \mathbf{U}_R \right)$ should be able to recover the same system as the original Jacobian such that

$$\bar{\mathbf{A}} \left(\mathbf{U}_L, \mathbf{U}_R \right) = \frac{\partial \mathbf{F}}{\partial \mathbf{U}}. \tag{5.58}$$

3. $\bar{\mathbf{A}}(\mathbf{U}_L, \mathbf{U}_R)$ is diagonalizable with real, distinct eigenvalues, and a complete set of linearly independent eigenvectors.

The first and second properties are necessary to obtain the correct net change of the conserved variables in each cell from one time step to the next. The third property is used in the transformation of conserved variables into characteristic variables.

The Roe approximate Riemann solver provides exact solutions to the systems of moment equations arising from the P_1 and P_3 spherical harmonic moment closures, since the latter are fully linear in nature. On the other hand, the systems of conservation laws resulting from the M_1 and M_2 closures are highly nonlinear, and a linearization of the

Jacobian matrix, given in Eq. (5.23) for M_1 and Eq. (5.33) for M_2, must be performed. The development of approximate Roe matrices for the M_N closures is certainly not a trivial task since the strong non-linearities associated with the closing relations make it impossible to apply the original approach proposed by Roe [157], in the context of the equations for steady and unsteady gas dynamics, for computing such matrices. As such, there has been very limited studies involving the use of Roe's approximate Riemann solver for evaluating the flux functions arising from the M_N-closure-based systems of moment equations. In particular, to date the only study concerned with the use of Roe's approximate solver for the M_N closures is due to Brunner and Holloway [51] and was concerned with the M_1 closure obeying Boltzmann statistics in one-dimensional physical space, for which an approximate form of the Roe matrix was proposed. In the context of radiative transfer problems in multi-dimensional physical space, there exist to date no closed-form expressions for the Roe matrices arising from the M_1 and M_2 closures, as well as from higher-order M_N closures. As part of this thesis research, new generalized Roe matrices for the M_1 and M_2 closures, in two-dimensional physical space, have been proposed and developed and are described in Appendix E. The development of Roe matrices, for the M_1 and M_2 closures, is presented in Sections E.1 and E.2 of Appendix E, respectively, and follows the Multiple Averages (MAs) methodology proposed by Rosatti and Begnudelli [165]. It is worth pointing out that the latter methodology has some similarities with the corrected average approach proposed by Brown [166] for providing approximate Roe Riemann solvers for moment models of dilute gases.

Once a Roe matrix has been determined, the characteristic variables associated with the left and right states can be evaluated as follows

$$W_{c,k}^{L,R} = \mathbf{l}_k.\mathbf{U}_{L,R}, \quad k = 1, 2, \ldots, N_c, \tag{5.59}$$

where N_c represents the number of conserved variables, and $\mathbf{l}_k$, $k = 1, 2, \ldots, N_c$, correspond to the left eigenvectors (row vectors) of the flux Jacobian (for P_1 and P_3) or of the Roe matrix (for the M_1 and M_2 closures). The matrix of left eigenvectors, $\mathbf{L} = [\mathbf{l}_1^T, \mathbf{l}_2^T, \ldots, \mathbf{l}_{N_c}^T]^T$ can be determined from the matrix of right eigenvectors, $\mathbf{R} = [\mathbf{r}_1, \mathbf{r}_2, \ldots, \mathbf{r}_{N_c}]$, as follows

$$\mathbf{L} = \mathbf{R}^{-1}. \tag{5.60}$$

The characteristic variables at the interface between two adjacent cells are then given by

$$W_{c,k} = \begin{cases} W_{c,k}^{L}, & \text{if} \quad \lambda_k > 0, \\ W_{c,k}^{R}, & \text{if} \quad \lambda_k < 0, \end{cases} \tag{5.61}$$

where λ_k correspond to the eigenvalues of the Roe matrix, making up the components of the diagonal matrix of eigenvalues, $\mathbf{\Lambda}$. The matrix of right eigenvectors associated with the Roe matrices of the P_1 and P_3 closures are given in Eqs. (5.17) and (5.21), respectively, and the corresponding diagonal matrices of eigenvalues are respectively given in Eqs. (5.16) and (5.19). In the context of the M_1 closure, for either gray or non-gray radiation, the matrix of right eigenvectors has the form given in Eq. (5.26), except that, instead of the original Jacobian of Eq. (5.23), the proposed approximate Roe matrix given in Section E.1 of Appendix E must be considered. The eigenvalues of the latter matrix can be computed by means of a cubic solver, and such a procedure is adopted herein. For both the gray and non-gray M_2 closures, the proposed approximate Roe matrix given in Section E.2 of Appendix E is used in lieu of the original Jacobian of Eq. (5.33), and the corresponding matrix of right eigenvectors as well as the diagonal matrix of eigenvalues are computed numerically via the LAPACK library.

The conserved solutions vector associated with the interface under consideration is derived from the characteristic variables, $W_{c,k}$, $k = 1, 2, \ldots, N_c$, as follows

$$\mathbf{U}_\star = \sum_{k=1}^{N_c} W_{c,k} \mathbf{r}_k, \tag{5.62}$$

and the flux vector at such an interface can also be computed using the following expression

$$\mathbf{F}_\star = \mathbf{A}(\mathbf{U}_L, \mathbf{U}_R)\mathbf{U}_\star = \frac{1}{2}\left(\mathbf{F}_R + \mathbf{F}_L\right) - \frac{1}{2}|\bar{\mathbf{A}}|\left(\mathbf{U}_R - \mathbf{U}_L\right), \tag{5.63}$$

where $\mathbf{F}_L$ and $\mathbf{F}_R$ correspond to the flux vectors associated with the left and right states, $\mathbf{U}_L$ and $\mathbf{U}_R$, respectively, and

$$|\bar{\mathbf{A}}| = |\bar{\mathbf{A}}(\mathbf{U}_L, \mathbf{U}_R)| = \mathbf{R}|\mathbf{\Lambda}|\mathbf{L}, \tag{5.64}$$

and $\mathbf{\Lambda}$ is again the diagonal matrix of eigenvalues.

HLL Riemann Solver

The HLL approximate Riemann solver [156] is based on a two-wave solution or 3-state approximate solution to the Riemann problem. In this approach, the corresponding flux

function is given by

$$\mathbf{F}(\mathbf{U}_L, \mathbf{U}_R, \vec{n}) = \begin{cases} \mathbf{F}_L & \text{if} \quad \lambda^- \geq 0, \\ \mathbf{F}_\star & \text{if} \quad \lambda^- \leq 0 \leq \lambda^+, \\ \mathbf{F}_R & \text{if} \quad \lambda^+ \leq 0, \end{cases}$$

where λ^- and λ^+ are the left and right signal velocities, respectively. The flux function $\mathbf{F}_\star$ in the intermediate region can be expressed in terms of the known quantities on the left and right states using Rankine-Hugoniot conditions [167]. Applying such conditions across each of the wavespeeds λ^- and λ^+ yields the following relationships

$$\mathbf{F}_\star - \mathbf{F}_L = \lambda^-(\mathbf{U}_\star - \mathbf{U}_L), \tag{5.65}$$

$$\mathbf{F}_\star - \mathbf{F}_R = \lambda^+(\mathbf{U}_\star - \mathbf{U}_R), \tag{5.66}$$

where $\mathbf{U}_\star$ is the intermediate state vector. Solving the system of equations formed by Eqs. (5.65) and (5.66) for the solution vector in the intermediate state as well as for the corresponding flux vector results in the following expressions

$$\mathbf{U}_\star = \frac{\lambda^+\mathbf{U}_R - \lambda^-\mathbf{U}_L}{\lambda^+ - \lambda^-} - \frac{\mathbf{F}_R - \mathbf{F}_L}{\lambda^+ - \lambda^-}, \tag{5.67}$$

$$\mathbf{F}_\star = \frac{\lambda^+\mathbf{F}_L - \lambda^-\mathbf{F}_R}{\lambda^+ - \lambda^-} + \frac{\lambda^+\lambda^-}{\lambda^+ - \lambda^-}(\mathbf{U}_R - \mathbf{U}_L). \tag{5.68}$$

One primary defect of this scheme is exposed by contact discontinuities, shear waves and material interfaces due to the missing intermediate waves. Einfeldt [164] proposed a modification of the HLL scheme, whereby the left and right signal velocities, λ^- and λ^+, respectively, are estimated as follows

$$\lambda^- = \min(\lambda_L^{\min}, \overline{\lambda}^{\min}(\mathbf{U}_L, \mathbf{U}_R)), \tag{5.69}$$

$$\lambda^+ = \max(\lambda_R^{\max}, \overline{\lambda}^{\max}(\mathbf{U}_L, \mathbf{U}_R)), \tag{5.70}$$

where $\overline{\lambda}$ represents Roe's averaged eigenvalue. Einfeldt's contribution yields a more effective and robust scheme, which is referred to in this work as the HLLE approximate Riemann solver.

5.2.2 Frame Rotation

For the purpose of dealing with the multi-dimensional nature of the quadrilateral computational grids considered herein, the hyperbolic numerical fluxes at each cell face are computed via the solution of the Riemann problem in a rotated frame. The new rotated coordinate frame is defined such that the x-axis is aligned and in the same direction as the outward vector normal to the cell face. The boundary conditions discussed in Section 5.3 also make use of such transformation in order to evaluate the full angular moments or numerical fluxes on the boundaries of the computational domain under consideration. This rotational transformation greatly simplifies the implementation of the moment closure methods in a computer code. In fact, instead of deriving expressions for the numerical fluxes or boundary conditions for each coordinate direction, the only expressions that are needed are those in the x-direction, and those in the other directions can be computed accordingly via appropriate rotational transformations of the coordinate frame.

In two-dimensional physical space, the rotational transformation from the original coordinate frame, (x, y), to the new frame, (x', y'), results in a transformation of angular moments up to third order according to the following relationships

$$I^{(1)}_{\eta,i} = R_{ij} I^{(1)\prime}_{\eta,j}, \qquad I^{(1)\prime}_{\eta,i} = R_{ji} I^{(1)}_{\eta,j}, \tag{5.71}$$

$$I^{(2)}_{\eta,ij} = R_{ip} R_{jq} I^{(2)\prime}_{\eta,pq}, \qquad I^{(2)\prime}_{\eta,ij} = R_{pi} R_{qj} I^{(2)}_{\eta,pq}, \tag{5.72}$$

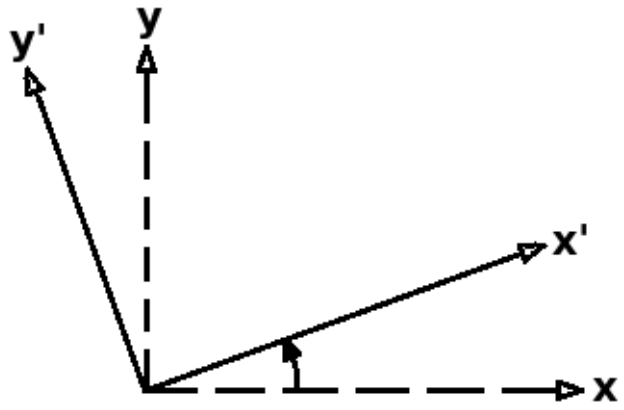

Figure 5.2: Frame rotation in two-dimensional physical space.

$$I^{(3)}_{\eta,ijk} = R_{ip}R_{jq}R_{rk}I^{(3)\prime}_{\eta,pqr}, \qquad I^{(3)\prime}_{\eta,ijk} = R_{pi}R_{qj}R_{kr}I^{(3)}_{\eta,pqr}, \tag{5.73}$$

where $I^{(i)\prime}_{\eta}$, $i = 0, 1, \ldots, 3$, denote the images of the angular moments, $I^{(i)}_{\eta}$, $i = 0, 1, \ldots, 3$, under the rotational transformation. In Eqs. (5.71)–(5.73), $\mathbf{R}$ denotes the rotation matrix characterizing the rotational transformation and reads as follows

$$\mathbf{R} = \begin{bmatrix} \cos\theta & -\sin\theta \\ \sin\theta & \cos\theta \end{bmatrix}, \tag{5.74}$$

where θ is the angle between the rotated coordinate system, (x', y'), and the original one, (x, y).

5.3 Characteristic Boundary Conditions

The numerical solution of systems of partial differential equations generally requires the prescription of boundary conditions in order to evaluate the numerical fluxes at the boundaries of the computational domain. In the context of the system of equations for the angular moments of the radiative intensity distribution resulting from the moment closures presented in this thesis, see Eq. (5.1), boundary conditions are generally prescribed in terms of the full moments at the interfaces describing the boundaries of the computational domain of interest.

The method of characteristics is an approach that allows the prescription of the solution vector of conserved variables, $\mathbf{U}_{\star}$, as well as the corresponding numerical flux vector, $\mathbf{F}_{\star}$, at the interface between two cells in terms of the solution vectors, $\mathbf{U}_L$ and $\mathbf{U}_R$, respectively associated with the mid-point of the cell face to the left and right sides of the interface. This is achieved by first computing the vector of characteristic variables, $\mathbf{W}_c$, at the interface in terms of those associated with the left, $\mathbf{W}^L_c$, or the right, $\mathbf{W}^R_c$, cells, depending on the nature of the corresponding wave (incoming or outgoing), as given in Eq. (5.61). The conserved solutions vector at the interface can then be obtained from the characteristic variables via the matrix of right eigenvectors using Eq. (5.62), whereas the associated numerical flux vector can be computed by means of Eq. (5.63), and this procedure is adopted herein to provide boundary conditions to the system of moments equations arising from the M_1, M_2, P_1 and P_3 moment closures.

In the case where the characteristics are computed along the unit normal vector pointing

outside the computational domain of interest (as is the case when the rotational transformation described in Section 5.2.2 is used), $\mathbf{U}_L$ then corresponds to the solution associated with the interior cell attached to the interface under consideration, whereas $\mathbf{U}_R$ is the vector of conserved variables associated the ghost cell, and containing full moments corresponding to the outgoing distribution of radiative intensity. For diffusely reflecting and emitting wall surfaces, as is the case in most practical combustion systems [69], the outgoing radiative intensity distribution can be expressed as follows

$$I_{\eta,w} = \epsilon_w I_{b\eta}(T_w) + \frac{(1-\epsilon_w)}{\pi} \int_{\Omega=2\pi} s_i I_\eta \mathrm{d}\Omega, \tag{5.75}$$

where T_w and ϵ_w represent the wall temperature and emissivity, respectively, I_η represents the spectral incoming distribution of radiative intensity, and s_i corresponds to the directional cosine associated with the normal direction on the boundary of interest. The derivation of the angular moments for distributions of the form given in Eq. (5.75) is rather straightforward for black walls ($\epsilon_w = 1$), which are of interest in this thesis. However, if the walls also reflect a portion of the incoming radiation, i.e, $\epsilon_w < 1$, computations of the full moments of the distribution of Eq. (5.75) would involve the partial first-order angular moment of the incoming intensity distribution. The latter moment can be evaluated in a rather straightforward manner with the P_N closures owing to the existence of closed-form analytical expressions for the partial angular moments of any order. For the M_N closures on the other hand, as has been mentioned throughout this thesis, closed-form analytical integrals of the underlying intensity distribution, whether full or partial, only exist for the first-order approximation, i.e, the M_1 closure, in the case of one-dimensional gray radiation obeying Bose-Einstein statistics. As such, computing moments of the distribution of Eq. (5.75) for $\epsilon_w < 1$ would present additional challenges as it would require on-the-fly numerical solution of the entropy optimization problem or more efficient alternative such as the development of interpolative-based approximations of the partial angular moments for the M_N closures.

5.4 Anisotropic Adaptive Mesh Refinement

Typical computational fluid dynamics (CFD) problems are usually hard to solve due to numerical stiffness associated with disparate spatial and temporal scales. More specifically, certain areas of the computational domain may require higher resolution than

others due to the existence of particular features (shock, steep gradients, discontinuities). A block-based hierarchical data structure can be used here in conjunction with the finite-volume scheme described above to facilitate automatic solution-directed mesh adaptation on multi-block meshes according to physics-based criteria. By changing the mesh based on the physics-based criteria as the computations are performed, areas with particular solution features are resolved with higher mesh densities, while areas with smaller solution changes are evaluated with coarser meshes. When combined with the finite-volume scheme described above, the overall solution procedure can be used to accurately treat problems with steep gradients in the radiation solutions and small length scales with reduced computational costs.

A flexible block-based AMR scheme has been proposed by Groth and co-workers [25, 26, 28, 29, 168], which is suitable for implementation on large-scale distributed-memory computing clusters and has been successfully used for a range of physically-complex flows. The scheme borrows aspects from previous work by Berger and co-workers [169–172], Quirk [173], and De Zeeuw and Powell [174] for Cartesian grids. In the AMR scheme, the systems of moment equations are first integrated forward in time on an initial structured, multi-block mesh in order to obtain volume-averaged solution quantities. The mesh is then adapted by coarsening or refining the block designated by the refinement criteria. A hierarchical tree-like data structure, shown in Fig. 5.3, is used to retain

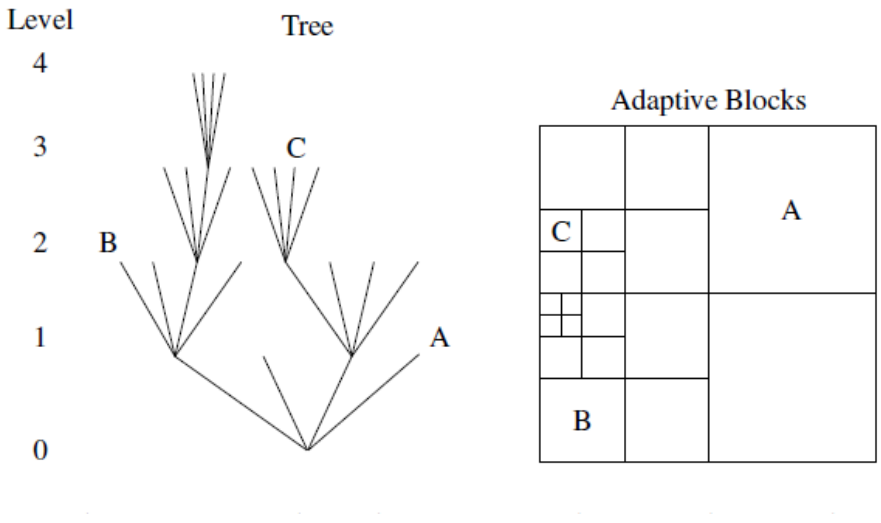

Figure 5.3: Adaptive mesh refinement quad-tree data structure and associated solution blocks for a quadrilateral mesh.

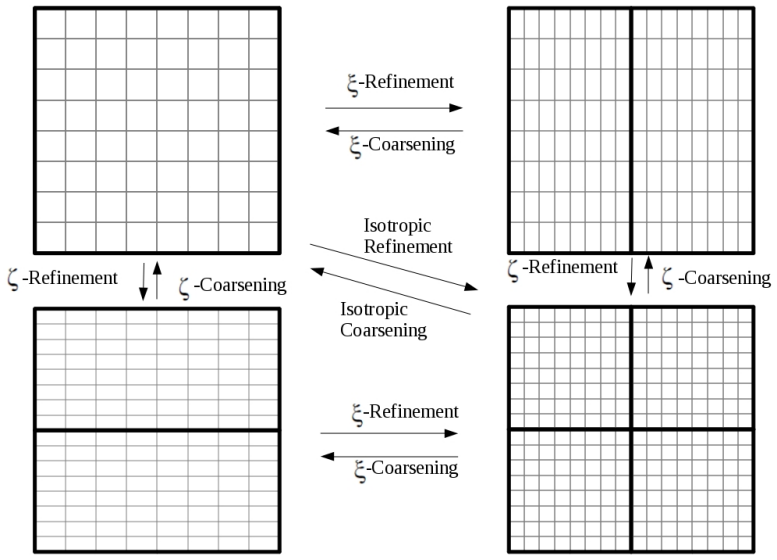

Figure 5.4: Illustration of refinement and coarsening of an 8 x 8 block, during (i) anisotropic AMR in ξ, (ii) anisotropic AMR in ζ and (iii) isotropic AMR cell division. Their geometrical relationships are also represented.

connectivity between solution blocks and track their refinement history. The blocks requiring refinement are termed "parents" and are divided into four new block called "children". Each child is a new block with the same number of cells as its parent, thereby doubling the mesh resolution in the corresponding region. Coarsening flagged blocks is carried out by reversing this process and combining four children into one single parent.

The AMR scheme described above refines the mesh equally in all directions based on the refinement criteria. However, in problems with anisotropic features, refinement of the mesh may only be needed in a specific direction. In such situations, an anisotropic variant of the isotropic AMR procedure can offer greater flexibility and further computational savings by adding directionality to the refinement process. Following the work by Groth *et al.* [175, 176] for computational magneto-hydrodynamics, Zhang and Groth [177] proposed an anisotropic AMR technique for computations in two-dimensional problems. Extensions to the three-dimensional case have also been considered by Freret *et al.* [178–182]. The procedure is somewhat similar to that of the isotropic AMR, the

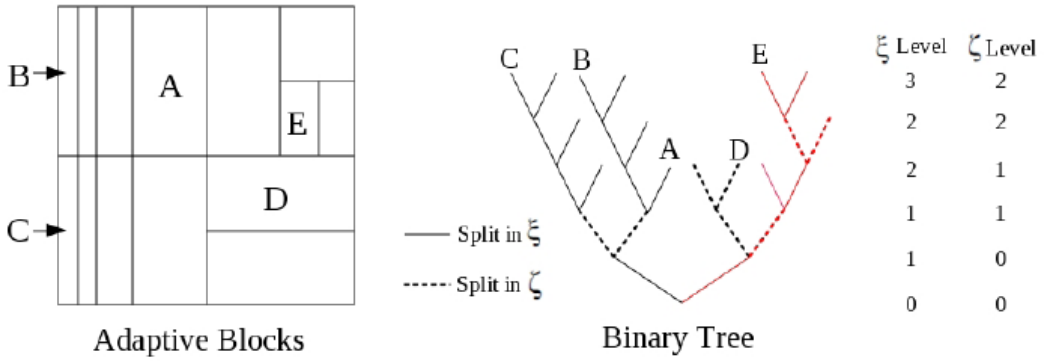

Figure 5.5: Adaptive mesh refinement binary-tree data structure and associated solution blocks for a quadrilateral mesh.

main distinction lying in the way blocks are divided. For a 2D Cartesian mesh, isotropic AMR divides each parent block into four children, which is equivalent to doubling the mesh resolution in both directions. In comparison, the anisotropic AMR technique allows each parent block to be divided into two children by splitting the parent blocks in either one of the directions of interest, as shown in Fig. 5.4. As a result, cell resolution doubles in the direction of interest, but remains the same in the other directions. Fig. 5.5 illustrates the hierarchical tree-like data structure used to retain connectivity between blocks and track their refinement history.

The refinement criteria used in this thesis are based on the gradient of the total radiative energy, $I^{(0)}$, computed numerically from neighbouring cells solutions. In the case of the isotropic AMR, for which the mesh is refined equally in both directions, the refinement criteria can be written as follows

$$\epsilon_1 \propto \frac{|\nabla I^{(0)}|}{I^{(0)}}, \tag{5.76}$$

and blocks are added wherever ϵ_1 is large. On the other hand, the criteria used in the anisotropic mesh refinement procedure can be written as follows

$$\epsilon_{1x} \propto \frac{|\nabla_x I^{(0)}|}{I^{(0)}}, \tag{5.77}$$

$$\epsilon_{1y} \propto \frac{|\nabla_y I^{(0)}|}{I^{(0)}}, \tag{5.78}$$

and the mesh refinement is performed in the x-direction when ϵ_{1x} is large while the refinement in the y-direction is dictated by values of ϵ_{1y}.

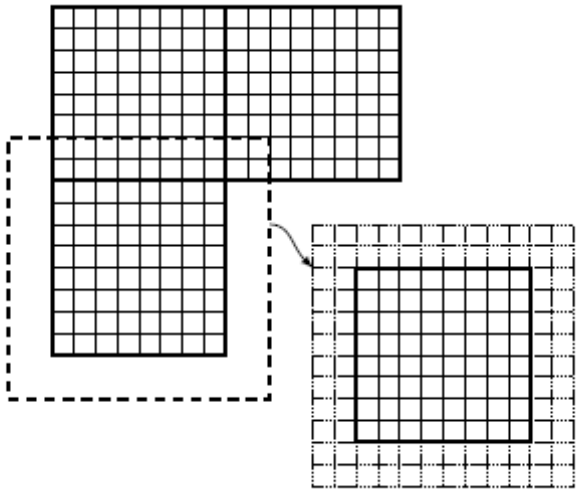

Figure 5.6: Sample multi-block grid and solution blocks depicting ghost cells.

To further decrease the overall computational time of the AMR schemes, integration of the governing equations is performed in parallel. This is achieved by distributing the computational blocks among available processors and simultaneously computing the solutions for each block on each processor. Both AMR schemes (isotropic and anisotropic) were implemented using the message passing interface (MPI) library of the C++ programming language [183].

Ghost cells which surround the solution block and overlap with cells on neighbouring blocks, as shown in Fig. 5.6, are used to share solution content through inter-block communication. The conservation properties of the finite-volume discretization are retained across blocks with resolution changes by using the fine-grid interface flux to correct the flux computed on neighbouring coarse blocks. Passing these flux corrections and the overlapping cell solution content between processors at each stage of the integration scheme accounts for the main source of inter-processor communication.

5.5 Newton Krylov Schwarz (NKS) Method

The finite-volume solution procedure adopted in the present study is based on a transformation of the governing equations in two dimensional physical space into the semi-discrete form given in Eq. (5.42). This procedure results in a coupled set of linear (in the case of

P_1 and P_3) or non-linear (in the case of M_1 and M_2) ODEs. In addition to the accurate evaluation of the numerical fluxes at the cell interfaces, which was discussed above in Section 5.2.1, a procedure for the evolution of the solution (in time for unsteady problems or to steady-state for steady problems) is also required in order to solve the coupled ODEs. It is however worth mentioning that only steady-state solutions of the RTE are of interest herein. This can be justified by the fact that the times scales associated with radiative heat transfer are much smaller compared to those of the other phenomena involved in most combustion processes.

Various numerical time-marching schemes can be used for the solution evolution procedure of Eq. (5.42), some of the more common being explicit Euler and Runge-Kutta methods. These two approaches are however conditionally stable and as such limited by the Courant-Friedrichs-Lewy (CFL) and von Neumann stability conditions [155]. For these reasons, they have difficulty in the context of numerically stiff systems of equations, for which they may involve excessive iterations to converge as they would generally require very small time-steps. Multigrid-based approaches [184] have shown promising results for aerodynamic simulations, where they were observed to be very good at accelerating convergence. In the context of turbulent non-premixed combustion however, Gao *et al.* [28, 185] found that a multigrid solution procedure still requires a relatively large number of iterations and/or time steps.

Implicit methods represent good candidates for effectively addressing the issues of stability and convergence, which may be encountered with explicit time-marching solution procedures. They are known to be much more stable than their explicit counterparts and are also less sensitive to numerical stiffness. This in turn implies that larger time steps can be used. Their additional robustness however comes at the expense of increases in computational efforts per iteration and memory overhead, which arise from the resulting linear system of equations that must be solved. Nevertheless, for many numerically stiff problems, the higher computational expenses per iteration resulting from fully implicit treatments can be compensated by the use of sufficiently large time steps, thereby yielding an overall more efficient solution procedure.

In the present study, Newton's method is applied to obtain steady-state solutions for the system of linear/non-linear moment equations given in Eq. (5.1) by relaxing the

semi-discrete form of the latter (see Eqs. (5.41) and (5.42)) to a steady-state such that

$$\mathbf{R}(\mathbf{U}) = \frac{d\mathbf{U}}{dt} = \mathbf{0}. \tag{5.79}$$

The particular implementation of Newton's method used here has been developed previously by Groth and Northrup [168] as well as Charest *et al.* [17, 29] for computations on large multi-processor parallel clusters. It consists of a Jacobian-free inexact Newton method coupled with an iterative Krylov subspace linear solver. Given an initial estimate $\mathbf{U}^0$, Newton's method seeks a solution to Eq. (5.79) by iteratively solving a sequence of linear systems until a desired reduction of the residual is achieved, i.e., $\|\mathbf{R}(\mathbf{U}^k)\| < \epsilon\|\mathbf{R}(\mathbf{U}^0)\|$, where the parameter ϵ is the tolerance and is given a value of 10^{-10} in this work. At the k^{th} Newton step iteration, the linear system to be solved has the form

$$\left(\frac{\partial \mathbf{R}}{\partial \mathbf{U}}\right)^k \Delta\mathbf{U}^k = \mathbf{J}(\mathbf{U}^k)\Delta\mathbf{U}^k = -\mathbf{R}(\mathbf{U}^k), \tag{5.80}$$

where $\mathbf{J} = \partial\mathbf{R}/\partial\mathbf{U}$ is the residual Jacobian, and the improved solution at the k^{th} step is determined using

$$\mathbf{U}^{k+1} = \mathbf{U}^k + \Delta\mathbf{U}^k. \tag{5.81}$$

The linear system of equations defined by Eq. (5.80) tends to be large, sparse, and non-symmetric. One effective approach that is widely used for solving systems of such type is the GMRES technique, developed by Saad and co-workers [186–189]. The GMRES is an Arnoldi-based solution technique which generates orthogonal bases of the Krylov subspace to construct the solution. A particularly attractive feature of the technique is the fact that explicit formulation of the Jacobian matrix, $\mathbf{J}$, is not required. Instead, only matrix-vector products are required at each iteration to create new trial vectors, hence reducing the required storage. Termination also generally only requires solving the linear system to some specified tolerance, $\|\mathbf{R}(\mathbf{U}^k) + \mathbf{J}(\mathbf{U}^k)\Delta\mathbf{U}^k\| < \zeta\|\mathbf{R}(\mathbf{U}^k)\|$, where ζ is typically in the range 0.1–0.5 [190].

The matrix-vector products required at each iteration of the GMRES method are computed in a approximate manner by means of numerical differentiation based on Fréchet derivatives [188, 191–196]. This procedure is referred to as a "matrix-free" or "Jacobian-free" approach, which, when applied to Eq (5.80) yields

$$\mathbf{J}\mathbf{v} \approx \frac{\mathbf{R}(\mathbf{U} + \varepsilon\mathbf{v}) - \mathbf{R}(\mathbf{U})}{\varepsilon}, \tag{5.82}$$

where $\mathbf{v}$ is a Krylov vector, $\mathbf{R}(\mathbf{U}+\varepsilon\mathbf{v})$ is the physical residual vector evaluated at some perturbed solution state and ε is a small scalar quantity, the choice of which directly impacts the performance of the Jacobian-free method. The study of Nielsen *et al.* [191] has shown that $\varepsilon = \varepsilon_\circ / ||\mathbf{v}||_2^{1/2}$ yields good performance, with $\varepsilon_\circ \approx 10^{-8}$–$10^{-7}$, and the current implementation therefore makes use of this expression.

To guarantee effectiveness of the GMRES method, right preconditioning of the matrix $\mathbf{J}$ is performed, which helps facilitate the solution of Eq. (5.80) without affecting the solution residual vector $\mathbf{b} = -\mathbf{R}(\mathbf{U}^k)$. The preconditioning is performed as follows

$$(\mathbf{J}\mathbf{M}^{-\mathbf{1}})(\mathbf{M}\mathbf{x}) = \mathbf{b}, \tag{5.83}$$

where $\mathbf{M}$ is the preconditioning matrix and $\mathbf{x} = \Delta\mathbf{U}^k$. A combination of an additive Schwarz preconditioner and a block incomplete lower-upper (BILU) local preconditioner is used which is easily implemented in the block-based anisotropic AMR scheme described in Section 5.4. The additive Schwarz preconditioner updates the solution in each block simultaneously whereas shared boundary data is not updated until a full cycle of updates has been performed on all domains. The preconditioner is defined as follows

$$\mathbf{M}^{-\mathbf{1}} = \sum_{k=1}^{N_B} \mathbf{B}_\mathbf{k}^\mathbf{T} \mathbf{M}_\mathbf{k}^{-\mathbf{1}} \mathbf{B}_\mathbf{k}, \tag{5.84}$$

where N_B is the number of blocks and $\mathbf{B_k}$ is the gather matrix for the k^{th} domain. The local preconditioner $\mathbf{M}_\mathbf{k}^{-\mathbf{1}}$ is based on block ILU(p) factorization [189] of the Jacobian for the first-order approximation of each domain. In this work, the level of fill, p, was maintained at 4 in order to minimize storage requirements.

In the context of gray radiation, the Jacobian matrices arising from the system of equations resulting from the M_1, M_2, P_1, and P_3 closures can be inverted very efficiently by means of the original implementation of the ILU(p) factorization algorithm for the purpose of preconditioning the system of equations given by Eq. (5.83). For non-gray radiation, on the other hand, the computational framework developed in this thesis consists of solving the RTE simultaneously at all the quadrature points used for the integration over the spectrum of frequencies. The resulting Jacobian matrix, for any the closure techniques investigated in this thesis, is however block diagonal, since the moment equations from one spectral location (or quadrature point) to another are not coupled. In this case, a more efficient alternative to the original implementation of the ILU(p) factorization

procedure has been proposed, which consists of preconditioning the Jacobian matrix for each quadrature point separately, instead of inefficiently inverting directly the full block diagonal Jacobian matrix as would be the case with the original implementation. It is worth mentioning that another alternative to the computational framework for non-gray radiation adopted herein exists, which consists of solving the RTE at each quadrature point separately, and such an approach couples naturally and efficiently with the original implementation of the ILU(p) factorization algorithm. However, for the radiation problems considered in this thesis, the procedure adopted herein for non-gray radiation, along with the improvements for the preconditioning algorithm, was observed to yield a better performance in terms of computational efficiency. This can be attributed to the fact that the latter approach, unlike its alternative, has less of a tendency to over-resolve wavenumbers associated with low radiative energy density.

The application of Newton's method to the system of moment equations does not yield an unconditionally stable scheme, and failure can occur, especially when the initial solution estimates fall outside the radius of convergence. To ensure global convergence of the algorithm, the implicit Euler startup procedure with switched evolution/relaxation (SER) that was proposed by Mulder and Van Leer [197] was used. Application of this startup procedure to the semi-discrete form of the governing equations gives

$$\left[-\frac{\mathbf{I}}{\Delta t^n}+\left(\frac{\partial \mathbf{R}}{\partial \mathbf{U}}\right)^n\right]\Delta \mathbf{U}^n=-\mathbf{R}^n, \tag{5.85}$$

where $\mathbf{I}$ is the identity tensor and Δt^n is the time step. In the SER approach, the time step is varied from some small finite value and gradually increased as the steady state solution is approached. As $\Delta t^n \to \infty$, Newton's method is recovered. In particular, a time step multiplier, ν^n, is introduced, which increases as the solution residual, $\mathbf{R}$, decreases, and is of the following form

$$\nu^n=\nu^{\min}\max\left(1,\frac{1}{||\mathbf{R}||_2}\right), \tag{5.86}$$

where the parameter, $\nu^{\min}$, also refereed to as CFL number, is an adjustable minimum or initial multiplier.

The time step size is then determined by applying the multiplier of Eq. (5.86) in conjunction with a set of stability conditions, thereby yielding

$$\Delta\tau^n=\nu^n\min\left(\min\left(\frac{\Delta x}{\lambda_i}\right),\left(\max\left(\frac{\partial \mathbf{S}}{\partial \mathbf{U}}\right)\right)^{-1}\right), \tag{5.87}$$

where λ_i, $i = 1, 2, \ldots, N_c$, are the eigenvalues of the system of moment equations under consideration. The terms $\Delta x/\lambda_i$ correspond to stability criteria arising from the wave propagation phenomena. On the other hand, the inverse of the maximum diagonal of the radiative source term Jacobian, $\partial \mathbf{S}/\partial \mathbf{U}$, is incorporated as a measure of radiative extinction time scales. A value for $\nu^{\min}$ or CFL number between 10–100 is typically used during the startup phase of the proposed Newton method.

Chapter 6

Numerical Results: Assessment in Gray Participating Media

In this section, the predictive performance and accuracy of the proposed interpolative-based second-order M_2 maximum-entropy moment closure for gray radiation are assessed. More specifically, its solutions are compared to and evaluated against those of its lower-order counterpart, i.e., the first-order M_1 maximum entropy closure, as well as those of the P_1 and P_3 spherical harmonic approximations and the DOM. The comparisons are performed in terms of the radiative energy density, $I^{(0)}$, the radiative heat flux, $I^{(1)}$, and the radiative source term, S_R, as defined in Eq. (2.13) of Chapter 2. The assumption of isotropic scattering ($\Phi(\vec{s}\,', \vec{s}) = 1$) is employed in all the problems where scattering effects are accounted for. In all of the cases studied, steady-state numerical solutions for the gray M_1, M_2, P_1, and P_3 closures are obtained using the upwind Godunov-type finite volume scheme and the NKS iterative procedure described earlier in Chapter 5. Moreover, the method of characteristics is used to provide boundary conditions to the systems of equations arising from the aforementioned moment closure techniques. For the DOM, the space marching iterative technique described by Charest *et al.* [29] is used to solve the resulting set of ODEs. Unless specified otherwise, the DOM is used with quadrature rules based on the T_4 scheme of Thurgood *et al.* [92]. For some of the cases studied herein, exact analytical solutions of the RTE are available and are therefore used as references in the comparisons.

The first set of test cases consists of radiative transfer between two parallel plates of

infinite length similar to those examined previously by Hauck [54,55]. Different scenarios are considered whereby the properties of the medium (optical properties and temperature distribution) between the two plates, as well as the separation distance between the plates, are varied in order to assess the impact on the predictive capabilities of the proposed M_2 closure. The next test problem involves radiative heat transfer throughout a cold (non-emitting) and absorbing medium contained within a square enclosure for which all of the walls have the same temperature. The final test problem aims at assessing the predictive capabilities of the proposed interpolative M_2 closure for gray radiation associated with two identical beams of radiative particles crossing at an angle of 90°. This last case was inspired by a similar problem studied previously by Pichard *et al.* [53] and is considered here for the purpose of illustrating the ability of the M_2 closure to capture accurately the crossing of two separate beams of photons.

Solution comparisons for all the radiation problems considered herein are made based on grid-independent results for the M_1, M_2, P_1, and P_3 moment closures, as well as the DOM. The procedure adopted herein to obtain grid-independent solutions consists of comparing predictions of each of the radiation models on a sequence of increasingly refined grids and subsequently selecting the mesh size for which no significant change in the solution is observed as the mesh is further refined. For each of the cases studied, comparisons of the relative computational costs of each solution method in terms of the total computational time to obtain a solution were also performed and are reported along with the mesh convergence study results.

Note that, when comparing the reported computational times, the computational/memory storage costs should also be taken into account. In particular, for the one- and two-dimensional canonical problems examined herein, the storage requirements for the M_1 and P_1 moment closures are such that three transport equations are solved at each location within the computational grid. For the M_2 closure, 6 moment equations are solved whereas the P_3 closure involves 10 unknowns and, for the DOM simulations, the T_4 angular quadrature scheme [92] is used with 64 angular directions at each point within the grid. It should be noted that the relative numbers of unknowns at each grid point would change for fully three-dimensional problems with the M_1 and P_1 closures involving 4 unknowns, the M_2 closure resulting in 10 unknowns, the P_3 closure involving 20 unknowns, and the DOM requiring the solution of 128 unknowns per grid point. The low-order M_1 and P_1 moment closures quite clearly offer significant savings in storage rel-

ative to the other methods. Finally, for all of the canonical-type gray radiation problems considered here having either one-dimensional or rectangular two-dimensional computational domains, the space marching solution method used here to obtain the DOM solutions [29] is extremely efficient and therefore the DOM solutions reported here generally require less computational effort in terms of computational time compared to the moment closure techniques. However, for practical applications involving more complex three-dimensional geometries combined with more realistic physics, space marching techniques can lose their effectiveness and the moment closures are expected to be far more competitive.

6.1 Parallel Plates

The geometry for the parallel plate test problems considered in the present study for the assessment of the proposed interpolative-based M_2 closure for gray radiation is illustrated in Fig. 6.1. The bounding wall surfaces are assumed to be black, i.e., with emissivities $\epsilon_L = \epsilon_U = 1$. As a first step, different plate separation distances are considered while the medium between the two plates is taken to be cold (non-emitting) and non-scattering. Next scattering is considered and its impact on the accuracy of the M_2 closure is assessed. Grid convergence analyses for the parallel plate test problems considered herein were performed on a sequence of increasingly refined grids, characterized by $N_{cells} = \{20, 40, 80, 160, 320\}$ cells. The accuracy of the predictions of the radiative source term associated with each of the grids in the sequence was assessed via the L^1 error with respect to solutions obtained on a reference grid with $N_{cells} = 640$ cells.

6.1.1 Exact Solution for Non-Scattering Case

For a non-scattering medium confined between two black, parallel plates, there exist an exact analytical solution to the radiative transfer equation, Eq. (2.14), as given by Modest [84]. The distribution of the radiative intensity emitted from the lower and upper plates, respectively, are given by

$$\begin{aligned} I^+(\tau,\mu) &= I_{w,L}e^{-\tau/\mu} + \tfrac{1}{\mu}\textstyle\int_0^\tau I_b(\tau\prime)e^{-(\tau-\tau\prime)/\mu}\mathrm{d}\tau\prime,\ 0<\mu<1, \\ I^-(\tau,\mu) &= I_{w,U}e^{(\tau_L-\tau)/\mu} + \tfrac{1}{\mu}\textstyle\int_0^\tau I_b(\tau\prime)e^{(\tau\prime-\tau)/\mu}\mathrm{d}\tau\prime,\ -1<\mu<0, \end{aligned} \tag{6.1}$$

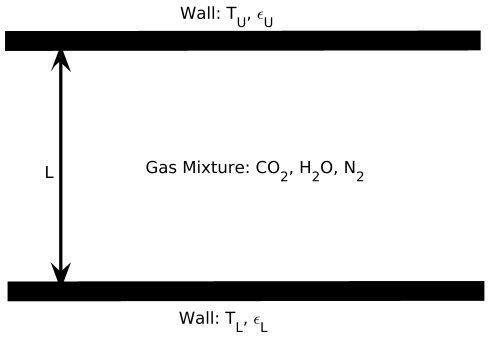

Figure 6.1: Illustration of geometry for test problems involving for gray radiative transfer between parallel plates.

where $\tau_L = \int_0^L \beta(s)ds$ is the optical thickness (or optical depth), L is the distance between the two plates, $I_{w,L}$ and $I_{w,U}$ are the intensities leaving the lower and upper plates respectively, and $I_b(\tau\prime) = I_b$ is the blackbody radiative intensity associated with optical depth $\tau\prime$.

The partial radiative energy densities, $I^{(0)\pm}$, and the partial radiative fluxes, $I^{(1)\pm}$, associated with the partial distributions, $I^{\pm}$, given in Eq. (6.1), can be accurately computed by means of a 20-point Gauss-Legendre quadrature rule, along with the appropriate quadrature weights and integration domains, as follows

$$I^{(0)\pm} = \pm 2\pi \int_0^{\pm 1} I^{\pm}(\tau, \mu)\mathrm{d}\mu = 2\pi \sum_{n=1}^{20} w_n I^{\pm}(\tau, \mu_n), \tag{6.2}$$

$$I^{(1)\pm} = \pm 2\pi \int_0^{\pm 1} \mu I^{\pm}(\tau, \mu)\mathrm{d}\mu = 2\pi \sum_{n=1}^{20} w_n \mu_n I^{\pm}(\tau, \mu_n), \tag{6.3}$$

where the abscissas, μ_n, and weights, w_n, are determined by the Gauss-Legendre quadrature in the appropriate domains (i.e., $\mu_n \in [0, 1]$ for lower plate and $\mu_n \in [-1, 0]$ for upper plate). The overall radiative energy at any optical distance, τ, between the two plates is the sum of the radiative energies arising from both the lower and upper plates, i.e., $I^{(0)} = I^{(0)+} + I^{(0)-}$. The same also holds for the overall radiative heat flux, i.e., $I^{(1)} = I^{(1)+} + I^{(1)-}$.

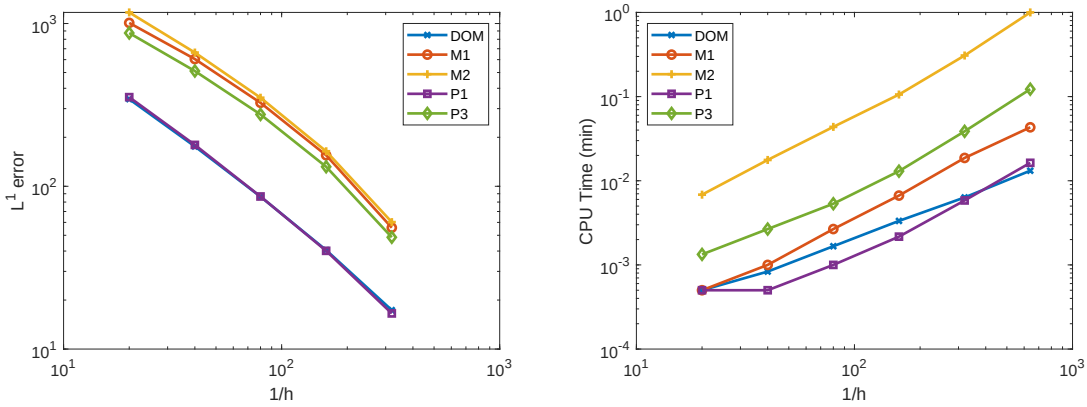

(a) (b)

Figure 6.2: Illustration of (a) grid convergence analysis on the predicted radiative source term for DOM, M_1, M_2, P_1, and P_3 and, (b) computational costs associated with each of the radiation models for the different mesh resolutions. Results are shown for radiative transfer within an absorbing, non-emitting ($T = 0\,\mathrm{K}$), non-scattering medium between two infinitely long parallel plates with a separation distance of 1 m.

6.1.2 Absorbing-Non-Emitting Medium with No Scattering

The first test problem involving gray radiative transfer between parallel plates consists of a cold (non-emitting, i.e., $T = 0\,\mathrm{K}$) and non-scattering medium with an absorption coefficient $\kappa = 2\,\mathrm{m}^{-1}$. The bounding plates are taken to be at a temperature of $T = 500\,\mathrm{K}$. Two plate separations are considered for the comparisons, i.e., $L = 1$ m and $L = 10$ m. Results of grid convergence analysis as well as comparisons of computational costs are illustrated in Fig. 6.2 for the smaller plate separation and Fig. 6.3 for the larger plate separation. Comparisons of the solutions obtained using the proposed M_2 interpolative-based closure to those of the M_1, P_1 and P_3 moment closures as well as the DOM are depicted in Fig. 6.4 for the smaller plate separation and in Fig. 6.5 for the larger separation distance. For both plate separations, the comparisons are made based on the solutions obtained on the second-finest grid, with $N_{cells} = 160$ cells. In fact, as can be seen in Fig. 6.2(a) and 6.3(a) for the smaller and larger plate separations, respectively, this mesh resolution falls well within the asymptotic range of convergence of the numerical method, thereby ensuring that the comparisons of the predicted solutions are not affected by spatial discretization errors.

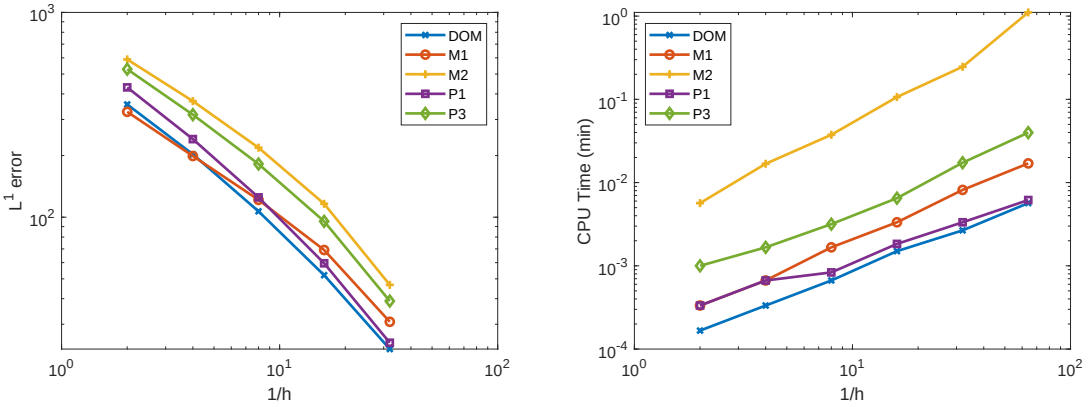

(a) (b)

Figure 6.3: Illustration of (a) grid convergence analysis on the predicted radiative source term for DOM, M_1, M_2, P_1, and P_3 and, (b) computational costs associated with each of the radiation models for the different mesh resolutions. Results are shown for radiative transfer within an absorbing, non-emitting ($T = 0\,\mathrm{K}$), non-scattering medium between two infinitely long parallel plates with a separation distance of 10 m.

For the small plate separation, it is readily apparent from Fig. 6.4 that the P_1 and P_3 closures yield somewhat better predictions than the M_1 maximum entropy closure, both qualitatively and quantitatively. It can also be observed that the M_1 model produces a nonphysical discontinuity in the radiative energy (and also consequently in the radiative source term). Near either of the bounding walls, the distribution of radiative intensity is beam-like as it is dominated by the incoming flux from the closest boundary, and the eigenvalues associated with the M_1 closure have the same sign. In the centre of the medium between the two plates on the other hand, the true solution is essentially two identical beam-like distributions pointed in opposite directions. This crossing of identical beam-like distributions, which is characterized by a zero net flux, cannot be properly captured by the M_1 closure, which predicts an isotropic distribution of the radiative intensity. This is due to the fact that the only available information in the M_1 distribution of radiative intensity for describing departures from the isotropic limit is the radiative flux. In the latter case, the M_1 closure (in the one-dimensional case) has two eigenvalues of opposite signs. As was illustrated by Brunner and Holloway [51], the transitions in the characteristic directions of the M_1 closure occur at the locations where the jumps in the radiative energy density are observed.

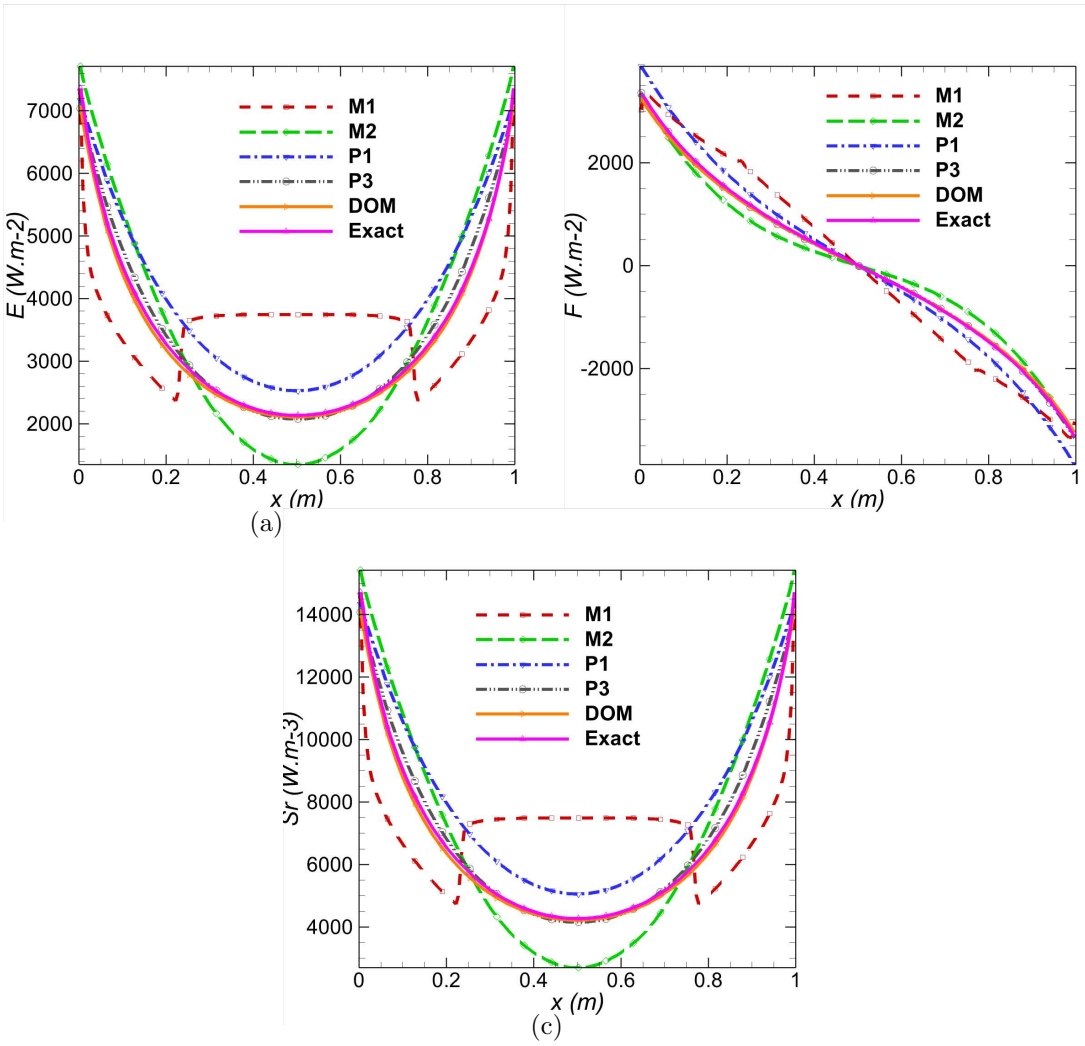

Figure 6.4: Numerical predictions of (a) the radiative energy, E; (b) radiative flux, F; and (c) the source of radiative energy transfer, S_r, obtained using the M_2 interpolative-based closure using a 160-node mesh compared to the exact analytical solution as well as the predictions of the M_1 maximum-entropy closure, P_1 and P_3 spherical harmonic closures, and DOM. Results are shown for radiative transfer within an absorbing, non-emitting ($T = 0\,\mathrm{K}$), non-scattering medium between two infinitely long parallel plates with a separation distance of 1 m.

For the larger plate separation, the M_1 closure still displays a jump in the solution of the radiative energy density and of the radiative source term, though not as significant as for the smaller plate separation distance. In fact, the increased distance between the bounding walls results in an increase in the optical depth of the medium between the plates which in turns translates into more substantial attenuation of the beams of

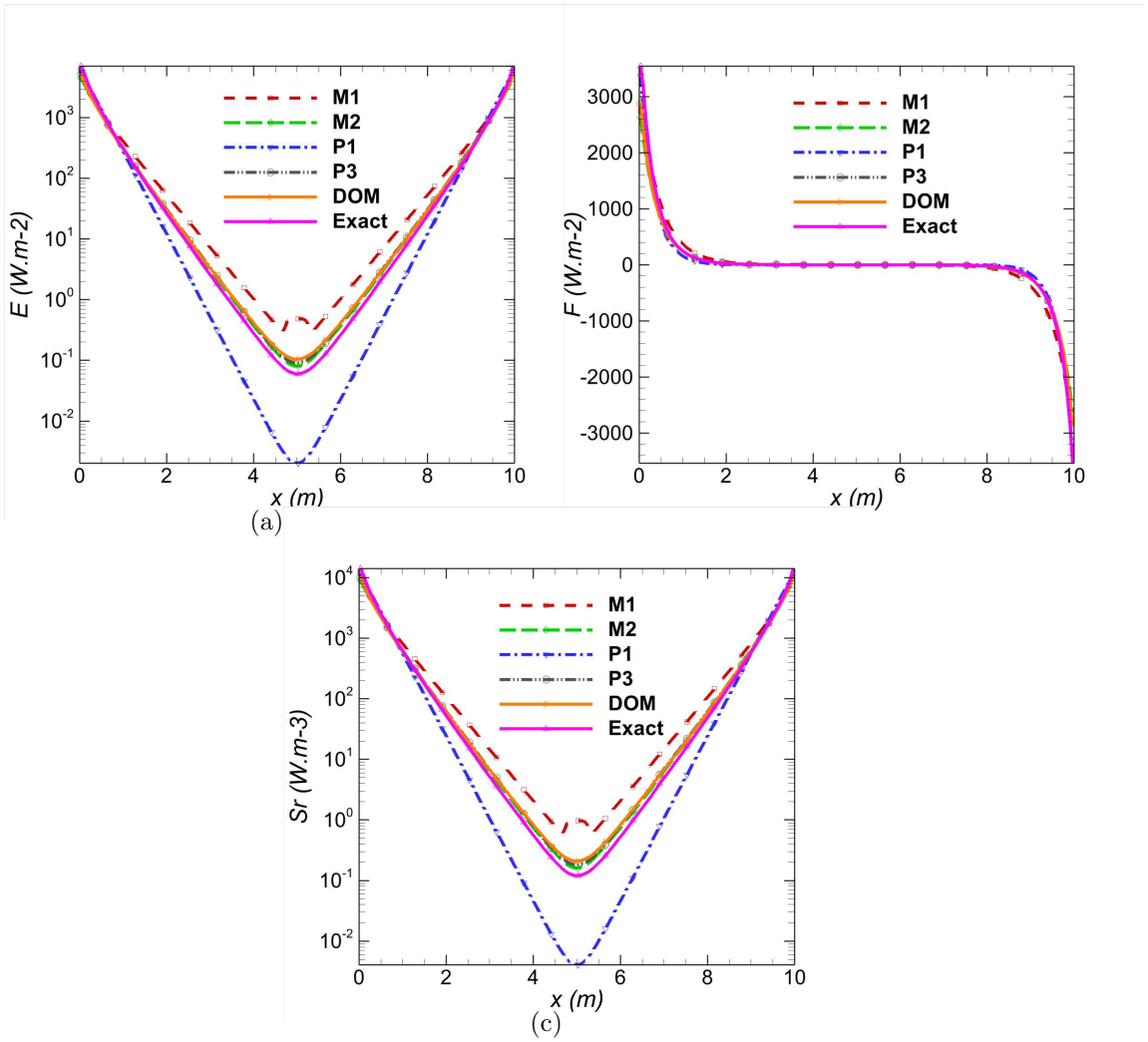

Figure 6.5: Numerical predictions of (a) the radiative energy, E; (b) radiative flux, F; and (c) the source of radiative energy transfer, S_r, obtained using the M_2 interpolative-based closure using a 160-node mesh compared to the exact analytical solution as well as the predictions of the M_1 maximum-entropy closure, P_1 and P_3 spherical harmonic closures, and DOM. Results are shown for radiative transfer within an absorbing, non-emitting ($T = 0\,\mathrm{K}$), non-scattering medium between two infinitely long parallel plates with a separation distance of 10 m.

radiative energy emanating from either walls, as the centre of the medium is approached.

For both plate separation distances, the proposed second-order interpolative-based M_2 closure quite clearly overcomes the inability of the M_1 model to adequately represent radiative transport in more than one direction and also results in improved solution

accuracy compared to the latter closure. More specifically, the proposed M_2 closure produces solutions that are qualitatively in very good agreement with the exact solutions, of similar accuracy to those of the P_1 closure for the small plate separation, and virtually identical to the P_3 closure results for the larger plate separation distance.

6.1.3 Absorbing-Non-Emitting Medium with Scattering

The next parallel plates test problem considered herein aims at evaluating the impact of scattering on the solutions of the proposed M_2 closure. A cold (non-emitting, i.e., $T = 0\,\mathrm{K}$) medium is again considered with an absorption coefficient $\kappa = 2\,\mathrm{m}^{-1}$ and a scattering coefficient $\sigma_s = 2.0\,\mathrm{m}^{-1}$. The separation distance between the two plates is $L = 1$ m and the bounding walls are taken to be at a temperature $T = 500\,\mathrm{K}$. Results of grid convergence analysis for this test problem as well as computational costs comparisons are shown in Fig. 6.6. The predictions for the radiative energy density, radiative heat flux, and radiative source term obtained using the proposed M_2 interpolative-based closure as well as the M_1, P_1 and P_3 moment closures and the DOM are compared in Fig. 6.7. Solutions obtained on the second-finest grid, with $N_{cells} = 160$ cells, are again used for the

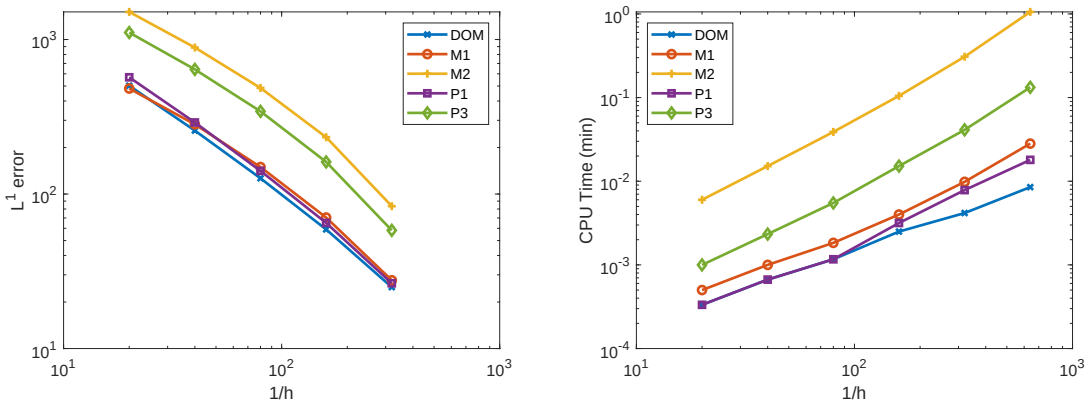

(a) (b)

Figure 6.6: Illustration of (a) grid convergence analysis on the predicted radiative source term for DOM, M_1, M_2, P_1, and P_3 and, (b) computational costs associated with each of the radiation models for the different mesh resolutions. Results are shown for radiative transfer within an absorbing-scattering, non-emitting ($T = 0\,\mathrm{K}$) medium between two infinitely long parallel plates with a separation distance of 1 m.

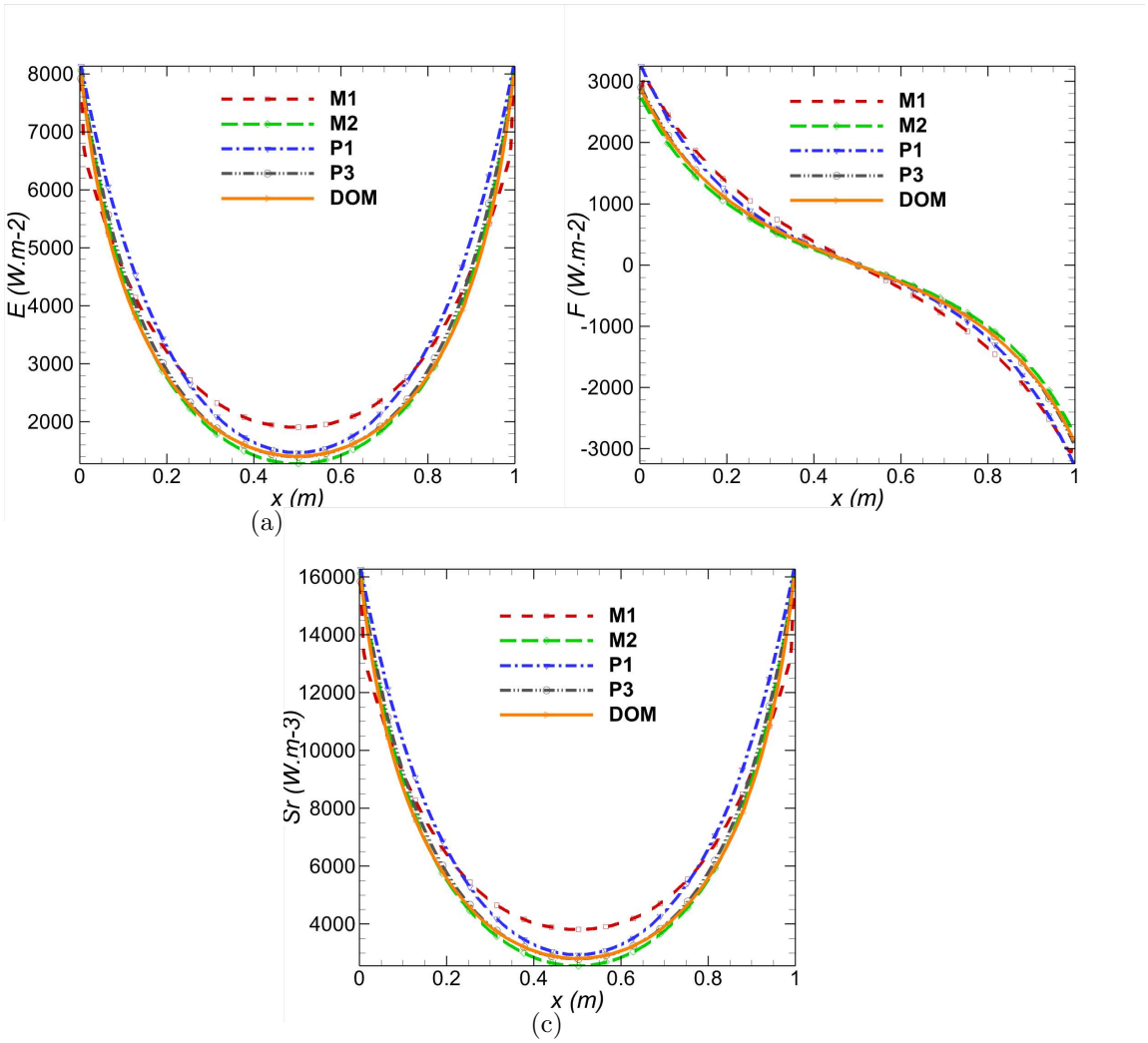

Figure 6.7: Numerical predictions of (a) the radiative energy, E; (b) radiative flux, F; and (c) the source of radiative energy transfer, S_r, obtained using the M_2 interpolative-based closure using a 160-node mesh compared to the exact analytical solution as well as the predictions of the M_1 maximum-entropy closure, P_1 and P_3 spherical harmonic closures, and DOM. Results are shown for radiative transfer within an absorbing-scattering, non-emitting ($T = 0\,\mathrm{K}$) medium between two infinitely long parallel plates with a separation distance of 1 m.

comparisons since this mesh resolution falls within the asymptotic range of convergence, as can be depicted in Fig. 6.6(a).

As an exact solution does not exist for this case, the DOM is taken as a reference for the comparisons. As can be seen in the results reported in Fig. 6.7, the M_1 closure

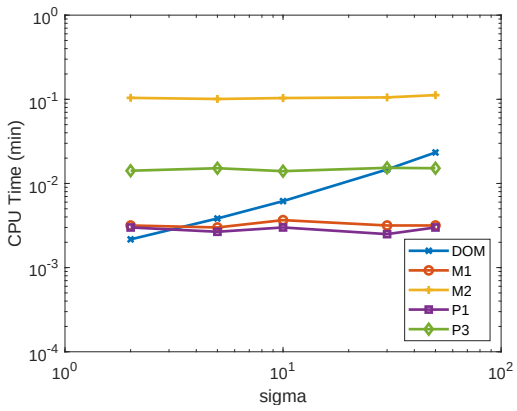

Figure 6.8: Comparison of computational costs associated with the DOM, M_1, M_2, P_1, and P_3 radiation models for different levels of scattering using a 160-node mesh. Results are shown for radiative transfer within an absorbing-scattering, non-emitting ($T = 0\,\mathrm{K}$) medium between two infinitely long parallel plates with a separation distance of 1 m..

no longer displays a non-physical jump in the solution of the radiative energy density and of the radiative source term, when isotropic scattering effects are also considered. This can be expected since the "isotropic" scattering terms yield a redistribution of the radiative intensity distribution equally along all directions of propagation spanning the full solid angle. In particular, the distributions leaving either bounding walls, in addition to being attenuated via absorption by the medium, are also redistributed uniformly along all possible directions of propagation of the photons, thereby resulting in more isotropy in the distributions compared to the non-scattering case studied in the previous section. In the centre of the medium between the two plates, the true solution is two identical and nearly isotropic distributions, and the M_1 closure is observed to properly capture this phenomenon, though its predictions are not as accurate as those of the P_1 and P_3 spherical harmonic moment closures. As can be expected, the proposed interpolative-based M_2 closure provides improved predictions of the radiative quantities under consideration when compared to its lower-order counterpart, i.e, the M_1 closure. Moreover, the M_2 closure yields more accurate predictions than the P_1 closure and is in very good agreement with the P_3 closure and the DOM.

To further asses the impact of scattering on the different radiation models of interest in the present study, the computational costs associated with these models for different levels of scattering, for a 160-node mesh, are reported in Fig.6.8. While the predictive

performance of the M_1, M_2, P_1, and P_3 moment closure techniques (in terms of computational efficiency) display little to no changes with increasing scattering effects, the DOM on the other hand loses its effectiveness as scattering becomes more important. In fact, the more important the scattering effects, the stronger the coupling between transport equations for the intensity distribution along the discrete directions involved in the DOM, and the more the number of iterations required for the space marching iterative technique used in solving the DOM equations to converge.

6.2 Square Enclosure

Radiative transfer within a square enclosure is now considered. The medium within the enclosure is cold (non-emitting, i.e., $T = 0\,\mathrm{K}$) with an absorption coefficient $\kappa = 20\,\mathrm{m}^{-1}$. All of the walls are taken to have identical temperatures of $T = 500\,\mathrm{K}$. Results of grid convergence analysis on the radiative source term, for the DOM, as well as the M_1, M_2, P_1, and P_3 moment closure techniques, are illustrated in Fig. 6.9(a). The latter analysis is performed on a sequence of increasingly uniformly refined two-dimensional grids, with $N_{cells} = \{20 \times 20, 40 \times 40, 80 \times 80, 160 \times 160, 320 \times 320\}$ cells. Moreover, the accuracy of the predictions of the radiative source term obtained on each of the grids in the sequence was assessed via the L^1 error with respect to solutions obtained on a reference grid with $N_{cells} = 640 \times 640$ cells. The grid with $N_{cells} = 160 \times 160$ cells can be observed to fall well within the asymptotic range of convergence and is deemed to provide sufficient accuracy for all the radiation models considered in the present analysis. As such, it is therefore used for the comparisons of the solutions so as to ensure that the latter are not influenced by numerical errors. Comparisons of computational costs associated with each of the approximate radiation models, for the mesh resolutions considered in the grid convergence study, are presented in Fig. 6.9(b).

The predicted distributions of the radiative energy density and the magnitude of the radiative flux within the two-dimensional enclosure, obtained using the DOM and the interpolative-based M_2 moment closure, respectively, are given in Fig. 6.10, for a (160×160)-node mesh. Additionally, the predictions of the proposed interpolative-based M_2 closure are compared to those of the M_1, P_1 and P_3 moment closures, as well as to those of the DOM, in Fig. 6.11. The comparisons are performed in terms of results for

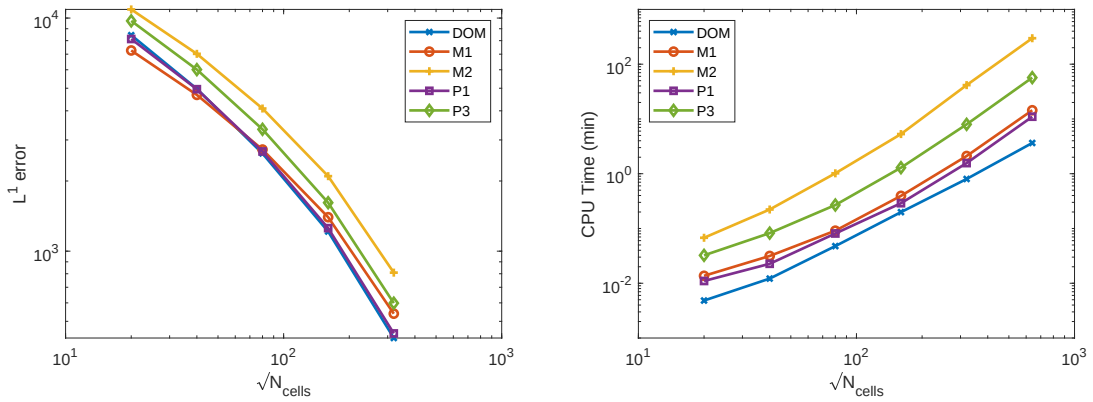

(a) (b)

Figure 6.9: Illustration of (a) grid convergence analysis on the predicted radiative source term for DOM, M_1, M_2, P_1, and P_3 and, (b) computational costs associated with each of the radiation models for the different mesh resolutions. Results are shown for test problem involving radiative transfer throughout an absorbing, non-emitting and non-scattering medium confined within a square enclosure with wall temperatures of $T = 500\,\mathrm{K}$.

the radiative energy density, magnitude of the radiative flux, and radiative heat source, along the line of the rectangular enclosure parameterized by $y = 0.5$ m.

Both the M_1 and P_1 moment closures fail to predict accurately the distributions of the radiative energy density and radiative source term near the centre of the medium within the square enclosure. In the absence of scattering and emission effects, absorption is the only mechanism via which the radiative field interacts with the background medium. In particular, radiative particles emanating from the bounding walls travel along straight lines while being attenuated via absorption processes only. Photons propagating towards the centre of the enclosure travel longer distances when emitted closer to the corners of the square enclosure as compared to radiative particles emanating from near the centre of one of the bounding walls. Since the level of attenuation increases with the optical depth, it therefore follows that the true solution at the centre of the square enclosure is a non-isotropic distribution which is symmetric with respect to both the x- and y-axis, with its maximum occurring along the aforementioned axes of symmetry, and is associated with a zero net flux of radiative particles. However, for angular distributions reconstructed with angular moments up to only first order, a net radiative flux of zero can only be associated with an isotropic distribution of the radiative intensity, given the

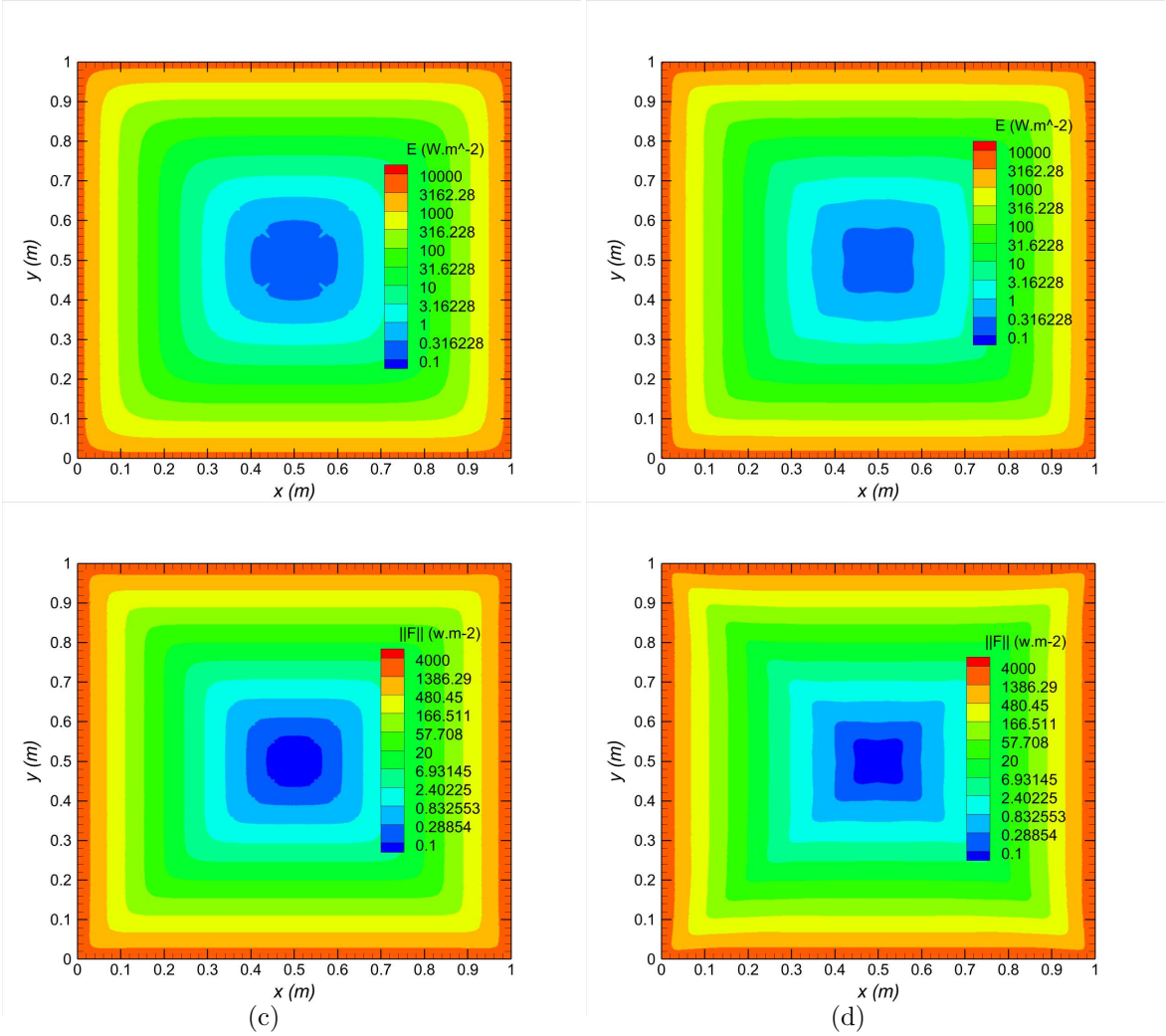

Figure 6.10: Predicted distribution of the radiative energy density using (a) the DOM & (b) the interpolative-based M_2 moment closure; and of the distribution of the magnitude of the radiative flux as obtained using (c) the DOM & (d) our interpolative-based M_2 moment closure, on a (160×160)-node mesh. Results are shown for test problem involving radiative transfer throughout an absorbing, non-emitting and non-scattering medium confined within a square enclosure with wall temperatures of $T = 500\,\mathrm{K}$.

fact that the first-order angular moment is the only available angular information for describing departures from the isotropic limit. This explains the fact that both the M_1 and P_1 closures fail to properly predict the distributions of the radiative energy density and radiative source term in the vicinity of the centre of the enclosure. As is evident from the results shown here, these limitations of the aforementioned first-order moment closure techniques can be overcome by providing additional angular information, via

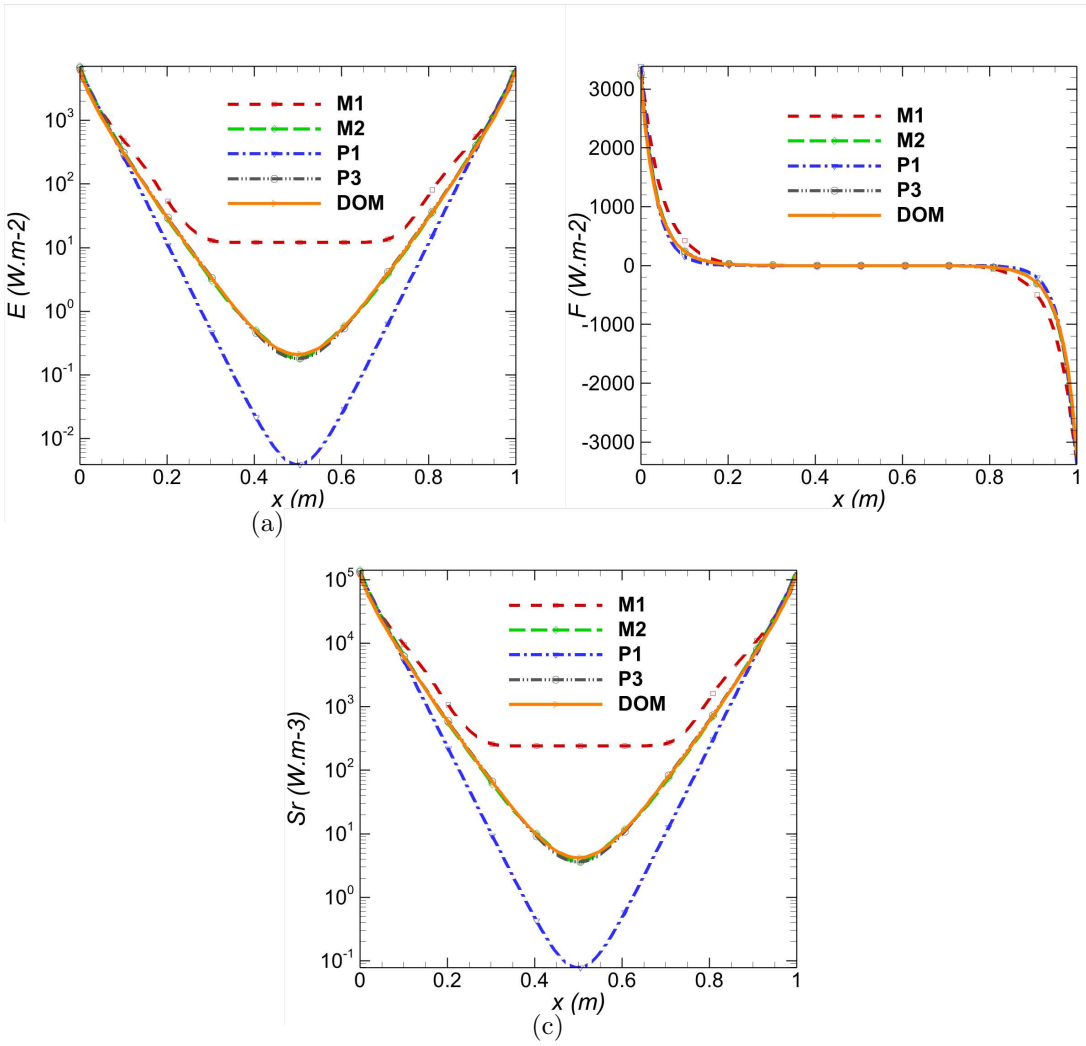

Figure 6.11: Numerical predictions of (a) the radiative energy, E; (b) magnitude of the radiative flux, $||F||$, (right top panel); and (c) the source of radiative energy transfer, S_r, along the centre line ($y = 0.5$ m) of the square enclosure, obtained using the M_2 interpolative-based closure using a (160×160)-node mesh compared to the predictions of the M_1 maximum-entropy closure, P_1 and P_3 spherical harmonic closures and DOM. Results are shown for test problem involving radiative transfer throughout an absorbing, non-emitting and non-scattering medium confined within a square enclosure with wall temperatures of $T = 500\,\mathrm{K}$.

consideration of higher-order angular moments, in the reconstruction of the assumed form of the radiative intensity distribution, thereby allowing the capture of more of the features of the true distribution. It is readily apparent from the comparisons that the predictions of both the newly proposed M_2 interpolative-based closure and the P_3 model

are superior to those of the M_1 and P_1 closures and virtually equivalent to those of the DOM. Furthermore, it should be noted that there is some indication of ray effects in the DOM T_4 results of Figs. 6.10(a) and these effects are clearly absent in the corresponding M_2 closure results. The lack of ray effects in the predictions of moment closure techniques is an obviously desirable feature.

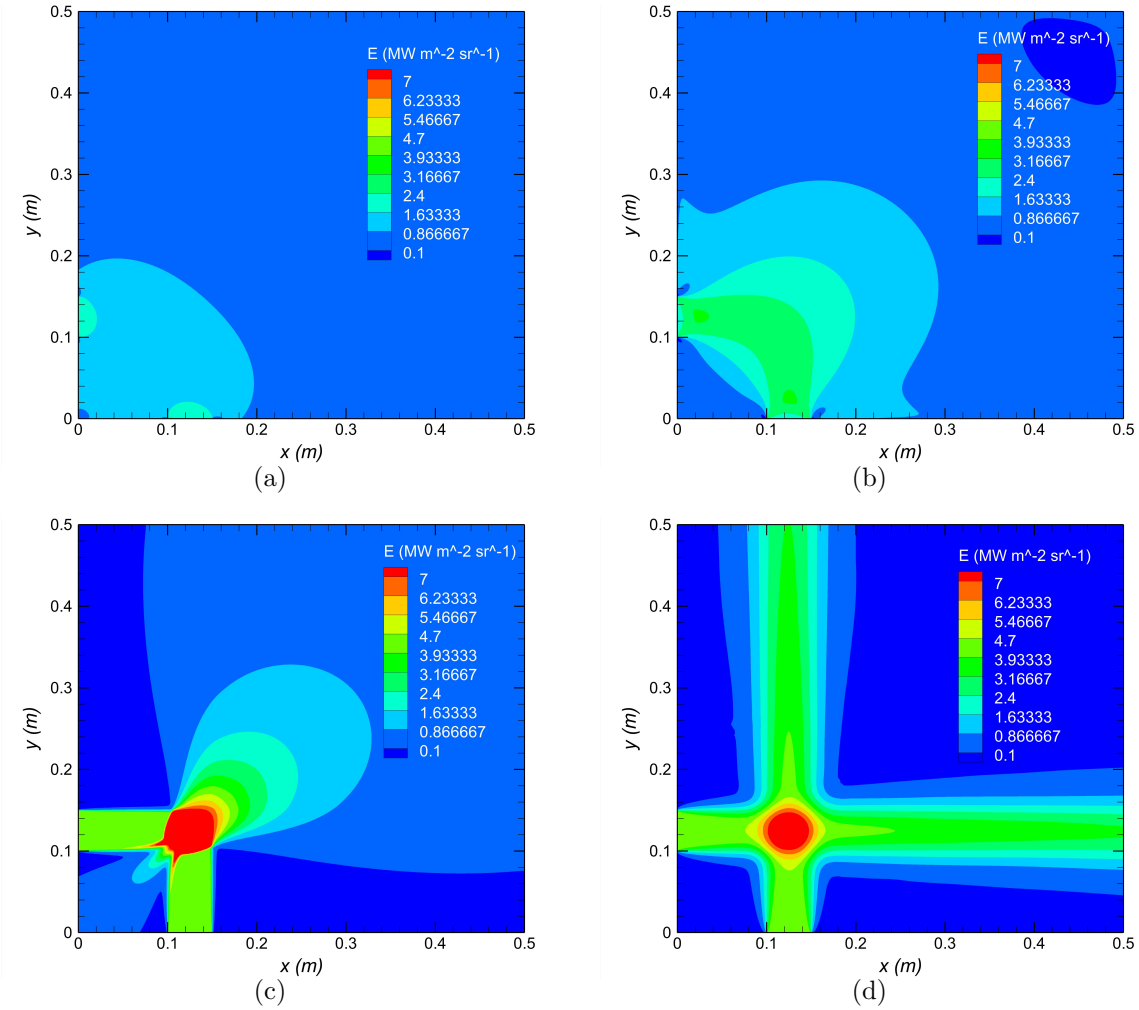

Figure 6.12: Predicted contours of the radiative energy density, $I^{(0)}$, obtained using the (a) P_1, (b) P_3, (c) M_1, and (d) M_2 moment closures with a (400×400)-node mesh. Results are shown for test problem involving identical beams of photons crossing at a 90° angle in a radiatively non-participating medium.

6.3 Crossing Beams in 2D Domain

The final gray-radiation test problem considered in this thesis involves two identical beams of radiative particles (photons) crossing at a 90° angle. It is considered herein for the purpose of illustrating the superiority of the M_N closures over the P_N models for radiative transfer problems involving highly anisotropic distributions of the radiative intensity. The present case also demonstrates again the importance of considering higher-order angular moments ($N > 1$) for certain types of radiative transfer problems. The computational domain consists of a square enclosure with side of 0.5 m in length. The medium within the enclosure is non-participating, i.e., no absorption, emission, or scattering of radiation. Two identical beams of photons, at a temperature of 4000 K each, emanate from the boundaries associated with $x = 0$ m (Beam 1) and $y = 0$ m (Beam 2), respectively. Beam 1 at $x = 0$ m emanates between $y = 0.1$ m and $y = 0.15$ m whereas Beam 2 at $y = 0$ m penetrates the computational domain between $x = 0.1$ m and $x = 0.15$ m. A (400×400)-node computational mesh was used to obtain solutions for the crossing beams problem, and no grid convergence study was performed in this case.

Contours of the predicted solutions, obtained using the P_1, P_3, M_1, and M_2 moment closures, are illustrated in Fig. 6.12 for the radiative energy density and in Fig. 6.13 for the magnitude of the radiative flux. It is evident from the two sets of results in the figures that both the P_1 and P_3 closures fail to capture the propagation of the two beams within the non-participating medium under consideration for the present test problem. This is due to the fact that these low-order closures are associated with polynomial-like distributions of the radiative intensity and as such cannot properly capture Dirac-delta-like distributions of the type encountered in this test case. It can however be observed that the P_3 closure predicts a deeper penetration of the beams that its lower-order counterpart, which can be attributed to the fact that the former closure can handle more anisotropy than the latter given the additional angular moments involved in the reconstruction of the assumed form of the distribution. The M_1 closure performs better than either one of the P_1 and P_3 closures and seems to properly predict the penetration and propagation of the two beams towards the crossing point, but however fails at capturing the crossing of the two beams. More specifically, at the point where the two incoming beams meet, the M_1 closure predicts a single beam propagating in the direction $(\vec{e}_1 + \vec{e}_2)$, where $\vec{e}_1$ and $\vec{e}_2$ are the unit vectors characterizing the original directions of propagation of Beam 1

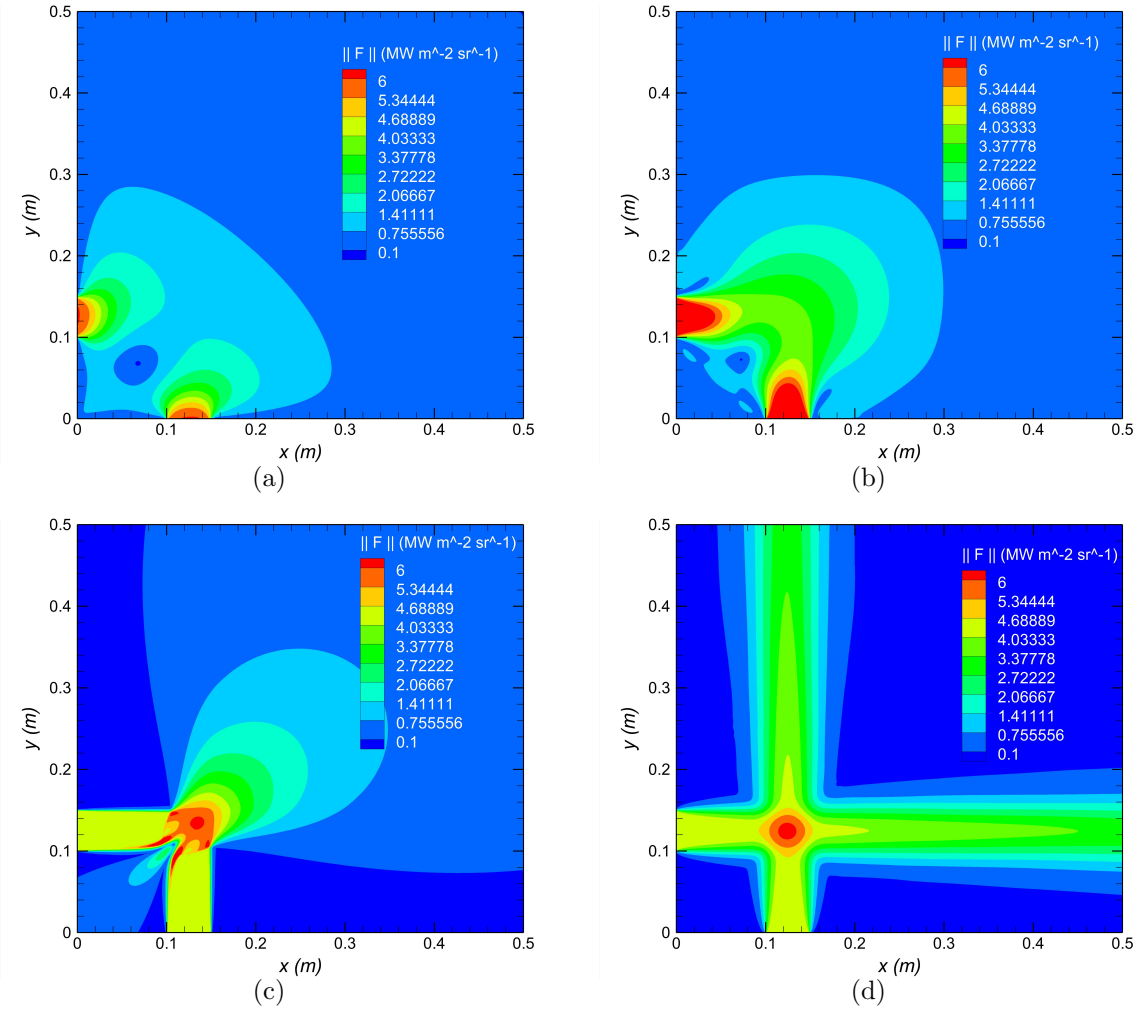

Figure 6.13: Predicted contours of the magnitude of the radiative flux, $\|I^{(1)}\|$, obtained using the (a) P_1, (b) P_3, (c) M_1, and (d) M_2 moment closures with a (400×400)-node mesh. Results are shown for test problem involving identical beams of photons crossing at a 90° angle in a radiatively non-participating medium.

and Beam 2, respectively. Finally, out of all of the radiation models considered here for the beam crossing problem, only the M_2 closure is able to predict in an accurate manner both the propagation and crossing of the two beams of radiative energy.

Chapter 7

Numerical Results: Assessment in Non-Gray Participating Media

In this section, the predictive capabilities of the proposed interpolative-based non-gray first-order, M_1, and second-order, M_2, maximum-entropy moment closures are assessed. As for the gray-radiation results of the previous Chapter 6, the assessments consist of comparing their solutions to those of the more commonly adopted first- and third-order spherical harmonic moment closures, P_1 and P_3, respectively, as well as those of the DOM, for a range of test cases involving non-gray radiative heat transfer in isotropically scattering ($\Phi_\eta(\vec{s}', \vec{s}) = 1$) real gases. In addition to the total (spectrally integrated) radiative energy density, $I^{(0)} = \int_0^\infty I_\eta^{(0)} d\eta$, and the total radiative heat flux, $I^{(1)} = \int_0^\infty I_\eta^{(1)} d\eta$, comparisons are also performed in terms of the total radiative source term, S_R, as defined by Eq. (2.13) of Chapter 2, which contributes to the source term in the conservation of energy equation of Eq (2.3). In all of the cases studied, the spectral dependence of the radiative properties of participating (absorbing, emitting and/or scattering) gases is treated using the statistical narrow-band correlated-k model. Moreover, similar to the case of gray radiation, steady-state numerical solutions for the non-gray M_1, M_2, P_1, and P_3 closures are obtained using the Godunov-type finite volume scheme and the NKS iterative procedure described earlier in Chapter 5. In all of the simulations, the method of characteristics is again used to provide boundary conditions to the systems of equations arising from the aforementioned moment closures. Furthermore, solutions of the set of ODEs resulting from the DOM are obtained using a space-marching iterative

technique [29], and quadrature rules based on the T_4 scheme of Thurgood *et al.* [92] are used for the discretization of the angular variables in the DOM.

The first set of test problems again involves radiative heat transfer between two parallel plates with various separation distances, medium temperature distributions, and gas mixture compositions, similar to those studied Sarr and Groth [124], which were inspired from the cases studied by Liu *et al.* [31]. For such test cases, exact analytical solutions of the RTE are available, and are therefore used as additional references for the comparisons, similar to the work by Sarr and Groth [124]. The newly-developed non-gray M_1 and M_2 closures are also applied to multi-dimensional radiative heat transfer problems by considering non-gray radiation within a rectangular enclosure, with specified distributions of the temperature and gas mixture compositions.

For all the radiation problems considered, solution comparisons are made based on grid-independent results for the M_1, M_2, P_1, and P_3 moment closures, as well as the DOM. The grid-independent solutions were obtained by comparing predictions of each of the radiation models on a sequence of increasingly refined grids and subsequently selecting the mesh size for which no significant change in the solution is observed as the mesh is further refined. The relative computational costs of each solution method in terms of the total computational time to obtain a solution in each case was also recorded and is reported along with the results of the mesh convergence study.

For the one- and two-dimensional canonical problems examined herein, the storage requirements for the M_1 and P_1 moment closures are such that three transport equations are solved for each quadrature point of each narrow band for a total of $3 \times 9 \times 4 = 108$ unknowns at each location within the computational grid. The M_2 closure involves the solution of 6 moment equations at each quadrature point for a total of $6 \times 9 \times 4 = 216$ unknowns. For the P_3 closure, 10 moment equations are solved at each quadrature point for a total of $10 \times 9 \times 4 = 360$ unknowns and, for the DOM simulations, the T_4 angular quadrature scheme [92] is used with 64 angular directions requiring the solutions for $64 \times 9 \times 4 = 2,304$ unknowns at each point within the grid. It is also important to note that the relative numbers of unknowns at each grid point would change for fully three-dimensional problems with the M_1 and P_1 closures involving $4 \times 9 \times 4 = 144$ unknowns, the M_2 closure resulting in $10 \times 9 \times 4 = 360$ unknowns, the P_3 closure involving $20 \times 9 \times 4 = 720$ unknowns, and the DOM requiring the solution of $128 \times 9 \times 4 = 4,608$

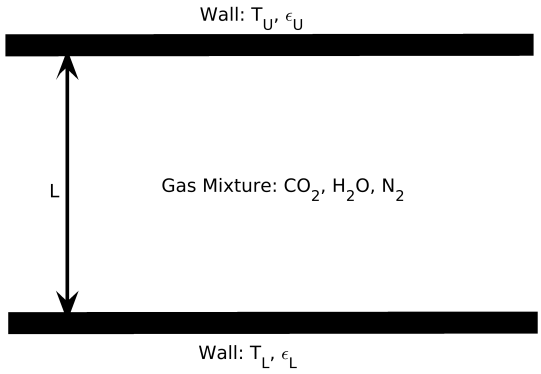

Figure 7.1: Illustration of parallel plate test case for non-gray radiation.

unknowns per grid point. Similar to the case of gray radiation of Chapter 6, the low-order M_1 and P_1 moment closures quite clearly offer significant savings in storage relative to the other methods. Moreover, for all of the canonical-type non-gray radiation problems considered here having either one-dimensional or rectangular two-dimensional computational domains, the space marching solution method used here to obtain the DOM solutions [29] is again extremely efficient and therefore the DOM solutions reported here generally require considerably less computational effort in terms of computational time compared to the moment closure techniques. However, as noted previously, for practical applications involving more complex three-dimensional geometries combined with more realistic physics, space marching techniques can lose their effectiveness and the moment closures are expected to be far more competitive.

Table 7.1: Computational Conditions for Parallel Plate Test Cases.

Case	**L (m)**	**Temperature Distribution**	**Mixture**
1	0.1 and 1.0	$T = 300 + 500\left[1 - \cos\left(\frac{2\pi x}{L}\right)\right]$	Pure H_2O
2	1.0	$T = 300 + 500\left[1 - \cos\left(\frac{2\pi x}{L}\right)\right]$	N_2 and H_2O with $f_{H_2O} = 4\left(1 - \frac{x}{L}\right)\frac{x}{L}$
3	0.2	$T = 1300 + 350\cos\left(\frac{\pi x}{L}\right) - 650\left[\cos\left(\frac{\pi x}{L}\right)\right]^2$	Pure H_2O
4	0.5	$T = 1300 + 350\cos\left(\frac{\pi x}{L}\right) - 650\left[\cos\left(\frac{\pi x}{L}\right)\right]^2$	10% CO_2, 20% H_2O, and 70% N_2 (mole basis)

7.1 Non-Gray Radiative Heat Transfer Between Parallel Plates

The geometry for the parallel plate test problems, considered in the present study for the assessment of the proposed interpolative-based non-gray M_1 and M_2 closures, is illustrated in Fig. 7.1. The bounding wall surfaces are assumed to be black, i.e., with emissivities $\epsilon_L = \epsilon_U = 1$, and the medium between the two plates is non-scattering at a uniform pressure of 1 atm. The computational parameters, specific to each of the test cases related to this geometry, are summarized in Table 7.1. Furthermore, for a non-scattering medium confined between two black, parallel plates, there exists an exact analytical solution to the radiative transfer equation [23], Eq. (2.9), the derivation of which is presented below. Similar to the gray radiation problems, grid convergence analyses for the parallel plate test problems considered herein are performed on a sequence of increasingly uniformly refined grids, characterized by $N_{cells} = \{20, 40, 80, 160, 320\}$ cells in the direction perpendicular to the plates. The accuracy of the predictions of the radiative source term associated with each of the grids in the sequence was assessed via the L^1 error with respect to computed solutions obtained on a reference grid with $N_{cells} = 640$ cells.

At any location between the two plates, the spectral incoming and outgoing angular distributions of the radiative intensity, I_η^+ and I_η^-, respectively, are given by

$$\begin{aligned} I_\eta^+(\tau_\eta, \mu) &= I_{w,L,\eta} e^{-\tau_\eta/\mu} + \tfrac{1}{\mu} \int_0^{\tau_\eta} I_{b\eta}(\tau\prime_\eta) e^{-(\tau_\eta - \tau\prime_\eta)/\mu} \mathrm{d}\tau\prime_\eta, \ 0 < \mu < 1, \\ I_\eta^-(\tau_\eta, \mu) &= I_{w,U,\eta} e^{(\tau_L - \tau_\eta)/\mu} + \tfrac{1}{\mu} \int_0^{\tau_\eta} I_{b\eta}(\tau\prime_\eta) e^{(\tau\prime_\eta - \tau_\eta)/\mu} \mathrm{d}\tau\prime_\eta, \ -1 < \mu < 0, \end{aligned} \tag{7.1}$$

where $\tau_\eta = \int_0^L \kappa_\eta(s) ds$ is the optical thickness (or optical depth), L is the separation distance between the two plates, $I_{w,L,\eta}$ and $I_{w,U,\eta}$ are the spectral intensities leaving the lower and upper plates respectively, $I_{b\eta}(\tau\prime_\eta)$ is the spectral blackbody radiative intensity associated with optical depth $\tau\prime_\eta$. The spectrally-dependent incoming and outgoing intensities, respectively, given in Eq. (7.1), can be integrated over the full spectrum of frequencies by means of the SNBCK model yielding the following expressions

$$\begin{aligned} I^+(\tau, \mu) &= \textstyle\sum_{j=1}^{N_b} \sum_{i=1}^{N_g} w_i I_{g_i}^+(\tau_{g_i}, \mu) \Delta\eta_j, \\ I^-(\tau, \mu) &= \textstyle\sum_{j=1}^{N_b} \sum_{i=1}^{N_g} w_i I_{g_i}^-(\tau_{g_i}, \mu) \Delta\eta_j, \end{aligned} \tag{7.2}$$

where

$$\begin{aligned} I^{+}_{g_i}(\tau_{g_i},\mu) &= I_{w,L,g_i} e^{-\tau_{g_i}/\mu} + \tfrac{1}{\mu}\int_0^{\tau_{g_i}} I_{b\eta_{cj}}(\tau\prime_{g_i}) e^{-(\tau_{g_i}-\tau\prime_{g_i})/\mu} \mathrm{d}\tau\prime_{g_i}, \\ I^{-}_{g_i}(\tau_{g_i},\mu) &= I_{w,U,g_i} e^{(\tau_{g_i,L}-\tau_{g_i})/\mu} + \tfrac{1}{\mu}\int_0^{\tau_{g_i}} I_{b\eta_{cj}}(\tau\prime_{g_i}) e^{(\tau\prime_{g_i}-\tau_{g_i})/\mu} \mathrm{d}\tau\prime_{g_i}. \end{aligned} \tag{7.3}$$

The total radiative energy density, $I^{(0)}$, and total radiative heat flux, $I^{(1)}$, then follow from the above expressions for the total radiative intensities by application of a Gauss-Legendre quadrature rule along with the appropriate angular weights for the moments of interest, i.e.,

$$I^{(0)\pm} = \pm 2\pi \int_0^{\pm 1} I^{\pm}(\tau,\mu)\mathrm{d}\mu = 2\pi \sum_{n=1}^{N} w_n I^{\pm}(\tau,\mu_n), \tag{7.4}$$

$$I^{(1)\pm} = \pm 2\pi \int_0^{\pm 1} \mu I^{\pm}(\tau,\mu)\mathrm{d}\mu = 2\pi \sum_{n=1}^{N} w_n \mu_n I^{\pm}(\tau,\mu_n), \tag{7.5}$$

where μ_n and w_n, respectively, correspond to the abscissas and weights determined by the Gauss-Legendre quadrature in the appropriate domains (i.e. $\mu_n \in [0,1]$ for the outgoing radiation and $\mu_n \in [-1,0]$ for the incoming radiation). The overall radiative energy density, at any optical distance between the two plates, corresponds to the sum of both incoming and outgoing contributions of radiative energy, i.e., $I^{(0)} = I^{(0)+} + I^{(0)-}$. The same also holds for the overall radiative flux, i.e., $I^{(1)} = I^{(1)+} + I^{(1)-}$. Very accurate estimates of both the zeroth- and first-order moments of the exact solutions of the radiative intensities can be achieved by using a 20-point Gauss-Legendre quadrature rule, i.e., $N = 20$. It is also worth pointing out that the expressions given in Eqs. (7.2) and (7.3) are exact up to the accuracy of the SNBCK treatment of the spectral absorption coefficient, κ_η. Since the same treatment is also used for the M_1, M_2, P_1, and P_3 moment closures, as well as for the DOM, it is therefore expected that any difference between the exact solutions and the predictions of the approximate radiation models, considered in the present study, would be entirely due to the approximate treatment of the directional dependence of the radiative intensity distribution.

7.1.1 Parallel Plate Case 1

The first parallel plate test problem is considered here to assess the ability of the proposed interpolative-based non-gray M_1 and M_2 closures to accurately capture radiative transfer for various optical conditions. The medium between the two plates consists of pure H_2O

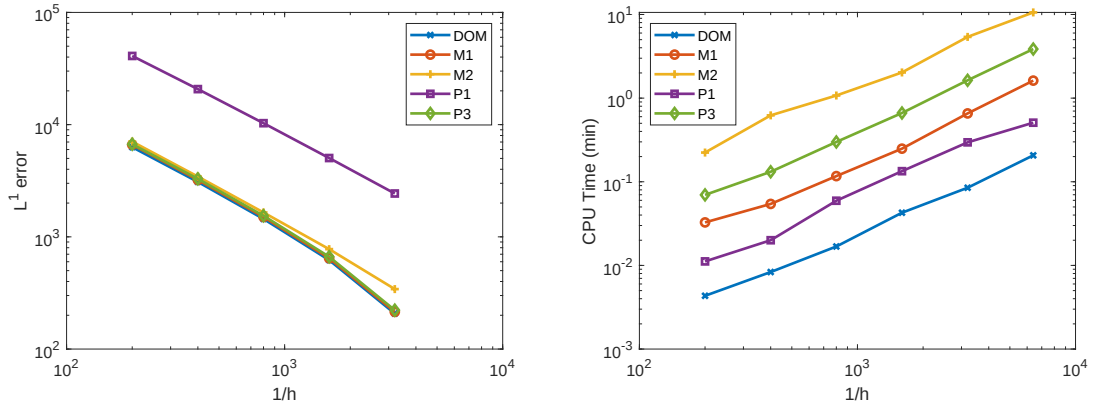

(a) (b)

Figure 7.2: Illustration of (a) grid convergence analysis on the predicted radiative source term for DOM, M_1, M_2, P_1, and P_3, for the small plate separation of Case 1 ($L = 0.1$ m) and, (b) computational costs associated with each of the radiation models for the different mesh resolutions.

with a temperature distribution of the form

$$T = 300 + 500\left[1 - \cos\left(\frac{2\pi x}{L}\right)\right], \tag{7.6}$$

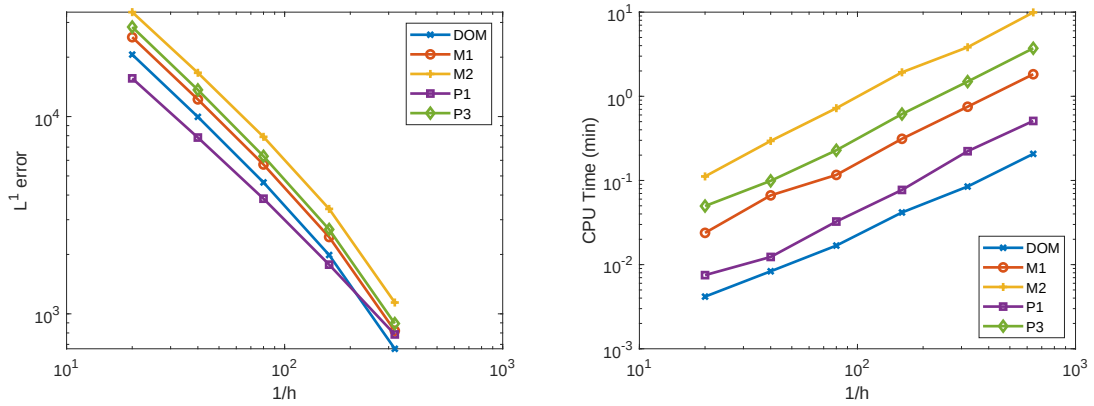

(a) (b)

Figure 7.3: Illustration of (a) grid convergence analysis on the predicted radiative source term for DOM, M_1, M_2, P_1, and P_3, for the larger plate separation of Case 1 ($L = 1$ m) and, (b) computational costs associated with each of the radiation models for the different mesh resolutions.

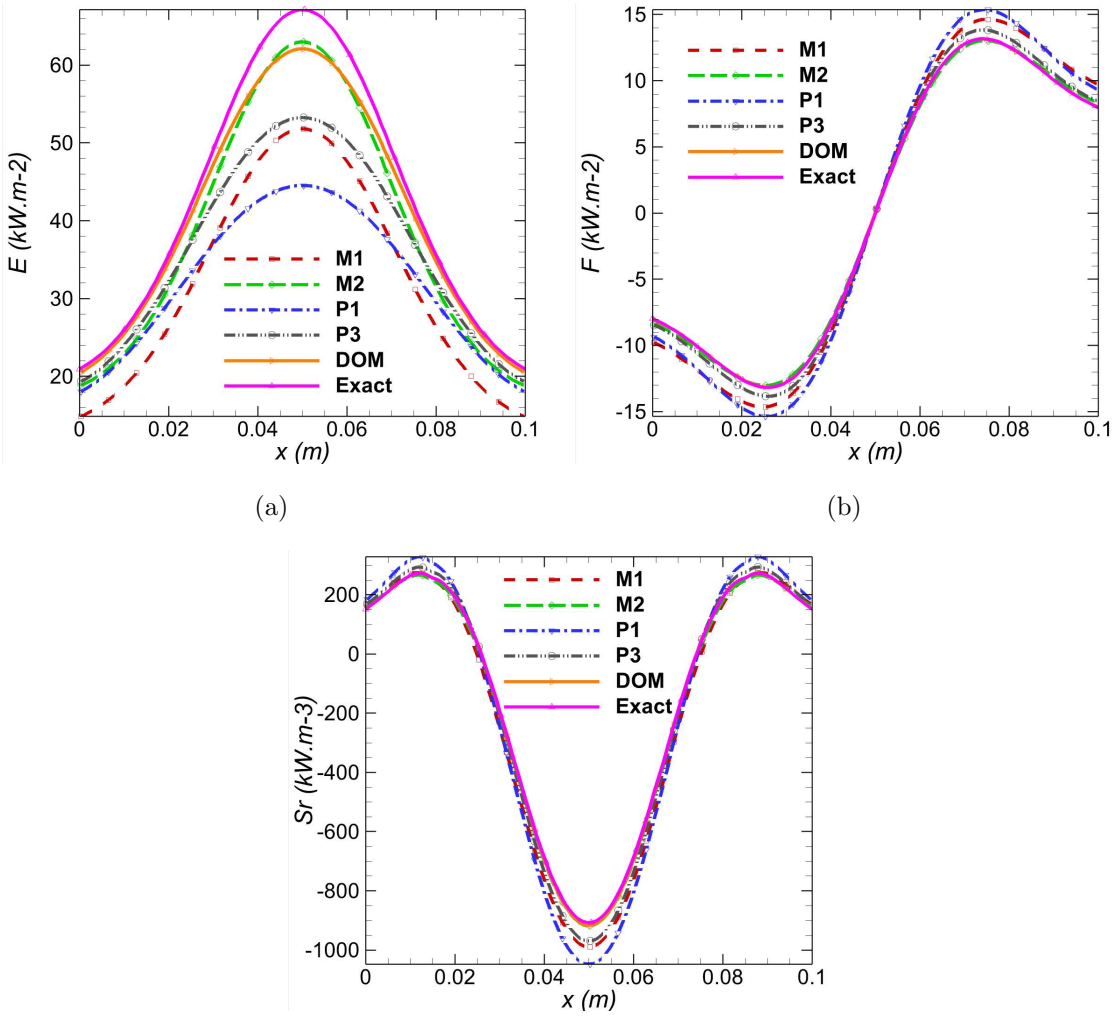

Figure 7.4: Predictions of (a) radiative energy density, (b) radiative heat flux, and (c) radiative source term for the small plate separation of Case 1 ($L = 0.1$ m) with a 160-node mesh obtained using the DOM, the M_1, M_2, P_1 and P_3 moment closures, with exact solution to the RTE used as reference for comparisons.

where x is the distance from the lower plate, and L represents distance between the bounding plates. Two plate separation distances are considered, i.e., $L = 0.1$ m and $L = 1$ m. Results of the grid convergence analysis, as well as comparisons of computational costs, are presented in Fig. 7.2 for the small plate separation and Fig. 7.3 for the larger plate separation. In addition, comparisons of the predictions of the radiative energy density, the radiative heat flux, and the radiative source term, for this test

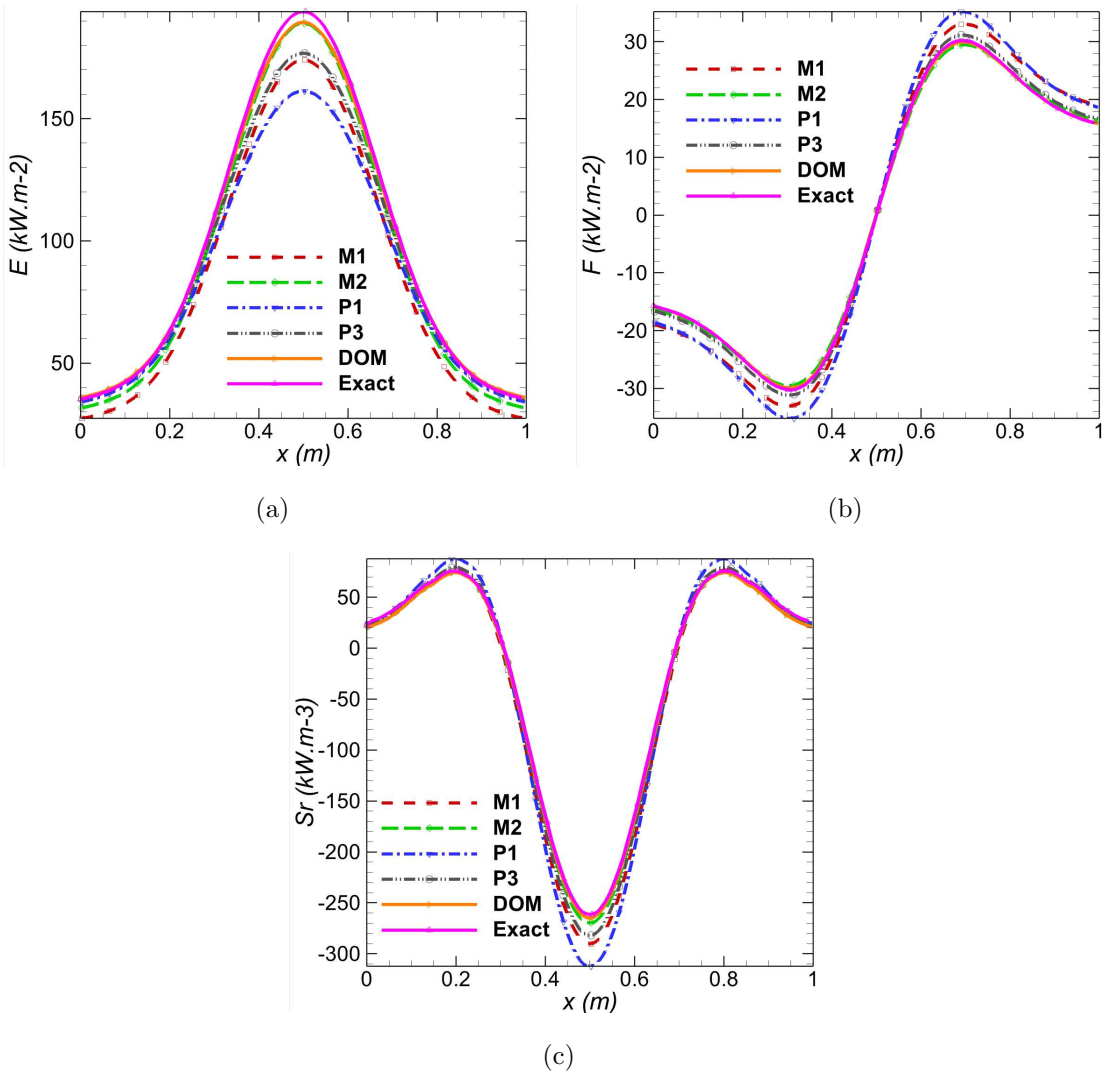

Figure 7.5: Predictions of (a) radiative energy density, (b) radiative heat flux, and (c) radiative source term for the larger plate separation of Case 1 ($L = 1$ m) with a 160-node mesh obtained using the DOM, the M_1, M_2, P_1 and P_3 moment closures, with exact solution to the RTE used as reference for comparisons.

problem, are also illustrated in Figs. 7.4 and 7.5, for the small and larger plate separations, respectively. For all the radiation models considered in this study, the solutions obtained on the second-finest grid, with $N_{cells} = 160$ cells, are used for the comparisons of spectrally integrated radiative quantities. This mesh resolution can be observed to fall well within the asymptotic range of convergence for both plate separations and has sufficient accuracy to ensure that numerical errors do not influence the comparisons of

the predicted solutions.

For the small plate separation, Fig. 7.4 reveals that the non-gray M_1 closure yields improved predictions of the radiative quantities under consideration relative to its spherical harmonic counterpart, i.e., the P_1 moment closure, and is even of comparable accuracy to the third-order spherical harmonic, P_3, moment closure as far as the radiative source term. However, as either one of the bounding walls is approached, the radiative energy density predicted by the non-gray M_1 closure seems to noticeably deviate from the predictions of the P_1 and P_3 moment closures which are in better agreement with the DOM and the exact solution. As can be expected, the non-gray M_2 closure yields improved predictions of the radiative solutions compared to its lower-order counterpart, i.e., the non-gray M_1 closure, and is even superior to the P_3 closure, while being of comparable accuracy to the DOM. Near the bounding walls however, predictions of the radiative energy density obtained using the M_2 closure deteriorate somewhat relative to those of the DOM, but are of comparable accuracy to those of the P_3 closure.

As the plate separation is increased, observations similar to those for the smaller plate separation can be made. In particular, the M_1 closure is observed to yield better solutions than the P_1 closure and provides predictions of the radiative energy density and of the radiative source term that are of comparable accuracy to those of the P_3 moment closure, as shown in Fig. 7.5. Moreover, the radiative energy density predicted by the M_1 closure is observed to deteriorate as either one of the bounding walls is approached and is less accurate than the predictions of both the P_1 and P_3 closures. The M_2 closure again outperforms all the other three moment closure techniques under consideration and is in very good agreement with both the DOM and the exact solutions. However, near the bounding plates, the radiative energy density predicted by the M_2 closure seems to slightly deteriorate compared to the DOM and is even less accurate than the P_1 and P_3, though still superior to its lower-order counterpart.

7.1.2 Parallel Plate Case 2

The next parallel plate problem is considered to assess the predictive capabilities of the non-gray M_1 and M_2 closures in the case of radiative transfer in non-homogeneous media with spatially varying species concentrations. More specifically, for this problem, the

medium between the two plates, with separation distance $L = 1$ m, is now a mixture of N_2 and H_2O, and the distribution of the mole fraction of H_2O in the mixture is given by

$$f_{H_2O} = 4\left(1 - \frac{x}{L}\right)\frac{x}{L}, \tag{7.7}$$

where x represents the distance from the lower plate and $L = 1\,\text{m}$ is the separation distance between the two plates. Similar to Case 1, the gas mixture follows a temperature distribution of the form

$$T = 300 + 500\left[1 - \cos\left(\frac{2\pi x}{L}\right)\right], \tag{7.8}$$

where again x is the distance from the lower plate, and L represents distance between the bounding plates. A grid convergence analysis, as well as comparisons of computational costs, have again been performed, the results of which, for this test problem, are illustrated in Fig. 7.6. It can be seen that again the solutions corresponding to the second-finest mesh, associated with $N_{cells} = 160$ cells, for all five of the radiation models, are indeed grid independent and are therefore used for the comparisons of total radiative quantities of interest illustrated in Fig. 7.7.

The numerical results of Fig. 7.7 show that the predictions of the M_1 closure are superior to those of the P_1 closure, the only exception being that the former yields less accurate

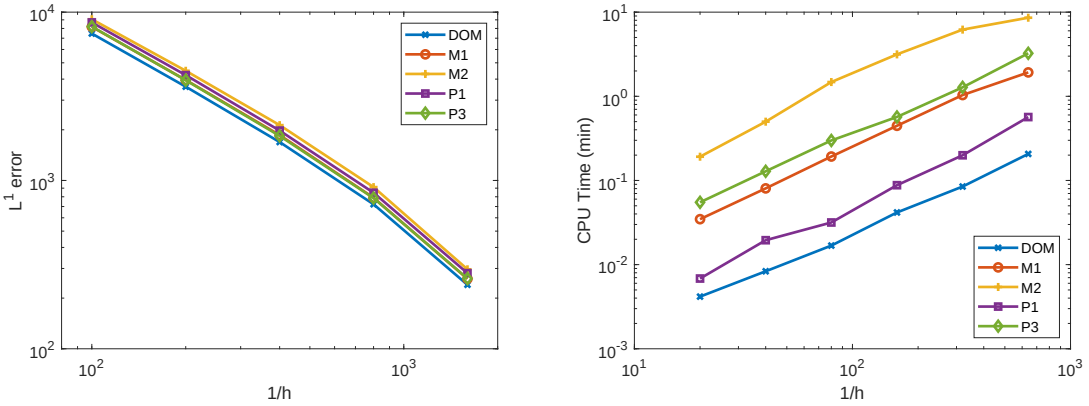

(a) (b)

Figure 7.6: Illustration of (a) grid convergence analysis on the predicted radiative source term for DOM, M_1, M_2, P_1, and P_3, for Case 2 ($L = 1$ m) and, (b) computational costs associated with each of the radiation models for the different mesh resolutions.

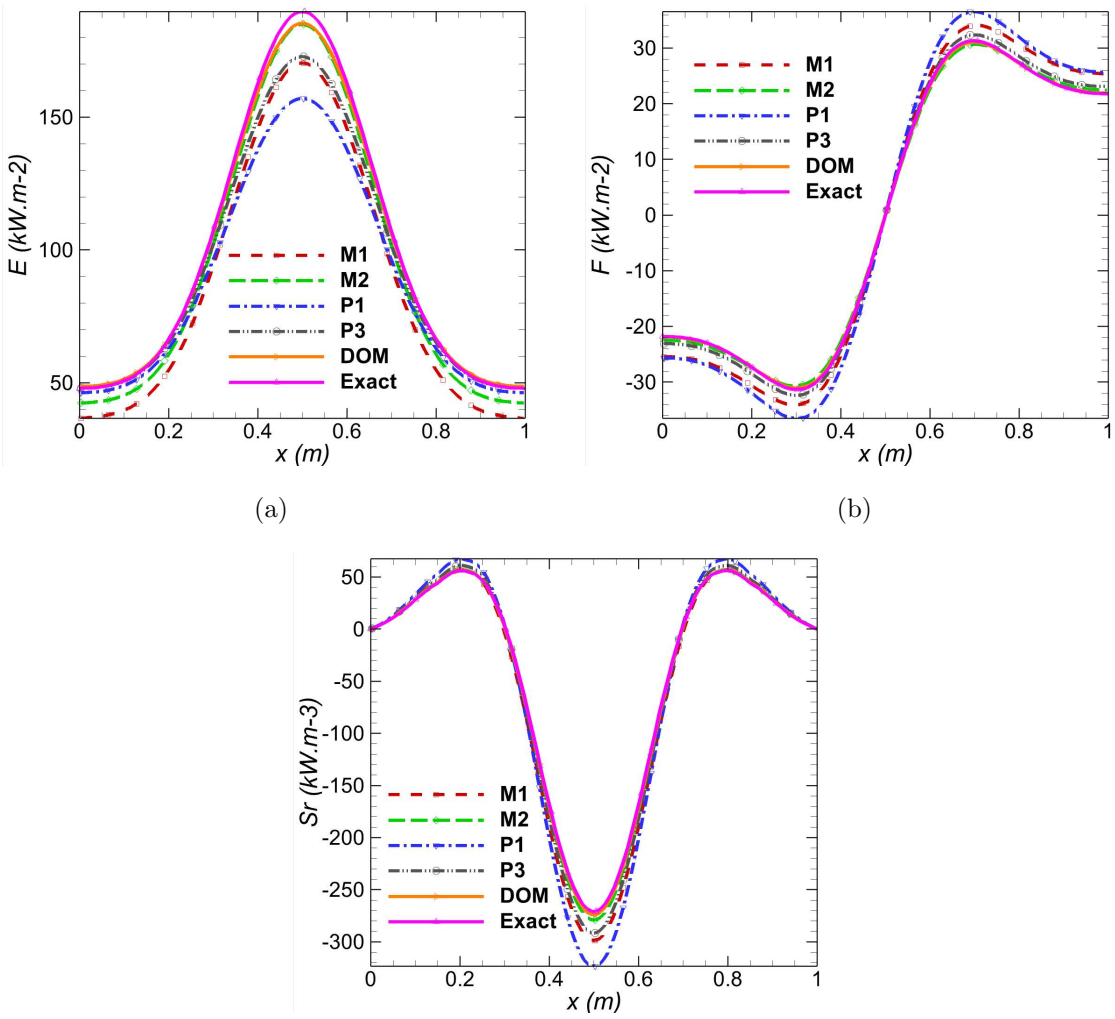

Figure 7.7: Predictions of (a) radiative energy density, (b) radiative heat flux, and (c) radiative source term for Case 2 ($L = 1$ m) with a 160-node mesh obtained using the DOM, the M_1, M_2, P_1 and P_3 moment closures, with exact solution to the RTE used as reference for comparisons.

predictions of the radiative energy density than the latter near the bounding walls. The M_1 closure is also observed to yield solutions of the radiative energy density and of the radiative source term of comparable accuracy to those obtained using the P_3 closure, especially away from the bounding walls. The M_2 closure on the other hand generally outperforms the M_1, P_1, and P_3 closures in terms of solution accuracy and is in close agreement with the DOM. However, as either one of the bounding plates is approached,

the radiative energy density predicted by the M_2 closure deviates from the predictions of the DOM and is even less accurate than the P_1 and P_3 solutions, though still superior to the M_1 solutions.

7.1.3 Parallel Plate Case 3

The parallel plate test case examined next, i.e., Case 3, aims at assessing the predictive capabilities of the M_1 and M_2 closures in problems involving strongly emitting wall surfaces. More specifically, radiative transfer between two parallel plates with a separation distance $L = 0.2\,\mathrm{m}$ is considered. The medium between the plates consists of pure H_2O, with a temperature distribution of the form

$$T = 1300 + 350\cos\left(\frac{\pi x}{L}\right) - 650\left[\cos\left(\frac{\pi x}{L}\right)\right]^2, \tag{7.9}$$

where again x represents the distance from the lower plate. Similar to the previous test cases, i.e., Case 1 and 2, grid convergence studies are performed on the solutions of the DOM, M_1, M_2, P_1, and P_3 radiation models, in particular on the predicted total radiative source term, as can be depicted in Fig. 7.8, which also illustrates comparisons of computational costs for the different radiation models. Moreover, numerical predictions

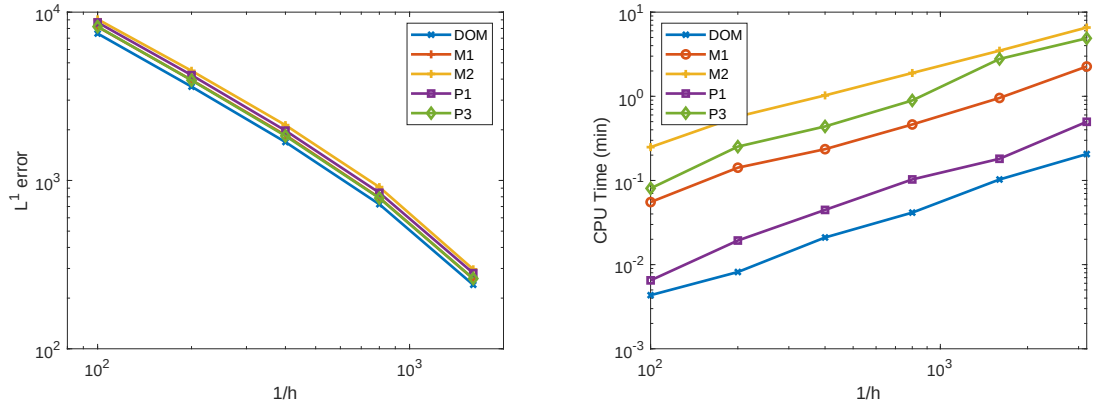

(a) (b)

Figure 7.8: Illustration of (a) grid convergence analysis on the predicted radiative source term for DOM, M_1, M_2, P_1, and P_3, for Case 3 ($L = 0.2$ m) and, (b) computational costs associated with each of the radiation models for the different mesh resolutions.

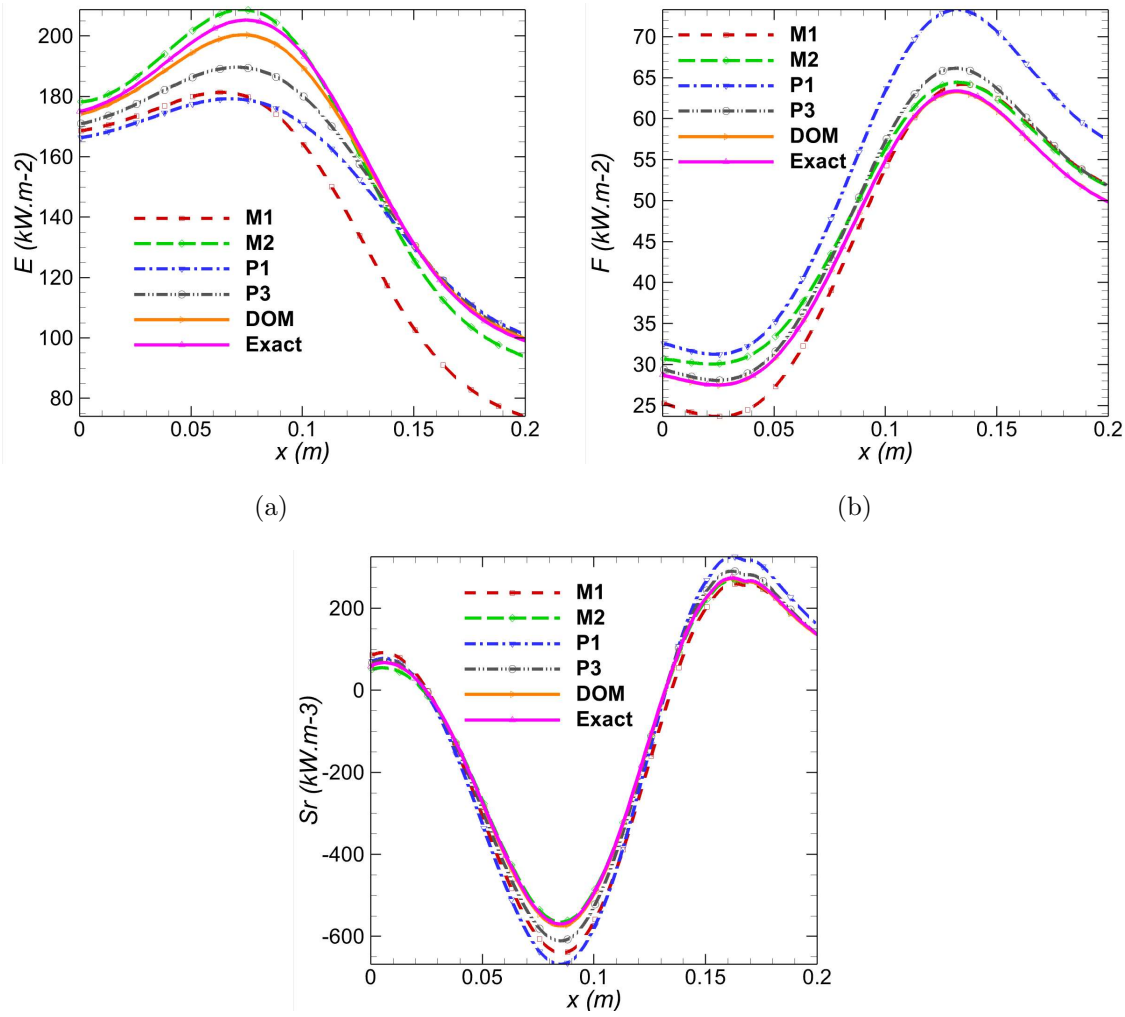

Figure 7.9: Predictions of (a) radiative energy density, (b) radiative heat flux, and (c) radiative source term for Case 3 ($L = 0.2$ m) with a 160-node mesh obtained using the DOM, the M_1, M_2, P_1 and P_3 moment closures, with exact solution to the RTE used as reference for comparisons.

of total radiative energy density, total radiative heat flux, and total radiative source term for Case 3 are also illustrated in Fig. 7.9.

The results shown in the latter figure were again obtained on the second finest mesh, corresponding to $N_{cells} = 160$ cells, which, as can be seen in Fig. 7.8(a), corresponds to grid-converged solutions well within the asymptotic range of convergence. The numerical results show that the radiative energy density predicted by the M_1 closure, though more

accurate than the P_1 predictions near the hotter plate, quickly deteriorates away from the latter and yields much less accurate solutions than the P_1 closure as the colder wall is approached. On the other hand, the radiative heat flux obtained using the M_1 closure, though seemingly equal in accuracy to the predictions of the P_1 closure near the hotter plate, improves further away from the latter and is even of comparable accuracy to the P_3 solutions. As far as the predictions of the radiative source term, the M_1 closure is generally superior to the P_1 closure. Improvements in the predictions of the radiative quantities, relative to the M_1 closure, can be achieved, as can be expected, by considering higher-order members of the hierarchy of M_N closures, in particular the M_2 closure. The latter closure is observed to provide substantial improvements in solution accuracy relative to its lower-order counterpart. Moreover, the M_2 closure generally yields more accurate predictions of the radiative quantities of interest compared to the P_1 and P_3 closures, despite yielding inferior predictions of the radiative energy density near the colder wall (relative to P_1 and P_3) and of the radiative heat flux near the hotter wall (relative to P_3).

7.1.4 Parallel Plate Case 4

The last test problem involving radiative transfer between parallel plates is similar to Case 3, except that the radiatively participating gas mixture now consists of 10% CO_2, 20% H_2O, and 70% N_2, where the percentages are given on a mole basis, and the plate separation is $L = 0.5\,\text{m}$. The results of the corresponding grid convergence analysis, based on the predicted radiative source term, for all the approximate radiation models of interest in the present study, are presented in Fig. 7.10. Comparisons of computational costs associated with the solutions of each of the radiation models, for the different mesh resolutions considered in the grid convergence study, are also reported in the same figure. Furthermore, numerical predictions of total radiative energy density, total radiative heat flux, and total radiative source term, obtained on the second-finest mesh, for which $N_{cells} = 160$ cells, are illustrated in Fig. 7.11.

The numerical results for this last parallel-plate test problem show trends somewhat similar to those of Case 3. This is expected since the only differences between the two cases, i.e., Case 3 and Case 4, are the composition of the radiatively participating gas mixture and the separation distance between the two plates. In particular, the M_1 closure

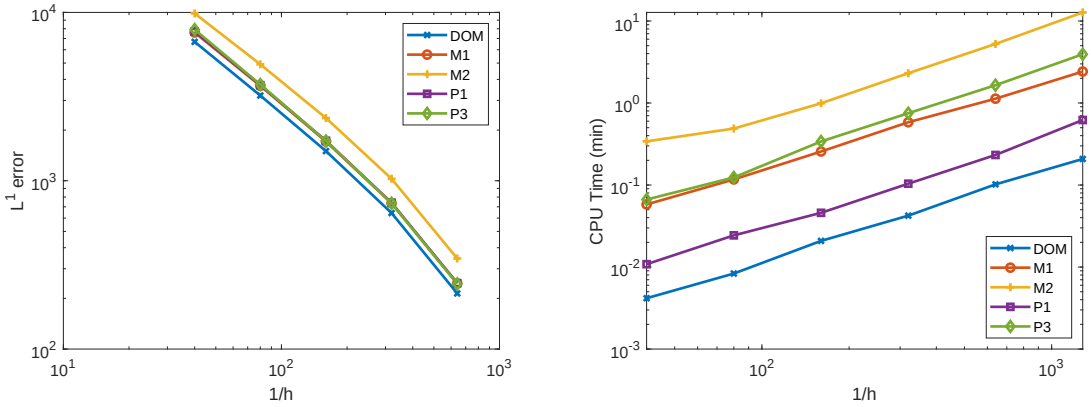

(a) (b)

Figure 7.10: Illustration of (a) grid convergence analysis on the predicted radiative source term for DOM, M_1, M_2, P_1, and P_3, for Case 4 ($L = 0.5$ m) and, (b) computational costs associated with each of the radiation models for the different mesh resolutions.

yields poor predictions of the radiative energy density near the colder wall, though it is of comparable accuracy to the P_1 closure near the hotter plate. The M_2 closure predicts radiative energy density solutions of comparable accuracy to the P_3 closure near the hotter wall but is less accurate than the P_1 and P_3 closures in the vicinity of the opposite plate. As far as the radiative heat flux, the M_1 closure provides better predictions than the P_1 approximation near the colder plate and is even of comparable accuracy to the M_2 and P_3 solutions, whereas its predictions near the hotter wall, while being at least as accurate as those of the P_1 closure, are somewhat less accurate than those of the M_2 and P_3 closures. The M_2 closure is also observed to be less accurate than the P_3 closure near the hotter plate. With respect to the radiative source term, the M_1 solutions are superior to the P_1 solutions but not as accurate as the P_3 solutions. On the other hand, the M_2 solutions outperform those of all the other three moment closures in terms of accuracy and are in close agreement with the DOM solutions.

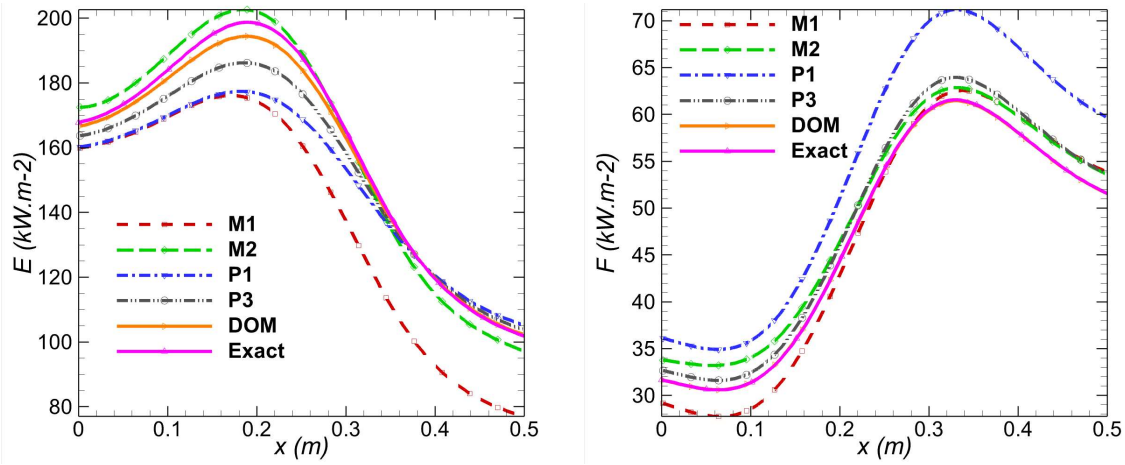

(a) (b)

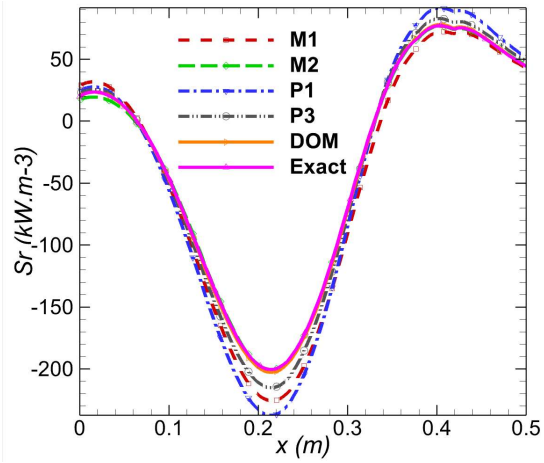

(c)

Figure 7.11: Predictions of (a) radiative energy density, (b) radiative heat flux, and (c) radiative source term for Case 4 ($L = 0.5$ m) with a 160-node mesh obtained using the DOM, the M_1, M_2, P_1 and P_3 moment closures, with exact solution to the RTE used as reference for comparisons.

7.2 Non-Gray Radiative Heat Transfer within Rectangular Enclosures

Radiative heat transfer within a rectangular enclosure is now considered with conditions similar to that which would be expected to occur in a typical hydrocarbon fuel combustor. The geometry of the latter, which is 4 m long and has a width of 2 m, is illustrated in Fig.

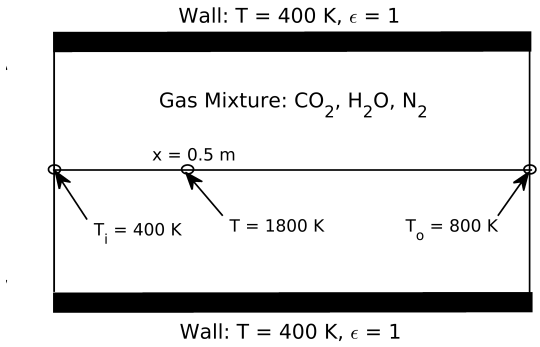

Figure 7.12: Illustration of rectangular enclosure test case for non-gray radiation.

7.12. The surrounding walls are black and cold at 400 K, while the gas mixture within the enclosure, which consists of 20% H_2O, 10% CO_2, and 70% N_2, where the percentages are expressed on a mole basis, is maintained at atmospheric pressure. The temperature of the gas inside the enclosure is not uniform but instead follows a distribution that is symmetric with respect to the centreline of the enclosure, and is taken to have the following form:

$$T = T_w + (T_c - T_w)\left(1 - 3|y|^2 + 2|y|^3\right), \tag{7.10}$$

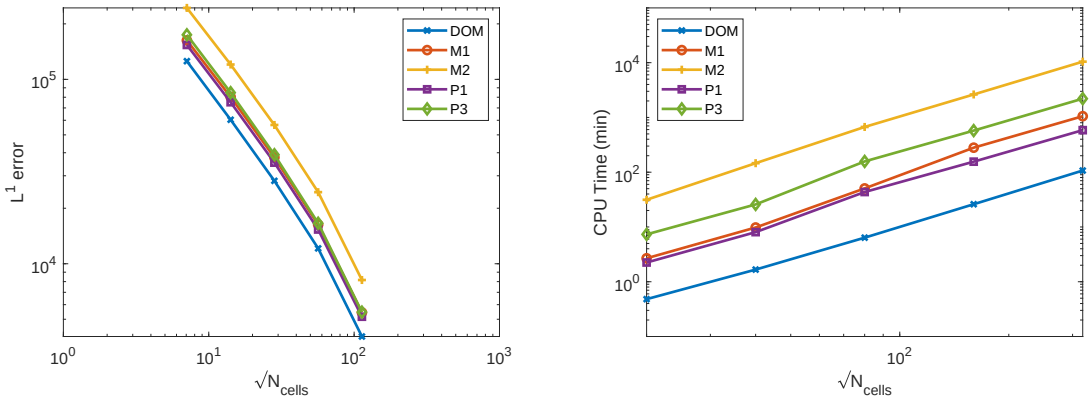

(a) (b)

Figure 7.13: Illustration of (a) grid convergence analysis on the predicted radiative source term for DOM, M_1, M_2, P_1, and P_3, for Case 5, involving radiative heat transfer in a rectangular enclosure and, (b) computational costs associated with each of the radiation models for the different mesh resolutions.

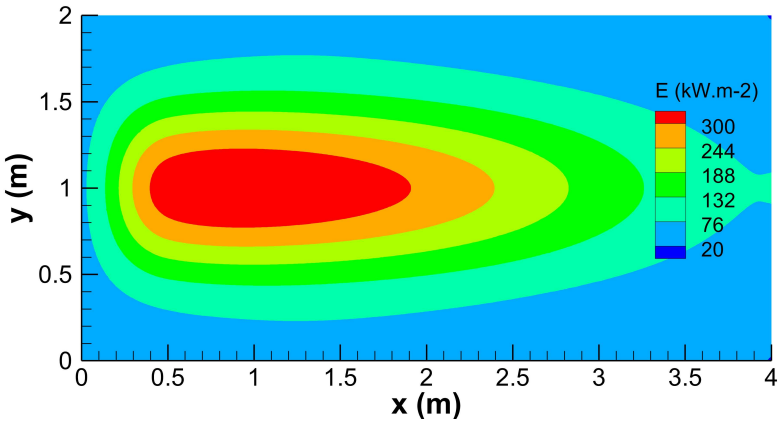

(a)

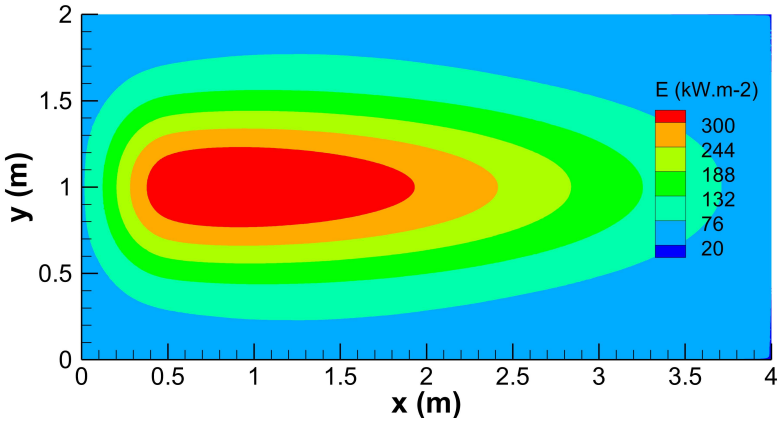

(b)

Figure 7.14: Contours of radiative energy density predicted by (a) the DOM, and (b) the non-gray M_2 closure for the rectangular enclosure test problem with a (160×160)-node mesh.

where the coordinate, y, corresponds to the radial distance from the centreline, $T_w = 400$ K represents the walls temperature, and T_c is the centreline temperature. The latter is taken to increase quadratically from $T_i = 400$ K at the inlet ($x = 0$ m) to $1,800$ K at $x = 0.5$ m, then decreases quadratically to $T_o = 800$ K at the exit ($x = 4$ m) via the following distribution

$$T_c = \begin{cases} -5,600x^2 + 5,600x + 400, & x < 0.5, \\ -\frac{1,000}{12.25}x^2 + \frac{1,000}{12.25}x + \frac{21,800}{12.25}, & x \geq 0.5. \end{cases} \tag{7.11}$$

Results of grid convergence analysis on the total radiative source term, for the DOM, as well as the M_1, M_2, P_1, and P_3 moment closure techniques, are illustrated in Fig. 7.13(a). The latter analysis is performed on a sequence of increasingly uniformly refined two-dimensional grids, with $N_{cells} = \{20 \times 20, 40 \times 40, 80 \times 80, 160 \times 160, 320 \times 320\}$ cells. Moreover, the accuracy of the predictions of the radiative source term obtained on each of the grids in the sequence was assessed via the L^1 error with respect to solutions obtained

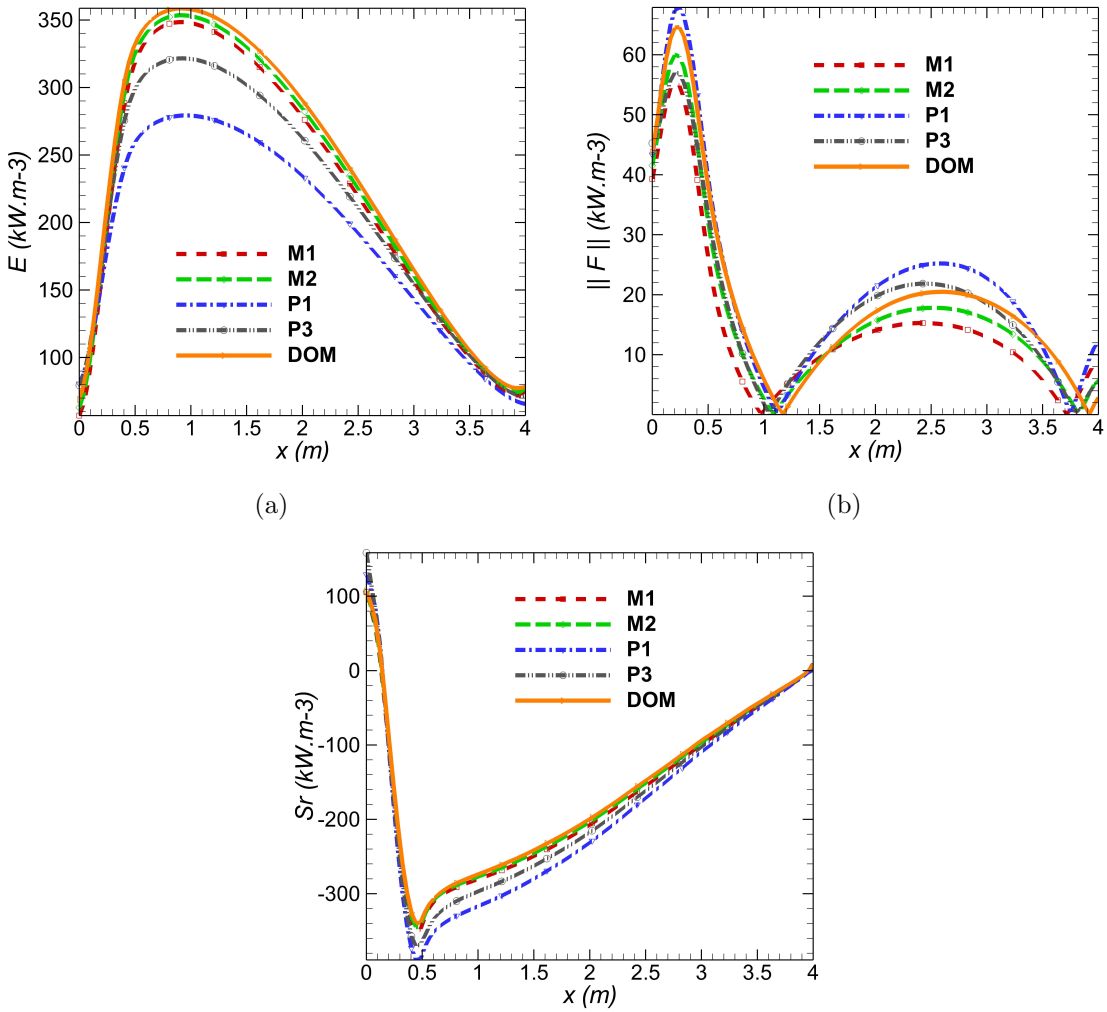

Figure 7.15: Predictions of (a) radiative energy density, (b) radiative heat flux, and (c) radiative source term for the rectangular enclosure test case with a (160×160)-node mesh obtained using the DOM, the M_1, M_2, P_1 and P_3 moment closures, with the DOM used as a benchmark for comparisons.

on a reference grid with $N_{cells} = 640 \times 640$ cells. The grid with $N_{cells} = 160 \times 160$ cells can be observed to fall well within the asymptotic range of convergence for all the radiation models considered in the present analysis and is therefore used for the comparisons of the solutions so as to ensure that the latter are not influenced by numerical errors.

Comparisons of computational costs associated with each of the approximate radiation models, for the mesh resolutions considered in the grid convergence study, are presented in Fig. 7.13(b). Moreover, predicted contours of total radiative energy density, $I^{(0)}$, within the rectangular enclosure are shown in Figs. 7.14(a) and (b) for the DOM and our non-gray M_2 closure, respectively. As can be expected, the radiative energy density takes its maximum values near the location of maximum temperature along the centreline, and then decreases towards either the inlet or the outlet, or radially towards the relatively cold walls, and such a behaviour is well captured by both the DOM and our non-gray M_2 closure.

Numerical predictions of the total radiative energy density, total radiative heat flux, and total radiative source term, along the centreline of the rectangular enclosure, obtained using our non-gray M_1 and M_2 closures, are now compared to those of the P_1 and P_3 moment closures, as well as those of the DOM, as shown in Fig. 7.15. It is worth mentioning that, due to the lack of exact analytical solutions to the equation of radiative transfer for this particular problem, solutions of the DOM are used as benchmark for the comparisons. The numerical results presented here show that even the non-gray M_1 closure provides solutions of the radiative energy density and the radiative source term at least as accurate as those of the P_3 moment closure, while being superior to the predictions of the P_1 moment closure technique. Furthermore, the proposed interpolative non-gray M_2 closure again yields improved predictions of the radiation solutions compared to its lower-order counterpart and is in better agreement with the DOM, when compared to the M_1, P_1, and P_3 radiation models.

Chapter 8

Numerical Results: Assessment in Laminar Non-Premixed Flames

In an effort to further assess the predictive capabilities of the proposed interpolative-based non-gray first-order, M_1, and second-order, M_2, maximum-entropy moment closures, numerical simulations of sooting laminar co-flow diffusion flames at elevated pressures are now considered. The assessment is again performed via comparisons of the predictions of the M_1 and M_2 closures to those of the first-order, P_1, and third-order, P_3, spherical harmonic moment closures, as well as those of the DOM. Methane-air co-flow diffusion flames for pressures ranging from standard atmospheric conditions up to 20 atm are considered in this assessment. For the range of pressures considered, the co-flow flames range from optically thin flames to flames for which radiation absorption is substantial. The computational framework used here for predicting soot formation in the laminar reactive flows of interest was originally developed by Charest *et al.* [17]. The latter was developed for the numerical prediction of laminar reactive flows with complex chemistry, non-gray radiative heat transfer, and soot formation and was specifically developed for use with large multi-processor parallel computers. The capabilities of the framework have been previously demonstrated in an extensive number of studies of laminar co-flow diffusion flames under both high pressure and low gravity conditions [17, 19–22] as well as in the prediction of flame extinction in laminar counter-flow diffusion flames [198, 199]. Additionally, this computational framework was more recently extended by Xing *et al.* [73] to allow for the treatment and solution of fractional-order quadrature-based moment clo-

sures for describing the soot aerosol dynamics and by Sarr *et al* [74] for the description of radiative heat transfer via moment approaches. A further extension of the framework for the prediction of turbulent sooting flames has also been developed by Xing [75]. For the laminar flames considered in this thesis, the semi-empirical two-equation model of Liu *et al.* [78] with an acetylene-based nucleation model is used to describe the soot particle transport and formation.

For all the cases studied, the SNBCK spectral radiation model [31], described in Chapter 4, is used for the treatment of the spectral absorption coefficient of participating gases. Additionally, absorption properties of the soot particulates are estimated using the Rayleigh approximation as described in Chapter 4. Finally, the GRI 3.0 mechanism [200] (53 species and 325 reactions) was used to represent the gas-phase reactions.

In what follows, the configuration of the high-pressure co-flow burner used for the flame simulations is first described. A summary of the parameters and details relevant to the computations is then given, and, finally, numerical results for the methane-air laminar flames under consideration are presented and analyzed.

8.1 Computational Domain and Boundary Conditions

The laboratory-scale, high-pressure axisymmetric burner for laminar methane co-flow flames [22] considered in this study consists of a central fuel tube with 3 mm inner diameter and a concentric tube of 25.4 mm inner diameter that supplies the co-flow air. The fuel tube wall has a thickness of 0.4 mm. Although experimental data is available for some of the flames considered, the focus here is on a direct comparison of the predictive capabilities of the interpolative-based closures relative to those of the DOM and comparisons to experimental measurements of quantities, such as temperature and soot volume fraction, were not considered here. For the computations performed as part of this study, the temperature of the fuel and air supplied to the burner are assumed to be equal to 473 K and the air mass flow rate is kept constant at 340 mg/s. Furthermore, the methane mass flow rate is held at 1.221 mg/s in order to maintain a carbon mass flow rate of 0.914 mg/s.

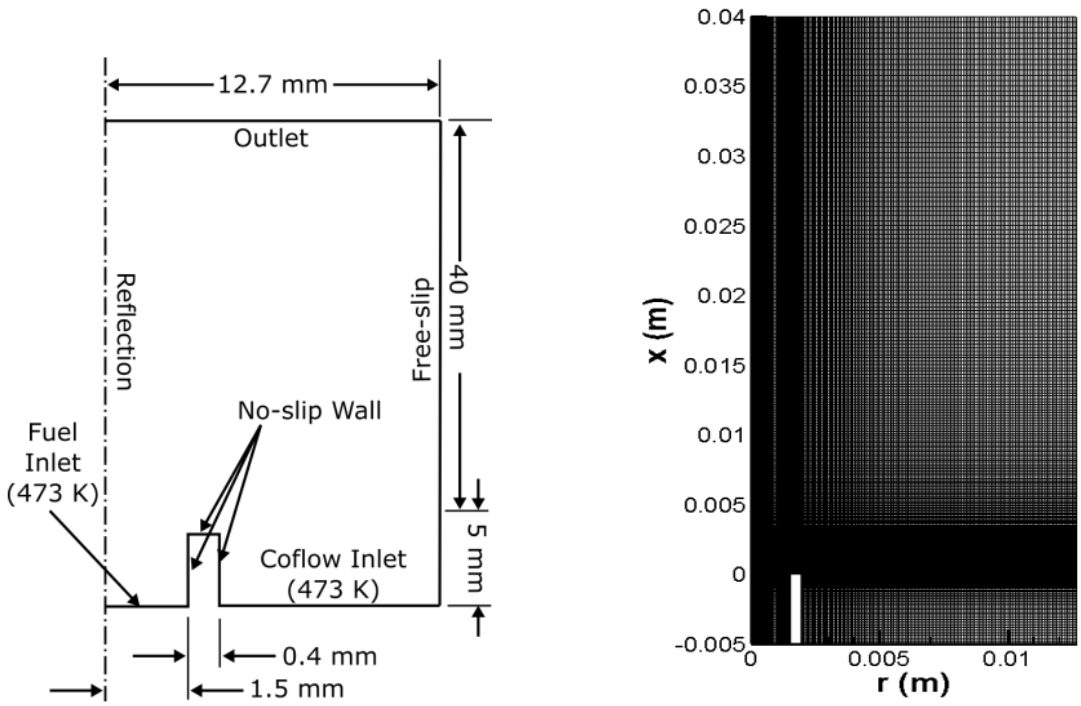

(a) Schematic Diagram

(b) Computational grid

Figure 8.1: Schematic diagram and 2D axisymmetric computational grid for the co-flow laminar methane diffusion flame.

The two-dimensional computational domain used for the purpose of modelling the burner described above in the numerical simulations of methane-air co-flow diffusion flames is shown schematically in Fig. 8.1(a), along with the boundary conditions used for the computations. The domain extends radially outwards 12.7 mm to the walls of the chimney and 40 mm downstream. It also extends 5 mm upstream into the fuel and air tubes to account for the effects of fuel preheating [99] and better represent the inflow velocity distribution. The three surfaces that lie along the tube wall were modelled as fixed-temperature walls at 473 K with zero-slip conditions on velocity. Reflection boundary conditions were applied along the centreline. The far-field boundary was treated using a free-slip condition, which neglects any shear imparted by the chimney walls to the co-flow air. At the outlet, temperature, velocity, species mass fractions, and soot number density are extrapolated while pressure is held fixed. The gas/soot mixture is specified at the inlet along with its velocity and temperature while pressure is extrapolated. For the radiation solvers, all boundaries except for the axis of symmetry (for which axisymmetric

boundary conditions are prescribed) are assumed to be black. More specifically, for the moment closure techniques, boundary conditions based on the method of characteristics were used for black surfaces, whereas the axisymmetric boundary conditions based on incoming partial moments were used for the axis of symmetry.

The computational domain depicted in Fig. 8.1(a) was subdivided into 192 cells and 16 blocks in the radial direction and 320 cells and 32 blocks in the axial direction to form a structured, non-uniformly-spaced mesh of $60,000$ cells. The cells were clustered towards the burner exit plane to capture interactions near the fuel tube walls and also towards the centreline to capture the core flow and main features of the flame. The resulting mesh, which was employed for all calculations in the present study, is illustrated in Fig. 8.1(b). This level of mesh resolution, which was used previously by Charest *et al.* [22], has been shown to be more than sufficient in order to capture the essential features of the methane-air laminar co-flow diffusion flames associated with the high-pressure burner of interest here.

8.2 Methane-Air Co-flow Flames

The predictive capabilities of the proposed interpolative-based non-gray M_1 and M_2 closures are now assessed in the context of numerical simulations of methane-air laminar co-flow diffusion flames for pressures of 1, 5, and 20 atm. The set of pressures considered herein allow to assess the M_1 and M_2 closures for a wide range of optical thicknesses, with the latter being an increasing function of pressure. The higher the optical thickness, the more important the heat losses due to radiative transfer. The assessment is performed via comparisons of the solutions of the M_1 and M_2 closures to those of the P_1 and P_3 closures, as well as those of the DOM. The first set of comparisons are concerned with the predicted distributions of temperature and soot volume fraction. Such comparisons also include flame solutions obtained in the absence of radiative transfer (i.e., the radiative heat transfer is set to zero in the simulations) in order to illustrate the importance of taking into account radiative heat losses for accurate predictions of both temperature distribution and soot volume fraction, among other quantities. The next set of comparisons involves the predicted distributions of radiative quantities such as the radiative heat flux and the radiative source term, obtained based on frozen field simulations of the radia-

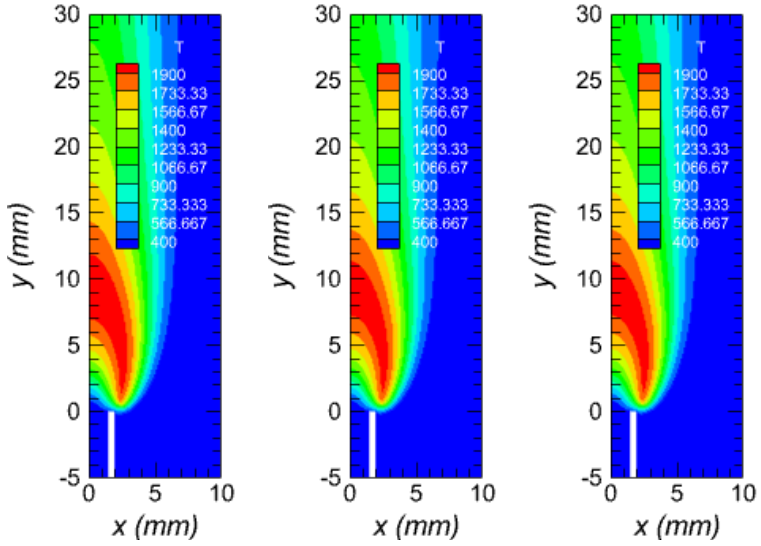

(a) No Rad (b) DOM (c) M_1

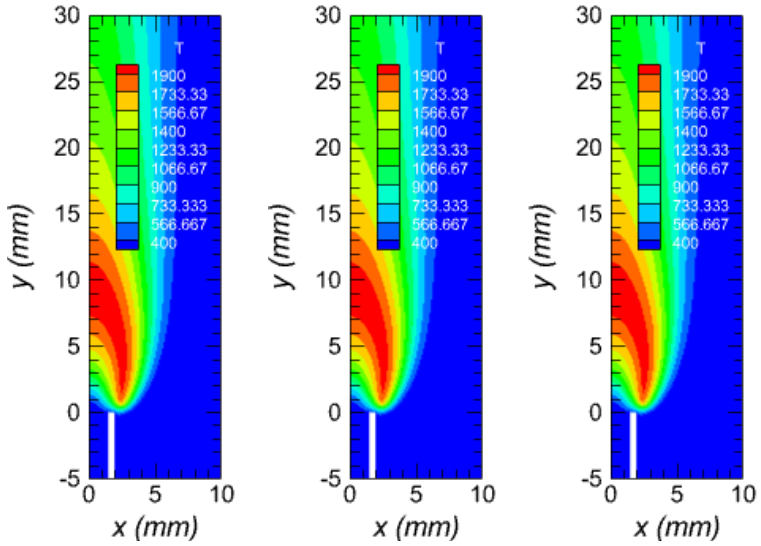

(d) M_2 (e) P_1 (f) P_3

Figure 8.2: Contours of temperature predicted by (a) the case where radiation is neglected, (b) the DOM, (c) the interpolative-based non-gray M_1 closure, (d) the interpolative-based non-gray M_2 closure, (e) the P_1 closure, and (f) the P_3 closure for methane at 1 atm.

tive heat transfer inside the burner. For such simulations, the converged flame solutions based on the DOM are used to specify the thermochemical properties of the background

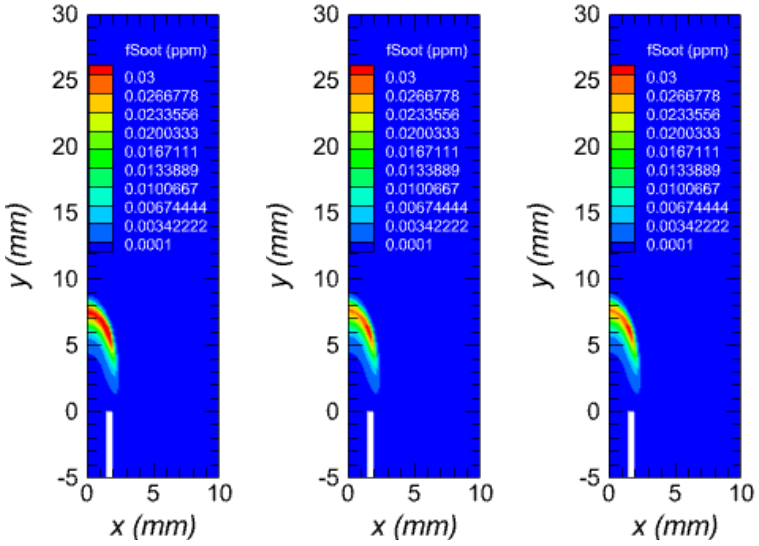

(a) No Rad (b) DOM (c) M_1

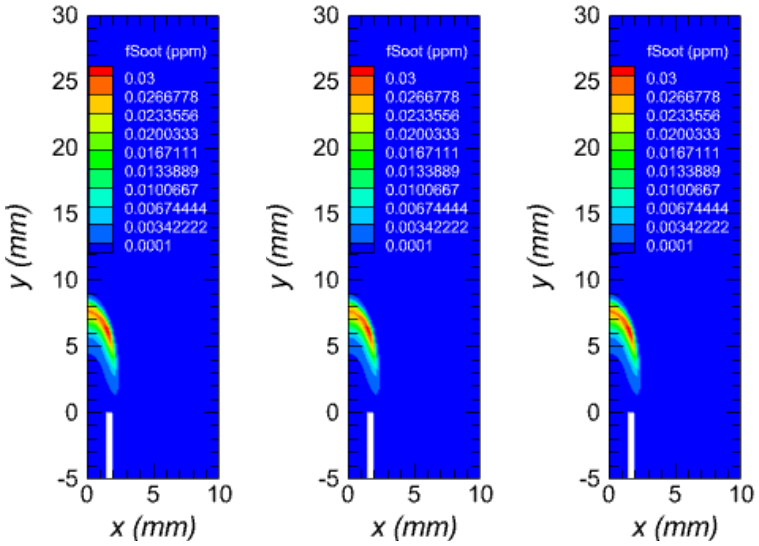

(d) M_2 (e) P_1 (f) P_3

Figure 8.3: Contours of soot volume fraction predicted by (a) the case where radiation is neglected, (b) the DOM, (c) the interpolative-based non-gray M_1 closure, (d) the interpolative-based non-gray M_2 closure, (e) the P_1 closure, and (f) the P_3 closure for methane at 1 atm.

medium for all the radiation models. This ensures that differences in the predicted radiative quantities are solely due to the different procedures used to solve the RTE. All of

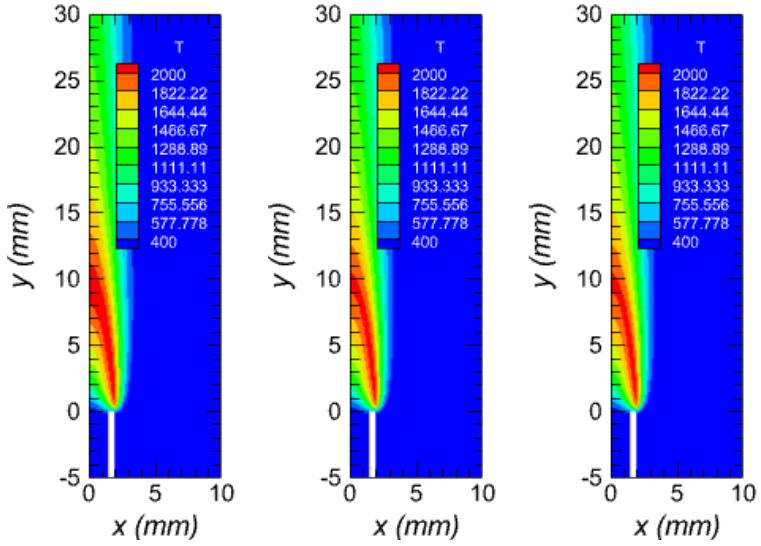

(a) No Rad (b) DOM (c) M_1

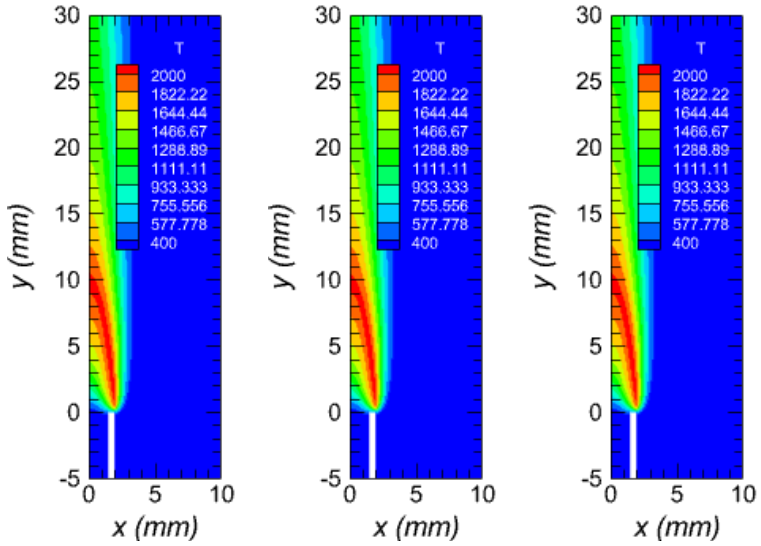

(d) M_2 (e) P_1 (f) P_3

Figure 8.4: Contours of temperature predicted by (a) the case where radiation is neglected, (b) the DOM, (c) the interpolative-based non-gray M_1 closure, (d) the interpolative-based non-gray M_2 closure, (e) the P_1 closure, and (f) the P_3 closure for methane at 5 atm.

the numerical simulations were performed using the computational conditions described previously in Section 8.1.

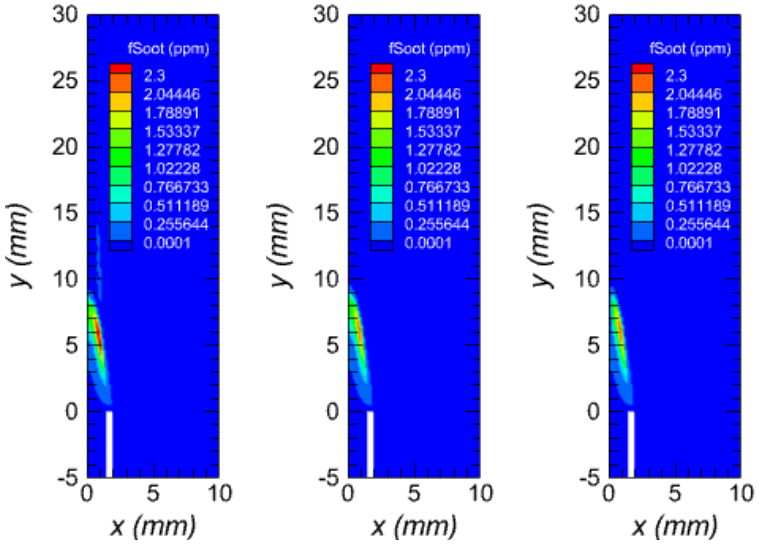

(a) No Rad (b) DOM (c) M_1

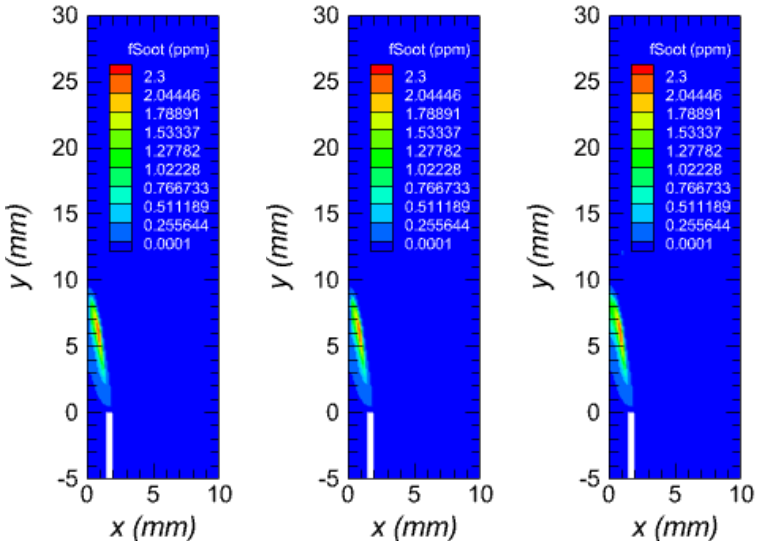

(d) M_2 (e) P_1 (f) P_3

Figure 8.5: Contours of soot volume fraction predicted by (a) the case where radiation is neglected, (b) the DOM, (c) the interpolative-based non-gray M_1 closure, (d) the interpolative-based non-gray M_2 closure, (e) the P_1 closure, and (f) the P_3 closure for methane at 5 atm.

The predicted two-dimensional distributions of temperature and soot volume fraction, obtained in the absence of radiative transfer, as well as those obtained using the DOM, the

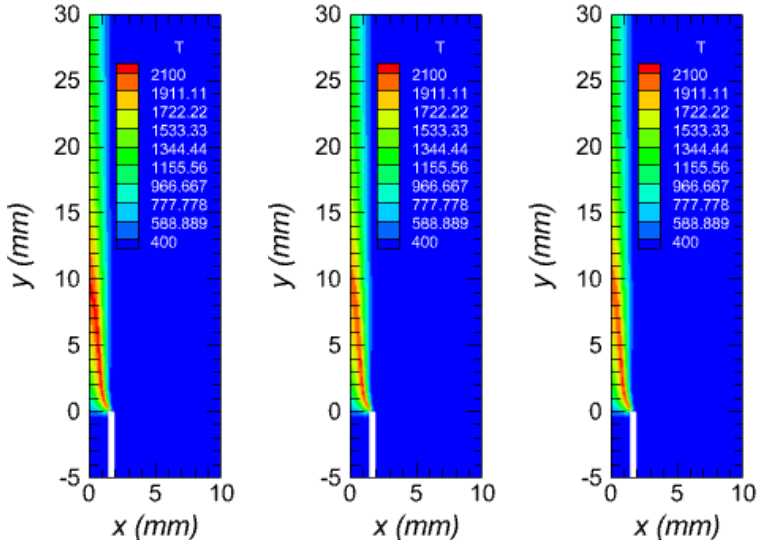

(a) No Rad (b) DOM (c) M_1

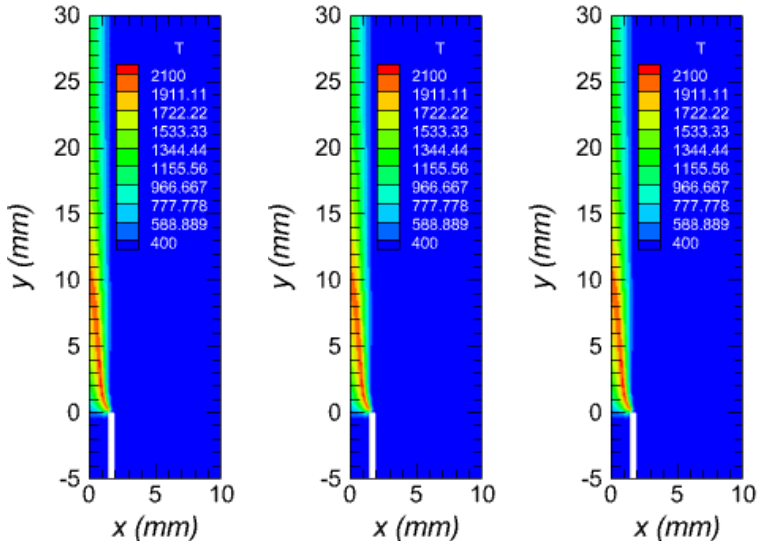

(d) M_2 (e) P_1 (f) P_3

Figure 8.6: Contours of temperature predicted by (a) the case where radiation is neglected, (b) the DOM, (c) the interpolative-based non-gray M_1 closure, (d) the interpolative-based non-gray M_2 closure, (e) the P_1 closure, and (f) the P_3 closure for methane at 20 atm.

proposed interpolative-based non-gray M_1 and M_2 maximum-entropy moment closures, and the P_1 and P_3 closures, are respectively depicted in Figs. 8.2 and 8.3 for atmospheric

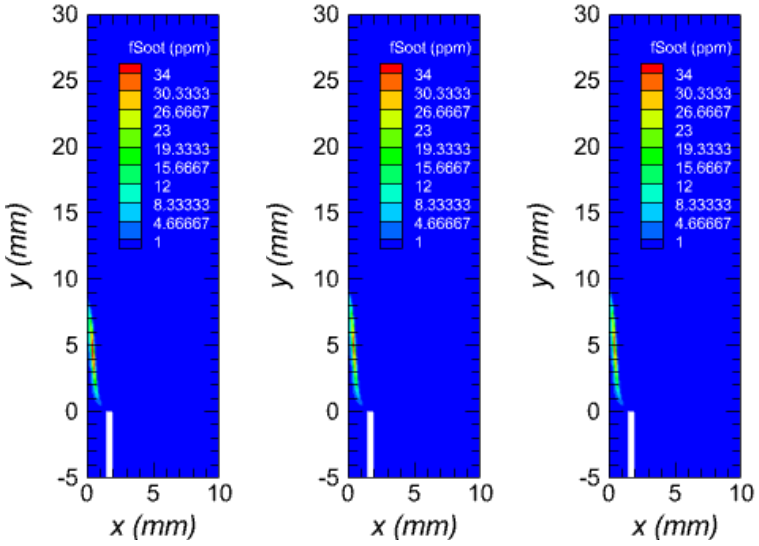

(a) No Rad (b) DOM (c) M_1

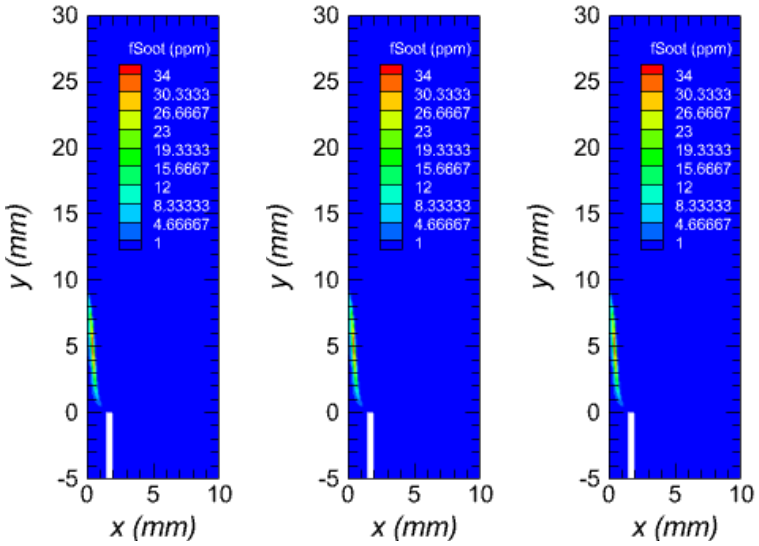

(d) M_2 (e) P_1 (f) P_3

Figure 8.7: Contours of soot volume fraction predicted by (a) the case where radiation is neglected, (b) the DOM, (c) the interpolative-based non-gray M_1 closure, (d) the interpolative-based non-gray M_2 closure, (e) the P_1 closure, and (f) the P_3 closure for methane at 20 atm.

pressure, Figs. 8.4 and 8.5 for 5 atm, and Figs. 8.6 and 8.7 for 20 atm. The corresponding predicted radial profiles of temperature and soot volume fraction at different axial

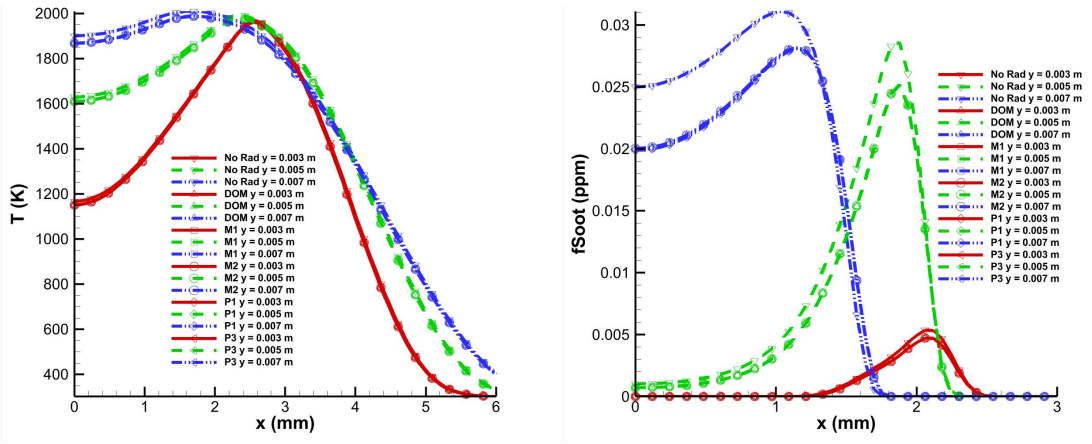

(a) Temperature (b) Soot volume fraction

Figure 8.8: Radial profiles of (a) temperature and (b) soot volume fraction at different axial locations for methane at 1 atm.

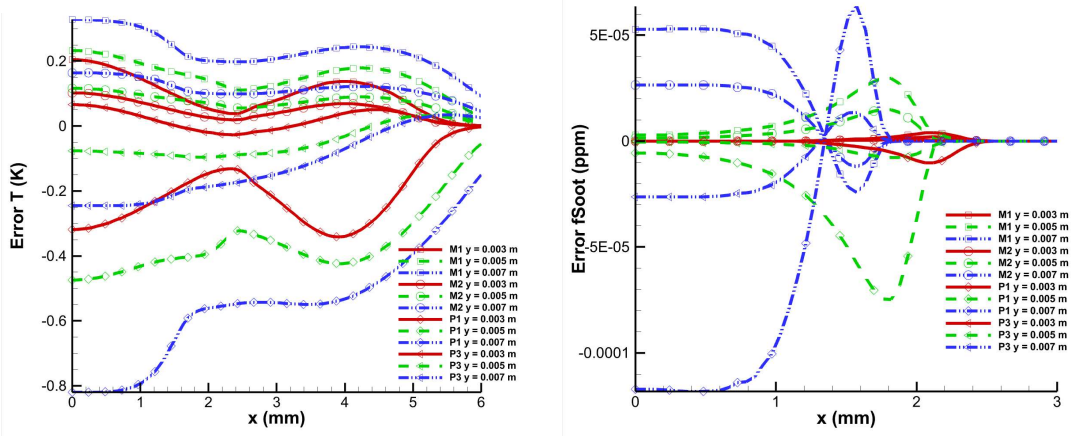

(a) Temperature (b) Soot volume fraction

Figure 8.9: Radial profiles of (a) temperature error and (b) soot volume fraction error for the M_1, M_2, P_1, and P_3 closures, computed with respect to the DOM solutions, at different axial locations for methane at 1 atm.

locations above the burner, are presented in Figs. 8.8, 8.10, and 8.12 for pressures of 1, 5, and 20 atm, respectively. While the latter figures clearly show differences between the solutions obtained in the absence of radiation and those for which radiative heat losses are accounted for, the differences in the predictions of the different radiation models are not as obvious. In order to gain more insight into the predictive capabilities of the M_1, M_2, P_1, and P_3 closures for the present cases, the predicted solution error associated with

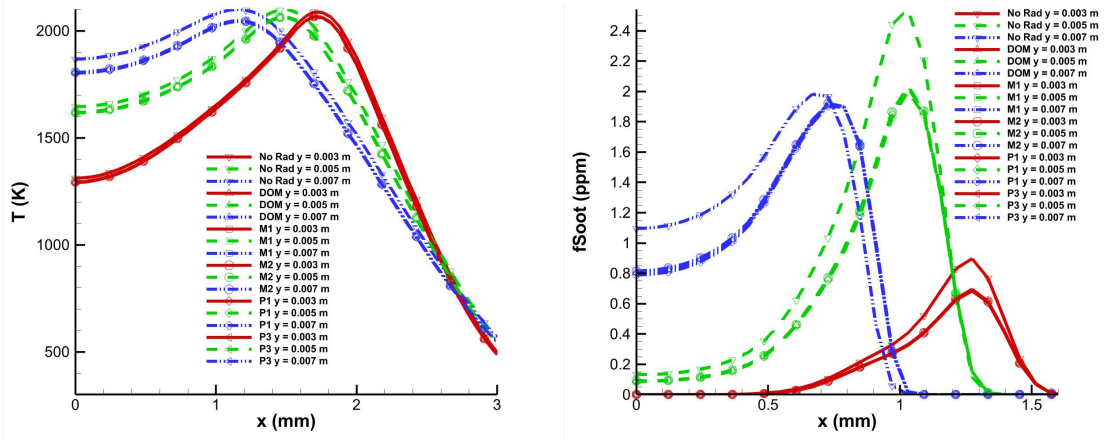

(a) Temperature (b) Soot volume fraction

Figure 8.10: Radial profiles of (a) temperature and (b) soot volume fraction at different axial locations for methane at 5 atm.

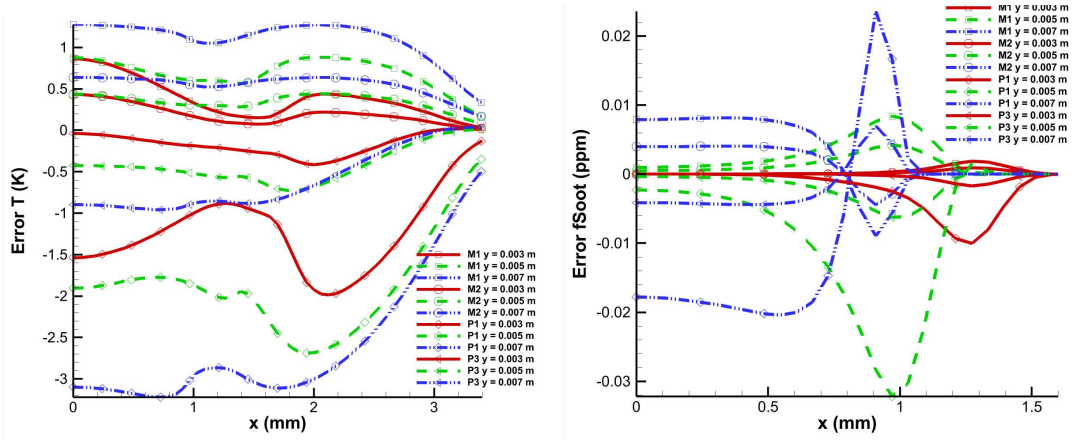

(a) Temperature (b) Soot volume fraction

Figure 8.11: Radial profiles of (a) temperature error and (b) soot volume fraction error for the M_1, M_2, P_1, and P_3 closures, computed with respect to the DOM solutions, at different axial locations for methane at 5 atm.

each of these closure techniques, as determined with respect to the DOM solutions, at the different axial locations, are compared and shown in Figs. 8.9, 8.11, and 8.13 for pressures of 1, 5, and 20 atm, respectively.

From the simulation results of Figs. 8.2–8.7, it is evident that the simulated flames reproduce the established expected structure of the laminar co-flow flames. The narrowing of

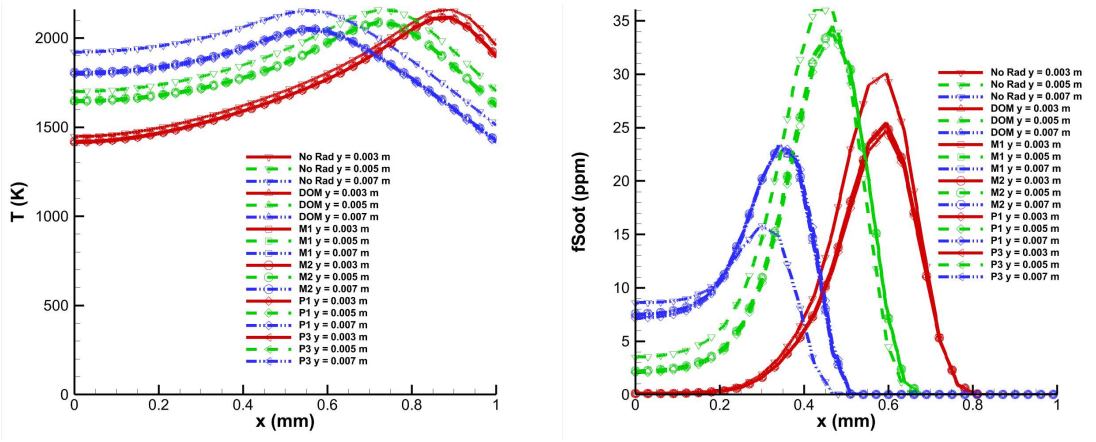

(a) Temperature (b) Soot volume fraction

Figure 8.12: Radial profiles of (a) temperature and (b) soot volume fraction at different axial locations for methane at 20 atm.

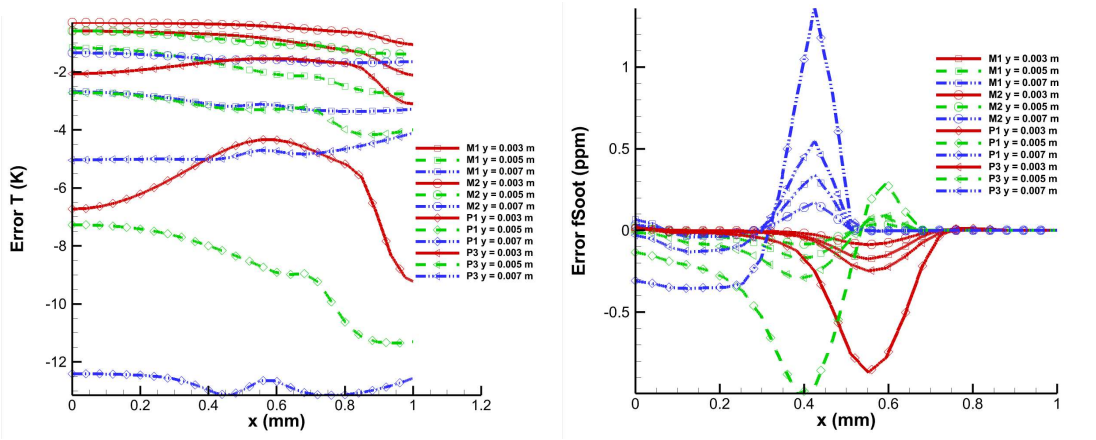

(a) Temperature (b) Soot volume fraction

Figure 8.13: Radial profiles of (a) temperature error and (b) soot volume fraction error for the M_1, M_2, P_1, and P_3 closures, computed with respect to the DOM solutions, at different axial locations for methane at 20 atm.

the flame with increasing pressure is clearly observed. This is also observed in related experimental flames. Moreover, the flame height remains essentially constant as expected for constant carbon mass flow associated with each flame. With increasing pressure, it can also be seen that the initial onset of soot formation begins earlier and that the annular structure becomes thinner and more pronounced.

Several observation can be made from the radial profiles of temperature and soot volume fraction shown in Figs. 8.8, 8.10, and 8.12 for pressures of 1, 5 and 20 atm, respectively. Soot is formed in an annulus downstream of the fuel tube rim and an increase in soot volume fraction is initially observed with height. Higher up in the flame, oxidative processes, which convert soot to gaseous species, cause soot levels to drop. In particular, soot is fully oxidized before leaving the flame resulting in non-smoking flames in each case. Peak values of soot concentration also converge towards the centerline as a result of the inward force exerted by inner accelerating core flow on soot particles. The temperature has an annular structure similar to soot volume fraction except that the radial locations of temperature peaks are at a slightly larger radius. As pressure is increased, the radial profiles of temperature and soot volume fraction contract radially inwards. Soot production also increases with pressure since the higher pressures and contracting flame result in higher gaseous species concentrations, larger mixture densities and faster reaction rates.

In the absence of radiation, the predicted temperature field is systematically overestimated compared to when radiation is accounted for, and this trend becomes more pronounced as pressure increases. This can be expected since radiation contributes to heat losses from the flame zone towards the colder surroundings, thereby yielding overall lower temperatures than cases where such heat losses are not accounted for. Moreover, the predicted soot volume fraction in the case where radiation is neglected is overesti-

Table 8.1: Maximum absolute errors for radial profiles of temperature.

		$\mathbf{M}_1$	$\mathbf{M}_2$	$\mathbf{P}_1$	$\mathbf{P}_3$	**No Rad**
	1 atm	0.204621	0.102311	0.341383	0.0660993	17.951
3 mm	5 atm	0.86057	0.430285	1.98548	0.413941	35.6047
	20 atm	2.11498	1.05749	9.2265	3.10011	59.5373
	1 atm	0.232521	0.116261	0.47436	0.0962005	19.2703
5 mm	5 atm	0.881601	0.4408	2.68747	0.728858	45.9169
	20 atm	2.77332	1.38666	11.3553	4.15822	82.4383
	1 atm	0.3286	0.1643	0.820466	0.245465	31.955
7 mm	5 atm	1.27834	0.63917	3.22358	0.958682	65.351
	20 atm	3.36182	1.68091	13.1546	5.03871	114.788

Table 8.2: Maximum absolute errors for radial profiles of soot.

		$\mathbf{M_1}$	$\mathbf{M_2}$	$\mathbf{P_1}$	$\mathbf{P_3}$	**No Rad**
	1 atm	4.00E-06	2.00E-06	1.03E-05	5.58E-07	0.000620058
3 mm	5 atm	0.00187349	0.000936745	0.0100533	0.00170855	0.203877
	20 atm	0.174664	0.0873321	0.869935	0.247861	5.30354
	1 atm	2.96E-05	1.48E-05	7.49E-05	7.78E-06	0.00387876
5 mm	5 atm	0.00838957	0.00419479	0.0322178	0.0062462	0.584235
	20 atm	0.172135	0.0860673	0.998472	0.297881	5.48135
	1 atm	5.31E-05	2.66E-05	0.000118337	2.64E-05	0.00502766
7 mm	5 atm	0.00894599	0.00447299	0.0235779	0.00700928	0.526559
	20 atm	0.340546	0.170273	1.35959	0.543783	12.3037

mated within the flame zone and correspondingly underestimated away from the latter. On the other hand, predicted peak soot concentrations in the absence of radiation are observed to be higher than cases involving radiative heat losses. This can be attributed to the higher temperature encountered in the case where radiation is not accounted for, which result in more soot production. Peak temperature in cases where radiation is accounted for increases with pressure at a slower rate than when it is neglected since any increase in heat release is counter-acted by radiative heat losses.

It is also evident from the results of Figs. 8.9, 8.11, and 8.13 that the radial profiles of temperature and soot volume fraction predicted by the interpolative-based M_1 closure are more accurate than those of the P_1 closure for all pressures studied and at all axial locations. For the lower pressures of 1 and 5 atm, the predictions of the P_3 closure are observed to be at least as accurate as those of the M_1 closure and of comparable accuracy to the M_2 closure. However, at higher pressures, the M_1 closure yields improved predictions compared to the P_3 closure at all axial locations. In all cases, the M_2 closure yields improved predictions compared to the M_1 closure and is generally at least as accurate as the P_3 closure. The maximum absolute errors for the M_1, M_2, P_1 and P_3 closures, as well as for the case where radiation is neglected, compared to the DOM at the different axial locations and for all the pressures considered, are summarized in Tables 8.1 and 8.2 for temperature and soot volume fraction, respectively. The maximum absolute errors associated with the radial profiles of temperature and soot volume fraction, for all the moment closures considered, at the axial location at 7 mm above the burner rim, are

illustrated in Fig. 8.14 with respect to pressure. It can be easily observed that the M_1 and M_2 closures yield better predictions of the temperature and soot volume fraction than the P_1 and P_3 closures as pressure increases, and these trends also become increasingly more significant as the pressure increases.

In addition to temperature and soot volume fraction, comparisons of the radiation models are also performed in terms of the radiative heat flux and the radiative source term. More specifically, predicted contours of the latter two radiative quantities are respectively presented in Figs. 8.15 and 8.16 for atmospheric pressure (1 atm), Figs. 8.17 and 8.18 for 5 atm, and Figs. 8.19 and 8.20 for a pressure of 20 atm. The aforementioned figures depict contours of the radiative heat flux and radiative source term for all five radiation models considered in the present study, i.e., the DOM and the M_1, M_2. P_1 and P_3 closures. The solutions for each of the five radiation models are obtained by freezing the flow field based on the DOM solutions and consequently performing steady-state simulations of the radiative heat transfer inside the burner. For each of the pressures considered in this study, the thermochemical properties associated with the radiatively participating background medium are chosen to be the same for all five radiation models and are based on converged flame solutions obtained with the DOM as the radiation model. As such, differences in the predicted solutions are solely due to the choice of

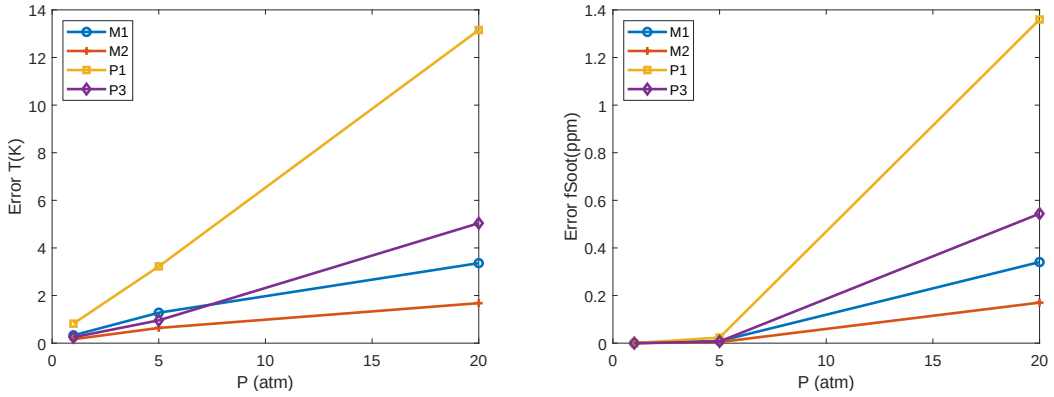

(a) Temperature (b) Soot volume fraction

Figure 8.14: Maximum absolute errors for radial profiles of (a) temperature and (b) soot volume fraction with respect to pressure for the axial location at 7 mm above burner rim. Results are shown for the M_1, M_2, P_1, and P_3 closures and the errors are computed with respect to the DOM solutions,.

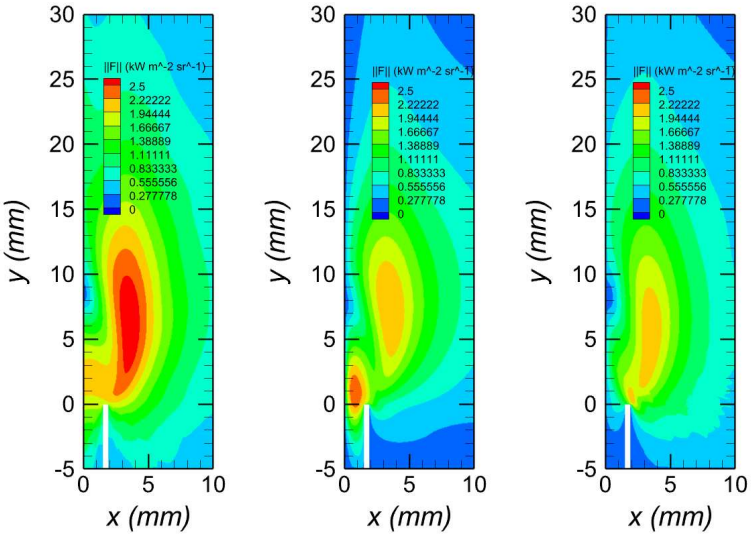

(a) DOM (b) M_1 (c) M_2

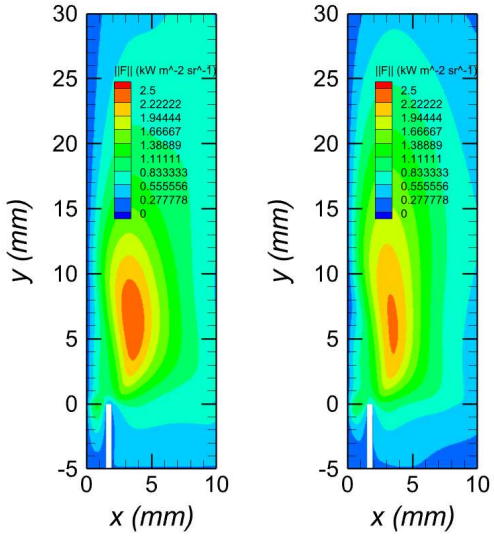

(d) P_1 (e) P_3

Figure 8.15: Contours of radiative heat flux predicted by (a) the DOM, (b) the interpolative-based non-gray M_1 closure, (c) the interpolative-based non-gray M_2 closure, (d) the P_1 closure and, (e) the P_3 closure for methane at 1 atm.

radiation model for solving the RTE.

Prior to discussing the results of Figs 8.15–8.20, it is useful to consider estimates of the optical depth for each flame. This will assist in and provide more insight into the

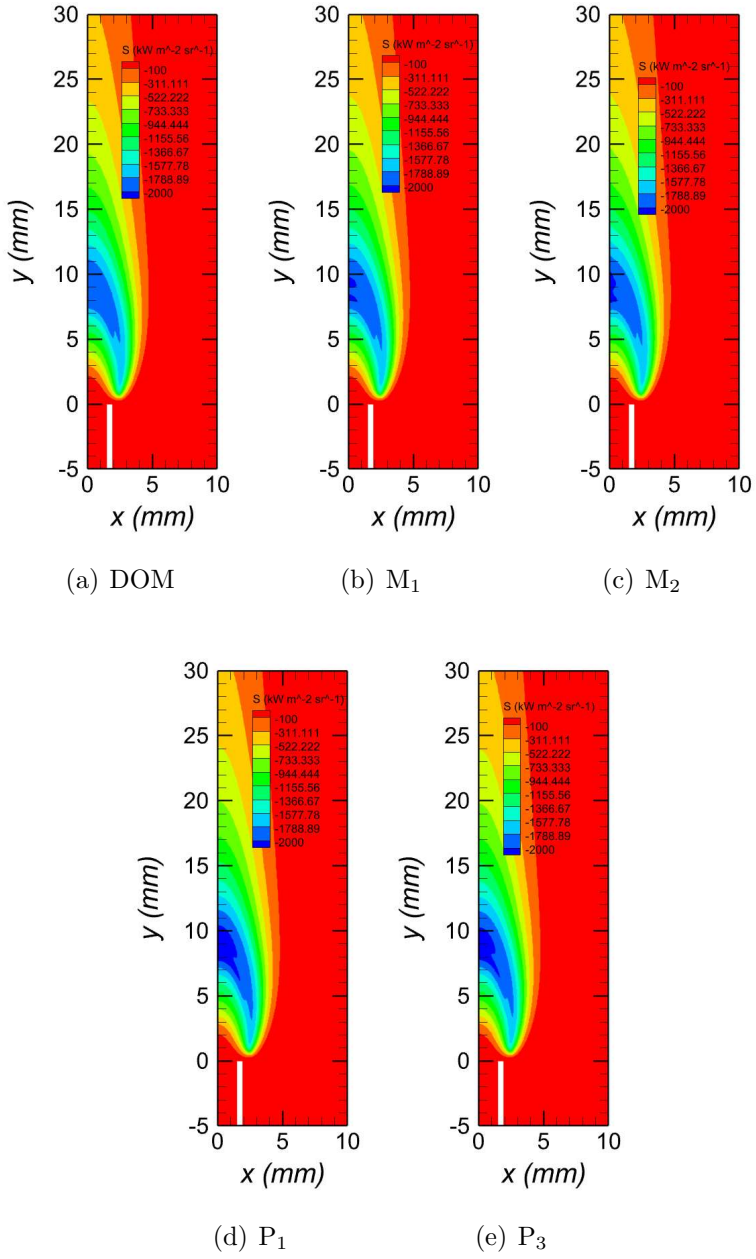

(a) DOM (b) M_1 (c) M_2

(d) P_1 (e) P_3

Figure 8.16: Contours of radiative source term predicted by (a) the DOM, (b) the interpolative-based non-gray M_1 closure, (c) the interpolative-based non-gray M_2 closure, (d) the P_1 closure and, (e) the P_3 closure for methane at 1 atm.

comparisons of the predictions of radiative heat transfer in the laminar diffusion flames of interest here at the three different values of pressure shown in the figures. An approximate estimate of the non-dimensional optical depth or thickness of flames can be obtained in

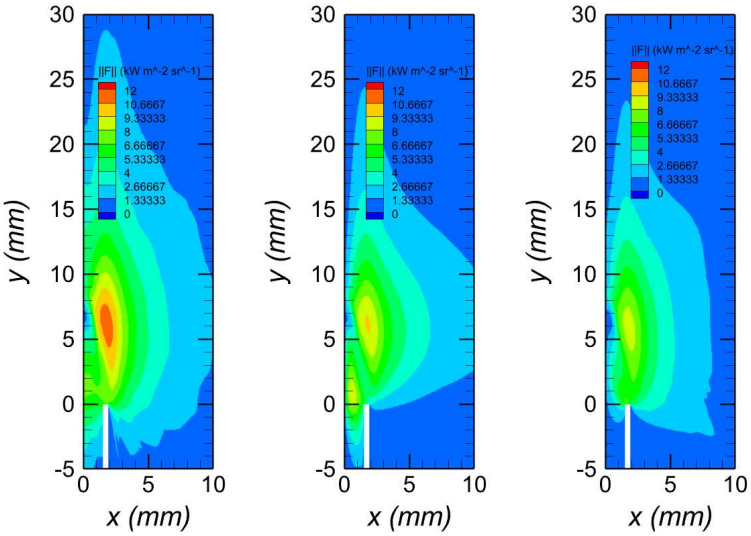

(a) DOM (b) M_1 (c) M_2

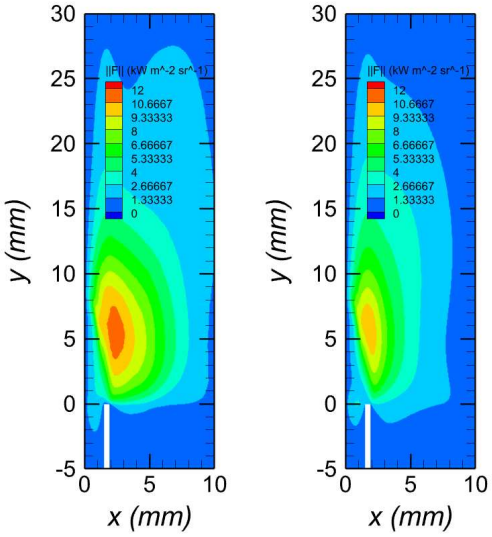

(d) P_1 (e) P_3

Figure 8.17: Contours of radiative heat flux predicted by (a) the DOM, (b) the interpolative-based non-gray M_1 closure, (c) the interpolative-based non-gray M_2 closure, (d) the P_1 closure and, (e) the P_3 closure for methane at 5 atm.

terms of a representative value for the Planck-mean absorption coefficient, κ_P, and a measure of the flame width [201]. For the three co-flow flames of interest, the diameter of the burner fuel nozzle, $d = 3$ mm, is taken as an estimate of the flame thickness and

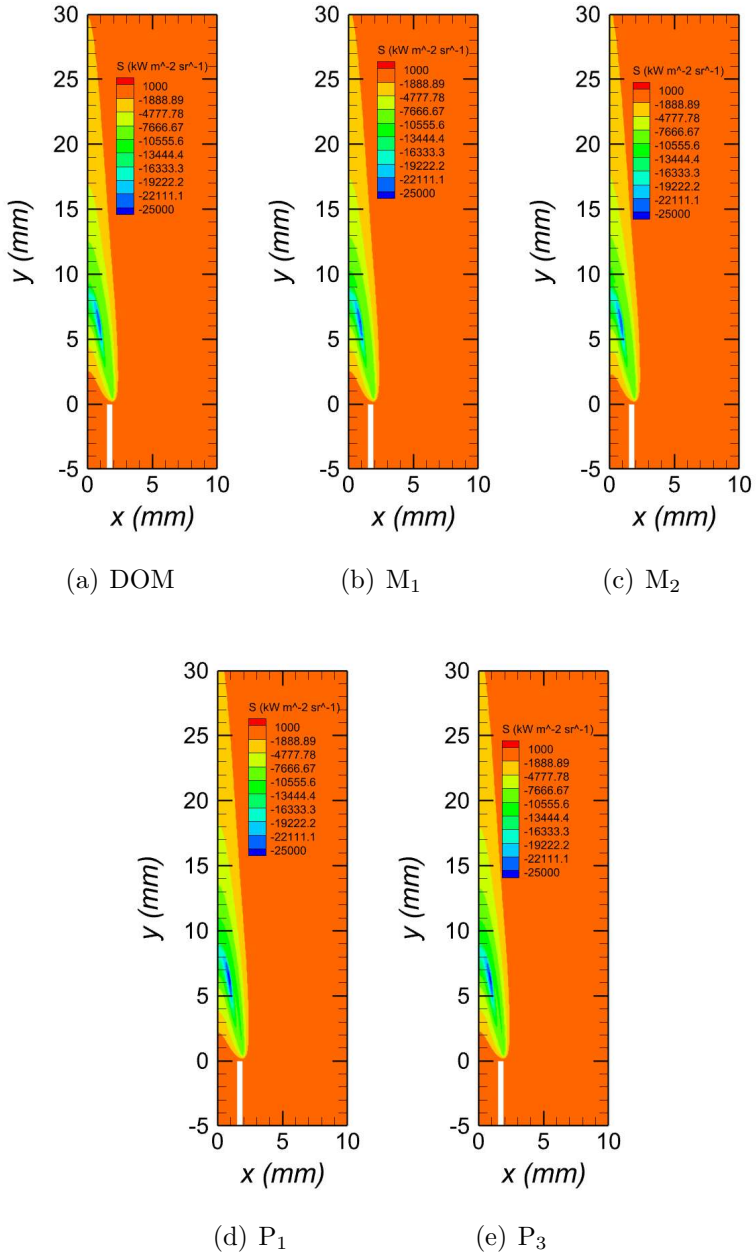

(a) DOM (b) M_1 (c) M_2

(d) P_1 (e) P_3

Figure 8.18: Contours of radiative source term predicted by (a) the DOM, (b) the interpolative-based non-gray M_1 closure, (c) the interpolative-based non-gray M_2 closure, (d) the P_1 closure and, (e) the P_3 closure for methane at 5 atm.

the maximum of the Planck-mean absorption coefficient within the flame was obtained from the flame simulations using the DOM. The product, $\tau = \kappa_P d$, is then taken as an estimate of the non-dimensional optical depth. For values of $\tau \ll 1$, the flame can be

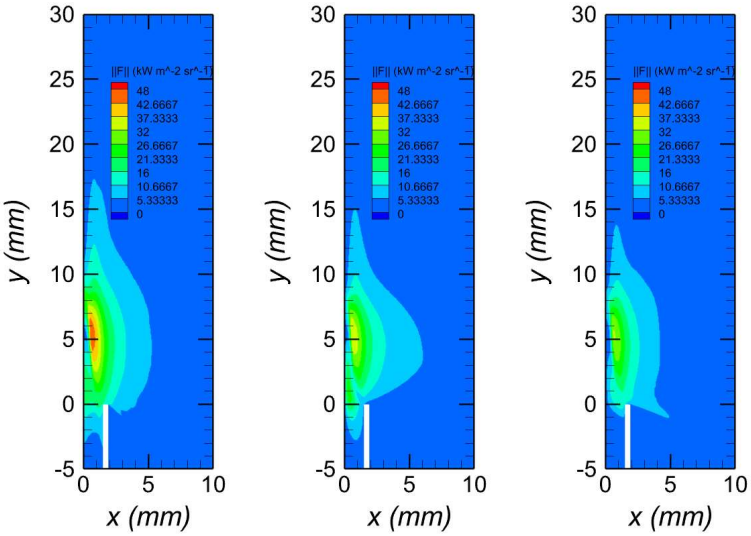

(a) DOM (b) M_1 (c) M_2

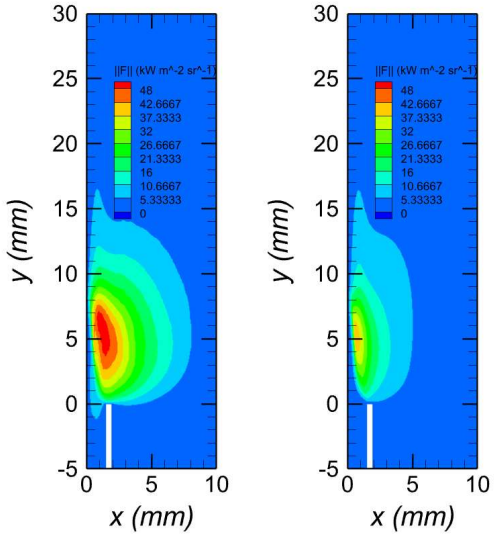

(d) P_1 (e) P_3

Figure 8.19: Contours of radiative heat flux predicted by (a) the DOM, (b) the interpolative-based non-gray M_1 closure, (c) the interpolative-based non-gray M_2 closure, (d) the P_1 closure and, (e) the P_3 closure for methane at 20 atm.

assumed to be optically thin and, for $\tau \gg 1$, the flame is taken to be optically thick. Table 8.3 provides a summary of estimates of the maximum Planck-mean absorption coefficients and non-dimensional optical depths for the three laminar co-flow flames at

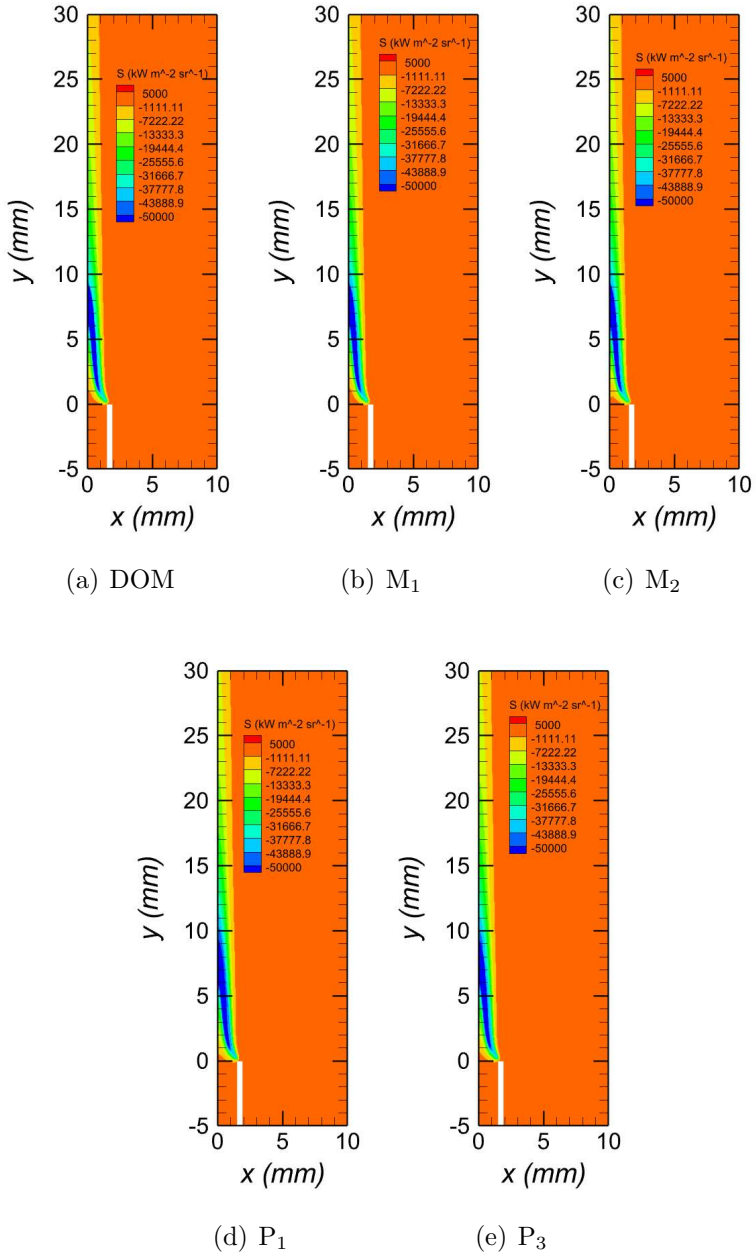

(a) DOM (b) M_1 (c) M_2

(d) P_1 (e) P_3

Figure 8.20: Contours of radiative source term predicted by (a) the DOM, (b) the interpolative-based non-gray M_1 closure, (c) the interpolative-based non-gray M_2 closure, (d) the P_1 closure and, (e) the P_3 closure for methane at 20 atm.

pressures of 1, 5, and 20 atm, respectively. The value of τ for the 1 atm flame is such that the flame is quite clearly optically thin and absorption of radiation is not expected to be significant in this case. As the pressure is increased the optical thickness of the flames

Table 8.3: Optical thickness and maximum Planck-mean absorption coefficient associated with the methane-air flame for pressures of 1, 5, and 20 atm.

	Non-dimensional Optical Depth, τ	Maximum Planck-Mean Absorption Coefficient, κ_P (m^{-1})
1 atm	0.008	2.63
5 atm	0.076	25.01
20 atm	0.320	106.31

increases substantially and, for the 20 atm flame, the non-dimensional optical thickness of 0.32 suggests that radiation absorption is significant within the flame.

Returning to Figs 8.15–8.20, as suggested by the results for the optical depths of each flame, radiation transport becomes more important with increasing pressure due to resulting increases in radiation absorption, which translate into higher peak radiative heat flux and radiative source term. The profiles of these latter two quantities are also observed to be more contracted toward the centreline as pressure increases. For the lower pressure of 1 atm, the P_1 and P_3 closure predict contours of the radiative heat flux that seem to be in better agreement with the DOM compared to the M_1 and M_2 closures. At higher pressures, the radiative heat flux predicted by the M_1 and M_2 closures become more accurate than the predictions of the P_1 closure, which generally tends to over-predict the radiative heat flux. The P_3 closure on the other hand still yields overall good predictions of the radiative heat flux compared to the DOM and is of comparable accuracy to the M_1 and M_2 closures. As far as the radiative source term, the M_1 and M_2 closures generally yield better predictions than the P_1 closure and are at least of comparable accuracy to the P_3 closure. It should also be pointed out that, as can be expected, the proposed interpolative-based M_2 closure yields improved predictions of the radiative quantities compared to its lower-order counterpart, i.e, the interpolative-based M_1 closure, for all the pressures studied.

Chapter 9

Conclusions and Future Work

9.1 Conclusions

Robust and computationally efficient interpolative-based maximum entropy moment closures have been proposed and developed as part of this thesis. In particular, new formulations of the second-order M_2 closure for gray radiation, as well as the first-order M_1 and second-order M_2 closures for non-gray radiation, were derived. These newly developed interpolative-based maximum entropy closures result in substantial computational savings compared to an approach that makes use of the direct numerical solution of the optimization problem for entropy maximization, while closely mimicking the solution quality and desirable properties of the original M_N closures. A new procedure has also been proposed for the implementation and coupling of the non-gray M_N closures with realistic absorption models, in particular the SNBCK spectral radiation model. Furthermore, new boundary conditions have been developed for use with the hyperbolic systems of equations arising from the new interpolative-based M_1 and M_2 closures, whether be it for gray or non-gray radiation.

An extensive investigation of the predictive capabilities of the newly proposed interpolative-based M_1 and M_2 closures, in terms of both accuracy and computational costs, was then carried out by considering various test problems involving radiative heat transfer. The first set of test cases was concerned with radiative heat transfer within gray participating media confined between parallel plates as well as within rectangular enclosures, and was considered for the assessment of the new interpolative gray M_2 closure. The next

set of test problems assessed the predictive capabilities of the new non-gray M_1 and M_2 closures in the context radiative transfer in non-gray participating media with realistic absorption models, whereby both parallel plates configurations and rectangular domains were also considered. For both of the aforementioned sets of test problems, radiatively participating/non-participating media with prescribed thermochemical quantities were considered. The final part of the assessment of the moment closures involved more practical numerical simulations of laminar reactive flows in burner-like configurations. In particular, sooting methane-air laminar co-flow diffusion flames at elevated pressures were investigated having a range of optical depths.

The numerical results obtained as part of the analysis for non-reactive flows revealed that the M_1 closure generally provides more accurate and more robust predictions of the radiative energy density, radiative heat flux, and radiative source term compared to the P_1 spherical harmonic closure. The only exception to the above statement are cases involving crossing streams of photons. In such cases, the M_1 closure generally yielded less accurate predictions of the radiative quantities of interest compared to the P_1 closure. Nevertheless, some of our findings illustrate than the M_1 closure can yield solutions of comparable accuracy to those of the P_3 closure, especially in terms of the radiative source term, the latter being the quantity of interest when the radiation solver is to be coupled with a reactive flow solver. The inability of the M_1 closure to properly capture crossing streams of photons travelling in different directions can be tackled by considering the next higher-order maximum entropy moment closure, namely the second-order, M_2, closure. The latter was observed to yield predictions of the radiative quantities at least as accurate as those of the P_3 closure. Furthermore, in many of the cases studied, the M_2 closure outperformed the P_3 closure in terms of solution accuracy and was even in very close agreement with the DOM. As can be expected, the interpolative-based M_2 closure was also observed to yield more accurate predictions of the radiative quantities compared to its lower-order counterpart, i.e., the M_1 closure, for all the cases considered.

As far as comparisons of computational costs are concerned, the M_1 closure for gray radiation and the interpolative-based non-gray M_1 closure were observed to result in rather minor or modest increases in computational expenses (storage and computing time) compared to the P_1 closure, while yielding appreciable improvement in computational efficiency relative to the P_3 closure. Moreover, the computational costs associated with the proposed interpolative-based M_2 closures for both gray and non-gray radiation,

though substantially lower than those associated with an approach making repeated use of the direct numerical solution of the entropy optimization problem, were more involved than those of the M_1, P_1 and P_3 closures for all the cases considered.

The reactive flow simulations performed as part of this thesis showed that the M_1 and M_2 closures yield better predictions of temperature distribution and soot concentration compared to the P_1 closure for all pressures considered, and these improvements become more substantial as the pressure increases. Furthermore, while the predictions of the P_3 closure were observed to be at least as accurate as those of the M_1 closure and of comparable accuracy to those of the M_2 closure at low pressures, for the higher pressures, the M_1 and M_2 closure yielded improved predictions compared to the P_3 closure at all axial locations. In all cases, the M_2 closure yielded improved predictions compared to the M_1 closure and was generally at least as accurate as the P_3 closure. The observed trends indicate that, relative to the P_1 and P_3 closures, the M_1 and M_2 closures would yield increasingly more accurate predictions of temperature and soot volume fraction with pressure. These improvements in solution accuracy would be expected to be even more significant for large-scale practical devices operating in turbulent regimes as the associated optical depths would thus be much larger than those corresponding to the smaller laboratory-scale burner for laminar flames studied as part of this thesis.

The findings of this thesis are of particular significance for applications related to transportation (automotive and aeronautical) systems as well as for industrial energy production, where mechanical energy is generally produced from the combustion of hydrocarbons at elevated pressures. The design phase of such engines often relies on numerical modelling, which generally involves solving transport equations for a wide range of coupled underlying physical phenomena in relatively complex geometries. In such cases, using the DOM for the solution of the RTE may become prohibitively expensive due to the relatively large number of unknowns involved as well as the large number ot iterations that may be required by the space marching iterative technique. The numerical results suggest that the proposed interpolative-based non-gray M_1 and M_2 moment closures would represent competitive alternatives to the DOM, in comparison to the P_1 and P_3 closures, for providing accurate and efficient approximate solutions to the equation of radiative transfer for such practical applications. In particular, a more attractive choice of radiation model for such applications would be the M_1 closure, as a result of its good balance between accuracy and computational costs. However, if better solution accuracy

is desired, the M_2 closure may be more suitable, though this may incur some increases in computational expenses compared to the M_1 closure.

While the main focus of the thesis was the development and assessment of radiative transfer models, using entropy-based closures, for applications relevant to transportation systems as well as industrial energy production, the above findings are also relevant to many other applications involving radiation transport. In the healthcare industry, radiation is used extensively whether be it for diagnosis (body imaging) or treatment of patients. Such medical procedures generally involve the passage of high-energy beams of radiation through a patients' body, and require accurate computations of the dose administered. In other applications related to active remote sensing, concentrated beams of radiation are emitted onto the target and the energy reflected back to the emitter is measured so as to determine the characteristics of the target.

As far as the development of climate models or for the purpose of weather forecasting, an important factor to consider is the incident radiation from the sun at the top of the atmosphere. The latter is beam-like as the photons emanating from the sun towards the earth travel through vacuum and are therefore unaffected as they travel towards the earth's atmosphere. Most of the incident radiation enters the earth's atmosphere where a portion of it (the incident radiation) is attenuated (via absorption, emission, scattering, reflection), while the most part reaches the earth's surface without attenuation.

The findings of the present thesis also suggest that the M_1 and M_2 closures, as a result of their ability to handle beam-like distributions, would represent better alternatives over the P_1 and P_3 closures for dose simulations in radiation-based therapy, for weather forecasting and climate modelling, as well as for remote sensing applications. Furthermore, in the case where crossing beams of radiation may arise in any of these applications, in particular for bimodal beams, the M_2 closure would represent a better choice over its lower-order counterpart as the latter cannot properly capture such phenomena.

9.2 Summary of Contributions

The contributions resulting from the research carried out as part of this thesis can be summarized as follows:

- A new formulation of the dual entropy optimization problem for non-gray radiation was proposed in order to facilitate the interpolation of maximum-entropy-based solutions over the full spectrum of frequencies. In particular, a parameterization was proposed, which allowed to combine the frequency variable and the radiative energy density into one parameter, instead of two separate parameters;

- A new, realizable and hyperbolic interpolative-based non-gray first-order maximum-entropy, M_1, moment closure was developed in order to accurately and efficiently reproduce the original maximum-entropy solutions for the second-order closing fluxes at a fraction of the computational costs associated with the numerical solution of the highly non-linear maximum entropy problem;

- New interpolation procedures for accurately and efficiently computing the third-order closing fluxes arising from both the gray and non-gray second-order maximum entropy, M_2, closures were also proposed. The new interpolative-based approaches for both gray and non-gray radiation allowed to accurately compute maximum entropy solutions for the third-order closing fluxes while allowing for substantial reductions in computational costs when compared to an approach which makes use of the direct numerical solution of the entropy optimization problem;

- New boundary conditions were developed for use with the governing equation arising from the M_1 and M_2 closures in the context of both gray and non-gray radiation in two-dimensional physical space;

- A new procedure for the incorporation of the maximum-entropy M_N closures with the state-of-the-art SNBCK spectral radiation model has been proposed;

- Finally, the thesis represents the first study involving application and assessment of non-gray maximum-entropy closures for the prediction of radiative heat transfer in real gases with realistic absorption models, for non-reactive flows as well as laminar reactive flows with soot formation.

9.3 Recommendations for Future Work

The analysis carried out as part of this thesis represents one step forward in the investigation and assessment of the predictive capabilities of maximum-entropy-based, M_N,

moment closures and has shown rather promising results. This thesis has also illustrated the potential of interpolative-based procedures to accurately mimic maximum-entropy based solutions for the closing fluxes while only requiring a fraction of the computational costs associated with the numerical solution of the original maximum entropy problem. These findings are rather promising and provide a solid foundation for future research related to the application and assessment of the M_1 and M_2 closures, as well as their higher-order extensions ($N \geq 3$).

Turbulence-Radiation Interactions (TRI)

As a follow-up for the assessment of the M_1 and M_2 closures in laminar flames with soot formation, it would seem natural to extend the investigations of the predictive capabilities of the latter closures to the case of sooting turbulent non-premixed flames at elevated pressures. In such types of reactive flows, time averaging or spatial filtering of the system of moment equations for either one of the interpolative M_1 and M_2 closures will result in an additional closure problem due to the non-linearity of the resulting higher-order closing fluxes in terms of the lower-order moments. A special treatment of the latter will be required in order to obtain closed description of the resulting system of moment equations. To our knowledge, the only study involving the development of TRI models for maximum-entropy-based moment closures is due to Ripoll [63]. The author of this previous study proposed a framework for providing closure to the RANS-based formulation of the system of moment equations arising from the M_1 moment closure technique for gray radiation. The original formulation was however rather complicated and very expensive for coupling with a reactive flow solver and further simplifications were subsequently proposed by Ripoll and Pitsch [64].

Incorporation with Full-Spectrum Correlated-k Spectral Technique

It would also be worthwhile to consider the implementation of the interpolative non-gray M_1 and M_2 closures in the context of the FSCK [34] spectral radiation model for further potential reductions in computational expenses compared to the SNBCK treatment. The FSCK is in fact expected to provide more efficient approximate radiation solutions, relative to the SNBCK model, as the reordering procedure for the spectral absorption coefficient is directly applied to the full spectrum of frequencies, such that

the total number of quadrature points required for integration over the full range of wavenumbers is reduced, compared to the SNBCK treatment.

Assessment of Different Types of Boundary Conditions

The proper prescription of boundary conditions is still an open problem for moment closure techniques applied to the RTE. While there has been a number of studies [67–69] dedicated to the assessment of boundary conditions for the P_N closures owing to their relative simplicity and the existence of closed form expressions, a very limited number of studies have been devoted to boundary data prescriptions for the M_N closures [51]. More specifically, to the author's knowledge to date, the only study aimed at systematically comparing different types of boundary conditions for the M_N closures is due to Brunner and Holloway [51] and this study was only concerned with the M_1 closure in one-dimensional physical space. In an effort to further improve our understanding of boundary data prescriptions on the M_N closures, it would be crucial to extend the analysis of Brunner and Holloway [51] to multi-dimensional physical space and also to higher-order entropy-based moment closures, i.e., $N \geq 2$.

Appendix A

Undetermined Forms of the Polynomial Expression for the Interpolative-Based Non-Gray M_1 Closure

The weighting function, g_{χ_2}, defined as a polynomial expansion in Eq. (3.22) can be directly computed from Eqs. (3.20) and (3.21), for sets of angular moments up to first-order away from both the isotropic and anisotropic limits, as follows

$$g_{\chi_2} = \frac{f_{\chi_2} - \|N^{(1)}\|^2}{\|N^{(1)}\|^2(1 - \|N^{(1)}\|^2)}, \tag{A.1}$$

where

$$f_{\chi_2} = \frac{3\chi_2 - 1}{2}. \tag{A.2}$$

For either the isotropic or the free-streaming limits, the expression given in Eq. (A.1) cannot be used directly to compute g_{χ_2}, and some mathematical manipulations must be carried out in order to obtain a computable expression. More specifically, in the isotropic limit, characterized by $\|N^{(1)}\| = 0$, we can write g_{χ_2} as follows

$$g_{\chi_2} = \lim_{\|N^{(1)}\| \to 0} \frac{f_{\chi_2} - \|N^{(1)}\|^2}{\|N^{(1)}\|^2(1 - \|N^{(1)}\|^2)}.$$

The latter expression can be reformulated as follows

$$g_{\chi_2} = \lim_{\|N^{(1)}\| \to 0} \frac{f_{\chi_2} - \|N^{(1)}\|^2}{\|N^{(1)}\|^2} \lim_{\|N^{(1)}\| \to 0} \frac{1}{1 - \|N^{(1)}\|^2},$$

which can be further simplified into the form

$$g_{\chi_2} = \lim_{\|N^{(1)}\|\to 0} \left(\frac{f_{\chi_2}}{\|N^{(1)}\|^2} \right) - 1.$$

Since $f_{\chi_2} \to 0$ as $\|N^{(1)}\| \to 0$, the limit in the latter equation can be computed by applying l'Hopital's rule, yielding

$$g_{\chi_2} = \lim_{\|N^{(1)}\|\to 0} \left(\frac{1}{2\|N^{(1)}\|} \frac{\partial f_{\chi_2}}{\partial \|N^{(1)}\|} \right) - 1.$$

The latter expression can still not be used to compute g_{χ_2}, due to the fact that $\partial f_{\chi_2}/\partial\|N^{(1)}\| \to 0$ as $\|N^{(1)}\| \to 0$, thereby still yielding an undetermined expression. This can be overcome by applying once again l'Hopital's rule, which yields

$$g_{\chi_2} = \frac{1}{2} \left(\frac{\partial^2 f_{\chi_2}}{\partial \|N^{(1)}\|^2} \right) \Bigg|_{\|N^{(1)}\|=0} - 1. \tag{A.3}$$

Substituting the expression for f_{χ_2} in terms of χ_2, given in Eq. (A.2), in the latter expression yields

$$g_{\chi_2} = \frac{3}{4} \left(\frac{\partial^2 \chi_2}{\partial \|N^{(1)}\|^2} \right) \Bigg|_{\|N^{(1)}\|=0} - 1. \tag{A.4}$$

The procedure for computing second derivatives of the Eddington factor with respect to the first-order normalized angular moment is summarized in D. In the case where the free-streaming limit is encountered, i.e., in the case where $\|N^{(1)}\| = 1$, g_{χ_2} can be written in the form

$$g_{\chi_2} = \lim_{\|N^{(1)}\|\to 1} \frac{f_{\chi_2} - \|N^{(1)}\|^2}{\|N^{(1)}\|^2(1 - \|N^{(1)}\|^2)},$$

which can be further simplified as follows

$$g_{\chi_2} = \lim_{\|N^{(1)}\|\to 1} \frac{f_{\chi_2} - \|N^{(1)}\|^2}{1 - \|N^{(1)}\|^2},$$

It is clear that the latter expression results in an undetermined form since $f_{\chi_2} \to 1$ as $\|N^{(1)}\| \to 1$. To circumvent this issue, we apply l'Hopital's rule, which yields the following expression for g_{χ_2}

$$g_{\chi_2} = 1 - \frac{1}{2} \frac{\partial f_{\chi_2}}{\partial \|N^{(1)}\|} \Bigg|_{\|N^{(1)}\|=1}. \tag{A.5}$$

Substituting the expression for f_{χ_2} in terms of χ_2, given in Eq. (A.2), in the latter allows us to write

$$g_{\chi_2} = 1 - \frac{3}{4} \frac{\partial \chi_2}{\partial \|N^{(1)}\|} \Bigg|_{\|N^{(1)}\|=1}. \tag{A.6}$$

Unlike the isotropic limit, the expression for g_{χ_2} in the free-streaming limit, Eq. (A.6), cannot be computed directly using a similar procedure as the one described in D, since the matrix, $H^{(1)}$, of first derivatives of the lower-order angular moments with respect to the Lagrange multipliers, required for such computations, becomes singular in such limit. As such, a finite difference approach is used to calculate the derivative appearing in Eq. (A.6).

Appendix B

Moment Realizability

B.1 Necessary and Sufficient Conditions for Realizability

Let us denote by $R_{M_2}^{diag}$ the rotation matrix which transforms the coordinates system such that the second-order tensor $N^{(2)} - N^{(1)}(N^{(1)})^T$ is diagonal. The necessary realizability conditions for the moments in the new coordinate frame, with realizability domain $\mathcal{R}_T^2$, can then be derived from those for the moments in the original frame, characterized by the realizability domain $\mathcal{R}^2$, by means of the transformation matrix, $R_{M_2}^{diag}$, as follows

$$\begin{aligned}\mathcal{R}_T^2 = \{(I'^{(0)}, I'^{(1)}, I'^{(2)}) \in \mathbb{R}^3 \times \mathbb{R}^{3\times 3}, \quad \text{s.t.} \quad & I'^{(0)} \geq 0, \quad \|N'^{(1)}\| \leq 1, \\ & N'^{(2)} - N'^{(1)}(N'^{(1)})^T \geq 0, \quad (R_{M_2}^{diag}\vec{n})^T N'^{(2)} (R_{M_2}^{diag})\vec{n} \leq 1 \quad \forall \quad \|\vec{n}\| \leq 1, \\ & tr(N'^{(2)}) = 1 \quad \text{and} \quad N_{ij}'^{(2)} = N_{ji}'^{(2)}\}.\end{aligned}$$

The transformation from one set of moments to the other is illustrated in Eq. (3.31). Since $(N_{ij}'^{(2)} - N_i'^{(1)} N_j'^{(1)})$ is diagonal, one can write

$$N_{ij}'^{(2)} - N_i'^{(1)} N_j'^{(1)} = \lambda_i \delta_{ij}$$

where λ_i correspond to the eigenvalues of $(N_{ij}'^{(2)} - N_i'^{(1)} N_j'^{(1)})$, with the associated eigenvector, $\vec{\eta}_i$, coinciding with the unit vector along the coordinate axes with all entries equal to 0 except for the i^{th} entry which is equal to 1. Using the trace identity for the

second-order moment, we can write

$$tr(N'^{(2)}_{ij} - N'^{(1)}_i N'^{(1)}_j) = \sum_{i=1}^{3} \lambda_i$$
$$tr(N'^{(2)}_{ij}) - tr(N'^{(1)}_i N'^{(1)}_j) = \sum_{i=1}^{3} \lambda_i$$
$$\sum_{i=1}^{3} \lambda_i = 1 - \|N^{(1)}\|^2$$

The latter identity can be further normalized by introducing normalized parameters γ_i such that

$$\lambda_i = (1 - \|N^{(1)}\|^2)\gamma_i$$

and hence

$$\sum_{i=1}^{3} \gamma_i = 1. \tag{B.1}$$

Furthermore, since $\vec{\eta}_i$ is an eigenvector of $(N'^{(2)}_{ij} - N'^{(1)}_i N'^{(1)}_j)$ with eigenvalue $\lambda_i = (1 - \|N'^{(1)}\|^2)\gamma_i$, it follows that

$$(N'^{(2)} - N'^{(1)}(N'^{(1)})^T)\vec{\eta}_i = \lambda_i \vec{\eta}_i$$
$$\vec{\eta}_i^T (N'^{(2)} - N'^{(1)}(N'^{(1)})^T)\vec{\eta}_i = \vec{\eta}_i^T \lambda_i \vec{\eta}_i$$
$$\vec{\eta}_i^T (N'^{(2)} - N'^{(1)}(N'^{(1)})^T)\vec{\eta}_i = \lambda_i \vec{\eta}_i^T \vec{\eta}_i$$
$$\vec{\eta}_i^T (N'^{(2)} - N'^{(1)}(N'^{(1)})^T)\vec{\eta}_i = \lambda_i \|\vec{\eta}_i\|$$

Since $\vec{\eta}_i$ is a unit vector, we have $\|\vec{\eta}_i\|$, and,

$$\vec{\eta}_i^T (N'^{(2)} - N'^{(1)}(N'^{(1)})^T)\vec{\eta}_i = \lambda_i$$
$$\vec{\eta}_i^T (N'^{(2)} - N'^{(1)}(N'^{(1)})^T)\vec{\eta}_i = (1 - \|N'^{(1)}\|^2)\gamma_i$$

From the realizability conditions described above, we have

$$\vec{\eta}_i^T (N'^{(2)} - N'^{(1)}(N'^{(1)})^T)\vec{\eta}_i \geq 0 \quad \text{and} \quad \|N'^{(1)}\| \leq 1$$

It therefore follows that

$$\gamma_i \geq 0, \quad i = 1, \ldots, 3. \tag{B.2}$$

B.2 Form of the Closure Relation on the Boundaries of the Realizability Domain

On the boundaries of the realizability domain for moments up to second-order, $\mathcal{R}_T^2$, in multiple space dimensions, which we denote $\partial\mathcal{R}_T^2$, the inequality constraints on the normalized first- and second-order moments become sharp, and some or all of the higher-order moments are uniquely determined in terms of the lower-order moments. More specifically $\partial\mathcal{R}_T^2$ can be written in the form

$$\begin{aligned}\partial\mathcal{R}_T^2 = \{(I'^{(0)}, I'^{(1)}, I'^{(2)}) \in \mathbb{R}^3 \times \mathbb{R}^{3\times 3}, \quad \text{s.t.} \quad & I'^{(0)} \geq 0, \\ & tr(N'^{(2)}) = 1, \qquad N'^{(2)}_{ij} = N'^{(2)}_{ji} \quad \text{and} \quad \|N'^{(1)}\| = 1 \\ \text{or} \quad & (R^{diag}_{M_2}\vec{n})^T(N'^{(2)} - N'^{(1)}(N'^{(1)})^T)(R^{diag}_{M_2}\vec{n}) = 0 \quad \forall \quad \vec{n} \in \mathbb{R}^3\backslash\mathbf{0} \\ \text{or} \quad & (R^{diag}_{M_2}\vec{n})^T N'^{(2)}(R^{diag}_{M_2}\vec{n}) = 1 \quad \forall \quad \|\vec{n}\| \leq 1\}.\end{aligned} \tag{B.3}$$

We will now discuss the characteristics of each of the boundaries and also present the form of the distribution in terms of the known finite of moments up to second-order.

In the case where $\|N'^{(1)}\| = 1$, which corresponds to the so-called free-streaming limit, we have

$$\begin{aligned}\|N'^{(1)}\|^2 = (N'^{(1)})^T N'^{(1)} &= 1 \\ (N'^{(1)})^T \frac{\|I'^{(1)}\|}{I'^{(0)}} &= 1 \\ (N'^{(1)})^T I'^{(1)} &= I'^{(0)} \\ (N'^{(1)})^T \int_{4\pi} \vec{s} I \mathrm{d}\Omega = \int_{4\pi} (N'^{(1)})^T \vec{s} I \mathrm{d}\Omega &= \int_{4\pi} I d\Omega \\ \int_{4\pi} (1 - (N'^{(1)})^T \vec{s}) I \mathrm{d}\Omega &= 0\end{aligned}$$

Since radiative intensity distribution is non-negative, i.e, $I \geq 0$, and by definition $1 - (N'^{(1)})^T\vec{s} \geq 0$, it therefore follows that the latter equality holds if and only if the intensity distribution I is equal to 0 everywhere except on the line $\vec{s} = N'^{(1)}$, in which case the distribution takes the form

$$I = I^{(0)}\delta(\vec{s} - N'^{(1)}) \tag{B.4}$$

The form of the distribution in Eq. (B.4) can be integrated directly to obtain analytical expression for $N^{(3)}$

$$N'^{(3)}_{ijk} = N'^{(1)}_i N'^{(1)}_j N'^{(1)}_k. \tag{B.5}$$

Let us now consider the case where $(R_{M_2}^{diag}\vec{n})^T(N'^{(2)} - N'^{(1)}(N'^{(1)})^T)(R_{M_2}^{diag}\vec{n}) = 0 \; \forall \quad \vec{n} \in \mathbb{R}^3\backslash\mathbf{0}$, and, in particular, the case where $R_{M_2}^{diag}\vec{n} = \vec{\eta_i}$, we then have

$$\vec{\eta_i}^T(N'^{(2)} - N'^{(1)}(N'^{(1)})^T)\vec{\eta_i} = (1 - \|N'^{(1)}\|^2)\gamma_i = 0.$$

For such relationship to hold for all $\|N^{(1)}\| \leq 1$, we must have

$$\gamma_i = 0,$$

which corresponds to one of the edges of the triangle ($\mathrm{P_1P_2P_3}$) illustrated in Fig. 3.7; more specifically the edge ($\mathrm{P}_j\mathrm{P}_k$), $i \neq j \neq k$. Along such an edge, we can write

$$N'^{(2)}_{ii} - N'^{(1)}_i N'^{(1)}_i = 0 \tag{B.6}$$

$$I'^{(2)}_{ii} - N'^{(1)}_i I'^{(1)}_i = I'^{(2)}_{ii} - 2N'^{(1)}_i I'^{(1)}_i + \frac{(I'^{(1)}_i)^2}{I'^{(0)}} = 0 \tag{B.7}$$

$$\int_{4\pi} s_i^2 I \mathrm{d}\Omega - 2N'^{(1)}_i \int_{4\pi} s_i I \mathrm{d}\Omega + \left(\frac{I'^{(1)}_i}{I'^{(0)}}\right)^2 \int_{4\pi} I \mathrm{d}\Omega = 0 \tag{B.8}$$

$$\int_{4\pi} (s_i^2 - 2N'^{(1)}_i s_i + (N'^{(1)}_i)^2) I \mathrm{d}\Omega = 0 \tag{B.9}$$

$$\int_{4\pi} (\Omega_i - N'^{(1)}_i)^2 I \mathrm{d}\Omega = 0 \tag{B.10}$$

Since $I \geq 0$ and by definition $(\Omega_i - N'^{(1)}_i)^2 \geq 0$, we can then conclude that the latter equality holds if and only if the intensity distribution I is equal to 0 everywhere except on the plane characterized by $s_i = N_i^{(1)}$. In the context of moment reconstruction using the principle of maximization of entropy, the distribution then takes the form

$$I = \frac{\delta(s_i - N'^{(1)}_i)}{\exp(\boldsymbol{\alpha}^T m(\vec{s})) - 1} \tag{B.11}$$

where the monomial basis for the angular moments, $m(\vec{s})$, reads as follows

- for $i = 1$
$$m(\vec{s}) = \left[1, \Omega_2, \Omega_3, \Omega_2^2, \Omega_2\Omega_3\right];$$
- for $i = 2$
$$m(\vec{s}) = \left[1, \Omega_1, \Omega_3, \Omega_1^2, \Omega_1\Omega_3\right];$$
- for $i = 3$
$$m(\vec{s}) = \left[1, \Omega_1, \Omega_2, \Omega_1^2, \Omega_1\Omega_2\right].$$

In the case where one of γ_i, $i = 1, \ldots, 3$, is equal to one as is the case at the vertices of the triangle (P_1 P_2 P_3), then $\gamma_j = 0$, $j \in \{1, 2, 3\}$ and $j \neq i$, and from the findings in Eq. (B.6), combined with the fact that $\vec{s}$ is a unit vector, it follows that the distribution is equal to zero everywhere except on the line

$$\vec{s} = \begin{cases} (\pm\sqrt{1 - \|N'^{(1)}\|^2 + (N_1'^{(1)})^2}, N_2'^{(1)}, N_3'^{(1)}) & \text{if} \quad \gamma_1 = 1, \\ (N_1'^{(1)}, \pm\sqrt{1 - \|N'^{(1)}\|^2 + (N_2'^{(1)})^2}, N_3'^{(1)}) & \text{if} \quad \gamma_2 = 1, \\ (N_1'^{(1)}, N_2'^{(1)}, \pm\sqrt{1 - \|N'^{(1)}\|^2 + (N_3'^{(1)})^2}) & \text{if} \quad \gamma_3 = 1, \end{cases} \tag{B.12}$$

and the distribution is then uniquely determined by a Dirac delta or a combination of Dirac deltas of the form

$$I_{P_i} = I'^{(0)} \left[\rho_i^+ \delta(\Omega_i - x_i^+) + \rho_i^- \delta(\Omega_i - x_i^-)\right] \delta(\Omega_j - N_j'^{(1)}) \delta(\Omega_k - N_k'^{(1)}), \tag{B.13}$$

where $(i, j, k) \in (1, 2, 3)$ with $i \neq j \neq k$ and ρ_i^+, ρ_i^-, x_i^+ and x_i^- are some parameters which must be determined from the realizablity constraints for moments up to first-order (since the second-order moments depend on the lower-order moments in this case), and read as follows

$$x_i^{\pm} = \pm\sqrt{1 - \|N'^{(1)}\|^2 + (N_i'^{(1)})^2}, \quad \text{and} \quad \rho_i^{\pm} = \frac{N_i'^{(1)} - x_i^{\mp}}{2x_i^{\pm}}. \tag{B.14}$$

B.3 Sufficiency of Realizability Conditions for Moments up to Second-Order

Let us consider a point P lying within the triangle ($\mathrm{P_1P_2P_3}$) (see Fig. 3.7) with corresponding set of moments ($I'^{(0)}, I'^{(1)}.I'^{(2)}$), an reconstruct the distribution at at the vertices of the triangle, given in Eq. (B.13), such that they exactly reproduce the zeroth and first-order moments, $I'^{(0)}$ and $I'^{(1)}$, respectively. We may then write the distribution at the point P as a convex combination of the distributions at the vertices of the triangle using the barycentric coordinates, γ_i, of the latter, as

$$I_P = \sum_{i=1}^{3} \gamma_i I_{P_i}, \tag{B.15}$$

From the above defined form of the distribution, it is clear, using Eq. (B.1), that I_P reproduces $I'^{(0)}$ and $I'^{(1)}$, since I_{P_i}, $i = 1, \ldots, 3$ reproduce such moments. For the

second-order moment, $I'^{(2)}$, we have

$$\int_{4\pi} \vec{s}^{\,2} I_P \mathrm{d}\Omega = \sum_{i=1}^{3} \gamma_i \int_{4\pi} \vec{s}^{\,2} I_{P_i} \mathrm{d}\Omega.$$

Computing the second-order moments at the vertices yield

$$\int_{4\pi} \Omega_m \Omega_n I_{P_i} \mathrm{d}\Omega = I'^{(0)} \int_{4\pi} \Omega_m \Omega_n \left[\rho_i^+ \delta(\Omega_i - x_i^+) + \rho_i^- \delta(\Omega_i - x_i^-)\right] \delta(\Omega_j - N_j'^{(1)}) \delta(\Omega_k - N_k'^{(1)}) d\Omega$$

$$\int_{4\pi} \Omega_m \Omega_n I_{P_i} \mathrm{d}\Omega = I'^{(0)} \begin{cases} \rho_i^+ \left(x_i^+\right)^2 + \rho_i^- \left(x_i^-\right)^2 & \text{if} \quad m = n = i, \\ \left(N_m'^{(1)}\right)^2 & \text{if} \quad m = n \neq i, \\ N_m'^{(1)} N_n'^{(1)} & \text{if} \quad m \neq n, \end{cases}$$

For simplicity, we set $I'^{(0)} = 1$ in the remainder of the derivation. We will now distinguish two cases:

- Case 1: $m \neq n$

$$\int_{4\pi} \Omega_m \Omega_n I_P \mathrm{d}\Omega = \sum_{i=1}^{3} \gamma_i N_m'^{(1)} N_n'^{(1)},$$

$$\int_{4\pi} \Omega_m \Omega_n I_P \mathrm{d}\Omega = N_m'^{(1)} N_n'^{(1)} \sum_{i=1}^{3} \gamma_i.$$

  Using Eq. (B.1), we then obtain

$$\int_{4\pi} \Omega_m \Omega_n I_P d\Omega = N_m'^{(1)} N_n'^{(1)}. \tag{B.16}$$

- Case 2: $m = n = i$

$$\int_{4\pi} (\Omega_m)^2 I_P r m d\Omega = \gamma_i \left[\rho_m^+ \left(x_m^+\right)^2 + \rho_m^- \left(x_m^-\right)^2\right] + \gamma_j \left(N_m'^{(1)}\right)^2 + \gamma_k \left(N_m'^{(1)}\right)^2,$$

$$\int_{4\pi} (\Omega_m)^2 I_P \mathrm{d}\Omega = \gamma_i \left[(\rho_m^+ + \rho_m^-) \left(x_m^+\right)^2\right] + \gamma_j \left(N_m'^{(1)}\right)^2 + \gamma_k \left(N_m'^{(1)}\right)^2.$$

  From Eq. (B.14), it is clear that $\rho_m^+ + \rho_m^- = 1$, and therefore Using Eq. (B.1), we then obtain

$$\int_{4\pi} (\Omega_m)^2 I_P \mathrm{d}\Omega = \gamma_i \left(x_m^+\right)^2 + \gamma_j \left(N_m'^{(1)}\right)^2 + \gamma_k \left(N_m'^{(1)}\right)^2,$$

$$\int_{4\pi} (\Omega_m)^2 I_P \mathrm{d}\Omega = \gamma_i \left(1 - \|N'^{(1)}\|^2 + (N_m'^{(1)})^2\right) + \gamma_j \left(N_m'^{(1)}\right)^2 + \gamma_k \left(N_m'^{(1)}\right)^2,$$

$$\int_{4\pi} (\Omega_m)^2 I_P \mathrm{d}\Omega = (\gamma_i + \gamma_j + \gamma_k) \left(N_m'^{(1)}\right)^2 + \gamma_i \left(1 - \|N'^{(1)}\|^2\right).$$

Again using Eq. (B.1), we then obtain

$$\int_{4\pi} (\Omega_m)^2 \, I_P \mathrm{d}\Omega = \left(N_m'^{(1)}\right)^2 + \gamma_i \left(1 - \|N'^{(1)}\|^2\right) \tag{B.17}$$

From the results given in Eq. (B.16) and (B.17), it is clear that I_P (with $\mathrm{P} \in \mathcal{R}_T^2$), given in Eq. (B.15) also reproduces $I'^{(2)}$.

Appendix C

Undetermined Forms of the Polynomial Expressions for the Interpolative-Based Gray and Non-Gray M_2 Closures

The weighting functions, $g_{N'^{(3)}_{111}}$, $g_{N'^{(3)}_{122}}$, and $g_{N'^{(3)}_{123}}$, defined, in the present study, as polynomial expressions of the form given in Eq. (3.51) for gray radiative transfer and Eq. (3.53) for non-gray radiation, can be directly computed from Eqs. (3.44) and (3.47), for $g_{N'^{(3)}_{111}}$, Eqs. (3.45) and (3.48), for $g_{N'^{(3)}_{122}}$, and Eqs. (3.46) and (3.49), for $g_{N'^{(3)}_{123}}$, for sets of angular moments up to second order away from both the isotropic and anisotropic limits, as well as away from the edges of the triangle (P_1, P_2, P_3), as follows

$$g_{N'^{(3)}_{111}} = \frac{f_{N'^{(3)}_{111}} - \gamma_1}{\gamma_1(1-\gamma_1)}, \quad f_{N'^{(3)}_{111}} = \frac{N'^{(3)}_{111} - (N'^{(1)}_1)^3}{N'^{(1)}_1(1 - \|N'^{(1)}\|^2)}, \tag{C.1}$$

$$g_{N'^{(3)}_{122}} = \frac{f_{N'^{(3)}_{122}} - \gamma_2}{\gamma_2(1-\gamma_2)}, \quad f_{N'^{(3)}_{122}} = \frac{N'^{(3)}_{122} - N'^{(1)}_1(N'^{(1)}_2)^2}{N'^{(1)}_1(1 - \|N'^{(1)}\|^2)}, \tag{C.2}$$

$$g_{N'^{(3)}_{123}} = \frac{f_{N'^{(3)}_{123}} - 1}{\gamma_1\gamma_2\gamma_3}, \quad f_{N'^{(3)}_{123}} = \frac{N'^{(3)}_{123}}{N'^{(1)}_1 N'^{(1)}_2 N'^{(1)}_3}. \tag{C.3}$$

In situations where the regime of radiation falls within one of the aforementioned limits, the expressions given in the above equations, i.e., Eqs. (C.1), (C.2), and (C.3), cannot be used directly to compute the weighting functions, $g_{N'^{(3)}_{111}}$, $g_{N'^{(3)}_{122}}$, and $g_{N'^{(3)}_{123}}$, and some

mathematical manipulations must be carried out in order to obtain computable expressions. The latter are obtained by suitably applying l'Hopital's rule, thereby resulting in expressions in terms of derivatives of the third-order closing fluxes with respect to the lower-order angular moments, and the procedure to compute these derivatives is presented in D. As a first step in the derivation of the expressions for computing the weighting functions, $g_{N'^{(3)}_{111}}$, $g_{N'^{(3)}_{122}}$, and $g_{N'^{(3)}_{123}}$, we advocate the following conversion from Cartesian to spherical coordinates

$$N'^{(1)}_1 = \cos\theta\|N'^{(1)}\|, \quad N'^{(1)}_2 = \sin\theta\cos\phi\|N'^{(1)}\|, \quad N'^{(1)}_3 = \sin\theta\sin\phi\|N'^{(1)}\|, \tag{C.4}$$

where θ and ϕ represent the polar and azimuthal angles describing the direction of the vector of first-order angular moments (see Eq. (3.50)).

C.1 Computations for $g_{N^{(3)}_{111}}$

In the case of the weighting function, $g_{N'^{(3)}_{111}}$, undetermined expressions are encountered for either $\mu = \cos\theta = 0$, $\|N'^{(1)}\| = 0$, $\|N'^{(1)}\| = 1$, $\gamma_1 = 0$, $\gamma_1 = 1$, or a combination of the latter regimes. In such situations, l'Hopital's rule can be used to derive expressions from which the weighting function can be directly computed.

For $\|N'^{(1)}\| = 0$, the expression for $f_{N'^{(3)}_{111}}$, given in Eq. (C.1), is undetermined, in which case $f_{N'^{(3)}_{111}}$ can be computed as follows

$$f_{N'^{(3)}_{111}} = \lim_{\|N'^{(1)}\|\to 0} \frac{N'^{(3)}_{111} - (\mu\|N'^{(1)}\|)^3}{\mu\|N'^{(1)}\|(1 - \|N'^{(1)}\|^2)},$$

which can be rewritten in the form

$$f_{N'^{(3)}_{111}} = \frac{1}{\mu} \lim_{\|N'^{(1)}\|\to 0} \frac{N'^{(3)}_{111}}{\|N'^{(1)}\|}.$$

Applying l'Hopital's rule then yields the following

$$f_{N'^{(3)}_{111}} = \frac{1}{\mu} \left(\frac{\partial N'^{(3)}_{111}}{\partial\|N'^{(1)}\|} \right) \Bigg|_{\|N'^{(1)}\|=0}.$$

Since the third-order closing flux, $N'^{(3)}_{111}$, is an even function of both $N'^{(1)}_2$ and $N'^{(1)}_3$, it therefore follows that

$$\frac{\partial N'^{(3)}_{111}}{\partial N'^{(1)}_2} = \frac{\partial N'^{(3)}_{111}}{\partial N'^{(1)}_3} = 0,$$

which allows us to further rewrite $f_{N_{111}'^{(3)}}$ in the following form

$$f_{N_{111}'^{(3)}} = \left(\frac{\partial N_{111}'^{(3)}}{\partial N_1'^{(1)}}\right)\Bigg|_{\|N'^{(1)}\|=0}. \tag{C.5}$$

The case $\|N'^{(1)}\| = 1$ also yields an undetermined form for $f_{N_{111}'^{(3)}}$, which can then be computed as follows

$$f_{N_{111}'^{(3)}} = \lim_{\|N'^{(1)}\|\to 1} \frac{N_{111}'^{(3)} - (\mu\|N'^{(1)}\|)^3}{\mu\|N'^{(1)}\|(1-\|N'^{(1)}\|^2)}.$$

Further manipulations of the latter expression yield

$$f_{N_{111}'^{(3)}} = \frac{1}{\mu}\lim_{\|N'^{(1)}\|\to 1} \frac{N_{111}'^{(3)} - (\mu\|N'^{(1)}\|)^3}{(1-\|N'^{(1)}\|^2)},$$

The limit in the last equation can be evaluated using again l'Hopital's rule, thereby yielding the following expression

$$f_{N_{111}'^{(3)}} = -\frac{1}{2\mu}\left[\frac{1}{\|N'^{(1)}\|}\frac{\partial N_{111}'^{(3)}}{\partial\|N'^{(1)}\|} - 3\mu^3\|N'^{(1)}\|^2\right]\Bigg|_{\|N'^{(1)}\|=1},$$

The last equation can be further simplified as follows

$$f_{N_{111}'^{(3)}} = \frac{3}{2}\mu^2 - \frac{1}{2\mu}\left(\frac{\partial N_{111}'^{(3)}}{\partial\|N'^{(1)}\|}\right)\Bigg|_{\|N'^{(1)}\|=1}. \tag{C.6}$$

For $\mu = 0$, $f_{N_{111}'^{(3)}}$ cannot be computed directly from Eq. (C.1), but can be formulated as follows

$$f_{N_{111}'^{(3)}} = \lim_{\mu\to 0} \frac{N_{111}'^{(3)} - (\mu\|N'^{(1)}\|)^3}{\mu\|N'^{(1)}\|(1-\|N'^{(1)}\|^2)},$$

Rearranging the terms in the latter expression allows us to write

$$f_{N_{111}'^{(3)}} = \frac{1}{\|N'^{(1)}\|(1-\|N'^{(1)}\|^2)}\lim_{\mu\to 0}\frac{N_{111}'^{(3)} - (\mu\|N'^{(1)}\|)^3}{\mu},$$

Applying again l'Hopital's rule to limit in the latter equation yields

$$f_{N_{111}'^{(3)}} = \frac{1}{\|N'^{(1)}\|(1-\|N'^{(1)}\|^2)}\left(\frac{\partial N_{111}'^{(3)}}{\partial\mu}\right)\Bigg|_{\mu=0}. \tag{C.7}$$

In situations where the last two cases occur simultaneously, i.e., for $\mu = 0$ and $\|N'^{(1)}\| = 1$, the expressions given in Eqs. (C.6) and (C.7), cannot be used to compute $f_{N_{111}'^{(3)}}$, as they

yield undetermined expressions. This problem can be circumvented by using the fact that, in such a case, $f_{N'^{(3)}_{111}}$ can be written in the following form

$$f_{N'^{(3)}_{111}} = \lim_{\|N'^{(1)}\|\to 1} \frac{1}{\|N'^{(1)}\|(1-\|N'^{(1)}\|^2)} \left(\frac{\partial N'^{(3)}_{111}}{\partial \mu}\right)\Bigg|_{\mu=0}.$$

Applying l'Hopital's rule then allows us to write

$$f_{N'^{(3)}_{111}} = -\frac{1}{2}\left(\frac{\partial^2 N'^{(3)}_{111}}{\partial \|N'^{(1)}\| \partial \mu}\right)\Bigg|_{\substack{\mu=0 \\ \|N'^{(1)}\|\to 1}}. \tag{C.8}$$

The expression for $g_{N'^{(3)}_{111}}$, given in Eq. (C.1), also yield undetermined forms on some of the boundaries of the realizable space for angular moments up to second-order, or, in other words, on some of the edges and or vertices of the triangle (P_1 P_2 P_3). In particular, for $\gamma_1 = 0$, $g_{N'^{(3)}_{111}}$ is computed as follows

$$g_{N^{(3)}_{111}} = \lim_{\gamma_1\to 0} \frac{f_{N^{(3)}_{111}} - \gamma_1}{\gamma_1(1-\gamma_1)},$$

$$g_{N^{(3)}_{111}} = \lim_{\gamma_1\to 0} \frac{1}{(1-\gamma_1)} \lim_{\gamma_1\to 0} \frac{f_{N^{(3)}_{111}} - \gamma_1}{\gamma_1},$$

$$g_{N^{(3)}_{111}} = \frac{\partial f_{N^{(3)}_{111}}}{\partial \gamma_1}\bigg|_{\gamma_1=0} - 1, \tag{C.9}$$

On the other hand, for $\gamma_1 = 1$, $g_{N'^{(3)}_{111}}$ is computed as follows

$$g_{N^{(3)}_{111}} = \lim_{\gamma_1\to 1} \frac{f_{N^{(3)}_{111}} - \gamma_1}{\gamma_1(1-\gamma_1)},$$

$$g_{N^{(3)}_{111}} = \lim_{\gamma_1\to 1} \frac{1}{\gamma_1} \lim_{\gamma_1\to 1} \frac{f_{N^{(3)}_{111}} - \gamma_1}{(1-\gamma_1)},$$

$$g_{N^{(3)}_{111}} = 1 - \frac{\partial f_{N^{(3)}_{111}}}{\partial \gamma_1}\bigg|_{\gamma_1=1}, \tag{C.10}$$

The expressions derived above can be summarized as follows

$$f_{N'^{(3)}_{111}} = \begin{cases} \left(\frac{\partial N'^{(3)}_{111}}{\partial N'^{(1)}_1}\right), & \text{if} \quad \|N'^{(1)}\| = 0, \\ \frac{3}{2}\mu^2 - \frac{1}{2\mu}\left(\frac{\partial N'^{(3)}_{111}}{\partial \|N'^{(1)}\|}\right), & \text{if} \quad \|N'^{(1)}\| = 1, \\ \frac{1}{\|N'^{(1)}\|(1-\|N'^{(1)}\|^2)}\left(\frac{\partial N'^{(3)}_{111}}{\partial \mu}\right), & \text{if} \quad \mu = 0, \\ -\frac{1}{2}\left(\frac{\partial^2 N'^{(3)}_{111}}{\partial \|N'^{(1)}\| \partial \mu}\right), & \text{if} \quad N'^{(1)}_1 = 0 \quad \text{and} \quad \|N'^{(1)}\| = 1, \end{cases} \tag{C.11}$$

and

$$g_{N'^{(3)}_{111}} = \begin{cases} \frac{\partial f_{N'^{(3)}_{111}}}{\partial \gamma_1} - 1, & \text{if} \quad \gamma_1 = 0, \\ 1 - \frac{\partial f_{N'^{(3)}_{111}}}{\partial \gamma_1}, & \text{if} \quad \gamma_1 = 1. \end{cases} \tag{C.12}$$

C.2 Computations for $g_{N^{(3)}_{122}}$

For the weighting function, $g_{N'^{(3)}_{122}}$, undetermined expressions are encountered for either $N'^{(1)}_1 = 0$, $\|N'^{(1)}\| = 1$, $\gamma_1 = 0$, $\gamma_2 = 0$, or a combination of the latter regimes. Once again, l'Hopital's rule can be used to derive the following expressions from which the weighting function can be directly computed in such situations

$$f_{N'^{(3)}_{122}} = \begin{cases} \left(\frac{\partial N'^{(3)}_{122}}{\partial N'^{(1)}_1}\right), & \text{if} \quad \|N'^{(1)}\| = 0, \\ \frac{3}{2}\left(N^{(1)}_2\right)^2 - \frac{1}{2\mu}\left(\frac{\partial N'^{(3)}_{122}}{\partial \|N'^{(1)}\|}\right), & \text{if} \quad \|N'^{(1)}\| = 1, \\ \frac{1}{(1-\|N'^{(1)}\|^2)}\left[\frac{1}{\|N'^{(1)}\|}\left(\frac{\partial N'^{(3)}_{122}}{\partial \mu}\right) - \left(N'^{(1)}_2\right)^2\right], & \text{if} \quad \mu = 0, \\ \frac{3}{2}\left(N'^{(1)}_2\right)^2 - \frac{1}{2}\left(\frac{\partial^2 N'^{(3)}_{122}}{\partial \|N'^{(1)}\| \partial \mu}\right), & \text{if} \quad \mu = 0 \quad \text{and} \quad \|N'^{(1)}\| = 1, \end{cases} \tag{C.13}$$

and

$$g_{N'^{(3)}_{122}} = \begin{cases} \frac{\partial f_{N'^{(3)}_{122}}}{\partial \gamma_2} - 1, & \text{if} \quad \gamma_2 = 0, \\ 1 - \frac{\partial f_{N'^{(3)}_{122}}}{\partial \gamma_2}, & \text{if} \quad \gamma_2 = 1. \end{cases} \tag{C.14}$$

C.3 Computations for $g_{N^{(3)}_{123}}$

In order to compute the weighting function, $g_{N'^{(3)}_{123}}$, for either $N'^{(1)}_1 = 0$, $N'^{(1)}_2 = 0$, $N'^{(1)}_3 = 0$, $\gamma_1 = 0$, $\gamma_2 = 0$, $\gamma_3 = 0$, or a combination of the latter regimes, where undetermined expressions are encountered, the following expressions, which are derived

by means of l'Hopital's rule, are employed

$$f_{N'^{(3)}_{123}} = \begin{cases} \frac{1}{N'^{(1)}_2 N'^{(1)}_3}\left(\frac{\partial N'^{(3)}_{123}}{\partial N'^{(1)}_1}\right), & \text{if} \quad N'^{(1)}_1 = 0, \\ \frac{1}{N'^{(1)}_1 N'^{(1)}_3}\left(\frac{\partial N'^{(3)}_{123}}{\partial N'^{(1)}_2}\right), & \text{if} \quad N'^{(1)}_2 = 0, \\ \frac{1}{N'^{(1)}_1 N'^{(1)}_2}\left(\frac{\partial N'^{(3)}_{123}}{\partial N'^{(1)}_3}\right), & \text{if} \quad N'^{(1)}_3 = 0, \\ \frac{1}{N'^{(1)}_3}\left(\frac{\partial^2 N'^{(3)}_{123}}{\partial N'^{(1)}_1 \partial N'^{(1)}_2}\right), & \text{if} \quad N'^{(1)}_1 = N'^{(1)}_2 = 0, \\ \frac{1}{N'^{(1)}_2}\left(\frac{\partial^2 N'^{(3)}_{123}}{\partial N'^{(1)}_1 \partial N'^{(1)}_3}\right), & \text{if} \quad N'^{(1)}_1 = N'^{(1)}_3 = 0, \\ \frac{1}{N'^{(1)}_1}\left(\frac{\partial^2 N'^{(3)}_{123}}{\partial N'^{(1)}_2 \partial N'^{(1)}_3}\right), & \text{if} \quad N'^{(1)}_2 = N'^{(1)}_3 = 0, \\ \left(\frac{\partial^3 N'^{(3)}_{123}}{\partial N'^{(1)}_1 \partial N'^{(1)}_2 \partial N'^{(1)}_3}\right), & \text{if} \quad N'^{(1)}_1 = N'^{(1)}_2 = N'^{(1)}_3 = 0, \end{cases} \tag{C.15}$$

and

$$g_{N'^{(3)}_{123}} = \begin{cases} \frac{1}{\gamma_2\gamma_3}\left(\frac{\partial f_{N'^{(3)}_{123}}}{\partial \gamma_1}\right), & \text{if} \quad \gamma_1 = 0, \\ \frac{1}{\gamma_1\gamma_3}\left(\frac{\partial f_{N'^{(3)}_{123}}}{\partial \gamma_2}\right), & \text{if} \quad \gamma_2 = 0, \\ \frac{1}{\gamma_1\gamma_2}\left(\frac{\partial f_{N'^{(3)}_{123}}}{\partial \gamma_3}\right), & \text{if} \quad \gamma_3 = 0, \\ \frac{1}{\gamma_3}\left(\frac{\partial^2 f_{N'^{(3)}_{123}}}{\partial \gamma_1 \partial \gamma_2}\right), & \text{if} \quad \gamma_1 = \gamma_2 = 0, \\ \frac{1}{\gamma_2}\left(\frac{\partial^2 f_{N'^{(3)}_{123}}}{\partial \gamma_1 \partial \gamma_3}\right), & \text{if} \quad \gamma_1 = \gamma_3 = 0, \\ \frac{1}{\gamma_1}\left(\frac{\partial^2 f_{N'^{(3)}_{123}}}{\partial \gamma_2 \partial \gamma_3}\right), & \text{if} \quad \gamma_2 = \gamma_3 = 0. \end{cases} \tag{C.16}$$

Appendix D

Procedure for Computing Derivatives of the Angular Moments

In our proposed interpolations for the non-gray first-order maximum-entropy, M_1, closure, as well as for the closing relations for both the gray and non-gray second-order maximum-entropy, M_2, moment closures, direct computations of the weighting functions, g_{χ_2} for the M_1 closure (see Eq. (A.1)), and $g_{N^{(3)}_{111}}$, $g_{N^{(3)}_{122}}$, and $g_{N^{(3)}_{123}}$, for the M_2 closure (see Eqs. (C.1), (C.2), and (C.3)), from the numerical solutions of the optimization problem for entropy maximization yield undetermined expressions in the isotropic limit as well as on the boundaries of the realizable domain, denoted by $\partial\mathcal{R}^{(1)}$ for the M_1 closure and $\partial\mathcal{R}^{(2)}$ for the M_2 closure. Applying l'Hopital's rule is such cases results in expressions involving derivatives of the highest-order moments in terms of the lower-order moments. In this section, the procedure adopted in the present study for computing such derivatives is presented.

Let us start by denoting by N the order of the highest angular moment in the unclosed system of moment equations, i.e., $N = 2$ for the M_1 closure and $N = 3$ for the M_2 closure. We also define the vector, E, containing all independent entries for the lower-

order angular moments as follows

$$\begin{aligned}
E &= \{I^{(0)}, \quad I^{(1)}\}, \quad \text{for the } \mathrm{M}_1 \text{ closure in 1D,} \\
E &= \{I^{(0)}, \quad I_1^{(1)}, \quad I_2^{(1)}, \quad I_3^{(1)}\}, \quad \text{for the } \mathrm{M}_1 \text{ closure in 3D,} \\
E &= \{I^{(0)}, \quad I_1^{(1)}, \quad I_2^{(1)}, \quad I_3^{(1)}, \quad I_{11}^{(2)}, \quad I_{12}^{(2)}, \quad I_{12}^{(2)}, \quad I_{22}^{(2)}, \quad I_{23}^{(2)}\}, \quad \text{for the } \mathrm{M}_2 \text{ closure.}
\end{aligned} \tag{D.1}$$

First-derivatives of the highest-order angular moments with respect to the lower-order angular moments can be expanded, using the chain rule of derivatives, as follows

$$\frac{\partial I^{(N)}}{\partial E_i} = \frac{\partial I^{(N)}}{\partial \alpha_p} \frac{\partial \alpha_p}{\partial E_i}, \tag{D.2}$$

where α_p are the Lagrange multipliers associated with the moment constraints.

Expressions for the second-derivatives of the closing fluxes with respect to the lower-order angular moments can be derived from the latter equation, Eq. (D.2), by taking its first-derivative and consequently applying the chain rule of derivatives, yielding

$$\frac{\partial^2 I^{(N)}}{\partial E_j \partial E_i} = \frac{\partial}{\partial E_j} \left(\frac{\partial I^{(N)}}{\partial \alpha_p} \frac{\partial \alpha_p}{\partial E_i} \right),$$

Applying the product rule to the derivatives in the latter equation results in the following expression

$$\frac{\partial^2 I^{(N)}}{\partial E_j \partial E_i} = \underbrace{\frac{\partial}{\partial E_j} \left(\frac{\partial I^{(N)}}{\partial \alpha_p} \right)}_{termA} \frac{\partial \alpha_p}{\partial E_i} + \frac{\partial I^{(N)}}{\partial \alpha_p} \underbrace{\frac{\partial}{\partial E_j} \left(\frac{\partial \alpha_p}{\partial E_i} \right)}_{termB}. \tag{D.3}$$

$termB$ in the latter equation can be rewritten as

$$termB = \frac{\partial^2 \alpha_p}{\partial E_j \partial E_i}. \tag{D.4}$$

To further simplify $termA$, we may again use the chain rule of derivatives as follows

$$termA = \frac{\partial}{\partial \alpha_q} \left(\frac{\partial I^{(N)}}{\partial \alpha_p} \right) \frac{\partial \alpha_q}{\partial E_j} = \left(\frac{\partial^2 I^{(N)}}{\partial \alpha_q \partial \alpha_p} \right) \frac{\partial \alpha_q}{\partial E_j}, \tag{D.5}$$

Plugging the resulting expressions for $termA$ and $termB$ in Eq. (D.3) then yields

$$\frac{\partial^2 I^{(N)}}{\partial E_j \partial E_i} = \frac{\partial \alpha_p}{\partial E_i} \frac{\partial \alpha_q}{\partial E_j} \left(\frac{\partial^2 I^{(N)}}{\partial \alpha_q \partial \alpha_p} \right) + \left(\frac{\partial^2 \alpha_p}{\partial E_j \partial E_i} \right) \frac{\partial I^{(N)}}{\partial \alpha_p}. \tag{D.6}$$

A similar procedure to that used to derive second-derivatives of the closing fluxes, $I^{(N)}$, with respect to the lower-order angular moments can also be adopted to obtain third-order derivatives of the latter. More specifically, we again take the first-derivative of the expression given in Eq. (D.6) as follows

$$\frac{\partial^3 I^{(N)}}{\partial E_k \partial E_j \partial E_i} = \frac{\partial}{\partial E_k}\left[\frac{\partial \alpha_p}{\partial E_i}\frac{\partial \alpha_q}{\partial E_j}\left(\frac{\partial^2 I^{(N)}}{\partial \alpha_q \partial \alpha_p}\right) + \left(\frac{\partial^2 \alpha_p}{\partial E_j \partial E_i}\right)\frac{\partial I^{(N)}}{\partial \alpha_p}\right].$$

Expanding the latter expression and apply the product rule for derivatives yields

$$\begin{aligned}\frac{\partial^3 I^{(N)}}{\partial E_k \partial E_j \partial E_i} = &\left(\frac{\partial^2 \alpha_p}{\partial E_k \partial E_i}\frac{\partial \alpha_q}{\partial E_j} + \frac{\partial \alpha_p}{\partial E_i}\frac{\partial^2 \alpha_q}{\partial E_k \partial E_j}\right)\frac{\partial^2 I^{(N)}}{\partial \alpha_q \partial \alpha_p} \\ &+\frac{\partial \alpha_p}{\partial E_i}\frac{\partial \alpha_q}{\partial E_j}\underbrace{\frac{\partial}{\partial E_k}\left(\frac{\partial^2 I^{(N)}}{\partial \alpha_q \partial \alpha_p}\right)}_{termC} + \frac{\partial^3 \alpha_p}{\partial E_k \partial E_j \partial E_i}\frac{\partial I^{(N)}}{\partial \alpha_p} \\ &+\frac{\partial^2 \alpha_p}{\partial E_j \partial E_i}\underbrace{\frac{\partial}{\partial E_k}\left(\frac{\partial I^{(N)}}{\partial \alpha_p}\right)}_{termD}.\end{aligned} \tag{D.7}$$

$termC$ can be further simplified using the chain rule for derivatives as follows

$$termC = \frac{\partial}{\partial \alpha_r}\left(\frac{\partial^2 I^{(N)}}{\partial \alpha_q \partial \alpha_p}\right)\frac{\partial \alpha_r}{\partial E_k} = \frac{\partial \alpha_r}{\partial E_k}\frac{\partial^3 I^{(N)}}{\partial \alpha_r \partial \alpha_q \partial \alpha_p}. \tag{D.8}$$

Similarly, for $termD$, application of the chain rule of derivatives allows us to rewrite the latter as follows

$$termD = \frac{\partial}{\partial \alpha_q}\left(\frac{\partial I^{(N)}}{\partial \alpha_p}\right)\frac{\partial \alpha_q}{\partial E_k} = \frac{\partial \alpha_q}{\partial E_k}\frac{\partial^2 I^{(N)}}{\partial \alpha_q \partial \alpha_p}. \tag{D.9}$$

Now, plugging the resulting expressions for $termC$ and $termD$ in Eq. (D.7) result in the following expression for the third-derivatives of the closing fluxes with respect to the lower-order angular moments

$$\begin{aligned}\frac{\partial^3 I^{(N)}}{\partial E_k \partial E_j \partial E_i} = &\frac{\partial \alpha_p}{\partial E_i}\frac{\partial \alpha_q}{\partial E_j}\frac{\partial \alpha_r}{\partial E_k}\frac{\partial^3 I^{(N)}}{\partial \alpha_r \partial \alpha_q \partial \alpha_p} + \frac{\partial^3 \alpha_p}{\partial E_k \partial E_j \partial E_i}\frac{\partial I^{(N)}}{\partial \alpha_p} \\ &+\left(\frac{\partial^2 \alpha_p}{\partial E_k \partial E_i}\frac{\partial \alpha_q}{\partial E_j} + \frac{\partial \alpha_p}{\partial E_i}\frac{\partial^2 \alpha_q}{\partial E_k \partial E_j} + \frac{\partial^2 \alpha_p}{\partial E_j \partial E_i}\frac{\partial \alpha_q}{\partial E_k}\right)\frac{\partial^2 I^{(N)}}{\partial \alpha_q \partial \alpha_p}.\end{aligned} \tag{D.10}$$

The expressions given in Eqs. (D.2), (D.6), and (D.10), provide means to compute the first-, second-, and third-derivatives of the closing fluxes (highest-order angular moments in the unclosed system of moment equations) in terms of the lower-order angular moments. However, while the derivatives up to third-order of the lower-order angular

moments with respect to the Lagrange multipliers, involved in such expression, can be computed directly from the known set of Lagrange multipliers, the calculations of the derivatives up to third-order of the Lagrange multipliers with respect to the lower-order angular moments, which are also required for our computations, is not as straightforward and somewhat requires extra mathematical derivations, which are shown below.

To obtain expressions for the first-derivatives of the Lagrange multipliers with respect to the lower-order moments, $\partial\alpha_i/\partial E_{(j)}$, we exploit the fact that the lower-order angular moments are independent from one another, thereby yielding the following relationships for the first-derivatives of the latter

$$\frac{\partial E_i}{\partial E_j} = \frac{\partial E_i}{\partial \alpha_p}\frac{\partial \alpha_p}{\partial E_j} = \delta_{ij}, \tag{D.11}$$

where the chain rule for derivatives has been employed, and the vector of independent lower-order angular moments, E, is given in Eq. (D.1). The latter relationship can be rewritten in tensor form as follows

$$H^{(1)}_{ip} A^{(1)}_{pj} = \delta_{ij}, \tag{D.12}$$

where $H^{(1)}$ is the Hessian matrix of first-derivatives, which reads as follows

$$H^{(1)}_{ij} = \frac{\partial E_i}{\partial \alpha_j}, \tag{D.13}$$

and $A^{(1)}$ is the matrix of first-derivatives of the Lagrange multipliers with respect to the lower-order moments, of the form

$$A^{(1)}_{ij} = \frac{\partial \alpha_i}{\partial E_j}, \tag{D.14}$$

and its entries can be readily computed via inversion of the system of equations given in Eq. (D.12), since the entries of $H^{(1)}$ can be calculated directly, via integration of the second-derivatives of the objective function of the associated dual optimization problem, once the Lagrange multipliers are known.

To obtain expressions for the second-derivatives of the Lagrange multipliers with respect to lower-order angular moments, we can directly take the first-derivative of Eq. (D.11) as follows

$$\frac{\partial^2 E_i}{\partial E_k \partial E_j} = \underbrace{\frac{\partial}{\partial E_k}\left(\frac{\partial E_i}{\partial \alpha_p}\frac{\partial \alpha_p}{\partial E_j}\right)}_{termE} = 0. \tag{D.15}$$

Applying the product rule of derivatives to $termE$ in the latter expression yields

$$termE = \frac{\partial}{\partial E_k}\left(\frac{\partial E_i}{\partial \alpha_p}\right)\frac{\partial \alpha_p}{\partial E_j} + \frac{\partial E_i}{\partial \alpha_p}\frac{\partial^2 \alpha_p}{\partial E_k \partial E_j}. \tag{D.16}$$

Using the chain rule of derivatives on the first term on the right hand side of the latter expression allows to further simplify $termE$ as follows

$$termE = \frac{\partial}{\partial \alpha_q}\left(\frac{\partial E_i}{\partial \alpha_p}\right)\frac{\partial \alpha_q}{\partial E_k}\frac{\partial \alpha_p}{\partial E_j} + \frac{\partial E_i}{\partial \alpha_p}\frac{\partial^2 \alpha_p}{\partial E_k \partial E_j}, \tag{D.17}$$

or

$$termE = \frac{\partial^2 E_i}{\partial \alpha_q \partial \alpha_p}\frac{\partial \alpha_q}{\partial E_k}\frac{\partial \alpha_p}{\partial E_j} + \frac{\partial E_i}{\partial \alpha_p}\frac{\partial^2 \alpha_p}{\partial E_k \partial E_j}. \tag{D.18}$$

Plugging the resulting expressions for $termE$ in Eq. (D.15), then yields

$$\frac{\partial^2 E_i}{\partial \alpha_q \partial \alpha_p}\frac{\partial \alpha_q}{\partial E_k}\frac{\partial \alpha_p}{\partial E_j} + \frac{\partial E_i}{\partial \alpha_p}\frac{\partial^2 \alpha_p}{\partial E_k \partial E_j} = 0. \tag{D.19}$$

Rearranging the latter equations then allows us to write

$$\frac{\partial E_i}{\partial \alpha_p}\frac{\partial^2 \alpha_p}{\partial E_k \partial E_j} = -\frac{\partial^2 E_i}{\partial \alpha_q \partial \alpha_p}\frac{\partial \alpha_q}{\partial E_k}\frac{\partial \alpha_p}{\partial E_j}, \tag{D.20}$$

or, in tensor form,

$$H^{(1)}_{ip} A^{(2)}_{pjk} = -H^{(2)}_{ipq} A^{(1)}_{qk} A^{(1)}_{pj}, \tag{D.21}$$

where the matrices, $H^{(1)}$ and $A^{(1)}$, are defined in Eqs. (D.13) and (D.14), respectively, and $H^{(2)}$ and $A^{(2)}$ are third-order tensors, whose respective entries correspond the second-derivatives of the lower-order moments with respect to the Lagrange multipliers and the second-derivatives of the Lagrange multipliers with respect to the lower-order angular moments, an can be written, respectively, in tensor notation as follows

$$H^{(2)}_{ijk} = \frac{\partial^2 E_i}{\partial \alpha_k \partial \alpha_j}, \tag{D.22}$$

and

$$A^{(2)}_{ijk} = \frac{\partial^2 \alpha_i}{\partial E_k \partial E_j}. \tag{D.23}$$

In Eq. (D.21), entries of both $H^{(1)}$ and $H^{(2)}$ can be computed directly from the known set of Lagrange multipliers associated with the moment constraints, and the matrix $A^{(1)}$ can be solved for via inversion of the system of equations given in Eq. (D.12). Consequently, once the matrices $A^{(1)}$, $H^{(1)}$ and $H^{(2)}$ are determined, the system of equations given in Eq. (D.21) can be readily inverted, for $A^{(2)}$, thereby providing second-derivatives of the Lagrange multipliers with respect to the lower-order angular moments.

For the purpose of deriving expressions for the third-derivatives of the Lagrange multipliers with respect to the lower-order angular moments, one may take the first-derivative of Eq. (D.21), yielding

$$\frac{\partial}{\partial E_l}\left(\frac{\partial E_i}{\partial \alpha_p}\frac{\partial^2 \alpha_p}{\partial E_k \partial E_j}\right) = -\frac{\partial}{\partial E_l}\left(\frac{\partial^2 E_i}{\partial \alpha_q \partial \alpha_p}\frac{\partial \alpha_q}{\partial E_k}\frac{\partial \alpha_p}{\partial E_j}\right). \tag{D.24}$$

The left hand side of Eq. (D.24) can be expanded using the product rule of derivatives, yielding

$$\frac{\partial}{\partial E_l}\left(\frac{\partial E_i}{\partial \alpha_p}\frac{\partial^2 \alpha_p}{\partial E_k \partial E_j}\right) = \frac{\partial}{\partial E_l}\left(\frac{\partial E_i}{\partial \alpha_p}\right)\frac{\partial^2 \alpha_p}{\partial E_k \partial E_j} + \frac{\partial E_i}{\partial \alpha_p}\frac{\partial^3 \alpha_p}{\partial E_l \partial E_k \partial E_j}. \tag{D.25}$$

Using the chain rule of derivatives on the first term on the right hand side of the latter equation results in the following expression

$$\frac{\partial}{\partial E_l}\left(\frac{\partial E_i}{\partial \alpha_p}\frac{\partial^2 \alpha_p}{\partial E_k \partial E_j}\right) = \frac{\partial^2 E_i}{\partial \alpha_q \partial \alpha_p}\frac{\partial \alpha_q}{\partial E_l}\frac{\partial^2 \alpha_p}{\partial E_k \partial E_j} + \frac{\partial E_i}{\partial \alpha_p}\frac{\partial^3 \alpha_p}{\partial E_l \partial E_k \partial E_j}. \tag{D.26}$$

The right hand side of Eq. (D.24) can also be expanded, using the product rule of derivatives, as follows

$$-\frac{\partial}{\partial E_l}\left[\left(\frac{\partial^2 E_i}{\partial \alpha_q \partial \alpha_p}\right)\frac{\partial \alpha_q}{\partial E_k}\frac{\partial \alpha_p}{\partial E_j}\right] = -\underbrace{\frac{\partial}{\partial E_l}\left(\frac{\partial^2 E_i}{\partial \alpha_q \partial \alpha_p}\right)}_{termF}\frac{\partial \alpha_q}{\partial E_k}\frac{\partial \alpha_p}{\partial E_j} - \frac{\partial^2 E_i}{\partial \alpha_q \partial \alpha_p}\underbrace{\frac{\partial}{\partial E_l}\left(\frac{\partial \alpha_q}{\partial E_k}\frac{\partial \alpha_p}{\partial E_j}\right)}_{termG}. \tag{D.27}$$

$termF$ in the latter expression can be simplified via the chain rule of derivatives, yielding

$$termF = \frac{\partial^3 E_i}{\partial \alpha_r \partial \alpha_q \partial \alpha_p}\frac{\partial \alpha_r}{\partial E_l}. \tag{D.28}$$

In order to simplify $termG$, on the other hand, one may employ the product rule of derivatives, which yields

$$termG = \frac{\partial^2 \alpha_q}{\partial E_l \partial E_k}\frac{\partial \alpha_p}{\partial E_j} + \frac{\partial \alpha_q}{\partial E_k}\frac{\partial^2 \alpha_p}{\partial E_l \partial E_j}. \tag{D.29}$$

Now, plugging the expressions for $termF$ and $termG$, as well as the relationship given in Eq. (D.26), in Eq. (D.24), results in the following relationship

$$\begin{aligned}\frac{\partial^2 E_i}{\partial \alpha_q \partial \alpha_p}\frac{\partial \alpha_q}{\partial E_l}\frac{\partial^2 \alpha_p}{\partial E_k \partial E_j} + \frac{\partial E_i}{\partial \alpha_p}\frac{\partial^3 \alpha_p}{\partial E_l \partial E_k \partial E_j} &= -\frac{\partial^3 E_i}{\partial \alpha_r \partial \alpha_q \partial \alpha_p}\frac{\partial \alpha_r}{\partial E_l}\frac{\partial \alpha_q}{\partial E_k}\frac{\partial \alpha_p}{\partial E_j} \\ &\quad -\frac{\partial^2 E_i}{\partial \alpha_q \partial \alpha_p}\left(\frac{\partial^2 \alpha_q}{\partial E_l \partial E_k}\frac{\partial \alpha_p}{\partial E_j} + \frac{\partial \alpha_q}{\partial E_k}\frac{\partial^2 \alpha_p}{\partial E_l \partial E_j}\right).\end{aligned} \tag{D.30}$$

Rearranging the latter equation yields an expression for the third-derivatives of the Lagrange multipliers with respect to the lower-order angular moments, of the form

$$\begin{aligned}\frac{\partial E_i}{\partial \alpha_p}\frac{\partial^3 \alpha_p}{\partial E_l \partial E_k \partial E_j} &= -\frac{\partial^3 E_i}{\partial \alpha_r \partial \alpha_q \partial \alpha_p}\frac{\partial \alpha_r}{\partial E_l}\frac{\partial \alpha_q}{\partial E_k}\frac{\partial \alpha_p}{\partial E_j} \\ -\frac{\partial^2 E_i}{\partial \alpha_q \partial \alpha_p}&\left(\frac{\partial \alpha_p}{\partial E_j}\frac{\partial^2 \alpha_q}{\partial E_l \partial E_k} + \frac{\partial \alpha_q}{\partial E_k}\frac{\partial^2 \alpha_p}{\partial E_l \partial E_j} + \frac{\partial \alpha_q}{\partial E_l}\frac{\partial^2 \alpha_p}{\partial E_k \partial E_j}\right),\end{aligned} \tag{D.31}$$

or, in tensor form

$$H^{(1)}_{ip} A^{(3)}_{pjkl} = -H^{(3)}_{ipqr} A^{(1)}_{pj} A^{(1)}_{qk} A^{(1)}_{rl} - H^{(2)}_{ipq}(A^{(1)}_{pj} A^{(2)}_{qkl} + A^{(1)}_{qk} A^{(2)}_{pjl} + A^{(1)}_{ql} A^{(2)}_{pjk}), \tag{D.32}$$

where the matrices, $H^{(1)}$ and $A^{(1)}$, are defined in Eqs. (D.13) and (D.14), respectively, the third-order tensors, $H^{(2)}$ and $A^{(2)}$, respectively, are given in Eqs. (D.22) and (D.23), and the fourth-order tensors, $H^{(3)}$ and $A^{(3)}$ respectively contain third-derivatives of the lower-order moments with respect to the Lagrange multipliers and third-derivatives of the Lagrange multipliers with respect to the lower-order angular moments, an can be written respectively in tensor notation as follows

$$H^{(3)}_{ijkl} = \frac{\partial^3 E_i}{\partial \alpha_l \partial \alpha_k \partial \alpha_j}, \tag{D.33}$$

and

$$A^{(3)}_{ijkl} = \frac{\partial^3 \alpha_i}{\partial E_l \partial E_k \partial E_j}. \tag{D.34}$$

While $H^{(1)}$, $H^{(2)}$ and $H^{(3)}$ can be readily computed from the known set of Lagrange multipliers associated with the moment constraints, the second- and third-order tensors, $A^{(1)}$ and $A^{(2)}$, respectively, can be calculated from Eqs. (D.12) and (D.21). Third-derivatives of the Lagrange multipliers with respect to the lower-order angular moments can then be readily obtained via inversion of the system of equations, given in Eq. (D.32).

Appendix E

Generalized Roe Matrices for the M_1 and M_2 Closures

In this appendix, new generalized Roe matrices for the systems of nonlinear equations arising from the M_1 and M_2 closures, for both gray and non-gray radiation, are proposed and derived. For notational simplicity, the wavenumber/reordered wavenumber subscript is dropped in the case of spectrally dependent quantities, though the expressions derived herein apply to both gray and non-gray radiative transport.

The procedure for developing the approximate Roe matrices starts with a suitable choice of a parameter vector, $\mathbf{W}$, for simplifying the problem of finding a generalized Roe matrix. Following the methodology originally proposed by Roe [157], the components of $\mathbf{W}$ are chosen such that the entries of the solution vector of conserved variables, $\mathbf{U}$, are merely quadratic in the components of the former vector. Following the selection of the parameter vector, $\mathbf{W}$, the Jacobian matrix associated with the x-direction flux vector can be expanded, using the chain rule of derivatives, as follows

$$\mathbf{A}(\mathbf{U}) = \mathbf{A}_{\mathbf{F}}(\mathbf{W})\mathbf{A}_{\mathbf{U}}^{-1}(\mathbf{W}), \tag{E.1}$$

where

$$\mathbf{A}_{\mathbf{U}}(\mathbf{W}) = \frac{\partial \mathbf{U}}{\partial \mathbf{W}}, \quad \mathbf{A}_{\mathbf{F}}(\mathbf{W}) = \frac{\partial \mathbf{F}}{\partial \mathbf{W}}. \tag{E.2}$$

The problem of determining the generalized Roe matrix then consists of solving the

following set of equations

$$\mathbf{A}_{\mathbf{U}}(\mathbf{W})(\mathbf{W}_R - \mathbf{W}_L) = \mathbf{U}_R - \mathbf{U}_L, \tag{E.3a}$$

$$\mathbf{A}_{\mathbf{F}}(\mathbf{W})(\mathbf{W}_R - \mathbf{W}_L) = \mathbf{F}_R - \mathbf{F}_L. \tag{E.3b}$$

In the classical Roe approach, the components of $\mathbf{W}$ are considered as the unknowns of the latter system. However, in the context of entropy-based, M_N, closures, the strong non-linearity of the resulting set of equations arising from Eq. (E.3) in the components of $\mathbf{W}$, combined with the fact that the number of equations involved in the latter system is much larger than the number of components of $\mathbf{W}$, would make the system under consideration extremely difficult or even impossible to solve via the classical Roe approach. To overcome this issue, the Multiple Averages (MAs) approach proposed by Rosatti and Begnudelli [165] is adopted herein in order to derive solutions for the systems of equations, of the form given in Eq. (E.3), arising from the M_1 and M_2 closures.

The first step of the MAs approach consists of evaluating the system of equations, Eq. (E.3), at some averaged state, $\widetilde{\mathbf{W}}$, which, in the present study, is chosen to correspond to an arithmetic average between the left and the right state, i.e.,

$$\widetilde{\mathbf{W}} = \frac{1}{2}\left(\mathbf{W}_L + \mathbf{W}_R\right). \tag{E.4}$$

It is worth mentioning that the choice of this average state, $\widetilde{\mathbf{W}}$, is not unique, as pointed out by Rosatti and Begnudelli [165].

The preceding produces a set of equalities, some of which are satisfied. For the remaining relationships that are unsatisfied, the next step consists of considering some of the terms involved as unknowns, while all the remaining terms are evaluated at the average state, $\widetilde{\mathbf{W}}$. The number of unknowns is taken to be equal to the number of unsatisfied equations so as to obtain a well-posed system. Solving for theses unknowns then yields a closed-form expression for the Roe matrix of Eq. (E.1).

E.1 Generalized Roe Matrix for the M_1 Closure

In the context of the M_1 closure, the parameter vector, $\mathbf{W}$, is chosen to be of the form

$$\mathbf{W} = [w_1, w_2, w_3]^T = \sqrt{I^{(0)}}\left[\ 1, N_1^{(1)}, N_2^{(1)}\ \right]^T. \tag{E.5}$$

With this choice of the parameter vector, $\mathbf{W}$, the matrices $\mathbf{A_U}(\mathbf{W})$ and $\mathbf{A_F}(\mathbf{W})$ (see Eq. (E.2)) can be respectively written as follows

$$\mathbf{A_U}(\mathbf{W}) = \begin{bmatrix} 2w_1 & 0 & 0 \\ w_2 & w_1 & 0 \\ w_3 & 0 & w_1 \end{bmatrix}, \tag{E.6}$$

and

$$\mathbf{A_F}(\mathbf{W}) = \begin{bmatrix} w_2 & w_1 & 0 \\ b_1 & w_1 \frac{\partial I_{11}^{(2)}}{\partial I_1^{(1)}} & w_1 \frac{\partial I_{11}^{(2)}}{\partial I_2^{(1)}} \\ c_1 & w_1 \frac{\partial I_{12}^{(2)}}{\partial I_1^{(1)}} & w_1 \frac{\partial I_{12}^{(2)}}{\partial I_2^{(1)}} \end{bmatrix}, \tag{E.7}$$

where the parameters b_1 and c_1 respectively have the following forms

$$b_1 = 2w_1 \frac{\partial I_{11}^{(2)}}{\partial I^{(0)}} + w_2 \frac{\partial I_{11}^{(2)}}{\partial I_1^{(1)}} + w_3 \frac{\partial I_{11}^{(2)}}{\partial I_2^{(1)}}, \tag{E.8}$$

$$c_1 = 2w_1 \frac{\partial I_{12}^{(2)}}{\partial I^{(0)}} + w_2 \frac{\partial I_{12}^{(2)}}{\partial I_1^{(1)}} + w_3 \frac{\partial I_{12}^{(2)}}{\partial I_2^{(1)}}. \tag{E.9}$$

Evaluating the resulting system of equations, Eq. (E.3), at the average state produces 6 equalities. It is a simple exercise to show that all the relationships appearing in Eq. (E.3a) are satisfied whereas, on the other hand, only the first equality of Eq. (E.3b) is verified, which then leaves the last two equations unsatisfied. Following the procedure highlighted above, the next step then consists of considering two of the terms appearing in the last two equations as unknowns, while all the remaining terms are evaluated at the average state, $\widetilde{\mathbf{W}}$. In the present derivation, the terms $w_2 = \sqrt{I^{(0)}} N_1^{(1)}$ and $w_3 = \sqrt{I^{(0)}} N_2^{(1)}$ are chosen as unknowns. Evaluating all the other terms in the last two equations of Eq. (E.3b) in $\widetilde{\mathbf{W}}$ then yields the following system

$$\begin{bmatrix} \widehat{b_1} & \widetilde{w_1} \widetilde{\frac{\partial I_{11}^{(2)}}{\partial I_1^{(1)}}} & \widetilde{w_1} \widetilde{\frac{\partial I_{11}^{(2)}}{\partial I_2^{(1)}}} \\ \widehat{c_1} & \widetilde{w_1} \widetilde{\frac{\partial I_{12}^{(2)}}{\partial I_1^{(1)}}} & \widetilde{w_1} \widetilde{\frac{\partial I_{12}^{(2)}}{\partial I_2^{(1)}}} \end{bmatrix} \Delta \mathbf{W} = \Delta \mathbf{F}', \tag{E.10}$$

where

$$\Delta \mathbf{W} = [\Delta w_1, \Delta w_2, \Delta w_3]^T = \mathbf{W}_R - \mathbf{W}_L, \tag{E.11}$$

and

$$\Delta \mathbf{F}' = [\Delta F_2, \Delta F_3]^T = \mathbf{F}'_R - \mathbf{F}'_L, \tag{E.12}$$

and where $\mathbf{F}'_R$ and $\mathbf{F}'_L$ are reduced flux vectors in which the first components of the associated original flux vectors are removed.

In Eq. (E.10), $\widehat{b_1}$ and $\widehat{c_1}$ are entries which contain the unknowns, $\widehat{w_2} = \widehat{\sqrt{I^{(0)}}N_1^{(1)}}$, and $\widehat{w_3} = \widehat{\sqrt{I^{(0)}}N_2^{(1)}}$, and have the following forms, respectively

$$\widehat{b_1} = 2\widetilde{w_1}\widetilde{\frac{\partial I_{11}^{(2)}}{\partial I^{(0)}}} + \widehat{w_2}\widetilde{\frac{\partial I_{11}^{(2)}}{\partial I_1^{(1)}}} + \widehat{w_3}\widetilde{\frac{\partial I_{11}^{(2)}}{\partial I_2^{(1)}}}, \tag{E.13}$$

$$\widehat{c_1} = 2\widetilde{w_1}\widetilde{\frac{\partial I_{12}^{(2)}}{\partial I^{(0)}}} + \widehat{w_2}\widetilde{\frac{\partial I_{12}^{(2)}}{\partial I_1^{(1)}}} + \widehat{w_3}\widetilde{\frac{\partial I_{12}^{(2)}}{\partial I_2^{(1)}}}, \tag{E.14}$$

where the tilde symbol over any quantity indicates that the latter is evaluated in terms of the averaged state, $\widetilde{\mathbf{W}}$, and the hat symbol over a given parameter signifies the latter is considered as unknown in the system of equations of interest. Solving Eq. (E.10) for the unknowns, $\widehat{w_2}$ and $\widehat{w_3}$, then yields the following expressions

$$\widehat{w_2} = \frac{1}{det}\left(\widetilde{f}_1\widetilde{\frac{\partial I_{12}^{(2)}}{\partial I_2^{(1)}}} - \widetilde{f}_2\widetilde{\frac{\partial I_{11}^{(2)}}{\partial I_2^{(1)}}}\right), \tag{E.15}$$

$$\widehat{w_3} = \frac{1}{det}\left(\widetilde{f}_2\widetilde{\frac{\partial I_{11}^{(2)}}{\partial I_1^{(1)}}} - \widetilde{f}_1\widetilde{\frac{\partial I_{12}^{(2)}}{\partial I_1^{(1)}}}\right), \tag{E.16}$$

where

$$det = \widetilde{\frac{\partial I_{11}^{(2)}}{\partial I_1^{(1)}}}\widetilde{\frac{\partial I_{12}^{(2)}}{\partial I_2^{(1)}}} - \widetilde{\frac{\partial I_{11}^{(2)}}{\partial I_2^{(1)}}}\widetilde{\frac{\partial I_{12}^{(2)}}{\partial I_1^{(1)}}}, \tag{E.17}$$

and where

$$\widetilde{f}_1 = \frac{1}{\Delta w_1}\left(\Delta F_2 - \widetilde{w_1}\widetilde{\frac{\partial I_{11}^{(2)}}{\partial I_1^{(1)}}}\Delta w_2 - \widetilde{w_1}\widetilde{\frac{\partial I_{11}^{(2)}}{\partial I_2^{(1)}}}\Delta w_3\right) - 2\widetilde{w_1}\widetilde{\frac{\partial I_{11}^{(2)}}{\partial I^{(0)}}}, \tag{E.18}$$

$$\widetilde{f}_2 = \frac{1}{\Delta w_1}\left(\Delta F_3 - \widetilde{w_1}\widetilde{\frac{\partial I_{12}^{(2)}}{\partial I_1^{(1)}}}\Delta w_2 - \widetilde{w_1}\widetilde{\frac{\partial I_{12}^{(2)}}{\partial I_2^{(1)}}}\Delta w_3\right) - 2\widetilde{w_1}\widetilde{\frac{\partial I_{12}^{(2)}}{\partial I^{(0)}}}. \tag{E.19}$$

E.2 Generalized Roe Matrix for the M_2 Closure

For the system of moment equations arising from the M_2 closure, the parameter vector, $\mathbf{W}$, is taken to have the following form

$$\mathbf{W} = [w_1, w_2, w_3, w_4, w_5, w_6]^T = \sqrt{I^{(0)}}\left[\ 1, N_1^{(1)}, N_2^{(1)}, N_{11}^{(2)}, N_{12}^{(2)}, N_{22}^{(2)}\ \right]^T. \tag{E.20}$$

The matrices $\mathbf{A_U}(\mathbf{W})$ and $\mathbf{A_F}(\mathbf{W})$ (see Eq. (E.2)) associated with such a choice of a parameter vector respectively take the following forms

$$\mathbf{A_U}(\mathbf{W}) = \begin{bmatrix} 2w_1 & 0 & 0 & 0 & 0 & 0 \\ w_2 & w_1 & 0 & 0 & 0 & 0 \\ w_3 & 0 & w_1 & 0 & 0 & 0 \\ w_4 & 0 & 0 & w_1 & 0 & 0 \\ w_5 & 0 & 0 & 0 & w_1 & 0 \\ w_6 & 0 & 0 & 0 & 0 & w_1 \end{bmatrix}, \tag{E.21}$$

and

$$\mathbf{A_F}(\mathbf{W}) = \begin{bmatrix} w_2 & w_1 & 0 & 0 & 0 & 0 \\ w_4 & 0 & 0 & w_1 & 0 & 0 \\ w_5 & 0 & 0 & 0 & w_1 & 0 \\ b_1 & w_1\frac{\partial I^{(3)}_{111}}{\partial I^{(1)}_1} & w_1\frac{\partial I^{(3)}_{111}}{\partial I^{(1)}_2} & w_1\frac{\partial I^{(3)}_{111}}{\partial I^{(2)}_{11}} & w_1\frac{\partial I^{(3)}_{111}}{\partial I^{(2)}_{12}} & w_1\frac{\partial I^{(3)}_{111}}{\partial I^{(2)}_{22}} \\ c_1 & w_1\frac{\partial I^{(3)}_{112}}{\partial I^{(1)}_1} & w_1\frac{\partial I^{(3)}_{112}}{\partial I^{(1)}_2} & w_1\frac{\partial I^{(3)}_{112}}{\partial I^{(2)}_{11}} & w_1\frac{\partial I^{(3)}_{112}}{\partial I^{(2)}_{12}} & w_1\frac{\partial I^{(3)}_{112}}{\partial I^{(2)}_{22}} \\ d_1 & w_1\frac{\partial I^{(3)}_{122}}{\partial I^{(1)}_1} & w_1\frac{\partial I^{(3)}_{122}}{\partial I^{(1)}_2} & w_1\frac{\partial I^{(3)}_{122}}{\partial I^{(2)}_{11}} & w_1\frac{\partial I^{(3)}_{122}}{\partial I^{(2)}_{12}} & w_1\frac{\partial I^{(3)}_{122}}{\partial I^{(2)}_{22}} \end{bmatrix}, \tag{E.22}$$

where the parameters b_1 and c_1 respectively have the following forms

$$b_1 = 2w_1\frac{\partial I^{(3)}_{111}}{\partial I^{(0)}} + w_2\frac{\partial I^{(3)}_{111}}{\partial I^{(1)}_1} + w_3\frac{\partial I^{(3)}_{111}}{\partial I^{(1)}_2} + w_4\frac{\partial I^{(3)}_{111}}{\partial I^{(2)}_{11}} + w_5\frac{\partial I^{(3)}_{111}}{\partial I^{(2)}_{12}} + w_6\frac{\partial I^{(3)}_{111}}{\partial I^{(2)}_{22}}, \tag{E.23}$$

$$c_1 = 2w_1\frac{\partial I^{(3)}_{112}}{\partial I^{(0)}} + w_2\frac{\partial I^{(3)}_{112}}{\partial I^{(1)}_1} + w_3\frac{\partial I^{(3)}_{112}}{\partial I^{(1)}_2} + w_4\frac{\partial I^{(3)}_{112}}{\partial I^{(2)}_{11}} + w_5\frac{\partial I^{(3)}_{112}}{\partial I^{(2)}_{12}} + w_6\frac{\partial I^{(3)}_{112}}{\partial I^{(2)}_{22}}, \tag{E.24}$$

$$d_1 = 2w_1\frac{\partial I^{(3)}_{122}}{\partial I^{(0)}} + w_2\frac{\partial I^{(3)}_{122}}{\partial I^{(1)}_1} + w_3\frac{\partial I^{(3)}_{122}}{\partial I^{(1)}_2} + w_4\frac{\partial I^{(3)}_{122}}{\partial I^{(2)}_{11}} + w_5\frac{\partial I^{(3)}_{122}}{\partial I^{(2)}_{12}} + w_6\frac{\partial I^{(3)}_{122}}{\partial I^{(2)}_{22}}. \tag{E.25}$$

Following the evaluation of the resulting system of equations, Eq. (E.3), at the average state, $\widetilde{\mathbf{W}}$, a set of 12 equalities are produced. Out of the resulting set equations, it can be readily shown that all the relationships appearing in Eq. (E.3a) are satisfied whereas, on the other hand, only the first three equalities of Eq. (E.3b) are verified, which then leaves the last three equations unsatisfied. In the next step, the three terms, $w_4 = \sqrt{I^{(0)}}N^{(2)}_{11}$, $w_5 = \sqrt{I^{(0)}}N^{(2)}_{12}$, and $w_6 = \sqrt{I^{(0)}}N^{(2)}_{22}$, are chosen as unknowns. Evaluating all the other terms in the last three equations of Eq. (E.3b) in the average state, $\widetilde{\mathbf{W}}$, then yields the

following system

$$\begin{bmatrix} \widehat{b_1} & \widetilde{w_1}\widetilde{\frac{\partial I^{(3)}_{111}}{\partial I^{(1)}_1}} & \widetilde{w_1}\widetilde{\frac{\partial I^{(3)}_{111}}{\partial I^{(1)}_2}} & \widetilde{w_1}\widetilde{\frac{\partial I^{(3)}_{111}}{\partial I^{(2)}_{11}}} & \widetilde{w_1}\widetilde{\frac{\partial I^{(3)}_{111}}{\partial I^{(2)}_{12}}} & \widetilde{w_1}\widetilde{\frac{\partial I^{(3)}_{111}}{\partial I^{(2)}_{22}}} \\ \widehat{c_1} & \widetilde{w_1}\widetilde{\frac{\partial I^{(3)}_{112}}{\partial I^{(1)}_1}} & \widetilde{w_1}\widetilde{\frac{\partial I^{(3)}_{112}}{\partial I^{(1)}_2}} & \widetilde{w_1}\widetilde{\frac{\partial I^{(3)}_{112}}{\partial I^{(2)}_{11}}} & \widetilde{w_1}\widetilde{\frac{\partial I^{(3)}_{112}}{\partial I^{(2)}_{12}}} & \widetilde{w_1}\widetilde{\frac{\partial I^{(3)}_{112}}{\partial I^{(2)}_{22}}} \\ \widehat{d_1} & \widetilde{w_1}\widetilde{\frac{\partial I^{(3)}_{122}}{\partial I^{(1)}_1}} & \widetilde{w_1}\widetilde{\frac{\partial I^{(3)}_{122}}{\partial I^{(1)}_2}} & \widetilde{w_1}\widetilde{\frac{\partial I^{(3)}_{122}}{\partial I^{(2)}_{11}}} & \widetilde{w_1}\widetilde{\frac{\partial I^{(3)}_{122}}{\partial I^{(2)}_{12}}} & \widetilde{w_1}\widetilde{\frac{\partial I^{(3)}_{122}}{\partial I^{(2)}_{22}}} \end{bmatrix} \Delta\mathbf{W} = \Delta\mathbf{F}', \tag{E.26}$$

where

$$\Delta\mathbf{W} = [\Delta w_1, \Delta w_2, \Delta w_3, \Delta w_4, \Delta w_5, \Delta w_6]^T = \mathbf{W}_R - \mathbf{W}_L, \tag{E.27}$$

and

$$\Delta\mathbf{F}' = [\Delta F_4, \Delta F_5, \Delta F_6]^T = \mathbf{F}'_R - \mathbf{F}'_L, \tag{E.28}$$

and where $\mathbf{F}'_R$ and $\mathbf{F}'_L$ are reduced flux vectors in which the first three components of the associated original flux vectors are removed.

In Eq. (E.26), $\widehat{b_1}$, $\widehat{c_1}$ and $\widehat{d_1}$ are entries which contain the unknowns, $\widehat{w_4} = \widehat{\sqrt{I^{(0)}N^{(2)}_{11}}}$, $\widehat{w_5} = \widehat{\sqrt{I^{(0)}N^{(2)}_{12}}}$, and $\widehat{w_6} = \widehat{\sqrt{I^{(0)}N^{(2)}_{22}}}$, and have the following forms, respectively

$$\widehat{b_1} = 2\widetilde{w_1}\widetilde{\frac{\partial I^{(3)}_{111}}{\partial I^{(0)}}} + \widetilde{w_2}\widetilde{\frac{\partial I^{(3)}_{111}}{\partial I^{(1)}_1}} + \widetilde{w_3}\widetilde{\frac{\partial I^{(3)}_{111}}{\partial I^{(1)}_2}} + \widehat{w_4}\widetilde{\frac{\partial I^{(3)}_{111}}{\partial I^{(2)}_{11}}} + \widehat{w_5}\widetilde{\frac{\partial I^{(3)}_{111}}{\partial I^{(2)}_{12}}} + \widehat{w_6}\widetilde{\frac{\partial I^{(3)}_{111}}{\partial I^{(2)}_{22}}}, \tag{E.29}$$

$$\widehat{c_1} = 2\widetilde{w_1}\widetilde{\frac{\partial I^{(3)}_{112}}{\partial I^{(0)}}} + \widetilde{w_2}\widetilde{\frac{\partial I^{(3)}_{112}}{\partial I^{(1)}_1}} + \widetilde{w_3}\widetilde{\frac{\partial I^{(3)}_{112}}{\partial I^{(1)}_2}} + \widehat{w_4}\widetilde{\frac{\partial I^{(3)}_{112}}{\partial I^{(2)}_{11}}} + \widehat{w_5}\widetilde{\frac{\partial I^{(3)}_{112}}{\partial I^{(2)}_{12}}} + \widehat{w_6}\widetilde{\frac{\partial I^{(3)}_{112}}{\partial I^{(2)}_{22}}}, \tag{E.30}$$

$$\widehat{d_1} = 2\widetilde{w_1}\widetilde{\frac{\partial I^{(3)}_{122}}{\partial I^{(0)}}} + \widetilde{w_2}\widetilde{\frac{\partial I^{(3)}_{122}}{\partial I^{(1)}_1}} + \widetilde{w_3}\widetilde{\frac{\partial I^{(3)}_{122}}{\partial I^{(1)}_2}} + \widehat{w_4}\widetilde{\frac{\partial I^{(3)}_{122}}{\partial I^{(2)}_{11}}} + \widehat{w_5}\widetilde{\frac{\partial I^{(3)}_{122}}{\partial I^{(2)}_{12}}} + \widehat{w_6}\widetilde{\frac{\partial I^{(3)}_{122}}{\partial I^{(2)}_{22}}}, \tag{E.31}$$

where the tilde symbol over any quantity indicates that the latter is evaluated in the averaged state, $\widetilde{\mathbf{W}}$, and the hat symbol over a given parameter signifies the latter is considered as unknown in the system of equations of interest.

Substituting the expressions of Eqs. (E.29), (E.30), and (E.31) into the system of equations Eq. (E.26) yields a set of three equations for the three unknowns $\widehat{w_4}$, $\widehat{w_5}$, and $\widehat{w_6}$. The latter can be directly expressed in terms of the known averages by solving the resulting system of equations, thereby yielding a solution to the system of equations, Eq. (E.3), and consequently providing a generalized Roe matrix for the M_2 closure for both gray and non-gray radiation.

Appendix F

Axisymmetric Treatment

In the case where axisymmetric computational domains are of interest, the governing moment equations arising from the M_1, M_2, P_1 and P_3 closures must be expressed in cylindrical coordinates (r, θ, z). Expressing the weak conservation form of the governing equations, Eq. (5.1), in such a coordinate frame yields

$$\frac{\partial \mathbf{U}}{\partial t} + \frac{\partial \mathbf{F}}{\partial r} + \frac{\partial \mathbf{G}}{\partial z} = -\frac{\mathbf{S}_A}{r} + \mathbf{S}\,, \tag{F.1}$$

where $\mathbf{U}$ is the vector of conserved moments, $\mathbf{F}$ and $\mathbf{G}$ are the flux vectors in the r- and z-coordinate directions, respectively, $\mathbf{S}$ represents the source term vector, and $\mathbf{S}_A$ corresponds to the axisymmetric source term vector. The latter, i.e., the axisymmetric source term vector, arises from taking the divergence of the flux vector in the cylindrical coordinates basis. In fact, partial derivatives of tensors in cylindrical coordinates frames have an added degree of complexity compared to similar derivatives in Cartesian coordinates. This can be attributed to the fact that there can be non-zero derivatives of the metric tensor for curvilinear coordinate frames, which in turn can lead to non-zero connection coefficients, or Christoffel symbols, Γ. Expressing the systems of moment equations arising from the M_1, M_2, P_1, and P_3 closures in cylindrical coordinates requires the divergence of tensors up to fourth order, the expression of which can be found

in most of the textbooks on the subject [147–150], and can be written as follows

$$\begin{aligned}
\nabla \cdot I_i^{(1)} &= \frac{\partial I_i^{(1)}}{\partial x_i} + \Gamma_{ri}^i I_r^{(1)}, \\
\nabla \cdot I_{ij}^{(2)} &= \frac{\partial I_{ij}^{(2)}}{\partial x_j} + \Gamma_{rj}^i I_{rj}^{(2)} + \Gamma_{rj}^j I_{ir}^{(2)}, \\
\nabla \cdot I_{ijk}^{(3)} &= \frac{\partial I_{ijk}^{(3)}}{\partial x_k} + \Gamma_{rk}^i I_{rjk}^{(3)} + \Gamma_{rk}^j I_{irk}^{(3)} + \Gamma_{rk}^k I_{ijr}^{(3)}, \\
\nabla \cdot I_{ijkl}^{(4)} &= \frac{\partial I_{ijkl}^{(4)}}{\partial x_l} + \Gamma_{rl}^i I_{rjkl}^{(4)} + \Gamma_{rl}^j I_{irkl}^{(4)} + \Gamma_{rl}^k I_{ijrl}^{(4)} + \Gamma_{rl}^l I_{ijkr}^{(4)},
\end{aligned} \tag{F.2}$$

where Γ denote the connection coefficients for the coordinate system. In the particular case of cylindrical coordinates, the connection coefficients read as follows

$$\Gamma^r = \begin{bmatrix} 0 & 0 & 0 \\ 0 & -\frac{1}{r} & 0 \\ 0 & 0 & 0 \end{bmatrix}, \qquad \Gamma^\theta = \begin{bmatrix} 0 & \frac{1}{r} & 0 \\ 0 & 0 & 0 \\ 0 & 0 & 0 \end{bmatrix}, \qquad \Gamma^z = \begin{bmatrix} 0 & 0 & 0 \\ 0 & 0 & 0 \\ 0 & 0 & 0 \end{bmatrix}. \tag{F.3}$$

It should be pointed out that the subscript, g (or η), has been dropped from the expressions given in Eq. (F.2) for notational simplicity, though the same relationships apply to both gray (non-spectrally dependent) and non-gray (spectrally dependent) radiation.

For the M_1 and P_1 closures, for which angular moments up to only first order are solved for, $\mathbf{U}$, $\mathbf{F}$ and $\mathbf{G}$ are respectively given by

$$\begin{aligned}
\mathbf{U} &= \left[\; I_g^{(0)}, I_{g,r}^{(1)}, I_{g,z}^{(1)} \; \right]^T, \\
\mathbf{F} &= c \left[\; I_{g,1}^{(1)}, I_{g,rr}^{(2)}, I_{g,rz}^{(2)} \; \right]^T, \\
\mathbf{G} &= c \left[\; I_{g,2}^{(1)}, I_{g,rz}^{(2)}, I_{g,zz}^{(2)} \; \right]^T.
\end{aligned} \tag{F.4}$$

The unknown second-order closing fluxes can be related to the known lower-order moments using the closure relations of Eq. (2.20) for P_1 or Eqs. (3.14), (3.17), and (3.20)–(3.24) for M_1. Furthermore, under the assumption of isotropic scattering, the source term column vector for the system of angular moment equations arising from either the M_1 or the P_1 closures, $\mathbf{S}$, is given by

$$\mathbf{S} = c \begin{bmatrix} k(g)(4\pi I_{b\eta_c} - I_g^{(0)}) \\ -(k(g)+\sigma_s) I_{g,r}^{(1)} \\ -(k(g)+\sigma_s) I_{g,z}^{(1)} \end{bmatrix}, \quad \mathbf{S}_A = c \begin{bmatrix} I_{g,r}^{(1)} \\ I_{g,rr}^{(2)} - I_{g,\theta\theta}^{(2)} \\ I_{g,rz}^{(2)} \end{bmatrix}. \tag{F.5}$$

In the context of the M_2 closure, which involves the solution of angular moments up to second order, $\mathbf{U}$, $\mathbf{F}$ and $\mathbf{G}$ are respectively given by

$$\begin{aligned}
\mathbf{U} &= \left[\ I_g^{(0)}, I_{g,r}^{(1)}, I_{g,z}^{(1)}, I_{g,rr}^{(2)}, I_{g,rz}^{(2)}, I_{g,zz}^{(2)}\ \right]^T, \\
\mathbf{F} &= c\left[\ I_{g,r}^{(1)}, I_{g,rr}^{(2)}, I_{g,rz}^{(2)}, I_{g,rrr}^{(3)}, I_{g,rrz}^{(3)}, I_{g,rzz}^{(3)}\ \right]^T, \\
\mathbf{G} &= c\left[\ I_{g,z}^{(1)}, I_{g,rz}^{(2)}, I_{g,zz}^{(2)}, I_{g,zrr}^{(3)}, I_{g,zrz}^{(3)}, I_{g,zzz}^{(3)}\ \right]^T.
\end{aligned} \tag{F.6}$$

In the context of the proposed interpolative-based non-gray M_2 closure, the unknown third-order closing fluxes are expressed in terms of the lower-order moments via the expressions given in Eqs. (3.41), (3.42), (3.44)–(3.50), (3.53)–(3.54) and (3.55). Under the assumption of isotropic scattering, the source term vector associated with the resulting system of angular moments up to second order can be written as follows

$$\mathbf{S} = c\begin{bmatrix} k(g)(4\pi I_{b\eta_c} - I_g^{(0)}) \\ -(k(g)+\sigma_s)I_{g,r}^{(1)} \\ -(k(g)+\sigma_s)I_{g,z}^{(1)} \\ \frac{1}{3}(4\pi k(g) I_{b\eta_c} + \sigma_s I_g^{(0)}) - (k(g)+\sigma_s)I_{g,rr}^{(2)} \\ -(k(g)+\sigma_s)I_{g,rz}^{(2)} \\ \frac{1}{3}(4\pi k(g) I_{b\eta_c} + \sigma_s I_g^{(0)}) - (k(g)+\sigma_s)I_{g,zz}^{(2)} \end{bmatrix}, \quad \mathbf{S}_A = c\begin{bmatrix} I_{g,r}^{(1)} \\ I_{g,rr}^{(2)} - I_{g,\theta\theta}^{(2)} \\ I_{g,rz}^{(2)} \\ I_{g,rrr}^{(3)} - 2I_{g,r\theta\theta}^{(3)} \\ I_{g,rrz}^{(3)} - I_{g,\theta\theta z}^{(3)} \\ I_{g,rzz}^{(3)} \end{bmatrix}. \tag{F.7}$$

The P_3 closure results in a system of angular moment equations whose unknowns consist of angular moments up to third order, and for which the vectors $\mathbf{U}$, $\mathbf{F}$ and $\mathbf{G}$ are respectively given by

$$\begin{aligned}
\mathbf{U} &= \left[\ I_g^{(0)}, I_{g,r}^{(1)}, I_{g,z}^{(1)}, I_{g,rr}^{(2)}, I_{g,rz}^{(2)}, I_{g,zz}^{(2)}, I_{g,rrr}^{(3)}, I_{g,rrz}^{(3)}, I_{g,rzz}^{(3)}, I_{g,zzz}^{(3)}\ \right]^T, \\
\mathbf{F} &= c\left[\ I_{g,r}^{(1)}, I_{g,rr}^{(2)}, I_{g,rz}^{(2)}, I_{g,rrr}^{(3)}, I_{g,rrz}^{(3)}, I_{g,rzz}^{(3)}, I_{g,rrrr}^{(4)}, I_{g,rrrz}^{(4)}, I_{g,rrzz}^{(4)}, I_{g,rzzz}^{(4)}\ \right]^T, \\
\mathbf{G} &= c\left[\ I_{g,z}^{(1)}, I_{g,rz}^{(2)}, I_{g,zz}^{(2)}, I_{g,zrr}^{(3)}, I_{g,zrz}^{(3)}, I_{g,zzz}^{(3)}, I_{g,zrrr}^{(4)}, I_{g,zrrz}^{(4)}, I_{g,zrzz}^{(4)}, I_{g,zzzz}^{(4)}\ \right]^T,
\end{aligned} \tag{F.8}$$

and the corresponding source term vector, $\mathbf{S}$, based on the assumption of isotropic scat-

tering, takes the form

$$\mathbf{S} = c\begin{bmatrix} k(g)(4\pi I_{b\eta_c} - I_g^{(0)}) \\ -(k(g)+\sigma_s)I_{g,r}^{(1)} \\ -(k(g)+\sigma_s)I_{g,z}^{(1)} \\ \frac{1}{3}(4\pi k(g) I_{b\eta_c} + \sigma_s I_g^{(0)}) - (k(g)+\sigma_s)I_{g,rr}^{(2)} \\ -(k(g)+\sigma_s)I_{g,rz}^{(2)} \\ \frac{1}{3}(4\pi k(g) I_{b\eta_c} + \sigma_s I_g^{(0)}) - (k(g)+\sigma_s)I_{g,zz}^{(2)} \\ -(k(g)+\sigma_s)I_{g,rrr}^{(3)} \\ -(k(g)+\sigma_s)I_{g,rrz}^{(3)} \\ -(k(g)+\sigma_s)I_{g,rzz}^{(3)} \\ -(k(g)+\sigma_s)I_{g,zzz}^{(3)} \end{bmatrix}, \quad \mathbf{S}_A = c\begin{bmatrix} I_{g,r}^{(1)} \\ I_{g,rr}^{(2)} - I_{g,\theta\theta}^{(2)} \\ I_{g,rz}^{(2)} \\ I_{g,rrr}^{(3)} - 2I_{g,r\theta\theta}^{(3)} \\ I_{g,rrz}^{(3)} - I_{g,\theta\theta z}^{(3)} \\ I_{g,rzz}^{(3)} \\ I_{g,rrrr}^{(4)} - 3I_{g,rr\theta\theta}^{(4)} \\ I_{g,rrrz}^{(4)} - 2I_{g,r\theta\theta z}^{(4)} \\ I_{g,rrzz}^{(4)} - I_{g,\theta\theta zz}^{(4)} \\ I_{g,rzzz}^{(4)} \end{bmatrix}. \tag{F.9}$$

The unknown fourth-order closing fluxes are expressed in terms of known lower-order moments via the relationships given in Eq. (2.21), thereby resulting in the P_3 closure.

References

[1] Genong Li and Michael F. Modest. Numerical simulation of turbulence–radiation interactions in turbulent reacting flows. *WIT Transactions on State of the Art in Science and Engineering*, 15(1), 2005.

[2] R. Viskanta and M. P. Menguc. Radiation heat transfer in combustion systems. *Progress in Energy and Combustion Science*, 13:97–160, 1987.

[3] I. Glassman and P. Yaccarino. The temperature effect in sooting diffusion flames. *Proceedings of the Combustion Institute*, 18:1175–1183, 1981.

[4] J. H. Kent and H. G. Wagner. Temperature and fuel effects in sooting diffusion flames. *Proceedings of the Combustion Institute*, 20:1007–1015, 1984.

[5] R. J. Santoro, T. T. Yeh, J. J. Horvath, and H. G. Semerjian. The transport and growth of soot particles in laminar diffusion flames. *Combustion Science and Technology*, 53:89–115, 1987.

[6] C. M. Megaridis and R. A. Dobbins. Comparison of soot growth and oxidation in smoking and non-smoking ethylene diffusion flames. *Combustion Science and Technology*, 66:1–16, 1989.

[7] Kevin T. Walsh, Joseph Fielding, Mitchell D. Smooke, Marshall B. Long, Amable Linan, Kalyan Annamalai, V. R. Katta, Jay Jeffries, and Bassam Dally. A comparison of computational and experimental lift-off heights of coflow laminar diffusion flames. *Proceedings of the Combustion Institute*, 30:357–365, 2005.

[8] B. M. Kumfer, S. A. Skeen, R. Chen, and R. L. Axelbaum. Measurement and analysis of soot inception limits of oxygen-enriched coflow flames. *Combustion and Flame*, 147(3):233–242, 2006.

[9] A. D'Anna and J. H. Kent. A model of particulate and species formation applied to laminar, nonpremixed flames for three aliphatic-hydrocarbon fuels. *Combustion and Flame*, 152(4):573–587, 2008.

[10] S. B. Dworkin, M. D. Smooke, and V. Giovangigli. The impact of detailed multicomponent transport and thermal diffusion effects on soot formation in ethylene/air flames. *Proceedings of the Combustion Institute*, 32(1):1165–1172, 2009.

[11] Q. Zhang, M. J. Thomson, H. Guo, F. Liu, and G. J. Smallwood. A numerical study of soot aggregate formation in a laminar coflow diffusion flame. *Combustion and Flame*, 156(3):697–705, 2009.

[12] H. Guo, K. A. Thomson, and G. J. Smallwood. On the effect of carbon monoxide addition on soot formation in a laminar ethylene/air coflow diffusion flame. *Combustion and Flame*, 156(6):1135–1142, 2009.

[13] R. S. Mehta, D. C. Haworth, and M. F. Modest. An assessment of gas-phase reaction mechanisms and soot models for laminar atmospheric-pressure ethylene-air flames. *Proceedings of the Combustion Institute*, In Press, Corrected Proof, 2008.

[14] M. R. J. Charest, C. P. T. Groth, and Ö. L. Gülder. Numerical study on the effect of gravity on flame shape and radiation in laminar diffusion flames. In *Proceedings of the Combustion Institute Canadian Section Spring Technical Meeting*, pages 84–89, Toronto, Canada, May 12–14 2008.

[15] M. R. J. Charest, C. P. T. Groth, and Ö. L. Gülder. Parallel solution adaptive method for prediction of sooting laminar diffusion flames. In *Proceedings of the Combustion Institute Canadian Section Spring Technical Meeting*, Université de Montréal, Québec, May 11–13 2009.

[16] M. R. J. Charest, C. P. T. Groth, and Ö. L. Gülder. Numerical prediction of sooting laminar diffusion flames using adaptive mesh refinement. In *Proceedings of the 6th U.S. National Combustion Meeting*, Ann Arbor, Michigan, May 17–20 2009. Paper 23H4.

[17] M. R. J. Charest, C. P. T. Groth, and Ö. L. Gülder. A computational framework for predicting laminar reactive flows with soot formation. *Combustion Theory and Modelling*, 14(6):793–825, 2010.

[18] M. R. J. Charest. *Numerical Modelling of Sooting Laminar Diffusion Flames at Elevated Pressures and Microgravity*. PhD thesis, University of Toronto, December 2010.

[19] M. R. J. Charest, H. I. Joo, C. P. T. Groth, and Ö. L. Gülder. Experimental and numerical study of soot formation in laminar ethylene diffusion flames at elevated pressures from 10 to 35 atm. *Proceedings of the Combustion Institute*, 33:549–557, 2011.

[20] M. R. J. Charest, C. P. T. Groth, and Ö. L. Gülder. Effects of gravity and pressure on laminar co-flow methane-air diffusion flames at pressures from 1 to 60 atmospheres. *Combustion and Flame*, 158(5):860–875, 2011.

[21] M. R. J. Charest, C. P. T. Groth, and Ö. L. Gülder. Numerical study on the effects of pressure and gravity in laminar ethylene diffusion flames. *Combustion and Flame*, 158(10):1933–1945, 2011.

[22] Marc R. J. Charest, Ömer L. Gülder, and Clinton P. T. Groth. Numerical and experimental study of soot formation in laminar diffusion flames burning simulated biogas fuels at elevated pressures. *Combustion and flame*, 161(10):2678–2691, 2014.

[23] M. F. Modest. *Radiative Heat Transfer*. Academic Press, New York, 3rd edition, 2013.

[24] S. K. Godunov. Finite-difference method for numerical computations of discontinuous solutions of the equations of fluid dynamics. *Matematicheskii Sbornik*, 47:271–306, 1959.

[25] J. S. Sachdev, C. P. T. Groth, and J. J. Gottlieb. A parallel solution-adaptive scheme for predicting multi-phase core flows in solid propellant rocket motors. *International Journal of Computational Fluid Dynamics*, 19(2):159–177, 2005.

[26] X. Gao and C. P. T. Groth. A parallel adaptive mesh refinement algorithm for predicting turbulent non-premixed combusting flows. *International Journal of Computational Fluid Dynamics*, 20(5):349–357, 2006.

[27] C. P. T. Groth and J. G. McDonald. Towards physically-realizable and hyperbolic moment closures for kinetic theory. *Continuum Mechanics and Thermodynamics*, 21(6):467–493, 2009.

[28] X. Gao, S. A. Northrup, and C. P. T. Groth. Parallel solution-adaptive method for two-dimensional non-premixed combusting flows. *Progress in Computational Fluid Dynamics*, 11(2):76–95, 2011.

[29] M. R. J. Charest, C. P. T. Groth, and Ö. L. Gülder. Solution of the equation of radiative transfer using a Newton-Krylov approach and adaptive mesh refinement. *Journal of Computational Physics*, 231:3023–3040, 2012.

[30] J. G. McDonald, J. S. Sachdev, and C. P. T. Groth. Application of Gaussian moment closure to micro-scale flows with moving and embedded boundaries. *AIAA Journal*, 51(9):1839–1857, 2014.

[31] F. Liu, G. J. Smallwood, and Ö. L. Gülder. Application of the statistical narrow-band correlated-k method to low-resolution spectral intensity and radiative heat transfer calculations — effects of the quadrature scheme. *International Journal of Heat and Mass Transfer*, 43(17):3119–3135, 2000.

[32] F. Liu, G. J. Smallwood, and Ö. L. Gülder. Band lumping strategy for radiation heat transfer calculations using a narrowband model. *Journal of Thermophysics and Heat Transfer*, 14(2):278–281, 2000.

[33] F. Liu, G. J. Smallwood, and Ö. L. Gülder. Application of the statistical narrow-band correlated-k method to non-grey gas radiation in CO_2-H_2O mixtures: Approximate treatments of overlapping bands. *Journal of Quantitative Spectroscopy and Radiative Transfer*, 68(4):401–417, 2001.

[34] Michael F. Modest and Hongmei Zhang. The full-spectrum correlated-k distribution for thermal radiation from molecular gas-particulate mixtures. *Journal of Heat Transfer*, 124:30, 2002.

[35] J. R. Howell. Application of monte carlo to heat transfer problems. *Advances in Heat Transfer*, 5:1–54, 1968.

[36] H. C. Hottel and A. F. Sarofim. *Radiative Transfer*. McGraw-Hill, New York, 1967.

[37] B. G. Carlson and K. D. Lathrop. Transport theory – The method of discrete ordinates. In H. Greenspan, C. N. Kelber, and D. Okrent, editors, *Computing Methods in Reactor Physics*, pages 171–266. Gordon and Breach, London, 1968.

[38] W. A. W. A. Fiveland. Discrete-ordinates solutions of the radiative transport equation for rectangular enclosures. *Journal of Heat Transfer*, 106(4):699–706, 1984.

[39] G. D. Raithby and E. H. Chui. A finite-volume method for predicting radiant heat transfer in enclosures with participating media. *Journal of Heat Transfer*, 112(2):415–423, 1990.

[40] H. Grad. On the kinetic theory of rarefied gases. *Communications on Pure and Applied Mathematics*, 2:331–407, 1949.

[41] J. H. Jeans. The equations of radiative transfer of energy. *Monthly Notices of the Royal Astronomical Society*, 78(1):28–36, 1917.

[42] V. Kourganoff. *Basic Methods in Transfer Problems*. Dover Publications, New York, 1963.

[43] S. Mazumder and M. F. Modest. A probability density function approach to modeling turbulence-radiation interactions in nonluminous flames. *International Journal of Heat and Mass Transfer*, 42(6):971–991, 1999.

[44] G. Li and M. F. Modest. Importance of turbulence-radiation interactions in turbulent diffusion jet flames. *Journal of Heat Transfer*, 125(5):831–838, 2003.

[45] M. F. Modest and R. S. Mehta. Modeling absorption TRI in optically thick eddies. *Proceedings of Eurotherm78 - Computational Thermal Radiation in Participating Media II*, 78:225–234, 2006.

[46] A. Gupta, M. F. Modest, and D. C. Haworth. Large-eddy simulation of turbulence-radiation interactions in a turbulent planar channel flow. *Journal of Heat Transfer*, 131(6):061704–1–061704–8, 2009.

[47] M. P. Menguc and R. Viskanta. Radiative transfer in three-dimensional rectangular enclosures containing inhomogeneous anisotropically scattering media. *Journal of Quantitative Spectroscopy & Radiative Transfer*, 33:533–549, 1985.

[48] J. K. Fletcher. The solution of the multigroup neutron transport equation using spherical harmonics. *Nuclear Science and Engineering*, 84(1):33–46, 1983.

[49] B. Dubroca and J.-L. Feugeas. Theoretical and numerical study on a moment closure hierarchy for the radiative transfer equation. *SIAM Journal on Numerical Analysis*, 329:915–920, 1999.

[50] E. T. Jaynes. Information theory and statistical mechanics. *Physical Review*, 106:620–630, 1957.

[51] T. A. Brunner and J. P. Holloway. One-dimensional Riemann solvers and the maximum entropy closure. *Journal of Quantitative Spectroscopy & Radiative Transfer*, 69:543–566, 2001.

[52] J. Tencer and J.R. Howell. A parametric study of the accuracy of several radiative transfer solution methods for a set of 2-D benchmark problems. *Proceedings of the ASME 2013 Summer Heat Transfer Conference, Minneapolis*, 2013.

[53] T. Pichard, G. W. Alldredge, S. Brull, B. Dubroca, and M. Frank. An approximation of the M_2 closure: Application to radiotherapy dose simulation. *Journal of Scientific Computing*, 71(1):71–108, 2017.

[54] C. D. Hauck. High-order entropy-based closures for linear transport in slab geometry. Report ORNL/TM-6023, Oak Ridge National Laboratory, 2010.

[55] C. D. Hauck. High-order entropy-based closures for linear transport in slab geometry. *Communications in Mathematical Sciences*, 9(1):187–205, 2011.

[56] P. Monreal and M. Frank. Higher order minimum entropy approximations in radiative transfer. arXiv Online Article arXiv:0812.3063v1, Cornell University Library, 2008.

[57] J. G. McDonald and C. P. T. Groth. Towards realizable hyperbolic moment closures for viscous heat-conducting gas flows based on a maximum-entropy distribution. *Continuum Mechanics and Thermodynamics*, 25:573–603, 2013.

[58] J. G. McDonald and M. Torrilhon. Affordable robust moment closures for CFD based on the maximum-entropy hierarchy. *Journal of Computational Physics*, 251:500–523, 2013.

[59] R. Li and W. Li. 3D B_2 model for radiative transfer equation part I: Modelling. *International Journal of Numerical Analysis and Modeling*, 17(1):118–150, 2020.

[60] Steffen Schotthöfer, Tianbai Xiao, Martin Frank, and Cory Hauck. Structure preserving neural networks: A case study in the entropy closure of the boltzmann equation. In *Proceedings of the 39th International Conference on Machine Learning*, volume 162, pages 19406–19433, 2022.

[61] W.A. Porteous, M.T. Laiu, and C.D. Hauck. Data-driven, structure-preserving approximations to entropy-based moment closures for kinetic equations. *Communications in Mathematical Sciences*, 21(4):885–913, 2023.

[62] Michael R. A. Abdelmalik, Zhenning Cai, and Teddy Pichard. Moment methods for the 3d radiative transfer equation based on φ-divergences. arXiv 2304.01758, 2023.

[63] J.-F. Ripoll. An averaged formulation of the m1 radiation model with mean absorption coefficients and presumed probability density functions for turbulent flows. *Journal of Quantitative Spectroscopy and Radiative Transfer*, 83(3-4):493–517, 2004.

[64] J.-F. Ripoll and H. Pitsch. Modelling turbulence-radiation interactions for large sooting turbulent flames. *Center for Turbulence Research-Annual Research Briefs*, pages 41–52, 2002.

[65] R. Turpault. Construction of a multigroup M1 model for the radiative transfer equations. *C. R. Acad. Sci. Paris*, Ser. I 334:331–336, 2002.

[66] R. Turpault. A consistent multigroup model for radiative transfer and its underlying mean opacities. *Journal of Quantitative Spectroscopy and Radiative Transfer*, 94:357–371, 2005.

[67] Edward W. Larsen and G. C. Pomraning. The pn theory as an asymptotic limit of transport theory in planar geometry i: Analysis. *Nuclear Science and Engineering*, 109(1):49–75, 1991.

[68] Robert P. Rulko, Edward W. Larsen, and G. C. Pomraning. The pn theory as an asymptotic limit of transport theory in planar geometry ii: Numerical results. *Nuclear Science and Engineering*, 109(1):76–85, 1991.

[69] F. Liu, J. Swithenbank, and E. S. Garbett. The boundary condition of the P_N approximation used to solve the radiative transfer equation. *International Journal of Heat and Mass Transfer*, 35(8):2043–2052, 1992.

[70] J. Taine and A. Soufiani. Gas IR radiative properties: From spectroscopic data to approximate models. *Advances in Heat Transfer*, 33:295–414, 1999.

[71] A. A. Lacis and V. Oinas. A description of the correlated k distribution method for modeling nongray gaseous absorption, thermal emission, and multiple scattering in vertically inhomogeneous atmospheres. *Journal of Geophysical Research*, 96(D5):9027–9063, 1991.

[72] Thomas H Pulliam and David W Zingg. *Fundamental Algorithms in Computational Fluid Dynamics*. Springer International Publishing, 2014.

[73] J. Y. Xing, C. P. T. Groth, and J. T. C. Hu. On the use of fractional-order quadrature-based moment closures for predicting soot formation in laminar flames. *Combustion Science and Technology*, 194(1):22–44, 2019.

[74] J. A. R. Sarr, C. P. T. Groth, and J. T. C. Hu. A maximum entropy-inspired interpolative closure for the prediction of radiative heat transfer in laminar co-flow diffusion flames. *Combustion Science and Technology*, 194(1):45–79, 2022.

[75] J. Y. Xing. *Quadrature-Based Moment Closures for Predicting Soot Formation in Laminar and Turbulent Non-Premixed Flames*. PhD thesis, University of Toronto, 2022.

[76] M. D. Smooke, M. B. Long, B. C. Connelly, M. B. Colket, and R. J. Hall. Soot formation in laminar diffusion flames. *Combustion and Flame*, 143:613–628, 2005.

[77] K. K. Kuo. *Principles of Combustion*. John Wiley & Sons, Inc., New Jersey, 2nd edition, 2005.

[78] F. Liu, H. Guo, G. J. Smallwood, and Ö. L. Gülder. Effects of gas and soot radiation on soot formation in a coflow laminar ethylene diffusion flame. *Journal of Quantitative Spectroscopy & Radiative Transfer*, 73:409–421, 2002.

[79] K. M. Leung, R. P. Lindstedt, and W. P. Jones. A simplified reaction mechanism for soot formation in nonpremixed flames. *Combustion and Flame*, 87:289–305, 1991.

[80] M. Fairweather, W. P. Jones, and R. P. Lindstedt. Predictions of radiative transfer from a turbulent reacting jet in a cross-wind. *Combustion and Flame*, 89:45–63, 1992.

[81] J. O. Hirschfelder, C. F. Curtiss, and R. B. Byrd. *Molecular Theory of Gases and Liquids*. John Wiley & Sons, New York, 1969.

[82] M. D. Smooke, C. S. McEnally, L. D. Pfefferle, R. J. Hall, and M. B. Colket. Computational and experimental study of soot formation in a coflow, laminar diffusion flame. *Combustion and Flame*, 117:117–139, 1999.

[83] I. M. Kennedy, W. Kollmann, and J. Y. Chen. A model for the soot formation in a laminar diffusion flame. *Combustion and Flame*, 81:73–85, 1990.

[84] M. F. Modest. *Radiative Heat Transfer*. Academic Press, New York, 2nd edition, 2003.

[85] H. C. Hottel and E. S. Cohen. Radiant heat exchange in a gas-filled enclosure: Allowance for nonuniformity of gas temperature. *AIChE Journal*, 4(1):3–14, 1958.

[86] John C. Chai, HaeOk S. Lee, and Suhas V. Patankar. Finite volume method for radiation heat transfer. *Journal of Thermophysics and Heat Transfer*, 8(3):419–425, 1994.

[87] F. C. Lockwood and N. G. Shah. A new radiation solution method for incorporation in general combustion prediction procedures. *Proceedings of the Combustion Institute*, pages 1405–1414, 1981.

[88] M. F. Modest. The weighted-sum-of-gray-gases model for arbitrary solution methods in radiative transfer. *Journal of Heat Transfer*, 113(3):650, 1991.

[89] V. Goutiere, Fengshan Liu, and A. Charette. An assessment of real-gas modelling in 2D enclosures. *Journal of Quantitative Spectroscopy & Radiative Transfer*, 64(3):299–326, 2000.

[90] Richard Goody, Robert West, Luke Chen, and David Crisp. The correlated-k method for radiation calculations in nonhomogeneous atmospheres. *Journal of Quantitative Spectroscopy & Radiative Transfer*, 42(6):539–550, 1989.

[91] K. D. Lathrop and B. G. Carlson. Discrete ordinates angular quadrature of the neutron transport equation. Report LA 3186, Los Alamos Scientific Laboratory, 1965.

[92] C. P. Thurgood, A. Pollard, and H. A. Becker. The T_N quadrature set for the discrete ordinates method. *ASME Journal of Heat Transfer*, 117(4):1068–1070, 1995.

[93] F. Liu, K. Thomson, H. Guo, and G. J. Smallwood. Numerical and experimental study of an axisymmetric coflow laminar methane-air diffusion flame at pressures between 5 and 40 atmospheres. *Combustion and Flame*, 146:456–471, 2006.

[94] A. D'Anna, A. D'Alessio, and J. H. Kent. A computational study of hydrocarbon growth and the formation of aromatics in coflowing laminar diffusion flames. *Combustion and Flame*, 125:1196–1206, 2001.

[95] A. D'Anna and J. H. Kent. Aromatic formation pathways in non-premixed methane flames. *Combustion and Flame*, 132(4):715–722, 2003.

[96] A. D'Anna, G. Mazzotti, and J. Kent. Modeling of particulate formation in a coflowing diffusion flame. *Combustion Science and Technology*, 176(5-6):753–767, 2004.

[97] F. Liu, H. Guo, G. J. Smallwood, and Ö. L. Gülder. Numerical modelling of soot formation and oxidation in laminar coflow non-smoking and smoking ethylene diffusion flames. *Combustion Theory and Modelling*, 7:301–315, 2003.

[98] Hongsheng Guo, Fengshan Liu, Gregory J. Smallwood, and Ömer L. Gülder. A numerical study of the influence of transport properties of inert diluents on soot formation in a coflow laminar ethylene/air diffusion flame. *Proceedings of the Combustion Institute*, 29:2359–2365, 2002.

[99] Hongsheng Guo, Fengshan Liu, Gregory J. Smallwood, and Ömer L. Gülder. The flame preheating effect on numerical modelling of soot formation in a two-

dimensional laminar ethylene-air diffusion flame. *Combustion Theory and Modelling*, 6:173–187, 2002.

[100] H. Guo, F. Liu, G. J. Smallwood, and O. L. Gülder. A numerical investigation of thermal diffusion influence on soot formation in ethylene/air diffusion flames. *International Journal of Computational Fluid Dynamics*, 18(2):139–151, 2004.

[101] Hongsheng Guo, Fengshan Liu, Gregory J. Smallwood, and Ömer L. Gülder. Numerical study on the influence of hydrogen addition on soot formation in a laminar ethylene-air diffusion flame. *Combustion and Flame*, 145(1-2):324–338, 2006.

[102] Hongsheng Guo and Gregory J. Smallwood. The interaction between soot and NO formation in a laminar axisymmetric cofow ethylene/air diffusion flame. *Combustion and Flame*, 149(1-2):225–233, 2007.

[103] Hongsheng Guo and Gregory J. Smallwood. A numerical study on the influence of CO2 addition on soot formation in an ethylene/air diffusion flame. *Combustion and Flame*, 2007. in press.

[104] Q. Zhang, H. Guo, F. Liu, G. J. Smallwood, and M. J. Thomson. Modeling of soot aggregate formation in a laminar ethylene/air coflow diffusion flame with detailed PAH chemistry and an advanced sectional aerosol dynamics model. In *Proceedings of the Combustion Institute Canadian Section Spring Technical Meeting*, pages 102–107, Toronto, Canada, May 12-14 2008.

[105] Q. Zhang, H. Guo, F. Liu, G. J. Smallwood, and M. J. Thomson. Implementation of an advanced fixed sectional aerosol dynamics model with soot aggregate formation in a laminar methane/air coflow diffusion flame. *Combustion Theory and Modelling*, 12(4):621–641, 2008.

[106] F. Liu, H. Guo, and G. J. Smallwood. Effects of radiation model on the modeling of a laminar coflow methane/air diffusion flame. *Combustion and Flame*, 138(1-2):136–154, 2004.

[107] P. J. Coelho. The role of ray effects and false scattering on the accuracy of the standard and modified discrete ordinates methods. *Journal of Quantitative Spectroscopy & Radiative Transfer*, 73(2-5):231–238, 2002.

[108] P. J. Coelho. Bounded skew high-order resolution schemes for the discrete ordinates method. *Journal of Computational Physics*, 175(2):412–437, 2002.

[109] M. Sakami, A. El Kasmi, and A. Charette. Analysis of radiative heat transfer in complex two-dimensional enclosures with obstacles using the modified discrete ordinates method. *Journal of Heat Transfer*, 123(5):892–900, 2001.

[110] R. Koch, W. Krebs, S. Wittig, and R. Viskanta. Discrete ordinates quadrature schemes for multidimensional radiative transfer. *Journal of Quantitative Spectroscopy & Radiative Transfer*, 53(4):353–372, 1995.

[111] M. A. Ramankutty and A. L. Crosbie. Modified discrete ordinates solution of radiative transfer in two-dimensional rectangular enclosures. *Journal of Quantitative Spectroscopy & Radiative Transfer*, 57(1):107–140, 1997.

[112] H. Amiri, S. H. Mansouri, and P. J. Coelho. Application of the modified discrete ordinates method with the concept of blocked-off region to irregular geometries. *International Journal of Thermal Sciences*, 50(4):515–524, 2011.

[113] R. E. Marshak. Note on the spherical harmonic method as applied to the Milne problem for a sphere. *Physical Review*, 71(7):443–446, 1947.

[114] V. S. Arpaci and D. Gözüm. Thermal stability of radiating fluids: The Bénard problem. *Physics of Fluids*, 16(5):581–588, 1973.

[115] J. Fort. Information-theoretical approach to radiative transfer. *Physica A: Statistical Mechanics and its Applications*, 243(3-4):275–303, 1997.

[116] S. G. Johnson. The NLopt nonlinear-optimization package. http://github.com/stevengj/nlopt, 2014.

[117] D. Kraft. A software package for sequential quadratic programming. Technical Report DFVLR-FB 88-28, Institut für Dynamik der Flugsysteme, Oberpfaffenhofen, July 1988.

[118] D. Kraft. Algorithm 733; tomp—Fortran modules for optimal control calculations. *ACM Transactions on Mathematical Software*, 20(3):262–281, 1994.

[119] G. W. Alldredge, C. D. Hauck, D. P. O'Leary, and A. L. Tits. Adaptive change of basis in entropy-based moment closures for linear kinetic equations. *Journal of Computational Physics*, 258:489–508, 2014.

[120] G. W. Alldredge, C. D. Hauck, and A. L. Tits. High-order entropy-based closures for linear transport in slab geometry II: A computational study of the optimization problem. *SIAM Journal on Scientific Computing*, 34(4):B361–B391, 2012.

[121] R. V. Abramov. An improved algorithm for the multidimensional moment-constrained maximum entropy problem. *Journal of Computational Physics*, 226:621–644, 2007.

[122] R. V. Abramov. The multidimensional moment-constrained maximum entropy problem: A BFGS algorithm with constraint scaling. *Journal of Computational Physics*, 228:96–108, 2009.

[123] C.D. Levermore. Relating Eddington factors to flux limiters. *Journal of Quantitative Spectroscopy & Radiative Transfer*, 31(2):149–160, 1984.

[124] J. A. R. Sarr and C. P. T. Groth. A first-order maximum-entropy-inspired interpolative closure for radiative heat transfer in non-gray participating media. *Journal of Quantitative Spectroscopy and Radiative Transfer*, 2022.

[125] J. Cernohorsky and S. A. Bludman. Maximum entropy distribution and closure for bose-einstein and fermi-dirac radiation transport. *The Astrophysical Journal*, 433(2):250, 1994.

[126] D. Kershaw. Flux limiting nature's own way. Technical report, Lawrence Livermore Laboratory, 1976.

[127] J. M. Peña and Thomas Sauer. On the multivariate horner scheme. *SIAM Journal on Numerical Analysis*, 37(4):1186–1197, 2000.

[128] Johannes Czekansky and Tomas Sauer. The multivariate horner scheme revisited. *BIT Numerical Mathematics*, 55(4):1043–1056, 2014.

[129] J. A. R. Sarr and C. P. T. Groth. Maximum-entropy inspired interpolative closure for radiative heat transfer in gray participating media. In *Proceedings of the 9th*

International Symposium on Radiative Transfer, RAD-19, June 3-7, 2019, Athens, Greece, pages 253–260. International Centre for Heat and Mass Transfer, 2019.

[130] J. A. R. Sarr and C. P. T. Groth. A second-order maximum-entropy inspired interpolative closure for radiative heat transfer in gray participating media. *Journal of Quantitative Spectroscopy and Radiative Transfer*, 255:107–238, 2020.

[131] P. Monreal. *Moment Realizability and Kershaw Closures in Radiative Transfer*. PhD thesis, RWTH Aachen University, November 2012.

[132] M. G. Blyth and C. Pozrikidis. A lobatto interpolation grid over the triangle. *IMA Journal of Applied Mathematics*, 71(1):153–169, 2006.

[133] Albert Arking and Kenneth Grossman. The influence of line shape and band structure on temperatures in planetary atmospheres. *Journal of the Atmospheric Sciences*, 29(5):937–949, 1972.

[134] P. Y. C. Lee, K. G. T. Hollands, and G. D. Raithby. Reordering the absorption coefficient within the wide band for predicting gaseous radiant exchange. *Journal of Heat Transfer*, 118(2):394, 1996.

[135] K. C. Tang and M. Q. Brewster. K-distribution analysis of gas radiation with nongray, emitting, absorbing, and anisotropic scattering particles. *Journal of Heat Transfer*, 116(4):980, 1994.

[136] L. S. Rothman, I. E. Gordon, A. Barbe, D. C. Benner, P. F. Bernath, M. Birk, V. Boudon, L. R. Brown, A. Campargue, J. P. Champion, K. Chance, L. H. Coudert, V. Dana, V. M. Devi, S. Fally, J. M. Flaud, R. R. Gamache, A. Goldman, D. Jacquemart, I. Kleiner, N. Lacome, W. J. Lafferty, J. Y. Mandin, S. T. Massie, S. N. Mikhailenko, C. E. Miller, N. Moazzen-Ahmadi, O. V. Naumenko, A. V. Nikitin, J. Orphal, V. I. Perevalov, A. Perrin, A. Predoi-Cross, C. P. Rinsland, M. Rotger, M. Šimečková, M. A. H. Smith, K. Sung, S. A. Tashkun, J. Tennyson, R. A. Toth, A. C. Vandaele, and J. Vander Auwera. The HITRAN 2008 molecular spectroscopic database. *Journal of Quantitative Spectroscopy & Radiative Transfer*, 2009.

[137] W. Malkmus. Random Lorentz band model with exponential-tailed s^{-1} line-intensity distribution function. *Journal of the Optical Society of America*, 57(3):323–329, 1967.

[138] A. Soufiani and J. Taine. High temperature gas radiative property parameters of statistical narrow-band model for H_2O, CO_2 and CO, and correlated-k model for H_2O and CO_2. *International Journal of Heat and Mass Transfer*, 40(4):987–991, 1997.

[139] Michael F. Modest. Narrow-band and full-spectrum k-distributions for radiative heat transfer - correlated-k vs. scaling approximation. *Journal of Quantitative Spectroscopy and Radiative Transfer*, 76(1):69–83, 2003.

[140] Ph. Rivière, A. Soufiani, and J. Taine. Correlated-k and fictitious gas methods for h2o near 2.7 µm. *Journal of Quantitative Spectroscopy and Radiative Transfer*, 48(2):187–203, 1992.

[141] PH. Rivière, A. Soufiani, and J. Taine. Correlated-k fictitious gas model for h2o infrared radiation in the voigt regime. *Journal of Quantitative Spectroscopy and Radiative Transfer*, 53(3):335–346, 1995.

[142] V. Goutiere, A. Charette, and L. Kiss. Comparative performance of nongray gas modeling techniques. *Numerical Heat Transfer, Part B: Fundamentals*, 41(3-4):361–381, 2002.

[143] S. C. Lee and C. L. Tien. Effect of soot shape on soot radiation. *Journal of Quantitative Spectroscopy & Radiative Transfer*, 29(3):259–265, 1983.

[144] J. D. Felske and C. L. Tien. Use of the Milne-Eddington absorption coefficient for radiative heat transfer in combustion systems. *Journal of Heat Transfer*, 99(3):458–465, 1977.

[145] P. D. Lax. *Hyperbolic Systems of Conservation Laws and the Mathematical Theory of Shock Waves*, volume 11 of *CMBS–NSF Regional Conference Series in Applied Mathematics*. SIAM, Philadelphia, 1973.

[146] C. D. Levermore. Moment closure hierarchies for kinetic theories. *Journal of Statistical Physics*, 83:1021–1065, 1996.

[147] J. G. McDonald. Numerical modeling of micron-scale flows using the Gaussian moment closure. Master's thesis, University of Toronto, 2005.

[148] D. C. Kay. *Schaum's outline of theory and problems of tensor calculus*. McGraw-Hill, New York, 1988.

[149] A. D. Michal. *Matrix and tensor calculus: With applications to mechanics, elasticity, and aeronautics*. J. Wiley & Sons, inc, New York, 1947.

[150] I. S. Sokolnikoff. *Tensor analysis: Theory and applications*. Wiley, New York, 1951.

[151] E. Anderson, Z. Bai, C. Bischof, S. Blackford, J. Demmel, J. Dongarra, J. Du Croz, A. Greenbaum, S. Hammarling, A. McKenney, and D. Sorensen. *LAPACK Users' Guide*. Society for Industrial and Applied Mathematics, Philadelphia, PA, third edition, 1999.

[152] E. F. Toro. *Riemann Solvers and Numerical Methods for Fluid Dynamics: A Practical Introduction*. Springer-Verlag, New York, 1999.

[153] C. Hirsch. *Numerical Computation of Internal and External Flows, Volume 1, Fundamentals of Numerical Discretization*. John Wiley & Sons, Toronto, 1989.

[154] C. Hirsch. *Numerical Computation of Internal and External Flows, Volume 2, Computational Methods for Inviscid and Viscous Flows*. John Wiley & Sons, Toronto, 1990.

[155] H. Lomax, T. H. Pulliam, and D. W. Zingg. *Fundamentals of Computational Fluid Dynamics*. Springer-Verlag, New York, 2001.

[156] A. Harten. High resolution schemes for hyperbolic conservation laws. *Journal of Computational Physics*, 49:357–393, 1983.

[157] P. L. Roe. Approximate Riemann solvers, parameter vectors, and difference schemes. *Journal of Computational Physics*, 43:357–372, 1981.

[158] J. P. Boris and D. L. Book. Flux-corrected transport. I. SHASTA, a fluid transport algorithm that works. *Journal of Computational Physics*, 11:38–69, 1973.

[159] B. van Leer. Towards the ultimate conservative difference scheme. II. Monotonicity and conservation combined in a second order scheme. *Journal of Computational Physics*, 14:361–370, 1974.

[160] V. Venkatakrishnan. On the accuracy of limiters and convergence to steady state solutions. Paper 93-0880, AIAA, January 1993.

[161] T. J. Barth. Recent developments in high order k-exact reconstruction on unstructured meshes. Paper 93-0668, AIAA, January 1993.

[162] J. J. Gottlieb and C. P. T. Groth. Assessment of Riemann solvers for unsteady one-dimensional inviscid flows of perfect gases. *Journal of Computational Physics*, 78:437–458, 1988.

[163] S. Osher and F. Solomon. Upwind difference schemes for hyperbolic systems of conservation laws. *Mathematics of Computation*, 38(158):339–374, 1982.

[164] B. Einfeldt. On Godunov-type methods for gas dynamics. *SIAM Journal on Numerical Analysis*, 25:294–318, 1988.

[165] Giorgio Rosatti and Lorenzo Begnudelli. A closure-independent generalized Roe solver for free-surface, two-phase flows over mobile bed. *Journal of Computational Physics*, 255:362–383, 2013.

[166] S. L. Brown. *Approximate Riemann Solvers for Moment Models of Dilute Gases*. PhD thesis, University of Michigan, 1996.

[167] E. F. Toro, M. Spruce, and W. Speares. Restoration of the contact surface in the HLL-Riemann solver. *Shock Waves*, 4(1):25–34, 1994.

[168] S. A. Northrup and C. P. T. Groth. Solution of laminar diffusion flames using a parallel adaptive mesh refinement algorithm. Paper 2005–0547, AIAA, January 2005.

[169] M. J. Aftosmis, M. J. Berger, and J. E. Melton. Robust and efficient Cartesian mesh generation for component-based geometry. *AIAA Journal*, 36(6):952–960, 1998.

[170] M. J. Berger and P. Colella. Local adaptive mesh refinement for shock hydrodynamics. *Journal of Computational Physics*, 82:64–84, 1989.

[171] M. J. Berger and J. Oliger. Adaptive mesh refinement for hyperbolic partial differential equations. *Journal of Computational Physics*, 53:484–512, 1984.

[172] M. J. Berger and J. S. Saltzman. AMR on the CM-2. *Applied Numerical Mathematics*, 14:239–253, 1994.

[173] J. J. Quirk and S. Karni. On the dynamics of a shock-bubble interaction. *Journal of Fluid Mechanics*, 318:129–163, 1996.

[174] D. De Zeeuw and K. G. Powell. An adaptively refined Cartesian mesh solver for the Euler equations. *Journal of Computational Physics*, 104:56–68, 1993.

[175] C. P. T. Groth, D. L. De Zeeuw, T. I. Gombosi, and K. G. Powell. Three-dimensional MHD simulation of coronal mass ejections. *Advances in Space Research*, 26(5):793–800, 2000.

[176] C. P. T. Groth, D. L. De Zeeuw, K. G. Powell, T. I. Gombosi, and Q. F. Stout. A parallel solution-adaptive scheme for ideal magnetohydrodynamics. Paper 99-3273, AIAA, June 1999.

[177] Z. J. Zhang and C. P. T. Groth. Parallel high-order anisotropic block-based adaptive mesh refinement finite-volume scheme. Paper 2011-3695, AIAA, June 2011.

[178] L. Freret and C. P. T. Groth. Anisotropic non-uniform block-based adaptive mesh refinement for three-dimensional inviscid and viscous flows. Paper 2015-2613, AIAA, June 2015.

[179] L. Freret, L. Ivan, H. De Sterck, and C. P. T. Groth. A high-order finite-volume method with anisotropic AMR for ideal MHD flows. Paper 2017-0845, AIAA, January 2017.

[180] L. Freret, C. P. T. Groth, T. B. Nguyen, and H. De Sterck. High-order finite-volume scheme with anisotropic adaptive mesh refinement: Efficient inexact Newton method for steady three-dimensional flows. Paper 2017-3297, AIAA, June 2017.

[181] L. Freret, L. Ivan, H. De Sterck, and C. P. T. Groth. High-order finite-volume method with block-based AMR for magnetohydrodynamics flows. *Journal of Scientific Computing*, 79(1):176—208, 2019.

[182] L. Freret, M. Williamsche, and C. P. T. Groth. Parallel anisotropic non-uniform block-based adaptive mesh refinement for three-dimensional inviscid and viscous flows. submitted to the Journal of Computational Physics, July 2020.

[183] W. Gropp, E. Lusk, and A. Skjellum. *Using MPI*. MIT Press, Cambridge, Massachussets, 1999.

[184] A. Jameson. Solution of the Euler equations by a multigrid method. *Applied Mathematics and Computation*, 13:327–356, 1983.

[185] X. Gao and C. P. T. Groth. A parallel solution-adaptive method for three-dimensional turbulent non-premixed combusting flows. *Journal of Computational Physics*, 229(5):3250–3275, 2010.

[186] Y. Saad and M. H. Schultz. GMRES: A generalized minimal residual algorithm for solving nonsymmetric linear equations. *SIAM Journal for Scientific and Statistical Computing*, 7(3):856–869, 1986.

[187] Y. Saad. Krylov subspace methods on supercomputers. *SIAM Journal for Scientific and Statistical Computing*, 10(6):1200–1232, 1989.

[188] P. N. Brown and Y. Saad. Hybrid Krylov methods for nonlinear systems of equations. *SIAM Journal for Scientific and Statistical Computing*, 11(3):450–481, 1990.

[189] Y. Saad. *Iterative Methods for Sparse Linear Systems*. PWS Publishing Company, Boston, 1996.

[190] R. S. Dembo, S. C. Eisenstat, and T. Steihaug. Inexact newton methods. *SIAM Journal on Numerical Analysis*, 19(2):400–408, 1982.

[191] E. J. Nielsen, W. K. Anderson, R. W. Walters, and D. E. Keyes. Application of Newton-Krylov methodology to a three-dimensional unstructured Euler code. Paper 95-1733-CP, AIAA, June 1995.

[192] T. J. Barth and S. W. Linton. An unstructured mesh newton solver for compressible fluid flow and its parallel implementation. Paper 95-0221, AIAA, January 1995.

[193] D. A. Knoll, P. R. McHugh, and D. E. Keyes. Newton-Krylov methods for low-Mach-number compressible combustion. *AIAA Journal*, 34(5):961–967, 1996.

[194] A. Pueyo and D. W. Zingg. An efficient Newton-GMRES solver for aerodynamic computations. Paper 97-1955, AIAA, June 1997.

[195] H. Luo, J. D. Baum, and R. Löhner. A fast, matrix-free implicit method for compressible flows on unstructured grids. *Journal of Computational Physics*, 146:664–690, 1998.

[196] P. R. McHugh, D. A. Knoll, and D. E. Keyes. Application of Newton-Krylov-Schwarz algorithm to low-Mach-number compressible combustion. *AIAA Journal*, 36(2):290–292, 1998.

[197] W. A. Mulder and B. van Leer. Experiments with implicit upwind methods for the Euler equations. *Journal of Computational Physics*, 59:232–246, 1985.

[198] W. Wang, A. E. Karataş, C. P. T. Groth, and Ö. L. Gülder. Experimental and numerical study of laminar flame extinction for syngas and syngas-methane blends. *Combustion Science and Technology*, 190(8):1455–1471, 2018.

[199] W. Wang, A. E. Karataş, C. P. T. Groth, and Ö. L. Gülder. Combined experimental and numerical study of ethanol laminar flame extinction. *Combustion Science and Technology*, 190(8):1472–1487, 2018.

[200] Gregory P. Smith, David M. Golden, Michael Frenklach, Nigel W. Moriarty, Boris Eiteneer, Mikhail Goldenberg, C. Thomas Bowman, Ronald K. Hanson, Soonho Song, William C. Gardiner, Jr., Vitali V. Lissianski, and Zhiwei Qin. Gri-mech 3.0, 2002. http://www.me.berkeley.edu/gri_mech/.

[201] Molina. A, Schefer R.W., and Houf W.G. Radiative fraction and optical thickness in large-scale hydrogen-jet fires. *Proceedings of the Combustion Institute*, 31(2):2565–2572, 2007.